

Carnegie Mellon University

CARNEGIE INSTITUTE OF TECHNOLOGY

THESIS

SUBMITTED IN PARTIAL FULFILLMENT OF THE REQUIREMENTS

FOR THE DEGREE OF Doctor of Philosophy

TITLE *Modeling the Fate of Engineered Metal and Metal Oxide Nanoparticles in Surface Waters and Sediments: Environmental Drivers, Particle Properties, and Implications for Model Design*

PRESENTED BY **Amy Lauren Dale**

ACCEPTED BY THE DEPARTMENT OF

Engineering and Public Policy & Civil and Environmental Engineering

Elizabeth A. Casman
ADVISOR, MAJOR PROFESSOR

April 25, 2016
DATE

Gregory Lowrey
ADVISOR, MAJOR PROFESSOR

April 25, 2016
DATE

Douglas Sicker
DEPARTMENT HEAD

April 25, 2016
DATE

David A. Dzombak
DEPARTMENT HEAD

April 29, 2016
DATE

APPROVED BY THE COLLEGE COUNCIL

Vijayakumar Bhagavatula
DEAN

May 5, 2016
DATE

**MODELING THE FATE OF ENGINEERED METAL AND METAL OXIDE
NANOPARTICLES IN SURFACE WATERS AND SEDIMENTS:
Environmental drivers, particle properties, and implications for model design**

Submitted in partial fulfillment of the requirements for

the degree of

Doctor of Philosophy

in

Engineering and Public Policy
Civil and Environmental Engineering

Amy Lauren Dale

B.S., Bioinformatics, University of Pittsburgh
M.S., Civil and Environmental Engineering, Carnegie Mellon University

Carnegie Mellon University
Pittsburgh, PA

May 2016

DEDICATION

I dedicate this work to the memory of Luke Davies, my "academic brother" and friend, who was far too young to die. If lust for life were all we needed, Luke would have outlived us all.

ACKNOWLEDGEMENTS

This research rests, not on the shoulders of giants, but on the shoulders of an uncountable number of people whose life and work have intersected in both great and small ways with my own. It is a sign of my great fortune that this dissertation has been shaped by too many friends, colleagues, and mentors to name here. Certain omissions, however, would be nothing short of criminal.

First and foremost, I am indebted to my research advisors, Dr. Elizabeth Casman and Dr. Gregory Lowry. Liz and Greg: Thank you for taking a big chance on a Bioinformatics major who really wanted to be an engineer. Thank you for five years of guidance, encouragement, patience, latitude, and – yes – just the right amount of pressure. Thank you as well to the remaining members of my thesis committee: Dr. Mitchell Small, Dr. Peter Adams, and Dr. Robert Tilton. Your support and your brilliant insights helped me out of more than one major research rut. Your passion for your work is an inspiration.

Thank you to the researchers and institutions that hosted me during my graduate studies. I owe an especial debt of gratitude to Lewis Linker, Gary Schenk, Gopal Bhatt, and Matthew Johnston at the Chesapeake Bay Program Office of the U.S. EPA, who not only gave me invaluable research advice but also made me feel at home for a summer in Annapolis, M.D. I owe similar thanks to Dr. Martin Scheringer and Dr. Antonia Praetorius for hosting my visit to ETH Zürich in 2014. Thank you in particular to Antonia for her support as a friend, her unrivaled culinary skills, and her willingness to engage in heated debates about the path forward for environmental fate modeling of nanomaterials. Thank you to Robert Ambrose and Timothy Wool at the U.S. EPA for providing guidance on WASP7, and to Dr. Frédérique Laurent-Nègre at École Centrale Paris for her guidance regarding the Extended Quadrature Method of Moments.

Thank you to Dr. M. Granger Morgan, Dr. Inês Azevedo, and Dr. Marvin Sirbu for bringing me on as a teaching assistant during my graduate studies. Thank you for introducing me to the art

of teaching and grading, and for your infinite patience on those (hopefully few) weeks when I failed to successfully juggle one too many time commitments. Thank you finally to the CMU staff who have streamlined the administrative side of my doctoral studies or otherwise enriched them, including (but not limited to) Vicki Finney, Patti Steranchak, Barbara Bugosh, Adam Loucks, Maxine Leffard, Mireille Mobley, and Erika Ninos.

To mom, grandma, and grandpa: Thank you for everything you ever did for me, and everything I ever dared to do. I live my life by your example. To Lisa, Dan, Lua, and Ira: Thank you for always reminding me what really matters. To my brother Nate: Now it's your turn. (Just kidding! You can't be the cooler twin AND be just as over-educated.)

To Jon, Catharine, Katherine, Ethan, Eleanor, Auntie Jayne, and the rest of the Dale/Roseberry/King/Trinovitch/Catlin/Lester/Hipschman clan: Thank you for being my second family, in name and in deed.

To my husband Alex: Wow, who knew our first five years of marriage would look like this? Thank you for better and for worse. Thank you for sinus infections and the Swiss Alps, for late nights and long-distance phone calls, for the outside perspective and the out-of-doors, for the leftovers and the backrubs and the easy silences. Who I was without you, I can do without.

Finally, I owe thanks to the many agencies and organizations that have funded my research. This work was supported by a Carnegie Institute of Technology Dean's Fellowship, a National Science Foundation NEEP (Nanotechnology--Environmental Effects and Policy) IGERT Fellowship, a Dowd-ICES Fellowship (as selected by Philip and Marsha Dowd and administered by the Carnegie Mellon Institute for Complex Engineered Systems), and a U.S. Environmental Protection Agency Science to Achieve Results (STAR) Fellowship. Additional support included an ARCS (Achievement Rewards for College Scientists) Scholarship, the Innovyze Excellence in Computational Hydraulics/Hydrology Award co-sponsored by Innovyze and AAEES (American

Academy of Environmental Engineers and Scientists), and an Anchor QEA Scholarship. Finally, I would like to thank the NSF and EPA-funded Transatlantic Initiative for Nanotechnology and the Environment (TINE) and Center for the Environmental Implications of Nanotechnology (CEINT) for providing funding and for promoting collegial and collaborative research at the cutting edge.

ABSTRACT

Mathematical models improve our fundamental understanding of pollutant fate in the environment and facilitate risk assessment, environmental management, and policy development activities. For nearly a decade, researchers have struggled with the question of how to model nanoparticles (NPs), an emerging class of environmental contaminants whose behavior in surface waters and sediments is controlled by complex interactions between particle properties and environmental factors.

Population balance models, which track the size distribution of a particle population as it changes due to physicochemical processes, are a promising alternative to classical mass balance models that only track the total NP mass. However, the strengths and weaknesses of different population balance methods have not yet been explored in-depth for NPs. This work introduces three projects that, together, (1) probe the influence of spatiotemporal variation in environmental conditions on NP fate, (2) investigate the influence of common simplifying assumptions on model predictions, and (3) explore population balance for problems of NP dissolution and aggregation in water. Focus is placed on spherical metal and metal oxide NPs. Chapter 1 reviews past and current approaches in NP fate modeling, highlights key challenges, and frames the scope and objectives of this work. Chapter 2 presents a sediment diagenesis model that explores the influence of organic carbon, dissolved oxygen, and naturally-occurring sulfides on the distribution and speciation of antibacterial silver NPs and their reaction by-products in freshwater sediments. Chapter 3 presents a coupled hydrologic, agricultural, and water quality model that predicts silver and zinc oxide NP fate in a freshwater watershed under spatiotemporally variable environmental conditions. This basin-scale model reveals the unintended consequences of simplifying assumptions commonly used in large-scale fate models of NPs. Chapter 4 compares alternative population balance modeling frameworks that vary with respect to runtimes, accuracy, and extensibility to environmentally relevant systems and complex particle types. Chapter 5 summarizes key findings and identifies high-priority research

areas for experimentalists and modelers interested in the development of next-generation models with greater relevance for scientific investigations at the laboratory scale as well as risk management and regulation at the river or watershed scale.

TABLE OF CONTENTS

1	Introduction	1
1.1	Motivation and Scope	1
1.2	Literature Review	3
1.3	Objectives and Approach	11
2	Modeling Nanosilver Transformations in Freshwater Sediments.....	13
2.1	Introduction	13
2.2	Methods.....	15
2.3	Results.....	25
2.4	Discussion	31
3	Stream dynamics and chemical transformations control the environmental fate of silver and zinc oxide nanoparticles in a watershed-scale model.....	35
3.1	Introduction	35
3.2	Methods.....	38
3.3	Results.....	42
3.4	Discussion	49
4	A comparison of population balance frameworks for models of nanoparticle aggregation and surface transformations in aqueous media.....	54
4.1	Introduction	54
4.2	Methods.....	56
4.3	Results.....	75
4.4	Discussion	83
5	Summary, Outlook, and Policy Implications.....	87
5.1	Summary of Key Findings.....	87
5.2	Recommendations for Future Work.....	88
5.3	Related Publications	98
	Bibliography.....	99

Appendix A. Supplement to Chapter 2, the Sediment Model.....	114
A.1 Supporting Methods.....	114
A.2 Supporting Tables.....	119
A.3 Supporting Figures	125
Appendix B. Supplement to Chapter 3, the Watershed Model.....	131
B.1 Supporting Methods.....	131
B.2 Supporting Tables.....	137
B.3 Supporting Figures	140
Appendix C. Supplement to Chapter 4, the Population Balance Models.....	148
C.1 Supporting Methods.....	148
C.2 Supporting Figures	184

LIST OF TABLES

Table 1-1. Metal and metal oxide NPs of environmental concern.....	1
Table 2-1. Ranges of sediment model parameters.....	24
Table 4-1. Runtime efficiencies of the three PB methods.....	78
Table A-1. Sediment model state variables	119
Table A-2. Sediment model reaction equations and terms.....	120
Table A-3. Justification of model parameter values in Table 2-1	121
Table A-4. Sediment model elasticities, ranked from highest to lowest.....	123
Table B-1. Land uses modeled in the Phase 5.3.2 Chesapeake Bay Watershed Model	137
Table B-2. James River Basin model inputs (constants only).....	138
Table B-3. Maximum of simulated 95 th percentile total metal concentrations originating from NP sources over all segments (averaged over 2 cm sediment depth) compared to observed metal concentrations (from all sources) in the James River basin downstream of the modeled region.....	139
Table B-4. Aeration tank model system parameters and outputs	139
Table B-5. ZnO speciation in the aeration tank model for different scenarios.....	139

LIST OF FIGURES

Figure 1-1. Chemical transformations impacting the toxicity and mobility of reactive NPs and their reaction by-products in the environment.....	5
Figure 2-1. Model schematic for the nanosilver sediment chemistry model.....	18
Figure 2-2. Sediment model calibration results.....	26
Figure 2-3. Results for the nominal case under five different Ag NP percent sulfidation scenarios.	28
Figure 2-4. System response to low, mid, and high levels of organic carbon for 85% sulfidized Ag NPs.....	30
Figure 3-1. Structure of the coupled WSM/WASP7 model.	37
Figure 3-2. Location and speciation over time of a) Zn from ZnO NPs and b) Ag from Ag NPs, expressed as percent by mass in the water column, oxic surface sediments, and anoxic deep sediments.....	44
Figure 3-3. Comparison of the cumulative total zinc and silver load to the river over time from effluent and agricultural runoff to the total mass remaining in the river and sediment bed over time	45
Figure 3-4. Cumulative distribution functions (CDFs) of total metal concentrations over time for each segment in surface water and sediment for Ag and Zn.	47
Figure 3-5. Average total metal concentrations in each river segment vs. the total metal load to that segment (upstream load + effluent load + runoff load) over the course of the simulation.....	48
Figure 3-6. Total Ag concentrations (ng Ag/L) for two river segments for the five-year period that includes the driest year and wettest year in the simulation	49
Figure 4-1. Approximation of the particle size distribution in the Sectional Method, the classical and Direct Quadrature Method of Moments, and the Extended Quadrature Method of Moments	60
Figure 4-2. Model results for aggregation, dissolution, and aggregation + dissolution of 100 g/m ³ of a lognormal population of ~50±10 nm NPs (aggregation, dissolution) or 50±2 nm NPs (aggregation + dissolution).....	77
Figure 4-3. Evolution of the particle size distribution (PSD) for the cases shown in Figure 4-2.	80
Figure 4-4. Effect of the number of size bins on error in the SM for dissolution of ~50±10 nm NPs.....	81
Figure 4-5. Comparison of a simple one-parameter, size-independent conventional mass balance model to benchmarked population balance models for initial distributions with varying polydispersity and skewness	83

Figure 5-1. NP fate processes that require univariate, bivariate, and trivariate methods.....	92
Figure A-1. Change in depth profiles of all state variables over time after a pulse input of 2.9 g of 85% sulfidized nanoparticles.....	125
Figure A-2. Sensitivity of seasonal trends in Ag^+ efflux to temperature coefficients and oxygen availability.....	126
Figure A-3. Loss of Ag^0 over time for a pulse input of 85% sulfidized Ag NPs.....	127
Figure A-4. System response to constant inputs of 85% sulfidized nanoparticles ($0.03 \text{ mg Ag/m}^2\text{-d}$)	128
Figure A-5. Change in concentration profile and sulfidation of Ag NPs in the sediment over time	129
Figure A-6. A diagram of the exponentially expanding grid space showing key variables.....	130
Figure B-1. GIS plots of the James River Basin	140
Figure B-2. Seasonal trends in key environmental drivers (system conditions)	141
Figure B-3. Non-point versus point sources of NP stream loads in the James River Basin model.....	142
Figure B-4. Resuspension and deposition rate predictions in the James River Basin model	143
Figure B-5. Sensitivity of the accumulation of Ag NPs in the river and sediments over time to spatiotemporal variability in sediment resuspension and deposition rates.....	144
Figure B-6. Total Ag concentrations for each segment in which concentrations are non-zero for the five year stretch which contains the driest and wettest years in the simulation.....	145
Figure B-7. Sensitivity of the predicted mass accumulation of Ag in the river and sediments at $t = 20$ years to assumptions about the strength of the association of Ag NPs with sediments in the water column and river bed.....	146
Figure B-8. Speciation of Zn in the WASP7 river simulation model for an alternative input scenario in which 85% of Zn in effluent is present as ZnO NPs (based on the aeration tank model sensitivity analysis, Table B-5) and the lowest ZnO dissolution rate is used.	146
Figure B-9. Total suspended solids (TSS) calibration details.	147
Figure C-1. Model results compared to experimental data for the calibration procedure used to provide an order-of-magnitude estimate of the ZnO NP dissolution rate and aggregation rate for all test cases	184
Figure C-2. Model results for dissolution of 100 g/m^3 of a lognormal population of NPs with different initial particle sizes for sink conditions.....	185

Figure C-3. Model results for dissolution of 100 g/m^3 of a lognormal population of NPs with different initial particle sizes for dissolution to equilibrium	186
Figure C-4. Model results for aggregation of 100 g/m^3 of a lognormal population of NPs with different initial particle sizes.....	187
Figure C-5. Error in the EQMOM, the DQMOM without ratio constraints, and the SM compared to the analytical solution for estimates of the evolution of the (normalized) number concentration during dissolution	188
Figure C-6. Initial particle size distributions in the Sectional Method for the error analysis shown in Figure 4-4.....	188
Figure C-7. Effect of the resolution of the size coordinate on error and runtimes in the SM for aggregation of $\sim 50 \pm 10 \text{ nm}$ NPs.....	189
Figure C-8. Initial particle size distributions used in the analysis presented in Figure 4-5 transformed to be in terms of the internal coordinate, particle mass.....	189
Figure C-9. First-order linear inhomogenous equation (Equation 4-24) fit for the case of dissolution to equilibrium	190

1 Introduction

"A number of choices need to be made at the start of any model development ... The compromise is between simplicity and realism. The best solution emphasizes the former without undue violence to the latter."

- Dominic Di Toro (2001)

1.1 Motivation and Scope

The recent emergence of a global market for textiles, paints and pigments, cosmetics, packaging, and other products containing metal or metal oxide nanoparticles (Me/MeO NPs) such as silver (Ag), zinc oxide (ZnO), copper oxide (CuO), and titania (TiO₂) (Table 1-1) has incited concerns about the potential ecotoxicity of these NPs following accidental release to the environment during product use or disposal.¹

Table 1-1. Metal and metal oxide NPs of environmental concern²

Me/MeO NP	Applications with high environmental releases	Max estimated global production (metric tons/year)
TiO ₂	Paints, protective coatings, UV filter in sunscreens & cosmetics	75,000
Fe & Fe Oxides	Pigments in coatings, plastics, cosmetics	19,000
ZnO	UV filter in cosmetics & sunscreen, antimicrobial agent	16,000
Al ₂ O ₃	Coatings and paints, cosmetics	12,000
Ag	Antibacterial coatings (textiles, plastics), antibacterial in cosmetics	300
Cu & Cu Oxides	Anti-microbial, -biotic, -fungal agent in coatings	50

Mathematical models of the transport and physicochemical transformation of Me/MeO NPs in the environment enhance scientific understanding and facilitate environmental decision-making. For scientific purposes, models can be used to test hypotheses, identify key uncertainties, and identify the processes controlling fate in complex systems. For regulatory purposes, modelers test release and exposure scenarios in the presence or absence of risk management practices in order to determine whether NPs pose environmental risks and guide management strategy development.³

To date, most models of NP fate and transport in rivers and lakes have been designed to predict environmental concentrations (PECs) and compare them to "no adverse effect"

concentrations (PNECs) in order to determine risk.⁴ However, models have also been used (with mixed success) to (1) compare the relative fate of NPs with different chemical identities and/or prioritize NPs for additional scrutiny,⁵⁻⁷ (2) identify important fate processes or parameters via parametric analysis or sensitivity analysis,^{8,9} (3) estimate potential for long-range transport,^{8,9} (4) estimate overall residence times,¹⁰ and (5) compare the impact of spatially and temporally heterogeneous environmental conditions on fate.¹¹ In the future, they may be used to (6) evaluate likely recovery times of contaminated environments should loadings cease, and (7) as a tool for ranking the sources and nature of contamination and proposed remediation strategies.

Many NP fate models rely on mathematical frameworks developed to describe homogeneous solutions of molecular and ionic contaminants. However, this approach can fall short when applied to particulates. Unlike solutions of dissolved contaminants, particle suspensions are two-phase systems controlled by surface chemistry and interfacial phenomena. Particle transport depends on kinetic processes with no direct analogue for dissolved contaminants, such as surface dissolution and particle-particle aggregation.¹² Process rates depend on complex interactions between environmental conditions (e.g., ionic strength, pH, redox, background particle composition) and particle properties (e.g., diameter, shape, surface area, surface charge).¹ Since 2010,¹³ the NP fate modeling community has therefore increasingly turned to “population balance” frameworks designed to describe colloidal (< 1 μm particulate) suspensions. Although these methods are theoretically superior, they can also be more mathematically complex, more computationally demanding, and more data-intensive. If scientific uncertainty is high, data are limited, and NP fate models are insensitive to NP properties, complex frameworks designed to explicitly model those properties may ultimately more harm than good.¹⁴

In short, the NP fate modeling enterprise presently struggles to distill the extensive and evolving scientific understanding of NP behavior in environmental media down to its most essential

features in order to develop models that are, as stated in the apocryphal quote by Einstein, “as simple as possible, but no simpler.” This body of work provides guidance for the development of a new generation of NP fate models that are more finely tuned to the particular needs of a given scientific or regulatory question. Focus is placed on (1) the impact of spatiotemporal variability in environmental conditions such as redox, river and surface hydrology, and sediment transport on Me/MeO NP transport and speciation in surface waters and sediments, (2) the impact of particle size on NP dissolution and aggregation in water, and (3) the impact of simplifying assumptions, spatiotemporal resolution, and framework selection on model runtimes and accuracy.

1.2 Literature Review

1.2.1 Processes Impacting NP Fate: Aggregation and Dissolution

Contaminants in natural surface waters will associate with water, suspended particulate matter (SPM), or bed sediments. Because ions, molecules, and NPs are all vanishingly small, their advective (unidirectional) and diffusive (multidirectional) transport in environmental media will mirror that of their carrier phase. NP transport, like that of any contaminant, therefore results primarily from stream flow, turbulent mixing, gravitational settling of suspended solids, sediment resuspension and deposition, and so on.

Models of ions, molecules, and particles may differ, however, with respect to their mathematical description of contaminant interactions with solid phases, a size-dependent process. Small molecules and ions are said to undergo reversible chemical or physical "sorption" to solid phases, which generally occurs rapidly enough to be treated as an equilibrium process. Large molecules and particles instead undergo aggregation (particle-particle) or deposition (particle-surface) processes, which are kinetically controlled and do not reach thermodynamic equilibrium.^{12, 15}

As the smallest possible particle size class, NPs can undergo especially rapid aggregation via Brownian motion in the presence of other nanoparticles (homoaggregation) or naturally-occurring SPM such as suspended sediment, microorganisms, macromolecules, or particulate organic matter (heteroaggregation).^{9, 16} Aggregation rates are, however, strongly impacted by surface charge, which depends on the chemical composition of the NP as well as the composition and morphology of surface coatings. Coatings include engineered polymer surfactants as well as natural sorbents (e.g., natural organic matter, polysaccharides).^{17, 18}

Some Me/MeO NPs, such as TiO₂ and SiO₂, are highly insoluble and thus virtually inert in the environment. Others exhibit complex and highly variable chemistry.¹⁹ Figure 1-1 summarizes the chemical transformations that impact the mobility and toxicity of soluble Me/MeO NPs in the environment. Dissolution of MeO NPs or oxidative dissolution of Me NPs, which occurs more rapidly and to a greater extent for small particles than for large particles,²⁰ forms dissolved metal ions, which are relatively bioavailable, potentially toxic, and which transport with the aqueous phase. NP sulfidation results in either the formation of a core-shell structure which inhibits further NP sulfidation and oxidation (e.g., Ag NPs)²¹ or the formation of 3-5 nm metal sulfide NPs that do not impact dissolution rates (e.g., ZnO and CuO NPs).^{22, 23} NPs and their sulfidation by-products travel primarily with the solid phase. Reaction of metal ions with naturally-occurring sulfides and metal ion complexation with solid phases (e.g., organic matter, inorganic mineral surfaces such as iron hydroxides²⁴) reduces toxicity.²⁵⁻²⁹ Metal ion speciation will ultimately depend on whether the metals are “hard” or “soft”—terms which refer to the polarizability of the metal’s electron cloud. Extremely soft metal ions like Ag⁺ preferentially form highly insoluble metal complexes with sulfide. Borderline metal ions like Cu²⁺ and Zn²⁺ form an array of species.

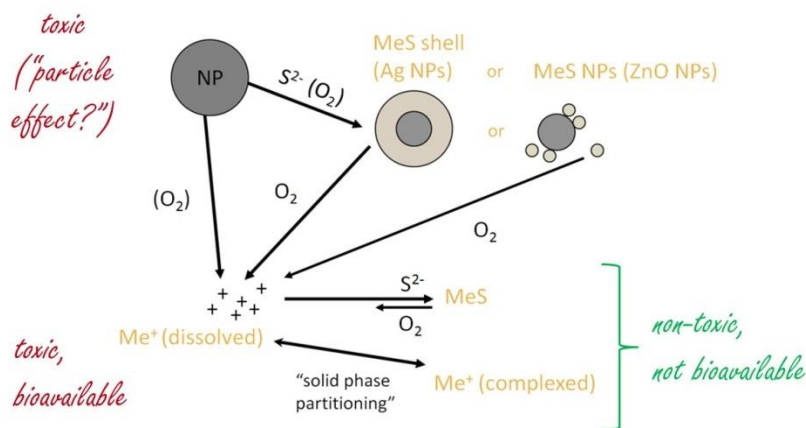


Figure 1-1. Chemical transformations impacting the toxicity and mobility of reactive NPs and their reaction by-products in the environment. Although as-manufactured NPs are known to be toxic, there is disagreement in the literature as to whether toxicity results solely from ion formation during dissolution or whether the particles themselves exhibit enhanced toxicity ("particle effect").

Ion complexation and solid phase partitioning are determined to a large extent by environmental conditions, especially redox potential and pH.³⁰ The EPA Framework for Metals Risk Assessment (2007) states, "Because the behavior of metals defies simple generalities, understanding the chemistry of the particular metal and the environment of concern is necessary."³⁰ The same is also true of NPs, whose chemistry is further complicated by surface area-dependent reaction kinetics and the formation of partially-transformed NPs such as core-shell structures. Dissolution, like aggregation, may also be impacted by engineered and natural surface coatings.³¹ The experimental and modeling challenges posed by surface coatings are considerable and still poorly understood, and will be only minimally addressed in this work.

1.2.2 Critical Review of Past and Current Approaches in NP Fate Modeling

1.2.2.1 Material Flow Analysis for Risk Assessment

Some of the earliest approaches to NP fate modeling relied on material flow analysis (MFA), a mass balance-based assessment methodology developed in the field of industrial ecology to track the

stocks and flows of substances into and between technological "compartments" (e.g., wastewater treatment plants, incinerators) and environmental "compartments" (e.g., soil, air, water) in order to conceptualize a material's life cycle.

In one of the most widely cited NP fate models, Mueller and Nowack (2008) predicted "best" and "worst case" estimates of environmental concentrations (PECs) of Ag, TiO₂, and carbon nanotubes released from products in air, water, soil, and landfills in Switzerland using a deterministic MFA model.³² All model parameters were later treated as probability distributions rather than single-value estimates in order to better account for large uncertainty in NP production volumes and behavior.³³ Probabilistic approaches continue to improve today.^{6,7} MFA models have also been applied recently at regional scales,^{34,35} and the first explicitly dynamic (time-resolved) MFA was published earlier this year.³⁶

MFAs spurred early research into the life cycle of NPs in the environment by identifying sewage treatment plants, biosolids, landfills, and incinerators as key intermediaries between the usage phase of nano-enabled products and the environment. They have provoked the risk community to ask if risk assessment methods (both for hazard and exposure) developed for other pollutants can be directly applied to NPs. They have highlighted ongoing uncertainties in the estimation of production volumes and emissions and have been used to rank the environmental risks from NPs. Because they are simple, they accommodate probabilistic or statistical methods such as Monte Carlo simulation more easily than other model types. Until data on NP production volumes and environmental releases become available or analytical methods are developed and applied, estimates of environmental emissions from MFAs will continue to be used in process-based numerical models such as those described below (e.g.,^{5,8,37}).

However, MFAs as they are currently applied to NPs lack spatial resolution (i.e., they average predicted contaminant mass over the entire environmental compartment, such as all surface water in

a nation) and thus are inappropriate for predicting environmental concentrations. In surface waters, rapid heteroaggregation leads to sedimentation and the accumulation of NMs in sediments at "hot spots" near points of release.^{9, 16, 38} Thus the nationally or even regionally averaged PECs reported in MFAs may have little practical relevance for regulatory purposes. MFA models also rely more extensively on simplifying assumptions than other fate model types. Particle properties, environmental conditions, and fate processes are generally not treated explicitly, but are implicit in the choice of transfer factors between environmental compartments.^{2, 33, 34} Recent probabilistic MFAs have included simple estimates of NP mass loss during sewage treatment due to Ag NP sulfidation and ZnO dissolution,⁶ but this modeling framework is not truly designed to handle the complexities of NP processes in wastewater treatment facilities and environmental media.

1.2.2.2 Numerical Modeling for Risk Assessment

Several NP fate models employ classical process-based numerical frameworks that predict changes over time in the total mass of a chemical species associated with a solid or fluid phase in one or more zero-dimensional (completely mixed) "control volumes" or "boxes" from the sum of all changes resulting from every relevant transformation or transport process occurring in that time step. Unlike MFAs, which lump all processes into a single inter-compartment transfer factor, numerical models of this type assign each process a different mathematical expression.^{3, 39} In addition, these models generally differ from MFAs in that they only describe NP fate in environmental media; emissions from sewage treatment facilities and other anthropogenic sources are treated as boundary conditions. Models which assign a single control volume to each environmental medium are called "multimedia box models" or "fugacity models."³

Boxall et al. (2007) were the first to predict NP concentrations in air, soil and water.⁴⁰ Blaser et al. (2008) used a model of the Rhine river to estimate silver PECs originating from biocidal

plastics and fabrics in wastewater treatment plant effluent, surface waters, and sediments.⁴¹

Gottschalk et al. (2011) estimated environmental concentrations of TiO₂, ZnO, and Ag NPs in a spatially resolved probabilistic model of Swiss rivers.⁴²

The numerical models and MFAs described up to this point either disregarded NP interaction with suspended particulate matter or relied on simple descriptors such as equilibrium partition coefficients. Recently published opinion pieces^{12, 15} favored the Smoluchowski equation, a kinetic descriptor of particle aggregation designed for use in size-resolved models that sum aggregation events across multiple size classes of interacting particles.⁴³

$$\frac{dn_k}{dt} = \frac{1}{2} \sum_{\substack{i+j \rightarrow k \\ i=1}}^{i=k-1} \alpha_{ij} \beta_{ij} n_i n_j - n_k \sum_{i=1}^{\infty} \alpha_{ik} \beta_{ik} n_i$$

Equation 1-1

where n_k is the number concentration of particles in size class k , β_{ij} is the rate of collisions between particles of size i and size j that could lead to formation of new aggregates of size k , and α_{ij} is the probability that collisions lead to a successful aggregation event. We will revisit this approach with greater rigor in Chapter 4.

While the theoretical superiority of Equation 1-1 over equilibrium descriptors is uncontested, a compelling case for its practical superiority in NP fate models designed for risk assessment purposes has not been made. Indeed, given the lack of kinetic data with which to parameterize or validate size-resolved NP frameworks at present, the relative complexity of size-resolved alternatives (which is at odds with the modeling principle of parsimony), and the speed with which NPs are expected to heteroaggregate in complex natural media in any case (which implies low

model sensitivity to the choice of aggregation rate law), approaches using Equation 1-1 may be less practical and more error-prone at present than models that rely on simple heuristics. For a more comprehensive treatment of this debate, we refer the reader to Dale et al. (2015).¹⁴

Nonetheless, Equation 1-1 is increasingly found in large-scale NP fate models. Some recent works apply it to systems that describe only one size class of heteroaggregates, homoaggregates, and/or unaggregated NPs.^{37,44} Most authors, however, employ the size-resolved form. In 2011, Arvidsson et al. described homoaggregation and sedimentation of TiO₂ NPs⁴⁵ in an aqueous suspension. In 2012, Praetorius et al.⁸ adapted the model by Blaser et al. (2008)⁴¹ to include Equation 1-1. Liu and Cohen (2014) later adapted this equation for use in a multimedia box model of NPs. Unlike previous authors, they used time-independent partitioning ratios in place of kinetic descriptors of aggregation.⁵ Sani-Kast et al. (2015) expanded the model by Praetorius et al. (2012) to account for the influence of spatial variation in water chemistry on NP heteroaggregation.¹¹ de Klein et al. (2016) introduced the first attempt to validate this class of models against field data.⁴⁶

Models that implement a size-resolved approach to Equation 1-1 implicitly take a “population balance” approach, or one in which the distribution of particle properties across the population (here, the particle size distribution) is tracked over time and space. By tracking size, population balance methods readily track changes in particle number concentrations and surface area concentrations as well as mass concentrations.⁸ These metrics are not very useful at present in NP risk assessment, since toxicity thresholds and regulatory limits are almost always expressed in terms of mass concentrations. Nonetheless, they are considered to be better indicators of NP toxicity than mass concentrations,⁴⁵ and may be useful in the future as more data become available. Finally, population balance can describe surface transformations as readily as it describes size-dependent NP aggregation kinetics. However, to my knowledge, it has only been used once to date in environmental fate models to describe NP dissolution.⁵

Environmental NP fate modelers that use process-based numerical models face several challenges beyond the debate over kinetic vs. equilibrium descriptors of heteroaggregation and the influence of NP size. Most models developed to date have assumed steady state conditions and therefore cannot capture time varying effects. Spatial resolution in most cases is either low or, in the case of multimedia box models, entirely lacking. However, recent models show a welcome trend towards increased spatial and/or temporal variation with respect to stream hydrology.^{44, 46-48} Processes of potential significance that exhibit high spatiotemporal variability but have largely escaped the attention of the modeling community to date include agricultural runoff of NP-containing biosolids into river and lakes (non-point source pollution)⁴⁹⁻⁵² and the deposition and scour of suspended sediments to and from river beds.⁵³

Modelers have been slow to adopt the most recent research on NP reaction kinetics, even though dissolution rates and other transformations rates have been published recently for several reactive metal and metal oxide NPs. Indeed, only one large-scale NP fate model to date included a kinetic description of NP dissolution;⁵ others either disregarded the chemical transformations of soluble NPs or simply assumed that reactions instantaneously reached thermodynamic equilibrium.^{32-34, 42, 48} Similarly, no numerical models to date have tracked dissolution by-products (metal ions) and their speciation, even though the generation of toxic dissolved ions is a primary source of reactive metal and metal oxide NP ecotoxicity.⁵⁴

1.2.2.3 Population Balance Modeling for Scientific Inquiry

In spite of the simplicity of current population balance approaches at the river scale or larger and their limited applicability at present, in the author's view, to NP fate models designed for decision-making, population balance has tremendous near-term potential for scientific investigations backed by experimental data. Hypothetically, detailed models can be used to elucidate the effect of a wide

range of particle sizes on a wide range of surface transformations and aggregation processes occurring simultaneously among many SPM types. They can be used to track changes in the distribution of properties other than size, such as surface area and surface charge. Models that track variation in multiple particle properties simultaneously can be used to study non-spherical particles, NP-SPM heteroaggregates, core-shell structures, natural and engineered surface coatings, and nanohybrids. Population balance methods developed to describe aerosol particle microphysics,^{55, 56} flocculation in surface waters,⁴³ droplet evaporation,⁵⁷ and crystal growth⁵⁸ may be useful in addressing NP modeling challenges.

Some of the introductory material presented here was published in 2015 in *Environmental Science: Nano*¹⁴ and *Environmental Science and Technology*.⁵⁹

1.3 Objectives and Approach

This work aims to

- (1) Explore the impact of spatiotemporal variability in environmental conditions on Me/MeO NP transport and speciation in surface waters and sediments,
- (2) Explore the impact of size on NP dissolution and aggregation in simple media,
- (3) Determine how assumptions and mathematical frameworks affect model runtimes and accuracy, and
- (4) Provide guidance for the development of improved scientific and regulatory models of NP fate in surface waters and sediments from the laboratory scale to the watershed scale.

I used three independent projects to narrow the project scope while still addressing these aims.

Each is presented here as a separate chapter.

CHAPTER 2: THE SEDIMENT MODEL. An existing one-dimensional sediment diagenesis modeling framework (Di Toro et al., 1996)⁶⁰ was adapted in order to explore the influence of organic carbon, dissolved oxygen, and naturally-occurring sulfides on the distribution and speciation of silver Ag NPs and their reaction by-products in quiescent freshwater sediments. This work was published in *Environmental Science & Technology* in 2013.⁶¹

CHAPTER 3. THE WATERSHED MODEL. A hydrologic and agricultural model, the Phase 5 Chesapeake Bay Watershed Model,⁶² was adapted and coupled to a river network water quality model in order to predict the fate of Ag NPs and ZnO NPs in a freshwater watershed. The model predicted the contribution of agricultural runoff to total metal stream loads from Ag and ZnO NPs and their reaction by-products, explored the combined impact of chemical transformations and sediment transport on the speciation and mobility of NP-derived metals in freshwater rivers, and explored the influence of spatial and temporal variability in environmental conditions on NP fate and effects in order to elucidate the influence of model resolution on fate predictions. This work was published in *Environmental Science & Technology* in 2015.⁶³

CHAPTER 4. THE POPULATION BALANCE MODELS. Three promising numerical approaches from the population balance literature were developed and compared with respect to runtime and accuracy for problems of surface area-dependent NP dissolution and homoaggregation in simple aqueous suspensions: the Sectional Method (SM), the Direct Quadrature Method of Moments (DQMOM), and the Extended Quadrature Method of Moments (EQMOM). Major sources of error and the potential future applications of each approach were identified and addressed.

2 Modeling Nanosilver Transformations in Freshwater Sediments

2.1 Introduction

The global market for nanotechnology is estimated to have reached \$16 billion in 2010 and is expected to grow to approximately \$27 billion by 2015.⁶⁴ Products containing silver nanoparticles (Ag NPs), such as antibacterial cosmetics and textiles, represent a major use of nanotechnology in the consumer goods sector.⁶⁵ Ag NPs are toxic to a wide range of organisms,²⁷ and textiles and cosmetics demonstrate relatively high environmental releases; initial estimates suggest Ag NP emissions to air, soil, and water during manufacturing, use, disposal, and/or recycling may equal as much as 50% of annual production.²

The toxic effects of as-manufactured, untransformed silver nanoparticles, which are mostly Ag⁰, have been observed in microorganisms, algae, fungi, vertebrates, invertebrates, and aquatic and terrestrial plants.²⁷ Ag NPs tend to oxidize in oxic aquatic environments.^{21, 66-69} This process releases silver ions (Ag⁺), which can non-selectively interfere with cell respiration and membrane transport.²⁷ The toxic effects of silver are exacerbated by the tendency of the ionic form to persist and bioaccumulate.^{70, 71}

Another particulate species, silver sulfide (Ag₂S), forms in the presence of naturally occurring sulfides. In an oxygen-mediated process termed “sulfidation,” the Ag NPs react with sulfide to form a surface layer of Ag₂S.⁷² Partial sulfidation results in what has been termed a core-shell structure, although TEM images have shown that complex Ag⁰-Ag₂S morphologies may also occur.^{21, 27, 72} Complete sulfidation is possible.⁷² In 2010, Kim et al. characterized Ag₂S NPs found in sewage sludge and proposed that the sulfide-rich, anoxic environment of sewage treatment plants (STPs) facilitates rapid sulfidation.⁷³ This transformation is of great importance, both because

the highly insoluble Ag_2S shell reduces the rate of Ag NP oxidation²¹ and because Ag_2S is less toxic to microorganisms than Ag^0 NPs and Ag^+ .^{26, 27, 74}

The differential toxicity of silver species necessitates the development of environmental fate models that can predict their relative abundance in a system of interest. Although several models have recently been developed to describe nanoparticle transport in environmental media,^{8, 32, 33, 41, 42, 45} no attempts have been made to model the complex chemical transformations of Ag NPs in surface waters or sediments.

Smoluchowski coagulation theory indicates nanoparticles will heteroaggregate rapidly with clays, minerals, and other natural colloids upon entering surface water.⁴³ Aggregation is expected to lead to settling, which will lead in turn to accumulation of NPs in sediments.^{13, 43, 75} This conclusion is borne out by laboratory experiments on the behavior of nanoparticles,^{76, 77} as well as the most recent mathematical models of nanoparticle fate and transport in surface waters.^{8, 33, 41, 45}

The biodiversity and health of aquatic systems can be negatively impacted by the biouptake of Ag NPs and toxic Ag^+ by sediment-dwelling organisms. Biomagnification resulting from ingestion of sediment-dwelling organisms by species higher in the food web is a potential concern,⁷⁸ since trophic transfer of NPs has been reported in a simulated terrestrial ecosystem.⁷⁹ Resuspension of particulate silver species and diffusion of silver ion from sediments are also possible sources of silver in the water column.

The model developed in this paper is based on a mass balance model by Di Toro et al.⁶⁰ that describes the speciation of cadmium in sediments in response to redox conditions established in the sediment as a function of oxygen consumption during organic carbon diagenesis, or mineralization.^{24, 80} As described below, this adaptation is appropriate because the speciation of both Ag and Cd in sediments is contingent on the displacement of iron from iron sulfide to form highly stable (i.e., very low solubility) metal sulfides.²⁹ The model was calibrated to experimental data

collected from Ag⁰ NP-dosed artificial freshwater wetland mesocosms operated by the Center for Environmental Implications of Nanotechnology (CEINT). The reader is referred to Lowry et al. (2012) for an in-depth treatment of the mesocosm experiment.³⁸ After calibration, several input scenarios were selected for further investigation.

2.2 Methods

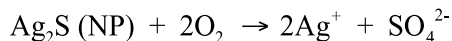
2.2.1 Model Structure and Framework

Figure 2-1 outlines the reactions and physical processes modeled. The diagram distinguishes between oxic and anoxic sediment layers for visual simplicity; however, concentrations of oxygen and all other species were modeled continuously over depth.

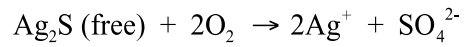
Silver ion, Ag⁺, is derived from the oxidation of the elemental silver (Ag⁰) core of the Ag NPs or from the oxidation of sulfur in silver sulfide. Silver sulfide exists either as a coating on the particle surface, Ag₂S (NP), or as a free (not bound to the initial Ag NP) inorganic precipitate formed by the interaction of iron sulfide with silver ion diffusing freely in the pore water, Ag₂S (free). This distinction between the two locations of Ag₂S, “NP” and “free,” was necessary to properly track the extent of sulfidation of the Ag NPs during the simulation. This approach distinguishes transformations undergone by the nanoparticles from those undergone by the silver ions released from the particles. No such distinction was necessary for Ag⁰, which is assumed to be present only in the Ag NP cores. The relevant reactions are:



Equation 2-1

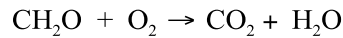


Equation 2-2



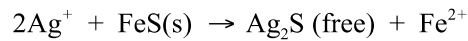
Equation 2-3

The main driver of aerobic Ag NP oxidation is the depth of oxygen penetration in the sediments, which depends primarily on its consumption during the microbially-mediated oxidation of particulate organic carbon (POC):



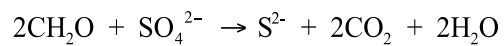
Equation 2-4

Silver ion freely diffusing in the pore water is converted to silver sulfide, $\text{Ag}_2\text{S (free)}$, via a displacement reaction, in which iron sulfide acts as the source of sulfide.

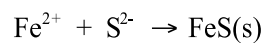


Equation 2-5

Iron sulfide serves as a proxy in the model for all available sulfides in the system (e.g., acid-volatile sulfide, or AVS). Iron sulfide is gained via the anaerobic oxidation of organic carbon, which reduces sulfate to sulfide,

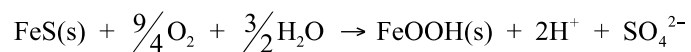


Equation 2-6



Equation 2-7

and is lost by oxidation to form iron oxyhydroxide (FeOOH):

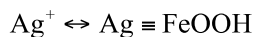


Equation 2-8

Finally, iron oxyhydroxide and particulate organic carbon reversibly sorb silver ion.



Equation 2-9



Equation 2-10

Physical processes modeled include particle mixing due to bioturbation, diffusive mixing of dissolved species, efflux of dissolved species as a result of diffusion at the sediment-water interface, and influx of organic carbon, Ag NPs, and oxygen. Note that, in the tradition of conventional mass balance models, “particle” refers here to all particulate (solid phase) species: POC, FeS, FeOOH, Ag^0 , Ag_2S (“NP” and “free”), $\text{Ag} \equiv \text{POC}$, and $\text{Ag} \equiv \text{FeOOH}$. “Nanoparticle” refers only to the particulate species representing the core and shell of the transforming Ag NP, Ag^0 and Ag_2S (NP).

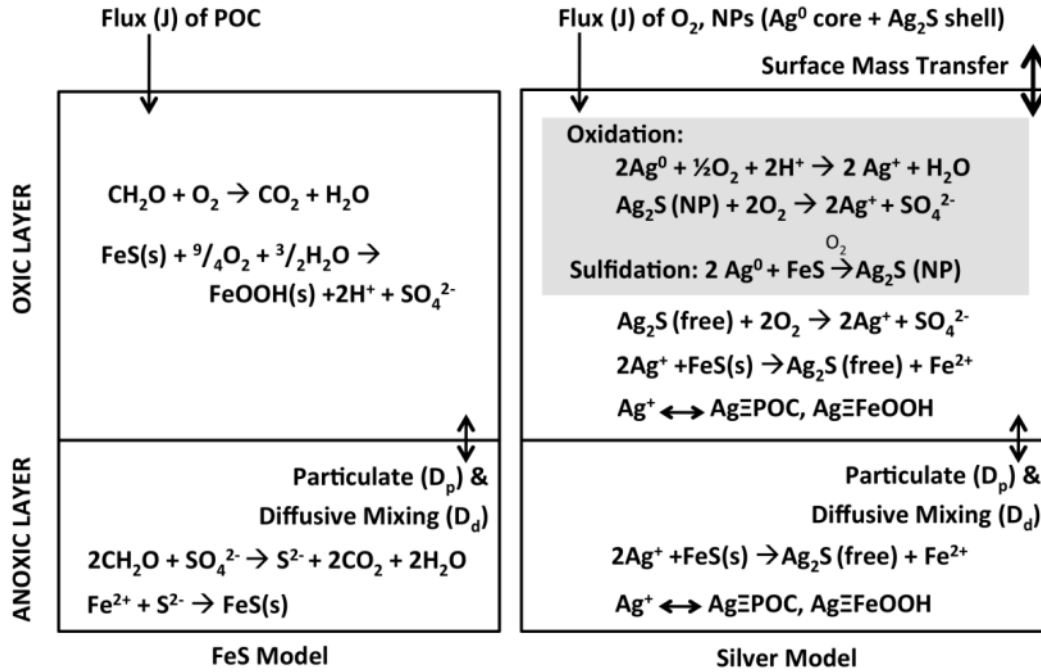


Figure 2-1. Model schematic for nanosilver sediment chemistry model (adapted from ⁶⁰). Nanoparticle reactions are highlighted in gray and represent an extension of the model proposed by Di Toro et al. (1996) for cadmium speciation and solid phase partitioning.

Table **A-1** lists the model state variables. Changes in the depth profile of each state variable over time are modeled dynamically using the one-dimensional continuous advective-dispersive mass balance equation:

$$\frac{\partial [C(z)]}{\partial t} - \frac{\partial}{\partial z} \left((f_p D_p(z) + f_d D_d) \frac{\partial [C(z)]}{\partial z} \right) = \sum_j R_j$$

Equation 2-11

where $C(z)$ is the concentration at depth z , f_p is the particulate fraction of the total concentration, D_p is the particle mixing coefficient, f_d is the dissolved fraction of the total concentration, D_d is the diffusive mixing coefficient, and $\sum_j R_j$ represents all reactions resulting in gain or loss of the species.

2.2.2 Reactions

In general, reaction rates were assumed to exhibit a linear dependence on the concentrations of all reactants.⁶⁰ The exceptions to the assumption of linear dependence were aerobic and anaerobic oxidation of organic carbon, for which we applied the Michaelis Menton expression for oxygen dependency. Table A-2 summarizes the reaction equations, which are of the general form

$$R_j = k_j \theta_j^{(T-20)} [C_1][C_2]$$

Equation 2-12

where k_j is the reaction rate constant, θ_j is the Arrhenius temperature coefficient, T is the temperature in degrees Celsius, and $[C_1]$ and $[C_2]$ are the concentrations of the reactants.

Previous work suggests the rate constants for Ag NP oxidation and Ag NP sulfidation, k_{Ag^0, O_2} and k_{sulf} , decrease exponentially in response to Ag NP sulfidation.^{21, 72, 81} The Ag NP oxidation rate was thus modeled using Equation 2-13, where S/Ag represents the molar ratio of sulfur to silver. Ag NP sulfidation, in contrast, could not be accurately modeled using Equation 2-13 without drastically reducing the time step (and vastly increasing model runtime). For fully unsulfidized Ag NPs, the rate of sulfidation was assumed to decrease rapidly upon dosing so that a constant “long-term average” sulfidation rate would be appropriate over the time scale considered (see Table A-3 for details). The effect of additional factors (e.g., temperature, pH, organic carbon, particle size, capping agent)^{66, 68} on the initial rate of Ag NP oxidation before sulfidation ($S/Ag = 0$) was captured by calibration.

$$S / Ag = \frac{[Ag_2S(NP)]}{[Ag^0] + 2[Ag_2S(NP)]}$$

$$k_{Ag^0, O_2} = \{k_{Ag^0, O_2} (S/Ag = 0)\} e^{c_{pass}(S/Ag)}$$

Equation 2-13

2.2.3 Partitioning

For simplicity, all dissolved sulfides were modeled as the dissolved form of FeS using the partitioning coefficient π_{FeS} . The governing equations for iron sulfide “partitioning” are provided by Di Toro et al. (1996). Equilibrium partitioning of silver between the sediment pore water (Ag^+) and the relevant solid phases ($Ag \equiv POC$ and $Ag \equiv FeOOH$) was described with a Langmuir isotherm analogous to that described by Di Toro et al. for cadmium.⁶⁰ Details are provided as supporting information (Equation A-1 to Equation A-7). The complexation of Ag with chloride ion, while strong, is significantly less so than for sulfide and for organic matter,⁸² and is assumed to be negligible in the freshwater (low chloride) environment. $AgCl(s)$ was not detected by XAS measurements on the mesocoms sediments.³⁸

2.2.4 Particle Mixing and Porosity

The particle mixing coefficient, which represents the rate of sediment mixing as a result of biological activity, is temperature-dependent and is assumed to decrease exponentially with depth, z , according to the equation

$$D_p(z) = D_p \theta_{D_p}^{(T-20)} e^{-z/z_{D_p}}$$

Equation 2-14

where z_{Dp} represents the depth of bioturbation.

Since sediments at depth are compacted by the weight of overlying layers, porosity was assumed to decrease exponentially with a decay constant of k_ϕ from a value of 0.99 at the interface (ϕ_0) to a value of 0.25 at depth. Porosity at the interface and at depth was estimated from mesocosm data³⁸ which produced good agreement between silver concentrations vs. depth observed in the mesocosms and those predicted by the model.

2.2.5 Temperature

Annual temperature variation is assumed to be sinusoidal. Coefficients were estimated from water column temperatures in the mesocosms used to calibrate the model³⁸ and air temperature data at the mesocosm site (<http://ceint.duke.edu/chart/mesocosm-air-temp>). Higher temperatures increase rates of reaction and solute diffusion via Arrhenius temperature coefficients (not shown in Table 2-1; see Table A-3) and correspond with increases in biological activity in the sediment and water column. This leads to higher particle mixing, higher organic carbon influx to the sediment, and the depletion of dissolved oxygen.

2.2.6 Parameter Values

Table 2-1 summarizes parameter values used in the simulations. Table A-3 presents the assumptions underlying the selected values. Sensitivity analysis revealed that model outputs were not overly sensitive to local variation in those parameters for which only point estimates were found (Table A-4).

The nominal values of four model parameters (k_{ϕ} , D_p , K_{oc} , $k_{Ag^0, O_2} (S/Ag = 0)$) were determined by calibration. System parameters were matched to conditions in the mesocosms, including loss on ignition (L.O.I. $\approx 2 * f_{oc}$ ³⁹ where f_{oc} is the initial organic carbon composition of the sediment), sediment AVS, oxygen concentration at the sediment-water interface, annual temperature variation, Ag NP mass input, and time of dosing.³⁸ The simulation was run for $t=18$ months after introducing a simulated pulse input of 2.9 g of “pristine” (unsulfidized) Ag⁰ NPs. The Ag NPs added to the mesocosms had a thin oxidized Ag (e.g. Ag₂O) shell,³⁸ which was an implicit determinant of the initial rate of nanoparticle oxidation, $k_{Ag^0, O_2} (S/Ag = 0)$. For the calibration, mean total silver concentrations calculated by the model over sediment depths of 0-1 cm, 1-2 cm, 2-4 cm, and > 4 cm were matched to the median silver concentrations observed in the mesocosms eighteen months after dosing. Model outputs were also matched to the relative abundances of Ag⁰, Ag⁺-organics, and Ag₂S in the surficial sediments of the mesocosms eighteen months after dosing, as determined from linear combination fits of X-ray Absorption Spectroscopy (XAS) spectra collected on surficial sediment in the mesocosms.³⁸ The calibration was performed using the non-linear parameter estimation software PEST (<http://www.pesthomepage.org/>), which minimizes the weighted sum of the squared residuals. Weights were calculated as the inverse standard deviation of each field observation.

Silver ion efflux from the sediment to the overlying water at time t was estimated by the model from the predicted concentration profile of Ag⁺ at the sediment-water interface.

2.2.7 Solution Method

A fully implicit finite difference approximation was used to simultaneously solve the mass balance equations for all state variables. The Gauss-Seidel iteration method (e.g., as described by

Ramaswami et al.³) was used to achieve rapid convergence. To avoid dynamic instability associated with the central differencing approach to numerical methods,³ model resolution ($\Delta z=1$ mm, $\Delta t=0.05$ days) was chosen to ensure

$$\Delta t \leq \frac{(\Delta z)^2}{2D_{\max}}$$

Equation 2-15

where D_{\max} was the maximum value of the time- and depth-dependent diffusion coefficients D_p and D_d .

An exponentially expanding spatial grid was implemented in order to focus computational efforts on transformations occurring near the sediment-water interface while eliminating undue computational burdens at depth (see Equation A-8 to Equation A-17 for details).^{83,84} Model results for the expanded grid were compared to those for an unexpanded grid to affirm the accuracy of the method.

The diagenetic model was run for a year before simulated introduction of the Ag NPs to ensure periodicity in seasonally variable redox conditions had been achieved.

Table 2-1. Ranges of sediment model parameters^{a,b}

Symbol	Parameter	Units	Value
ϕ_0	Sediment porosity at the sediment-water interface ⁸⁵	m ³ /m ³ -bulk	(0.25, 0.4, 0.99)
$k\phi$	Rate of decrease in sediment porosity with depth	m ⁻¹	0.058
ρ	Sediment density ²⁴	g-sed/m ³ -sed	(1.5x10 ⁶ , 2.5x10⁶ , 2.7x10 ⁶)
D_d	Diffusive mixing coefficient ²⁴	m ² /d	(7.0x10 ⁻⁵ , 7.5x10⁻⁵ , 1.7x10 ⁻⁴)
D_p	Particle mixing coefficient ⁸⁶	m ² /d	(5.5x10 ⁻¹¹ , 4.0x10⁻⁷ , 1x10 ⁻⁴)
z_{D_p}	e-folding depth of particle mixing ⁸⁶	m	(0.02, 0.10 , 0.30)
f_{POC_1}	Fraction of POC in G ₁ reactivity class ²⁴	[-]	0.50-0.65
f_{POC_2}	Fraction of POC in G ₂ reactivity class ²⁴	[-]	0.16-0.25
k_{POC_1,O_2}	Rate of aerobic oxidation of G ₁ carbon ²⁴	d ⁻¹	(0.019, 0.048 , 0.07)
k_{POC_2,O_2}	Rate of aerobic oxidation of G ₂ carbon ²⁴	d ⁻¹	(0.0038, 0.004 , 0.0088)
k_{POC_1,SO_4}	Rate of anaerobic oxidation of G ₁ carbon ²⁴	d ⁻¹	(0.02, 0.024 , 0.027)
k_{POC_2,SO_4}	Rate of anaerobic oxidation of G ₂ carbon ²⁴	d ⁻¹	(0.0012, 0.002 , 0.003)
K_{M,O_2}	Half saturation constant for POC oxidation using O ₂ ²⁴	mg O ₂ /m ³	100
k_{FeS,O_2}	Rate of oxidation of FeS to form FeOOH ²⁴	d ⁻¹ (mg O ₂ /m ³) ⁻¹	(3x10 ⁻⁶ , 0.001 , 3)
$k_{Ag^0,O_2} (S/Ag = 0)$	Rate of Ag ⁰ NP dissolution ^{21, 67, 69}	d ⁻¹ (mg O ₂ /m ³) ⁻¹	(1.3x10 ⁻⁸ , 8.5x10⁻⁶ , 5.1x10 ⁻⁴)
k_{sulf}	Rate of AgNP sulfidation (long-term average) ^{72, 81}	(mmol S ²⁻ /m ³) (mg O ₂ /m ³)d ⁻¹	(0, 2.0x10⁻⁷ , 3.5x10 ⁻⁵)
c_{pass}	Rate of decrease in k_{Ag^0,O_2} , k_{sulf} as a function of S/Ag ²¹	[-]	(14, 20 , 24)
$f_{Ag^0,init}$	Fraction Ag ⁰ by mass in input dose of NPs ⁸⁷	[-]	(0, 0.15 , 1.0)
k_{Ag_2S,O_2}	Rate of oxidation of sulfur in Ag ₂ S ⁸⁸	d ⁻¹ (mg O ₂ /m ³) ⁻¹	(0, 1.5x10⁻⁷ , 4.5x10 ⁻⁷)
k_{Disp}	Rate of displacement reaction ²⁴	d ⁻¹ (mmol FeS/m ³) ⁻¹	0.1
$J_{POC,max}$	Max flux of organic carbon from overlying water ^{89, 90}	mg/m ² -d	(75, 150 , 300)
$\log K_{OC}$	Partition coefficient to POC ⁹¹	L/kg	(4.1, 7.3 , 7.8)
σ_{OC}	Sorption capacity for POC ²⁴	μmol/g	1.7 x 10³
K_{FeOOH}	Partition coefficient to FeOOH ²⁴	m ³ /mmol	1.0 x 10³
σ_{FeOOH}	Sorption capacity for FeOOH ²⁴	mol/mol	0.2
π_{FeS}	Partition coefficient for FeS: [FeS _p]/[FeS _d] ²⁴	m ³ /g	10⁻⁴-10⁻²
Initial and Boundary Conditions			
O ₂ (z=0)	Oxygen concentration at the interface	mg/m ³	(500, 3600 , 14,000)
$f_{oc}(t=0)$	Fraction of organic carbon in sediment (at t=0) ^{24, 39}	[-]	(0.001, 0.02 , 0.15)
FeS(t=0)	Sediment iron sulfide (AVS) concentration (at t=0) ²⁴	μmol/g	(0.01, 10 , 100)

^a Nominal values are bolded and values determined by calibration are italicized. Note that nominal values represent a “typical” freshwater system and do not necessarily correspond with the values used to calibrate the model, which were selected to match conditions in the mesocosms.

^b See note in Table A-3 on the selection of Arrhenius temperature coefficients for mixing and reaction rates (not shown)

2.2.8 Initial and Boundary Conditions

No-flux boundary conditions were assumed at the sediment-water interface for all particulate species except those entering the system—POC, Ag^0 , and Ag_2S (NP)—which assumed known influx (Type II/Neumann) boundaries. This boundary condition was assumed to be sufficient to capture the net effect of particle deposition and resuspension in a quiescent wetland environment. Influx of organic carbon was described piecewise in time with a sine curve that peaked at $J_{\text{POC},\text{max}}$ in summer (mid-May to mid-September) and was $15 \text{ mg/m}^2\text{-d}$ in fall, spring, and winter. This idealized influx scenario agrees with seasonal trends in community respiration and carbon mineralization observed in a freshwater marsh.⁹² Known constant concentration (Type I/Dirichlet) boundaries were assumed for all dissolved species. ICP-MS analysis of mesocosm water column samples detected no total silver after initial settling (detection limit of $<2 \text{ } \mu\text{g/L}$),³⁸ so it was assumed that the silver ion concentration at the sediment-water interface could be approximated as zero. At $t=0$, the oxygen concentration was decreased linearly from its value at the interface to zero at a depth of 5 mm. The depth profile of oxygen exhibited exponential decay within one day of launching the simulation.

The mesocosms were dosed with 4.2 g of polydisperse, partially oxidized (80-85 wt % Ag^0) 30-80 nm PVP-coated Ag NPs, resulting in initial water column concentrations of 25 mg/L Ag NPs. Ag^0 was assumed to exhibit an exponentially declining flux such that all silver added to the water column as a finite square pulse input would penetrate the sediment within ten days, as observed in the mesocosms.³⁸ At depth, no-flux boundary conditions were implemented for all species.

2.3 Results

Figure 2-2 compares total Ag concentration vs. depth as measured in the mesocosm sediment to the simulated concentration profile of total silver, which represents the sum of all silver species in the system: Ag^0 , Ag_2S (“NP” and “free”), Ag^+ , $\text{Ag}\equiv\text{POC}$, and $\text{Ag}\equiv\text{FeOOH}$. Silver concentrations (in

mg Ag/kg dry weight of sediment) are highest at the sediment-water interface, since the dry weight of sediment in a given volume is lowest when porosity is high. Calibration to XAS data on the speciation of silver in the surficial sediments (~5 mm depth) of the mesocosms eighteen months after dosing ensured that, as reported,³⁸ silver was present as 55% Ag₂S (“NP” and “free,” in our model), 27% Ag⁺-organic compounds (Ag≡POC), and 18% Ag⁰. The concentrations of the other silver species considered in the model (Ag⁺, Ag≡FeOOH; see Figure 2-1) were low (<0.01%).

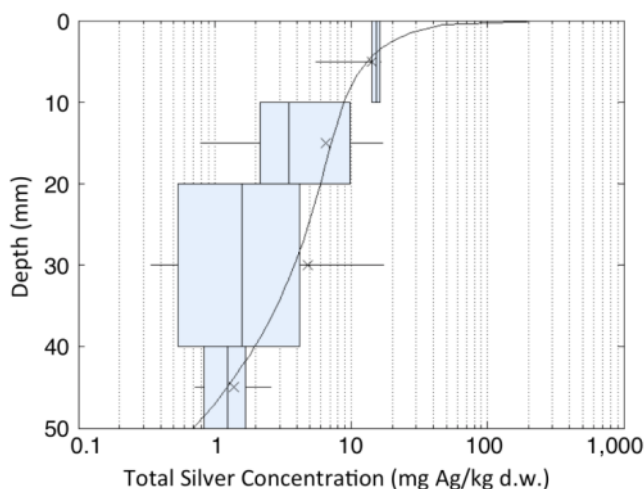


Figure 2-2. Sediment model calibration results. Total sediment silver concentration profile predicted by the model (curve) versus sample data collected from the water-column-dosed mesocosm eighteen months after dosing (boxplots). Boxplots describe the distribution of nine sample measurements (six measurements for the > 40 mm depth) at each of four sediment depths (0-10 mm, 10-20 mm, 20-40 mm, >40 mm). Crosses (×) indicate mean values.

For those parameters with ranges estimated from the literature ($k_{Ag^0, O_2}(S/Ag = 0)$, D_p , K_{oc}), calibrated values fall within their expected range (italicized values in Table 2-1). The initial rate of Ag NP dissolution, $k_{Ag^0, O_2}(S/Ag = 0)$, exceeds rate constants estimated from the equilibrium solubility of equivalently sized (38-80 nm) Ag NPs (3×10^{-8} to $2 \times 10^{-6} \text{ d}^{-1}(\text{mg O}_2/\text{m}^3)^{-1}$), assuming 8.6 mg/L DO (as reported) and the reaction rate equation used in the model.⁶⁹ The difference may

be explained by partial oxidation of the mesocosm Ag NPs before dosing (15-20 wt %),³⁸ which facilitates rapid initial oxidation.⁹³ In contrast, $k_{Ag^0, O_2}(S/Ag = 0)$ was lower than rates predicted for 40-80 nm Ag NPs at pH 4 (8.6 mg/L DO assumed).⁶⁷ The Ag NP oxidation rate is expected to decrease with an increase in pH.⁶⁶

The calibrated value of the silver ion-organic carbon partitioning coefficient is on the upper end of its expected range ($\log K_{oc} = 4.1-7.8$ L/kg). This suggests the organic carbon in the mesocosms sediments had a relatively high affinity for Ag^+ , perhaps due to the presence of strong chelating groups like reduced sulfur. The overall correlation coefficient representing agreement between model output and mesocosm data is 0.997.

Figure 2-3(a) shows the silver ion efflux from the sediment to the overlying water as a function of time for a simulated pulse input of 2.9 g of Ag NP under typical environmental conditions for a freshwater wetland (the “nominal” case; see bolded values in Table 2-1). The modeled system was ‘dosed’ in July in order to maximize initial efflux. This represents a worst-case scenario, in which the maximum amount of toxic Ag^+ escapes into the water column before the nanoparticles have the chance to sulfidize and Ag NP oxidation rates decrease.

Changes in the depth profile of all state variables over time are provided in Figure A-1. Oxygen concentration peaks in winter, as has been observed in natural systems.^{92, 94} However, Ag^+ efflux peaks in summer. Figure A-2 reveals the mid-July peak in Ag^+ efflux is driven by the temperature dependence of mixing and reaction rates.

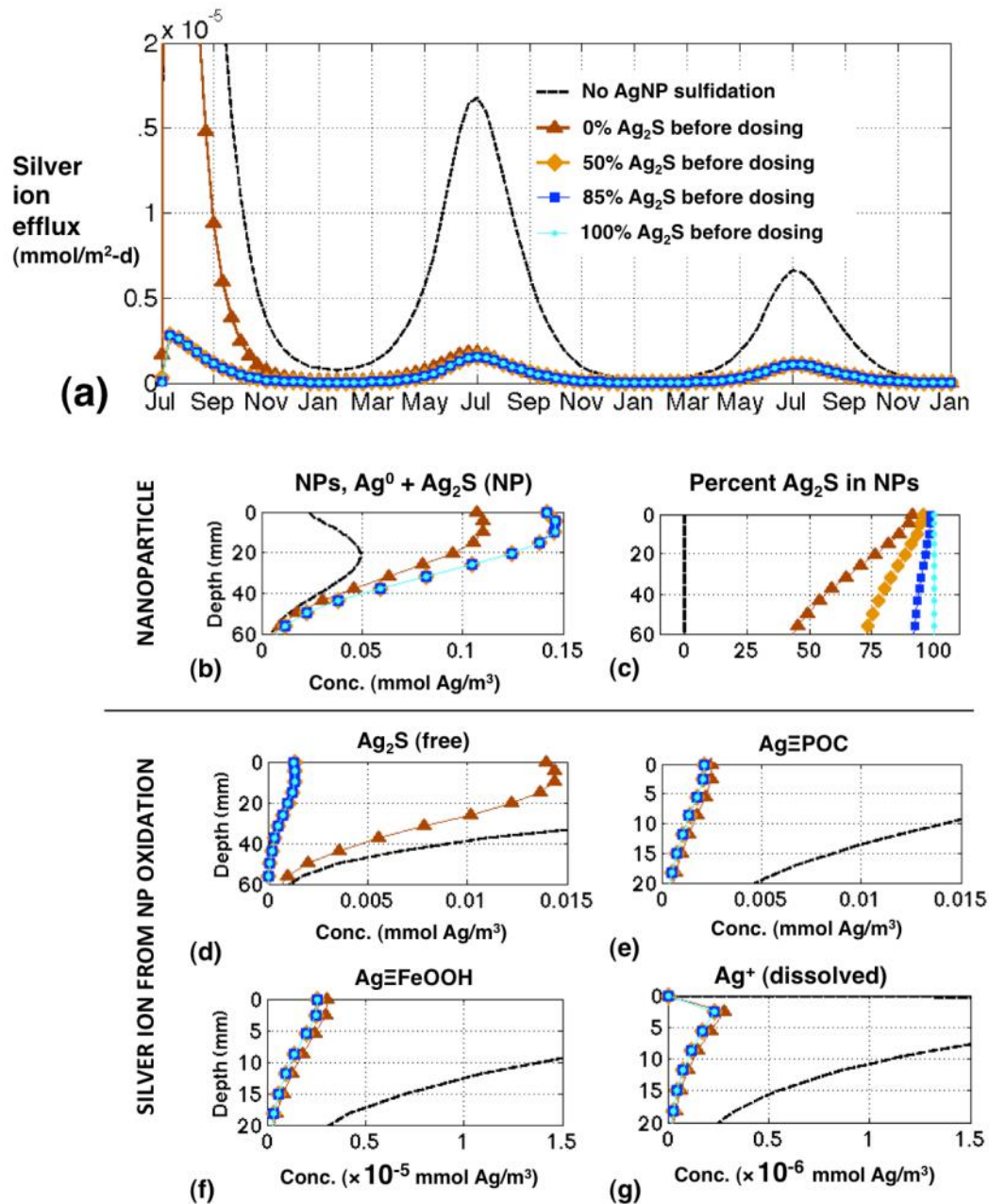


Figure 2-3. Results for nominal case under five different Ag NP percent sulfidation scenarios. a) Silver ion efflux vs. time after dosing, b) Concentration profiles in the sediment one year after dosing in July. The black dashed curve indicates the unrealistic upper bound on Ag NP oxidation, in which the system is dosed with pristine particles (0% Ag_2S) and sulfidation is not allowed to occur. Colored curves correspond with NP inputs that are 0%, 50%, 85%, and 100% sulfidized before dosing when sulfidation is allowed to occur.

The five scenarios in Figure 2-3 demonstrate the role sulfidation plays in the release of Ag^+ from Ag NPs. Scenarios include an unrealistic worst case, in which a pulse input of pristine Ag^0 NPs enters

the system ($t=0$) and the Ag NP sulfidation process is artificially turned off (i.e., nanoparticles remain 100% Ag⁰ over the course of the simulation). The other four scenarios demonstrate system responses to a dose of pristine particles (0% Ag₂S before dosing), fully sulfidized particles (100% Ag₂S before dosing), and partially sulfidized particles (50% and 85% Ag₂S before dosing) when sulfidation is allowed to occur. This last scenario (85% Ag₂S) reflects the extent of sulfidation expected for silver particles exiting a sewage treatment plant by way of effluent.⁸⁷ Figure 2-3(b) shows depth profiles under these four scenarios one year after dosing.

We observe no differences in the extent of Ag NP oxidation and the speciation, solid phase partitioning, and efflux of silver ion over time between 50%, 85%, and 100% Ag₂S nanoparticles. This is because the rate of Ag NP oxidation decreases exponentially with the extent of Ag NP sulfidation (Equation 2-13). Ag NPs that enter the system fully unsulfidized similarly behave as if fully sulfidized within a year of dosing, although elevated Ag₂S (free) concentrations are observed as a result of Ag NP oxidation—and subsequent reaction of the released Ag⁺ with sulfide—within the first several months.

Figure 2-3(b) (top right panel) reveals that the predominant form of silver in the sediment will be the partially or fully sulfidized nanoparticles. Percent sulfidation decreases with depth in this pulse input case because the Ag NPs that remain at the interface longer spend more time in the presence of O₂. Although FeS and O₂ do not coexist at equilibrium,⁷² O₂ mediates Ag NP sulfidation. The principal forms resulting from speciation and solid phase partitioning of Ag⁺ released during Ag NP oxidation are the thermodynamically favored species, Ag₂S (free), and Ag≡POC (silver associated with particulate organic carbon). This is unsurprising, since silver reacts strongly with the sulfur-containing functional groups prevalent in organic compounds. Ag≡POC may be especially high in this model because of the high K_{oc} value determined by calibration. Truly

dissolved (highly toxic) Ag^+ is present only at very low concentrations, consistent with observations in field samples.⁸⁸

The normalized sensitivities of model outputs to small ($\pm 0.05\%$) changes in model inputs around the nominal case (i.e., elasticities), reported in Table A-4, reveal that environmental conditions strongly affect the system response. Figure 2-4 describes oxidation, sulfidation, and persistence of the Ag NPs as a function of organic carbon content.

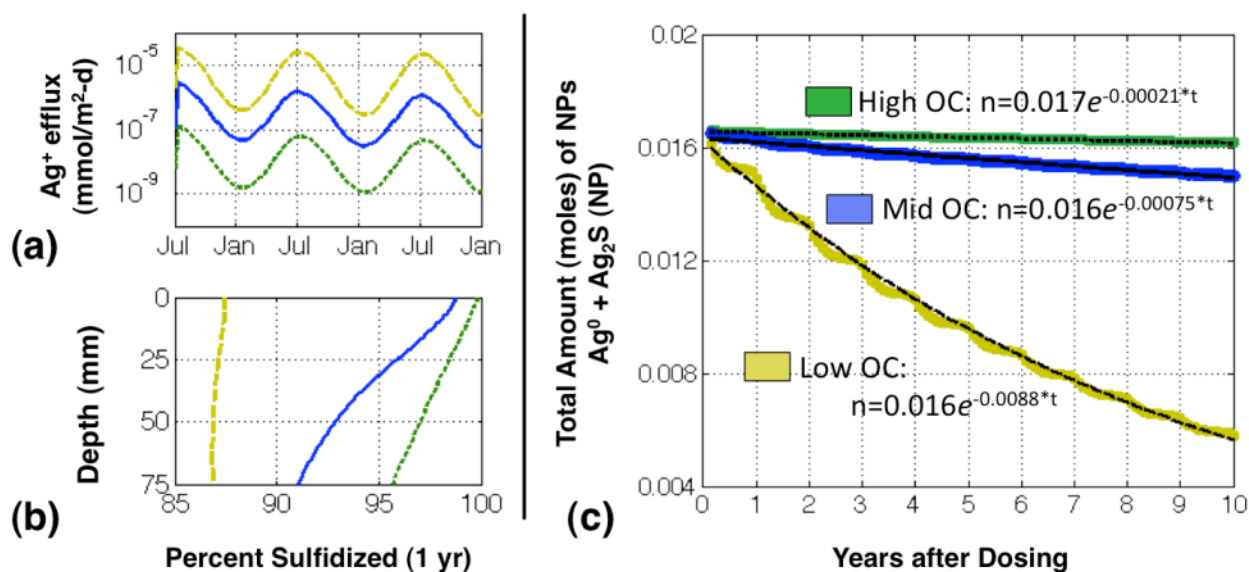


Figure 2-4. System response to low ($J_{POC,max}=75 \text{ mg/m}^2\text{-d}$, $f_{oc}=0.001$), mid ($J_{POC,max}=150 \text{ mg/m}^2\text{-d}$, $f_{oc}=0.02$; the “nominal” case in Figure 2-3), and high ($J_{POC,max}=300$, $f_{oc}=0.15$) levels of organic carbon (OC) for 85% sulfidized Ag NPs. (a) Ag^+ efflux vs. time. The semi-log scale reveals orders-of-magnitude differences between the three scenarios. (b) Ag NP sulfidation as a function of depth one year after dosing (July). (c) Total amount (moles) of Ag NPs in system over time. Nanoparticle half-life time is primarily a function of oxidant availability in the sediment. The decrease in total Ag NP amount within 10 years of dosing was fit to an exponential function, where t was expressed as months after dosing. Ag NP half-lives estimated from the best-fit curves are 6.6 years (low OC), 77 years (mid OC), and 280 years (high OC).

Aerobic diagenesis of carbon in high organic carbon systems results in low oxygen availability, and subsequent sulfate reduction results in high sulfide availability. Thus Ag^+ efflux occurs less readily (Figure 2-4, top left panel) but sulfidation occurs more readily (Figure 2-4, bottom left panel) in high

OC systems. The half-life of the 85% sulfidized Ag NPs was found to vary from 6.6 years to as much as 280 years in the model depending on oxygen availability (Figure 2-4, right panel). Ag NP half-lives were relatively insensitive to whether the particles were partially sulfidized or pristine (100% Ag⁰) upon dosing—half-lives for the pristine Ag NPs ranged from 3 months (low OC) to 280 years (high OC). Loss of Ag⁰ from the Ag NP cores (Figure A-3) results from Ag⁺ formation and sulfidation, and does not exhibit first-order exponential decay.

The mesocosm experiment used a single pulse input of a relatively high concentration of Ag NPs. A continuous input of low concentrations of nanoparticles from a wastewater treatment plant is a more realistic scenario. We assumed a continuous input scenario in which 20 million gallons per day of STP effluent (76,000 m³/d) containing 33 µg/L 85% sulfidized Ag NPs were released to a small (75 km²) lake, and that all silver entered the sediments. Results for the constant input case are provided in Figure A-4 and Figure A-5. Trends agree with those observed in the pulse input case (Figure 2-4). Ag NP accumulation occurs over time in this chronic low dose input case.

2.4 Discussion

Nanoparticles are expected to accumulate in sediments after release to surface waters. The toxicity of surface-reactive nanoparticles in environmental media depends greatly on chemical transformations undergone by the nanoparticles and released ions. Recent work has shown particle properties strongly affect Ag NP transformations.⁶⁷⁻⁶⁹ The present work reveals environmental conditions also play an important role.

Particulate organic carbon (POC) diagenesis has long been recognized as a key determinant of oxygen penetration depth and a driving force for sediment processes. The model suggests this process similarly drives Ag NP transformations in sediments. Eutrophic (high organic carbon, low oxygen, high AVS) systems maximize rates of Ag NP sulfidation and minimize toxic silver ion

production and diffusion into the water column. Ag NPs may persist in a partially or fully sulfidized form for over a century under these conditions.

Seasonal redox cycles may play a role in silver speciation, bioavailability, and toxicity. The model predicts Ag^+ efflux will be lowest in winter and highest in summer, although seasonal patterns in oxygen availability will vary across natural systems as a function of temperature, organic carbon, light, water currents, and bioturbation.⁹⁵ Figure 2-4 reveals that seasonal variation becomes relatively unimportant over long time scales, especially when compared to the importance of inter-site heterogeneity in sediment conditions.

The rate of Ag NP oxidation was assumed to decrease exponentially with Ag NP sulfidation (Equation 2-13). Because sulfidation occurs readily in the sediments in the nominal case, the initial extent of sulfidation becomes relatively unimportant within a year of dosing (Figure 2-3). Ag NPs that are $\geq 50\%$ Ag_2S by mass, as expected for Ag NPs released to natural waters, will exhibit behavior effectively identical to that of fully sulfidized (100% Ag_2S) NPs.

The Ag NP oxidation and sulfidation rates used here are specific to 30 nm Ag NPs. They do not account for the inverse relationship between Ag NP size and rates of transformation (e.g., as observed by^{26, 72, 81} and captured by the ranges in Table 2-1) or the effects of aggregation. In a toxicity study on earthworms, Shoults-Wilson et al. (2011) concluded that soil conditions are a more important determinant of Ag NP toxicity than size.⁹⁶ This is consistent with our finding that model predictions of Ag^+ release are relatively insensitive to the rates of Ag NP oxidation and sulfidation (Table A-4) compared to model variables describing the environmental conditions.

In several environmental risk studies of nanosilver,^{32, 33, 42} Predicted Environmental Concentrations (PECs) were compared to No Observed Effect Concentrations (NOECs) or LC_{50} values for the pristine Ag^0 NPs. Nanosilver risk is overestimated by this approach, which overlooks the significant reduction in acute toxicity expected after Ag NP sulfidation.²⁷ To improve risk

estimates, sediment PECs should be compared to toxicity thresholds for partially and fully sulfidized Ag NPs.

Even under oxic conditions, the toxic species Ag^+ represents <0.01 wt-% of the total silver in the system. Thus the toxicity of environmentally transformed Ag NPs and released ions may be quite low. However, Ag NP risk may be underestimated if, as has historically been the case, Ag^+ is considered the only bioavailable silver species in freshwater environments.^{29, 71, 78} Ingestion, uptake, or surface interactions with unsulfidized or partially sulfidized Ag NPs by aquatic plants and sediment organisms may lead to higher exposures.³⁸

Because Ag_2S is the principle product of Ag NP transformation, the rate of oxidation of sulfur in Ag_2S is of particular interest. Previous work reveals that complexation with metal ions stabilizes thiols and sulfides against oxidation under aerobic conditions.²⁷ Although Ag_2S is highly stable against dissolution ($K_{sp}=5.92 \times 10^{-51}$),^{27, 97} Ag_2S can exhibit greater solubility in the presence of sediments. The authors suggest this occurs because Fe(III) in the sediments facilitates oxidation.⁸⁸ At concentrations orders of magnitude higher than observed here ($\geq 10 \text{ mmol Ag/m}^3$), Ag^+ has been shown to transform into Ag^0 NPs in the presence of reduced humic acids.^{98, 99} This reaction occurs most rapidly in anoxic and suboxic environments. Because FeS and organic matter act as competing ligands in such environments, we do not anticipate that the in situ formation of Ag^0 NPs will play a significant role in nanoparticle fate for low-level releases of Ag^+ in sediments.

Future experimental work may reveal that other oxidants (e.g., Fe^{3+} , Mn^{4+} , NO_3^- , SO_4^{2-}) can oxidize Ag NP in sediments under non-equilibrium conditions. One strength of our approach is the ease with which different oxidants or transformative processes (e.g., bacterially mediated oxidation of sulfur in Ag_2S) can be incorporated into the model.

Regulatory and industry decision-making for the safe production, use, and disposal of nanomaterials requires models that can track the environmentally relevant species. Although

process-based models capable of describing the temporal evolution of particle size and aggregation state are highly desirable, they present unique theoretical challenges and computational demands. This work reveals that a mass balance model with no explicit inclusion of aggregation can successfully reproduce observations from a freshwater mesocosm experiment.

By omitting aggregation, the model assumes Ag NPs mix in the sediment at approximately the same rate as the sediment particles themselves. Since Ag NPs are largely expected to heteroaggregate (and thus co-transport) with sediments in natural environments,⁷⁵ this assumption appears justified. However, since the overall particle mixing rate (D_p) was determined by calibration, there is no way to test the assumption in this work. In general, data collected at high spatial and temporal density are needed on another Ag NP type or on a different environmental system to validate the model. Nonetheless, we believe the incorporation of nanoparticle chemistry into a conventional mass balance sediment metal modeling framework represents a significant step towards more accurate environmental risk models for nanoparticles.³¹

3 Stream dynamics and chemical transformations control the environmental fate of silver and zinc oxide nanoparticles in a watershed-scale model

3.1 Introduction

In the absence of monitoring data, mathematical models are commonly used to predict the concentrations and speciation of chemical contaminants in the environment. The predicted environmental concentrations (PECs) can then be compared to laboratory-determined dose-response information to estimate risk. Several recent large-scale models^{5, 6, 8, 10, 11, 32-34, 37, 40-42, 48} have estimated PECs and/or predicted the environmental fate of engineered nanoparticles (NPs), which are now entering surface waters at low levels due to their use in products such as paints, sunscreens, textiles, and cosmetics.²

Recent environmental fate models focus on "nano-specific" aspects of NP fate, or aspects that differentiate NPs from molecular contaminants (e.g., kinetic rather than equilibrium descriptors of NP heteroaggregation with soils and sediments^{5, 8, 11, 37, 45, 100}). Less attention has been paid to aspects of NP fate that are common to all contaminants, which are nonetheless important risk determinants. For example, most models have been solved at steady state^{8, 37, 41} and/or been spatially unresolved, averaging concentrations over large regions (e.g., nations).^{5, 6, 32, 33, 37} All have disregarded stream loads from surface runoff of NP-containing biosolids used as fertilizer or found them to be insignificant,^{5, 37} and none have considered spatiotemporal variability in sediment transport rates, described NP chemistry as a function of environmental conditions, or tracked NP reaction by-products (metal ions, metal sulfides, etc.). We present results from a watershed-scale model designed to predict the fate of two NPs with different chemistries, silver (Ag) and zinc oxide (ZnO), at comparatively high spatial and temporal resolution and assess the impact of these simplifying assumptions on the utility of NP fate models for risk assessment.

NPs and their reaction by-products primarily enter surface waters via municipal wastewater.² During sewage treatment, most NP mass associates with the solid waste (biosolids),^{6, 52} so agricultural runoff following the application of treated biosolids to crops may contribute to total metal stream loads in regions where biosolids are land-applied. Runoff is an important vehicle for many pollutants found in biosolids.⁴⁹⁻⁵¹

The affinity of NPs and metal ions for ubiquitous natural particles such as soil, sediment, micro-organisms, and insoluble organic matter, ensures that solids transport in the environment controls metal transport.^{75, 77, 101-103} Sediment deposition and scour in streams is highly variable. Deposition dominates in reservoirs and coastal plains, whereas scour dominates in mountainous regions with high bed slopes and water velocities. Scour also peaks during rain events.^{25, 26} Capturing the site-specific and dynamic (time-dependent) nature of sediment transport is essential in predicting the fate of strongly sediment-associated pollutants¹⁰¹⁻¹⁰³ but has not yet been attempted for NPs.

Finally, the environmental toxicity of reactive NPs such as ZnO and Ag depends upon their speciation, which is impacted by environmental factors such as temperature, pH, dissolved oxygen, and sulfide.³¹ Metal ions formed by NP dissolution can be highly toxic,^{54, 104} but reaction of NPs and metal ions with naturally-occurring sulfides and metal ion complexation with solid phases often reduces toxicity.²⁵⁻²⁹

We coupled the James River Basin (VA) portion of the Phase 5.3.2 Chesapeake Bay Watershed Model (WSM)⁶² to the USEPA's publically available water quality modeling suite WASP7¹⁰⁵ and configured both to model ZnO and Ag NP fate. The James River Basin contains large and small population centers, reservoirs, mountainous and low-lying stream reaches, forests, and extensive agricultural production (Figure 3-1, Figure B-1). ZnO and Ag NPs and their transformation by-products entered the model via wastewater treatment facility effluent and

biosolids applications to row crops, hay, and pasture land. Land-applied biosolids and soil were eroded and carried to streams during rain events. The river simulation calculated sediment transport rates as a function of spatiotemporal variability in stream flow; distinguished between oxic and anoxic sediment bed layers; and tracked temperature-dependent chemical reactions including ZnO NP dissolution, oxygen-dependent dissolution of Ag NPs, sulfide-dependent sulfidation of metal ions, and metal ion complexation with particulate phases.

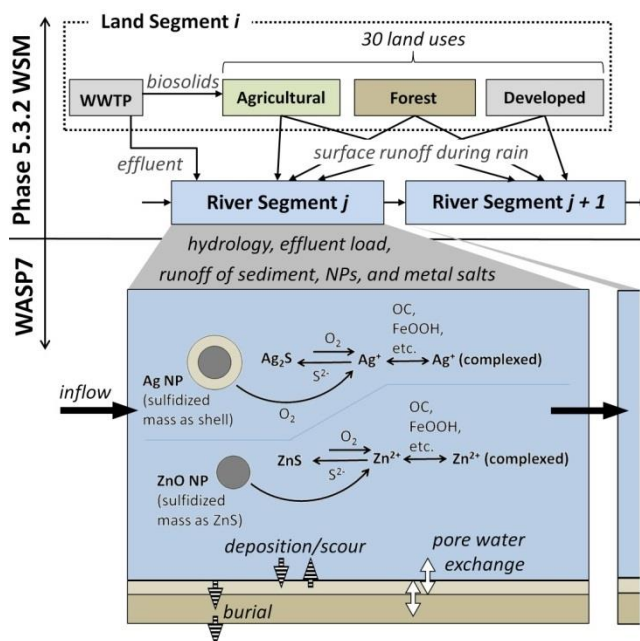


Figure 3-1. Structure of the coupled WSM/WASP7 model. The modeled region (Figure B-1) is divided into 65 land segments and 68 river segments. For each of 30 land use types in each land segment, runoff loads are apportioned to river segments. Runoff loads, effluent loads, and stream hydrology from the WSM are read into WASP7, which performs in-stream sediment and metal transport and chemical transformations. Physical processes in-stream affect either all chemical species (solid black arrows), solid-associated species (striped arrows), or dissolved species only (white arrows). Abbreviations: WWTP - wastewater treatment plant. NP - nanoparticles.

The coupled model was run for 20 years using historic hourly weather data and an NP loading scenario representing estimated 2010 concentrations of Ag and ZnO NPs in wastewater effluent and biosolids.³³ Although it can be considered representative of current conditions, this loading scenario

suffers from the same weakness of all such estimates: it is impossible to verify due to analytical and data limitations. Thus the simulation is not intended to predict the environmental concentrations in the region over a specific time period, but rather to explore natural variability in the environmental fate of NPs and to identify major factors controlling their behavior in rivers.

3.2 Methods

3.2.1 Model region

The modeled region was the 17,600 km² Upper and Lower James River Basins in Virginia (Figure B-1).^{106, 107} The region is 80% forest, 13% agriculture, and 5% developed. The basin encompasses Lynchburg and Charlottesville. Richmond lies at the lower boundary.

3.2.2 Model framework and resolution

The WSM is an implementation of HSPF (Hydrological Simulation Program--FORTRAN) designed to facilitate sediment and nutrient management planning in the Chesapeake Bay.⁶² We used the WSM to predict stream loads from surface runoff and effluent discharges and to configure the stream hydrology of the river model. The river model was implemented in WASP7 (Figure 3-1). Input data, code, and complete documentation for the WSM can be found at ches.communitymodeling.org/models/CBPhase5/index.php.

Like most pollutant fate models,^{3, 39} WASP7 and the WSM break the modeled region into environmental "compartments" in which constituent masses are assumed to be completely mixed.⁶²
¹⁰⁵ The land simulation has 3 soil layers x 30 land uses (listed in Table B-1) x 65 land segments, or 5,850 soil compartments. Land segment boundaries follow county boundaries according to a 1:100,000 scale data set, but were subdivided further in mountainous regions to differentiate ridges

from valleys. The drainage area for each river segment was specified using 30-meter-resolution Digital Elevation Map (DEM) data.⁶² The 68 stream segments have a mean hydraulic residence time of 0.6 days and a mean length of 30 km. Two stream segments represent reservoirs. The WSM has an hourly time step and outputs were averaged for use in WASP7, which has a daily time step. WASP7 uses a variable (< 1 day) computational time step as needed to ensure numerical accuracy.

Our WASP7 model used the WSM river segmentation scheme (channel length, width, and slope) and predicted stream hydrology (daily volume, velocity, and depth for each river segment), which was calibrated prior to this work to data from 33 monitoring stations in the modeled region.⁶² The simulation reflects the 20-year meteorological record from 1986-2005.⁶² Other WSM outputs used in WASP7 included daily effluent and runoff loads to each river segment (sediment and metals), average daily stream temperature, and average daily dissolved oxygen (DO) concentration.

3.2.3 NP Release Scenario

Parameter values and sources are provided in Table B-2 and Figure B-2. NP concentrations in effluent and biosolids were fixed at the mode of U.S. estimates by Gottschalk et al.,³³ which were more conservative (higher) than corresponding values predicted for Ag NPs by Hendren et al.¹⁰⁸ Effluent discharge volumes and biosolids application rates were based on 2010 data reported at the plant scale (effluent) or county scale (biosolids).⁶² Daily variation in effluent discharge was not considered. Thus metal mass loads from effluent remained constant over time, which is approximately correct if the use and disposal of Ag and ZnO NP-containing products also remains constant. The 82 municipal wastewater treatment facilities in the basin range in capacity from 8 to 43,000 m³/d. Two plants account for 68% of effluent loads.

Biosolids application rates were calculated with the Scenario Builder tool,⁴⁰ which was parameterized prior to this work using agricultural census data. Scenario Builder has a higher

resolution than the WSM (e.g., it includes over 100 crop types). Rates varied monthly according to crop nutrient need, reflecting spatiotemporal variation in tillage practice, crop type, and growing season.¹⁰⁷ Simulated biosolids applications occurred every third day and were split between the 1 cm surface layer (30% by mass) and the variable (~7-12 cm) upper soil layer (70%). Error resulting from these simplifying assumptions is minimized by calibration of the sediment and nutrient runoff predictions, as described below.

The ratio of NP-derived metal mass applied to the land surface versus discharged directly to the stream, as predicted by the WSM upon adaption for NPs, was 23:1. This ratio is consistent with a wastewater NP removal efficiency of 98%, which agrees well with literature values,^{2, 6} and with application of 48% of solid waste to fields as fertilizer, the estimated 2010 national average.¹⁰⁹ Average estimated application rates across all land uses and land segments were 0.3 kg Ag/km²-yr and 4.4 kg Zn/km²-yr. All Zn in soils was assumed to be complexed (particulate-associated) Zn²⁺, since ZnO NPs are converted to Zn²⁺ complexed with phosphate or adsorbed to ferrihydrite during aerobic post-processing of sewage sludge.^{110, 111} Zn in wastewater effluent was modeled as 7.5% ZnO NPs and 92.5% Zn²⁺ based on results from a simple sewage treatment plant chemistry model (Appendix B, Supporting Methods, "Aeration tank model"). AgNPs were assumed to be over 50% sulfidized in biosolids and effluent, as observed experimentally.^{81, 87} Sulfidized Ag NPs resist oxidative dissolution during aerobic treatment of biosolids.¹¹¹

The formation of a passivating shell of Ag₂S causes partially sulfidized Ag NPs to exhibit far lower solubility than untransformed Ag NPs.²¹ In contrast, sulfidation of ZnO NPs does not form a protective shell of ZnS on the NP or impact its dissolution rate²² (Figure 3-1). Because WASP7 cannot model core-shell structure formation, and because the reaction kinetics of > 50% Ag₂S Ag NPs are effectively the same as that of 100% Ag₂S Ag NPs,^{21, 61} further Ag NP sulfidation in the river and sediments was not modeled.

Direct environmental emissions during NP-containing product use were assumed to be insignificant. ZnO NPs in sunscreens may be an important exception. However, it would be very difficult to accurately predict sunscreen emissions from bathers swimming in the modeled region.

3.2.4 Land Simulation and River Network Simulation Assumptions

NPs were assumed to heteroaggregate completely in all media. For surface waters, the assumption is justified by characteristic times to heteroaggregation that are close to or below our daily time step. Therezein et al. predicted a half-life of less than a day for unaggregated particles when total suspended sediment (TSS) concentrations exceed ~ 15 mg/L and α (the probability of attachment upon particle collision) exceeds 0.05.⁹ For PVP-coated Ag NPs in freshwater when TSS = 9 mg/L (our modeled average), experimental rates reported by Quik et al. under quiescent conditions would result in unaggregated NP half-lives below 3 days.¹¹² In systems exhibiting periodic turbulence and resuspension, heteroaggregation would occur in 0.1-0.5 days.¹⁶ Aggregation may occur even more readily in soils than in surface waters due to high background particle concentrations. Meesters et al. (2014) predicted nearly complete NP heteroaggregation on soils.³⁷ We revisit this assumption in the Discussion.

Surface runoff of sediments during rain events was modeled for a "representative acre" of each land use in each land segment. The ability of tillage, plowing, and crop cover to promote or prevent runoff was handled separately for each land use. The fraction of the runoff that reached the stream was proportional to the land area for each land use and the average distance from the land use to the stream.⁶² Runoff predictions were calibrated prior to this work against expected annual runoff loads based on alternative models, observations, and the published literature.⁶² Assuming that NP transport is highly correlated with sediment transport, the calibrated sediment runoff predictions from the WSM should predict NP runoff equally well.

Sediment runoff loads were split at the stream edge into silts/fines (average diameter: 6 μm , approximately 95% of runoff) and sand (130 μm) using segment-specific factors previously calibrated for the WSM.⁶² All sediment-bound metals were assumed to transport with silts/fines because of the high surface area of the latter.¹¹ This is generally the case for strongly sediment-associating pollutants.¹¹³

Each modeled river segment has a 1 mm subaquatic surface sediment layer and a 10 cm deeper sediment layer. These depths are typical of two-layer sediment models.²⁴ The surface layer is assigned half the dissolved oxygen concentration of the overlying water. Deep sediments are anoxic. The sediment transport equations used by WASP7 to model sediment deposition and resuspension as a function of the spatiotemporally variable, flow-dependent shear stress at the sediment-water interface are presented in Appendix B (Supporting Methods, "WASP7 sediment transport equations").¹¹⁴ Related parameters (Table B-2) were determined by calibration of the simulated TSS concentrations to over 750 observations at a downstream monitoring station using established metrics (NSE, PBIAS, RSR)¹¹⁵ (Supporting Methods, "TSS calibration").

We used the midpoints of ranges of reported dissolution rates that included many NP sizes and surface coatings (Table B-2). Reaction rates were assumed to depend linearly on the concentrations of all reactants (NPs, O_2 , S^{2-}).

Following convention for hydrologic models,⁶² we minimized the influence of initial conditions on results by running the model for two years (meteorological years 1984-1985) prior to the first reported "simulation year."

3.3 Results

3.3.1 Agricultural runoff contributes to NP-derived metal stream loads

Runoff of land-applied biosolids during rain events accounted for 23% of the total stream load of Ag and Zn from NPs over 20 simulation years, even though only 1.3% of the metal mass applied to the land surface reached the river. Figure B-3 shows spatial and temporal trends in runoff. Daily total runoff of NP-derived metal loads exceeded daily total effluent loads on 2.5% of days. Runoff loads on these days exceeded effluent loads by up to two orders of magnitude.

3.3.2 Ag and ZnO NPs were extensively transformed

Figure 3-2 describes the simulated mass distribution and speciation of NP-derived (a) zinc and (b) silver in the water column, the oxic surface sediments, and the underlying anoxic sediments. The ZnO NPs in WWTP effluent (see Methods) dissolved so quickly in the river that they accounted for < 0.05% by mass of NP-derived Zn found in all layers. Dissolved Zn^{2+} , which is bioavailable and potentially toxic, was relatively abundant in oxic surface waters, whereas particle-associated Zn^{2+} predominated in oxic sediments. A drop in dissolved oxygen in summer in the usually oxic sediments resulted in annual peaks of ZnS, the dominant Zn species in the anoxic deep sediments. Results agree with expectations for Zn^{2+} in aerobic and anaerobic environments.^{116,117}

Following empirical studies, we assumed that >50% of the Ag had formed a shell of insoluble Ag_2S on the surface of the NPs prior to environmental release via effluent and biosolids (see Methods).^{81,87} Unlike ZnO NPs, these Ag_2S -coated NPs were highly persistent. The sediment half-life for sulfidized Ag NPs ranges from 5 years to over a century, depending on redox conditions, with a typical half-life of 77 years.⁶¹

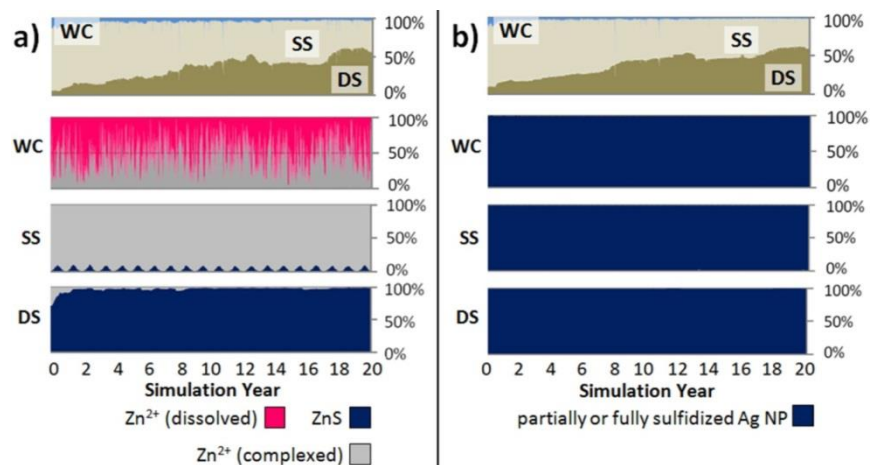


Figure 3-2. Location (top graphs) and speciation (bottom six graphs) over time of a) Zn from ZnO NPs and b) Ag from Ag NPs, expressed as percent by mass in the water column (WC), oxic surface sediments (SS), and anoxic deep sediments (DS). Both metals accumulate rapidly in surface sediments and penetrate deep sediments more slowly. ZnO NPs disappear due to rapid dissolution during sewage treatment and in the river. In contrast, Ag NPs persist in their partially or fully sulfidized form.

3.3.3 Most of the NP metal stream load escapes the basin

Comparing the cumulative stream load to the metal mass remaining in the river and sediment bed over time (Figure 3-3) reveals surprisingly high metal mobility. Only 5.4% of Ag and 2.6% of Zn loads were retained. Mobility was due to flow-dependent sediment transport. Transient peaks in flows prevented deposition and scoured the sediment bed where NPs and particle-associated metal ions accumulated. High deposition and low scour occurred in segments with low average stream velocities; low deposition and high scour occurred in segments with high average velocities (Figure B-4).

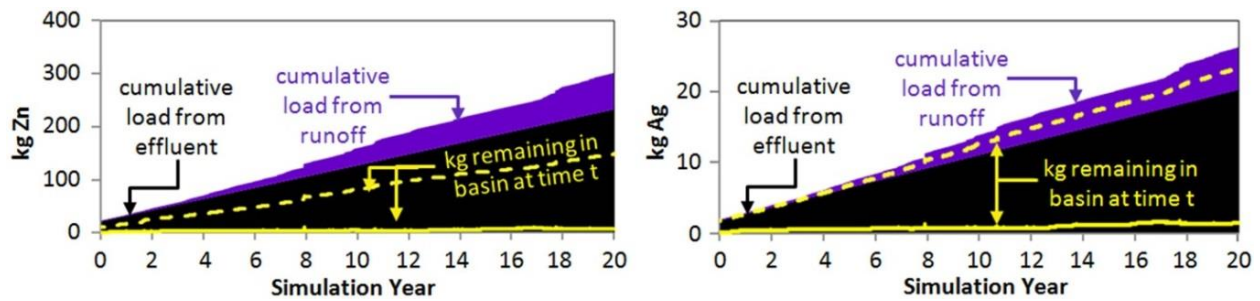


Figure 3-3. Comparison of the cumulative total zinc (left) and silver (right) load to the river over time from effluent (black) and agricultural runoff (purple) to the total mass remaining in the river and sediment bed over time (yellow). Little (<6%) metal accumulation occurs in the river (solid yellow line). Much more accumulates (42% Zn, 87% Ag) in a scenario where sediment resuspension and deposition rates are treated as spatiotemporally invariant (dashed yellow line).

We also present results for an alternative sediment transport scenario in which there was no barrier to deposition (gravitational settling only) and resuspension rates were held constant at their spatiotemporal average (1.2 mm/yr)--common assumptions in NP fate modeling.^{8,11,41} This scenario resulted in 87% of Ag and 42% of Zn loads accumulating in the river (Figure 3-3; dashed yellow lines). Overall, this scenario over-predicted surface sediment concentrations of Ag and Zn by a factor of 4,000 and a factor of 7, respectively, relative to the scenario with dynamic and geographically variable sediment transport assumptions. Figure B-5 reveals that over-prediction of accumulation occurs over the full range of expected average resuspension rates in rivers reported by ref¹¹³ (1-30 mm/year). It also shows that gravitational settling is not a good predictor of deposition rates in this river model, and that geographic variability had a greater influence than temporal variability.

Zn accumulated less than Ag because dissolved Zn^{2+} transported with the aqueous phase rather than the sediments.

3.3.4 Metal accumulation in sediments is observed locally but not basin-wide

To visualize spatiotemporal variation in predicted environmental concentrations (PECs), cumulative distribution functions (CDFs) of total NP-derived metal concentrations over time were plotted for each river segment (Figure 3-4). Sediment bed concentrations on a dry mass basis are reported here as the average concentration over 2 cm of depth in order to match model results to standard monitoring procedures (sediment coring) used to compare metal concentrations to regulatory standards. On a total volume basis (pore water and sediment), NP-derived metal concentrations were three orders of magnitude higher on average in the sediment bed than in the water column. Metal concentrations in the 1 mm surface sediment layer were, on average, two orders of magnitude higher than in the deeper sediments.

Predicted NP-derived Ag and Zn concentrations varied by several orders of magnitude across river segments. However, the PECs remained at least 75 times smaller than USEPA water quality criteria (WQC) and sediment quality guidelines (SQG) for metals (Figure 3-4) in all stream segments at all times (see Supplementary Methods, "Regulatory thresholds"). The PECs resulting from NP inputs were also smaller than total metal concentrations previously observed downstream of Richmond in the James River Basin (Table B-3). Because we are not confident that the loading scenario represents actual NP loads in the region, these comparisons should be viewed as suggestive but not definitive.

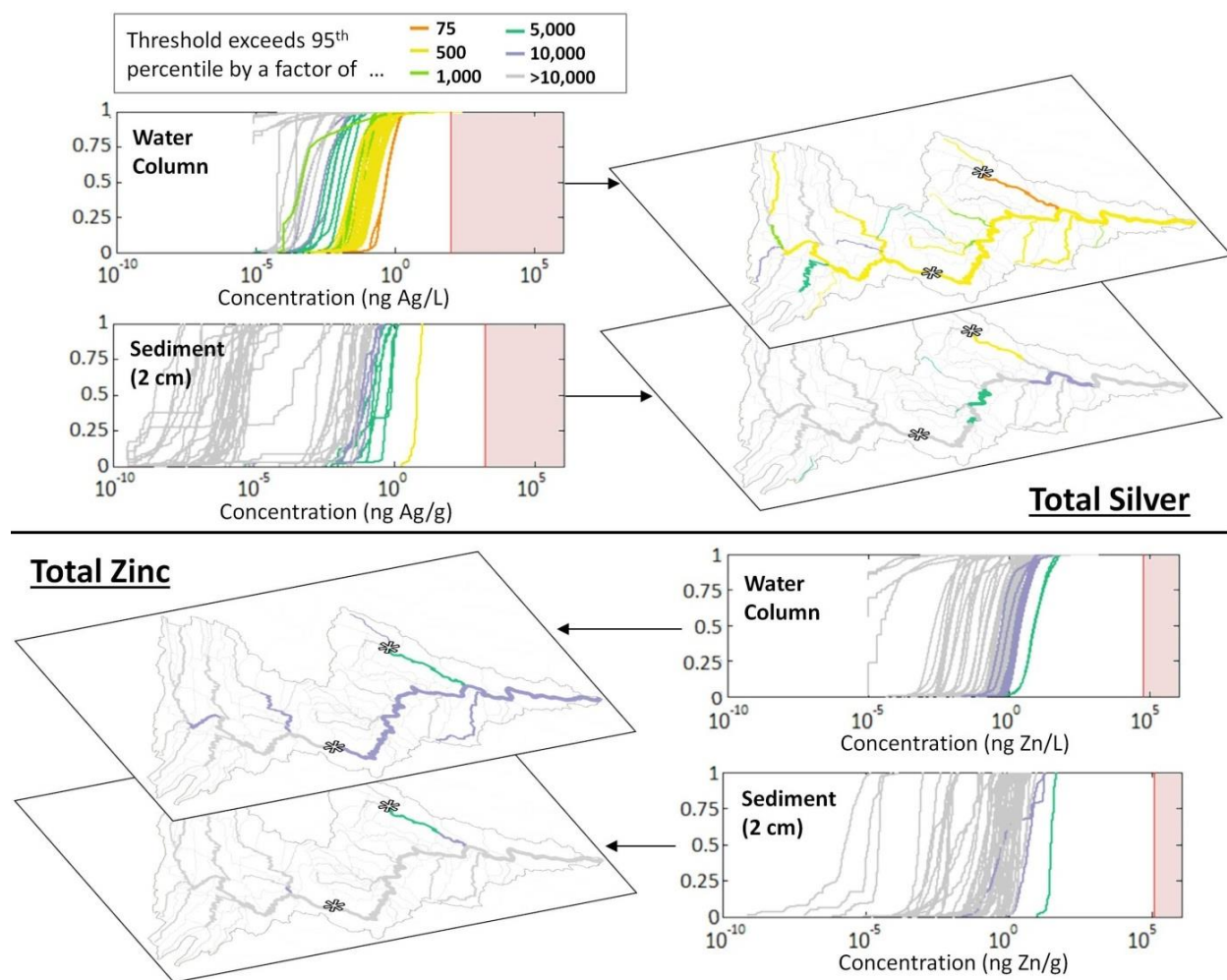


Figure 3-4. Cumulative distribution functions (CDFs) of total metal concentrations over time for each segment in surface water and sediment for Ag (above) and Zn (below). Concentrations do not exceed EPA water and sediment quality thresholds for metals (red vertical lines; see "Regulatory thresholds" in Appendix B, Supporting Methods). GIS plots show where in the modeled region 95th percentile concentrations are closest to exceeding thresholds. Large point source loads are marked by asterisks. The open-source software QGIS was used to visualize geospatial data.

Spatial variation in PECs (variation between CDFs in Figure 3-4) was greater than temporal variation (variation within CDFs). Figure 3-5 shows the extent to which spatial variation in temporally averaged predicted total metal concentrations in each segment can be explained solely by the total NP-derived metal loads from runoff, effluent, and upstream. Results show that the explanatory power of the total load is imperfect. The highest concentrations occurred, not in river

segments that received the highest loads, but in segments that also had low stream velocities and high sediment deposition. Total load is a particularly poor predictor of sediment Ag PECs because Ag (unlike Zn) moves entirely with sediments in this model.

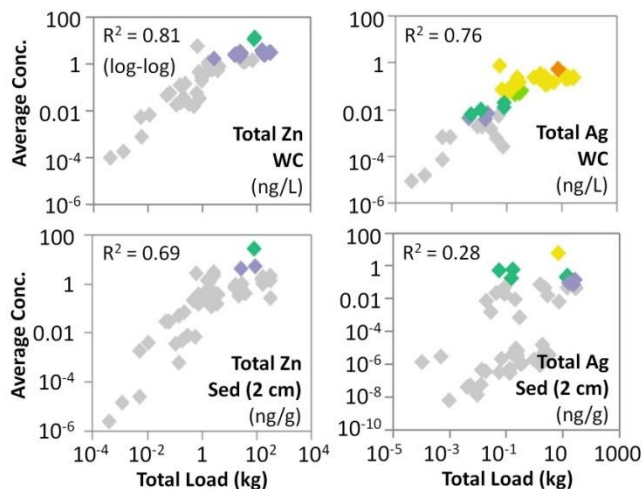


Figure 3-5. Average total metal concentrations in each river segment vs. the total metal load to that segment (upstream load + effluent load + runoff load) over the course of the simulation. Variation that is not explained by input load is explained by spatial differences in stream hydrology and sediment transport. Zn concentrations are better explained by load than Ag concentrations because Ag is present mostly as sediment-bound NPs in the water column and sediment bed whereas much of the Zn is present as dissolved ion. Sediment Ag concentrations are least well predicted by load alone. The highest metal concentrations occur in segments that experience low velocities as well as high loads. Colors as in Figure 3-4. Abbreviations: WC – water column, Sed – sediment.

Figure 3-6 shows the total Ag concentration vs. time for two segments over the five-year period that included both the driest (brown) and wettest (blue) year. When agricultural runoff was a significant fraction of stream loads to the segment and average stream velocities within the segment were low (left panel), concentrations increased during high flows (the wettest year). In contrast, concentrations were diluted by high flows when point sources predominated (right panel). Trends in sediment bed concentrations varied even more widely over this time period (Figure B-6).

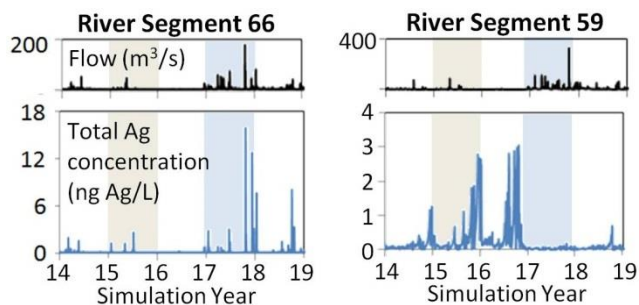


Figure 3-6. Total Ag concentrations (ng Ag/L) for two river segments (left and right) for the five-year period that includes the driest year (brown) and wettest year (blue) in the simulation. Segment 66 (left) has a low average water velocity and receives most of its Ag load from runoff, so Ag concentrations peak with high flows. In contrast, dilution is observed during high flows for Segment 59 (right) receiving primarily effluent loads.

3.4 Discussion

Previous NP fate models have relied on relatively simple representations of sediment transport, agricultural runoff, and NP chemistry. Our results suggest that models neglecting or oversimplifying these processes have under-predicted NP mobility in rivers and misrepresented risk. The high spatiotemporal variability observed here suggests that spatially averaged and steady state models have limited use for risk assessment at the watershed scale or larger.

Metal mobility was strikingly high in our model due to flow-dependent sediment scour and deposition. A spatiotemporally invariant alternate sediment transport scenario based on prevailing approaches in NP fate models^{8, 11, 37, 41} did not share this high metal mobility. In the case of Ag, 87% of input Ag loads accumulated in the river under the constant transport scenario compared to less than 6% under more realistic sediment transport assumptions. Note that associating the NPs with sand-sized particles rather than silts/fines did not appreciably change their mobility; accumulation in the river and sediment bed remained below 6% (not shown). Mobility may be even higher than predicted here due to bedload shift.^{8, 11, 41} However, bedload shift is not usually an important transport process for silts/fines, our assumed NP-carrying sediment fraction.¹¹³ Metals that escape

the basin will accumulate in tidal, estuarine, or coastal sediments downstream, and there is a need for better understanding of NP fate and toxicity in such environments.

As expected from experiments in soils¹¹⁸ and sediments,³⁸ simulated metal concentrations were highest in the surface sediment layer. Penetration to deep sediments was slow. Average sediment PECs varied up to nine orders of magnitude across the basin and average water column PECs varied five orders of magnitude (Figure 3-4), which calls into question the relevance of the practice of averaging PECs over regions or nations.^{5, 6, 32, 33, 37} In agreement with refs^{42, 48}, we find that spatial variation in loading is important. Indeed, its importance is probably under-predicted here because we did not consider variation in biosolids and effluent concentrations (see Table B-2 for reported ranges). In agreement with ref¹⁰, we find that natural variation in system hydrology and sediment transport must also be considered in order to identify regions of enhanced metal accumulation at spatial scales that are relevant for regulatory and management efforts (Figure 3-5). Low velocity environments such as river impoundments or wetlands downstream from point source discharges are of particular concern.

The model predicted that agricultural runoff was a non-trivial source of total metal stream loads (23%). This agrees with recent findings for non-NP metals^{51, 119} but contrasts with predictions from two recent NP models that lacked spatial resolution.^{5, 37} Spatial and temporal resolution are needed to model runoff, which is highly localized and transient in nature.

Several NP fate models have predicted biosolids, effluent, or environmental concentrations of ZnO or Ag NPs without modeling chemical transformations (beyond simply noting that transformations may occur).^{32-34, 40, 42, 48} And yet, in agreement with experiments,^{20-22, 61, 81, 87, 110, 111, 120-123} we found that Ag and ZnO NPs will not be released to surface waters or occur in the environment in their as-manufactured state (Figure 3-2). Risk model predictions for untransformed NPs are thus environmentally irrelevant. Sulfidized Ag NPs persisted in both oxic and anoxic environments.^{21, 61}

ZnO NPs dissolved rapidly regardless of our choice of NP dissolution rate (see Appendix B, Supporting Methods, "Aeration tank model" for sensitivity analysis).

Calibration and validation of NP concentrations in fate models is precluded at present by the same lack of field data that makes their development so necessary. This potential handicap is not of great concern here, since our NP loading scenario is purely illustrative. Our goal was not to predict environmental concentrations of NPs with certainty, but rather to determine the effect of environmental variability on NP fate and explore the influence of simplifying assumptions on the accuracy and usefulness of model predictions. Nonetheless, we believe that transport is generally well-predicted by the model, since NPs are strongly sediment-associating and our sediment predictions were calibrated to observed data.

Several shortcomings of the model should be noted. First, including a background pool of metal ions from non-NP sources would have created a concentration gradient that promoted net metal transport from the sediment bed during pore water exchange, rather than the net transport to the sediments that occurred in our model when sediment concentrations were zero. However, turning off pore water exchange in our model only decreased Zn accumulation in sediments by 1%, so this effect was not significant. For Ag NPs, no effect was observed. Second, at the moderate spatial resolution employed here (30 km average stream segment length), overall advective transport (contaminant mobility) is accurate, but spatial variation is underpredicted, and transient concentration peaks during high- or low- flow events may be somewhat dampened.^{124, 125} Thus improving the spatial resolution of the model would only strengthen our conclusions about the importance of spatiotemporal variability. Third, not all metal ion complexation reactions form soluble products, so the reversibility of complexation that is assumed when using metal ion partition coefficients will not always be correct. For this reason, the formation and dissolution of low-solubility metal sulfides was treated separately (Figure 3-1). We did not treat $Zn_3(PO_4)_2$ separately

from other Zn^{2+} complexes in this work, since it is only one of many Zn species found in biosolids, effluent, and the environment and its dissolution rate is (to our knowledge) unknown. However, $Zn_3(PO_4)_2$ can account for up to 40% of transformed ZnO NP mass in sewage biosolids.^{110,111} If $Zn_3(PO_4)_2$ dissolution is exceedingly slow, the mobility of the NP-derived Zn will approach that of the highly insoluble Ag_2S NPs. Fourth, this model did not consider overbank flow and the possible deposition of NPs in the floodplain. Depending on the river system, this could significantly change NP transport rates.¹²⁶

Unlike many recent works,^{5, 8, 11, 37, 45} we do not account for "nano-specific" aspects of NP fate such as surface area-dependent reaction kinetics and size-dependent, kinetic NP heteroaggregation. For ZnO NPs, "nano-specific" aspects of fate are moot because the ZnO NPs are present at less than 0.05 wt-% in all media relative to transformed species. NP size and Ag_2S shell layer thickness similarly had little effect on Ag NP dissolution, since dissolution was very low regardless. Finally, rather than using a mechanistic, population balance-based colloid model (the Smoluchowski coagulation equation) to describe NP-sediment heteroaggregation, we assumed fast heteroaggregation leading to 100% NP association with sediments (see Methods). In spite of this assumption, over 90% of the Ag NPs escaped the basin because the sediments themselves were highly mobile. The sensitivity analysis shown in Figure B-7 reveals that predicted Ag NP accumulation dropped from 5% to 0.15% as the assumed affinity of the NPs for the solid phase decreased. Note that, even if we had used the Smoluchowski equation, we would still have predicted complete association of NPs with sediments, since heteroaggregate break-up is generally not modeled at present and NPs are likely to undergo at least one successful collision with solid particles in sewage treatment plants or on crop fields before release to surface waters. Ultimately, lack of model sensitivity to NP-specific effects suggests that fate processes common to all contaminants drive NP fate. However, this is a major topic of current research. Next-generation models that

account for heteroaggregate break-up and the stabilizing influence of environmental factors such as organic carbon¹¹ may yet disprove our hypothesis.

Of course, conditions in the James River Basin are not representative of all basins worldwide. For instance, in countries that do not allow the land application of biosolids, non-point sources--and their influence on stream concentrations --would be irrelevant. NPs such as TiO_2 and SiO_2 are chemically inert in aquatic systems. Nonetheless, it is clear that environmental fate models for NPs must be careful to describe environmental variability at the level of detail needed to identify, locate and quantify environmental risks from these emerging chemical pollutants.

4 A comparison of population balance frameworks for models of nanoparticle aggregation and surface transformations in aqueous media

4.1 Introduction

Within the past decade, rising concerns about the environmental and human health risks posed by nanoscale pollutants have motivated the development of mathematical models that capture nanoparticle (NP) behaviors and fate in laboratory suspensions and natural surface waters.

Although early efforts relied on frameworks designed to describe chemical reactions and/or sorption processes in homogenous solutions of molecular and ionic contaminants (e.g., material flow analysis, mass balance), the field has increasingly moved towards frameworks designed to describe colloidal suspensions.^{12, 14, 59}

Implicitly or explicitly, all NP fate models based on colloid science are either representative of, or are variants upon, "population balance" frameworks, a modeling method that has historically been applied to a diverse array of particle processes including aerosol particle microphysics,^{55, 56} flocculation during water treatment,⁴³ contaminant transport in granular media filters,¹²⁷ microbe transport in soils,¹²⁸ crystal growth,⁵⁸ soot particle formation in flames,¹²⁹ and droplet formation during spray combustion.⁵⁷ Although population balance is often defined simply as an implementation of the population balance equation (PBE), a continuity equation that describes the evolution of a particle size distribution over time and/or space during particle aggregation/fragmentation and growth/dissolution,^{58, 130} population balance more generally describes the evolution of the distribution of any particle property or combination of properties (so-called "internal coordinates") over time and space ("external coordinates").¹³¹ However, as the definitional property of NPs, size is the major focus of this work.

Population balance methods can model every particle in a population separately,¹³² treat size distributions as continuous, or model every possible aggregate size. The last of these approaches has

in fact already been applied to problems of NP homoaggregation and settling.^{45, 133} However, because these alternatives are computationally burdensome, even intractable, most models instead discretize the size distribution to reduce computational demands. The three most popular PB frameworks are the sectional method, Monte Carlo methods, and moment methods.^{58, 134-136}

In the sectional method (SM) or the "method of classes,"^{58, 129} the size domain is divided into sections, or bins, and the particle size distribution is treated like a histogram. Therezien et al. (2014) used the SM to describe the homoaggregation and heteroaggregation of monodisperse NP suspensions.⁹ Simplified variants on classical sectional approaches have also been developed at the river scale in order to assess the environmental fate of NPs. NP and aggregate populations in river models have typically been described by 5 or fewer size bins divided at even intervals across a fixed grid.^{8, 11, 37, 44, 46} Most such models have only described NP transport processes (e.g., advection, heteroaggregation, and settling), but one also included surface-dependent NP dissolution kinetics.⁵

Monte Carlo (MC) simulation explicitly models a finite population of (e.g., $> 10^3$ - 10^4) particles.^{58, 136, 137} Although MC simulation is considered too computationally expensive for incorporation with computational fluid dynamics (CFD) code or for use in systems with more than one internal coordinate,^{131, 134, 138} it is a reasonable alternative for the treatment of particle size in batch reactor-type systems. MC simulations have been used to describe NP synthesis^{139, 140} as well as NP homoaggregation in simple media.¹³⁷ A MC model of silver NP homoaggregation and dissolution was also recently developed to predict dosimetry in cellular toxicity studies.¹⁴¹

Relative to MC and the SM, moment methods conserve computational resources by tracking the lower-order statistical moments of a particle size distribution instead of tracking the entire distribution.^{58, 142} As described shortly, the moments capture the essential descriptive metrics associated with a distribution and can also, in specific cases, be used to reconstruct it. Moment

methods have been used extensively to describe the intentional and incidental synthesis of NPs,^{129, 143, 144} but they have not yet been applied to problems of NP fate and behavior in aqueous media.

For this work, we applied three population balance models to problems of NP dissolution, aggregation, and simultaneous dissolution and aggregation: two moment methods (Direct Quadrature Method of Moments^{131, 145} and the Extended Quadrature Method of Moments⁵⁷) and the SM.^{130, 146} We chose moment methods because they were previously unexplored in the NP fate literature and their computational efficiency makes them a compelling alternative to the SM. Results were analyzed with respect to runtime and accuracy. The SM was then investigated in greater detail.

4.2 Methods

This section provides a brief overview of the population balance frameworks for tracking particle transformations developed for this work. Interested readers will find more details in the Supporting Methods (Appendix C).

2.1 General Principles of Population Balance

2.1.1 The Population Balance Equation

The following population balance equation (PBE) describes the time evolution of the particle size distribution, f , due to simultaneous dissolution and aggregation^{43, 55, 56, 58, 130, 142}

$$\frac{\partial f}{\partial t} = -\frac{\partial(Af)}{\partial m} + \frac{1}{2} \int_0^m \alpha(m-m', m')\beta(m-m', m')f(m-m')f(m') dm' - f(m) \int_0^\infty \alpha(m, m')\beta(m, m')f(m') dm'$$

Equation 4-1

where m (particle mass) was our chosen internal coordinate, $A=dm/dt$ describes the change in particle size due to dissolution,^{130, 142, 146} β is the frequency of particle-particle collisions that can lead to an aggregation event, and α is the probability that two particles will remain attached upon collision. α is alternatively called the "sticking coefficient" or "attachment efficiency," and is a major focus of current nanoparticle research.^{112, 147, 148} Equation 4-1 can also include terms for processes such as aggregate breakage or settling.

We chose to describe NP size using particle mass, rather than radius, for several reasons. The mass of every newly formed aggregate can be calculated exactly from the masses of the colliding species. In contrast, the radius of a new aggregate must be estimated from the assumed geometry of the colliding species and the aggregate itself.⁹ In Supporting Methods (Appendix C), we also show that using mass instead of radius resolves a potentially crippling problem with population balance equations that rely on the Nernst-Brunner modified Noyes Whitney equation to describe dissolution. For this rate law (which we do not employ in our model for reasons discussed in the Appendix), $A=dr/dt$ approaches infinity as particles become infinitely small.⁵⁶

The second and third terms on the right-hand side, which is the Smoluchowski equation for particle aggregation, describe (respectively) the formation of new aggregates of size m via the aggregation of particles or aggregates of size $(m-m')$ with those of size m' , and the loss of particles of size m due to the aggregation of particles of that size with those of any other size. The Smoluchowski equation applies equally to heteroaggregation⁹ and to homoaggregation, the focus of this work.

2.2 The Sectional Method

2.2.1. Binning Approach

In the Sectional Method (the SM), Equation 4-1 is discretized. Particles are distributed into bins at time 0 based on their size and are re-binned during each time step according to their rates of aggregation and dissolution (Figure 4-1). Rates may or may not be size-dependent.

We used the binning method and numerical solution proposed by Lister et al.¹³⁰ This method differs from sectional methods used to date in the NP environmental fate literature at the river scale in that the size grid is not broken into evenly spaced bins.^{8, 11, 46} Rather, a geometric series is used to create a grid with increasing bin sizes. This approach has two benefits: (1) it allows the modeler to capture a particle size distribution that is spread over many orders of magnitude in size (e.g., aggregates typically occur in the micron size range)^{20, 120, 122} with a relatively small number of bins, and (2) it places the highest model resolution (and computational burden) on the smallest particles, for which aggregation and dissolution occur more rapidly, numerical error is more likely to arise, and the dissolution flux (introduced in Section 2.3.2) must be estimated.⁵⁵

A ratio, m_{rat} , is chosen such that the representative particle size at the lower boundary of each bin $i+1$, $m_{i+1,lo}$, is related to the size of the lower boundary of next smallest bin, bin i , by the non-negative integer q .

$$m_{rat} = m_{i+1,lo}/m_{i,lo} = 2^{1/q} \quad q \geq 1$$

Equation 4-2

When $q = 1$, each bin is twice the size of the previous bin.¹⁴⁶ We observed little to no benefit for model resolutions above $q = 7$.

2.2.2 Numerical Solution for Dissolution

We used a Second Order Finite Difference approximation^{146, 149} as described in Supporting Methods (Section C.1.3.b) to describe particle dissolution:

$$\left(\frac{dN_i}{dt}\right)_{diss} = \frac{1}{m_{i,lo}} (aA_{i-1}N_{i-1} + bA_iN_i + cA_{i+1}N_{i+1})$$

$$\text{where } a = -\frac{2m_{rat}}{(1+m_{rat})(m_{rat}^2-1)}$$

$$b = -\frac{2}{1+m_{rat}}$$

$$c = \frac{2m_{rat}}{(1+m_{rat})(m_{rat}^2-1)}$$

Equation 4-3

N_i is the number of particles in bin i at time t , and A_i is $A=dm/dt$ evaluated for particles in bin i according to their representative size.

2.2.3 Numerical Solution for Aggregation

We used the formulation by Lister et al.¹⁵⁰ to capture all possible re-binning events that occur on the geometric grid described by Equation 4-2 during aggregation between two particles of any size.

$$\begin{aligned} \left(\frac{dN_i}{dt}\right)_{agg} &= \sum_{j=1}^{i-Q(q)-1} \alpha_{i-1,j} \beta_{i-1,j} N_{i-1} N_j \frac{2^{\frac{j-i+1}{q}}}{2^{\frac{1}{q}-1}} \\ &+ \sum_{k=2}^q \sum_{j=i-Q(q-k+2)-k+1}^{i-Q(q-k+1)-k} \alpha_{i-k,j} \beta_{i-k,j} N_{i-k} N_j \frac{2^{\frac{j-i+1}{q}-1+2\frac{k-1}{q}}}{2^{\frac{1}{q}-1}} \\ &+ \frac{1}{2} \alpha_{i-q,i-q} \beta_{i-q,i-q} N_{i-q}^2 \end{aligned}$$

$$\begin{aligned}
& + \sum_{k=2}^q \sum_{j=i-Q(q-k+1)-k+1}^{i-Q(q-k+1)-k+1} \alpha_{i-k+1,j} \beta_{i-k+1,j} N_{i-k+1} N_j \frac{-2 \frac{j-i}{q} + 2^{\frac{1}{q}-2} - \frac{k-1}{q}}{\frac{1}{2^q-1}} \\
& - \sum_{j=1}^{i-Q(q)} \alpha_{i,j} \beta_{i,j} N_i N_j \frac{\frac{j-1}{2^q}}{\frac{1}{2^q-1}} \\
& - \sum_{j=i-Q(q)+1}^{\infty} \alpha_{i,j} \beta_{i,j} N_i N_j \quad \text{where } Q(q) = \sum_{l=1}^q l
\end{aligned}$$

Equation 4-4

Equation 4-4 is a rigorous alternative to the "weight ratio" approximation in which volume-conserving ratios are used to apportion newly formed aggregates into the two adjacent bins that most closely approximate the aggregate size.⁹

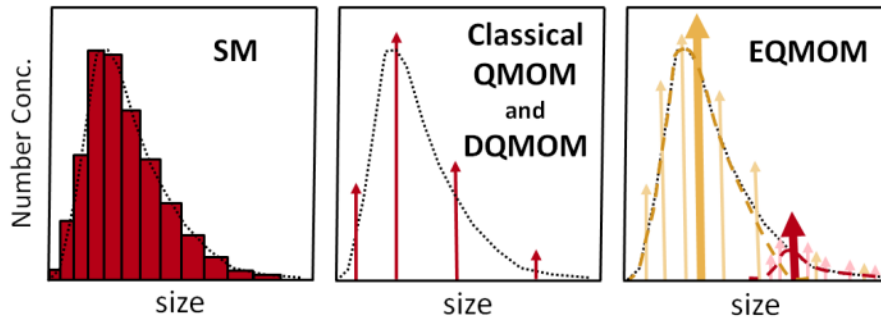


Figure 4-1. Approximation of the particle size distribution (dotted line) in the Sectional Method, the classical and Direct Quadrature Method of Moments, and the Extended Quadrature Method of Moments. The SM breaks the distribution into size bins (note that, in order to overlay the distributions, as shown here, the number concentration in each bin must be divided by the bin width). The DQMOM and classical QMOM represent the distribution with a small number ($N < 6$) of quadrature points, the sum of which equals the total particle number concentration (the area under the distribution). The EQMOM represents the distribution with a set of primary ($N < 6$) quadrature points (bold arrows) surrounded by a set of secondary quadrature points (thin arrows). The distribution is then approximated as the sum of beta distributions (dashed lines) reconstructed from each set of secondary quadrature points.

2.3 Moment Methods

2.3.1 General Principles

The statistical moments, μ_k , of a particle size distribution, $f(m)$, are defined as¹⁴²

$$\mu_k = \int m^k f(m) dm$$

Equation 4-5

μ_0 (the "zeroth moment") is the total particle number concentration. By the same logic, the moment sequence $k = 0, 1/3, 2/3, 1$ can be shown to be directly proportional to the total particle number concentration, the sum of all particle radii (which can be used to estimate the mean particle size), the surface area concentration, and the total mass concentration of the particle population. By tracking this moment sequence over time, we are thus able to track any descriptive metric of practical interest in assessments of NP bioavailability or risk. Note that, if we were to select radius instead of mass as the internal coordinate, the metrics described here would correspond with the integer sequence $k = 0, 1, 2, 3$.

In classical quadrature-based moment methods, Equation 4-5 is replaced with a discrete approximation using an n -point Gaussian quadrature rule.¹⁴²

$$\mu_k \approx \sum_{i=1}^n m_i^k w_i$$

Equation 4-6

In effect, the continuous function $f(m)$ is replaced with a discrete approximation defined by its "quadrature points," or the set of n "abscissas" and "weights" (m_i, w_i) that exactly predict the lower

$2n-1$ moments of the distribution. Quadrature points are calculated from the (known) moments of the distribution using a matrix inversion algorithm such as Product-Difference or the modified Wheeler algorithm (as described by ^{58, 142, 152}). Quadrature-based approaches are generally much faster than sectional approaches because they allow the modeler to track the moments of the distribution using a small number (e.g., $N < 6$) of quadrature points in lieu of many size bins (Figure 4-1).

In classical QMOM, the PBE (Equation 4-1) is replaced with a continuity equation (the "moment evolution equation") that balance the moments of the distribution. For the processes of dissolution and aggregation, ¹⁴²

$$\begin{aligned} \frac{d\mu_k}{dt} &= \left[\frac{d\mu_k}{dt} \right]_{diss} + \left[\frac{d\mu_k}{dt} \right]_{agg} \\ \left[\frac{d\mu_k}{dt} \right]_{diss} &= k \int_0^{\infty} m^{k-1} A(m) f(m) dm \\ \left[\frac{d\mu_k}{dt} \right]_{agg} &= \frac{1}{2} \int_0^{\infty} \int_0^{\infty} \alpha(m, m') \beta(m, m') [(m + m')^k - m^k - (m')^k] f(m) f(m') dmdm' \end{aligned}$$

Equation 4-7

The quadrature approximation of Equation 4-7 is

$$\frac{d\mu_k}{dt} \approx k \sum_{i=1}^n m_i^{k-1} A_i w_i + \frac{1}{2} \sum_{i=1}^n \sum_{j=1}^n \alpha_{ij} \beta_{ij} [(m_i + m_j)^k - m_i^k - m_j^k] w_i w_j$$

Equation 4-8

In classical QMOM, quadrature points are estimated from the moments calculated during the previous time step (or the initial conditions) using matrix inversion. The moments of the distribution are then updated at each time step according to Equation 4-8.

2.3.2 The Dissolution Flux Problem

As particles dissolve completely, they cross the lower boundary of the size domain. This creates an efflux of particles from the system, φ , which may be estimated (for a lower boundary of zero) as⁵⁷

$$\varphi = A(0)f(0)$$

Equation 4-9

In moment methods, only the moments of the distribution are known. Thus we have no way of evaluating $f(0)$. Because the classical QMOM typically tracks six or fewer quadrature points, abscissas rarely lie close enough to the lower boundary to permit an accurate estimate of $f(0)$. We will refer to this as the "dissolution flux problem." It has only recently gained attention in the population balance literature at large for the case of evaporating droplets (for which it is referred to as the "evaporative flux problem").^{57, 145, 153} In this work, we test three proposed solutions to the generic problem of disappearing particle fluxes: The Direct Quadrature Method of Moments with and without ratio constraints, and the Extended Quadrature Method of Moments.

2.3.3 The Direct Quadrature Method of Moments

2.3.3.1 General Principles

The DQMOM approximates the particle size distribution as a sum of i Dirac delta functions with n weights w_i at locations (abscissas) $m_i, i = 1 \dots n$.

$$f(m) = \sum_{i=1}^n w_i \delta(m - m_i)$$

Equation 4-10

In the univariate case (i.e., for one internal coordinate), this representation is mathematically identical to the quadrature point approximation used in the classical QMOM (Figure 4-1).¹³¹ In the DQMOM, however, the PBE (Equation 4-1) is re-written in terms of the derivatives of the weights and abscissas of the distribution so that the quadrature points may be evolved *directly* at each time step. This approach is much faster than the classical approach.¹³¹

2.3.3.2 Numerical Solution of the DQMOM

Let a_i and b_i describe the evolution of weights and weighted abscissas over time

$$a_i = \frac{\partial w_i}{\partial t}, b_i = \frac{\partial(w_i m_i)}{\partial t}$$

Equation 4-11

a_i and b_i may then be found by solving the following system of equations, where \overline{S}_k is a vector of terms describing the evolution of the moments over time (Equation 4-8).¹⁵⁴

$$(1 - k) \sum_{i=1}^n m_i^k a_i + k \sum_{i=1}^n m_i^{k-1} b_i = \overline{S}_k$$

Equation 4-12

Thus the set of quadrature points is evolved directly, and the moments of the distribution can be calculated *ex post facto* using Equation 4-6.

2.3.3.3 Estimating Dissolution Flux with Ratio Constraints

As described in Section 2.3.2, a flux term must be added to Equation 4-12 when NPs are able to undergo complete dissolution. For a lower size boundary of zero,

$$(1 - k) \sum_{i=1}^n m_i^k a_i + k \sum_{i=1}^n m_i^{k-1} b_i - \delta_{k0} \varphi = \overline{S}_k$$

Equation 4-13

δ_{k0} equals one for $k=0$ and zero for any other value of k .

Since moment methods cannot evaluate φ , this system of equations has one too many unknowns. We can solve this problem by adding constraints.¹⁴⁵ Fox et al. suggest the following "ratio constraints," which simply state that the change in the particle size distribution due to dissolution will be smooth.

$$\frac{d}{dt} \left(\frac{w_i}{w_{i+1}} \right) = 0, \quad \frac{d}{dt} \left(\frac{m_i}{m_{i+1}} \right) = 0$$

Equation 4-14

Ratio constraints are expected to perform poorly for highly monodisperse particle populations, for which the entire population dissolves completely and instantaneously in a stepwise manner. In such cases, traditional DQMOM (without ratio constraints) may suffice. In this method, the weight associated with an abscissa is simply set to zero when the abscissa crosses the lower size boundary.¹⁴⁵

2.3.3.4 Initial Conditions

The DQMOM does not specify initial values for the set (w_j, m_j) . To determine initial conditions, we used a matrix inversion procedure (the Product-Difference algorithm⁵⁸) to estimate initial quadrature points from the (known) initial moments of the distribution.

2.3.4 Extended Quadrature Method of Moments

2.3.4.1 General Principles

As its name suggests, the extended quadrature method of moments⁵⁷ is an extension of the classical QMOM. In both methods, the particle size distribution is approximated by a set of quadrature points calculated from the lower-order moments of the distribution at each time step using a matrix inversion algorithm, and the moments are evolved directly.

Unlike the classical QMOM and the DQMOM, which treat each abscissa like a discrete node, the EQMOM assumes that each abscissa describes the central tendency of a statistical distribution, $\delta_{\sigma_\beta}(m, m_i)$. The entire particle size distribution is thus described by a weighted sum of n probability density functions:

$$f(m) = \sum_{i=1}^n w_i \delta_{\sigma_\beta}(m, m_i)$$

Equation 4-15

$\delta_{\sigma_\beta}(m, m_i)$ takes a pre-specified form. When it represents a beta distribution, $f(m)$ may be rewritten as follows:

$$f(m) = \sum_{i=1}^n w_i \frac{m^{m_i-1}(1-m)^{\mu_i-1}}{B(\lambda_i, \mu_i)}$$

Equation 4-16

where $\lambda_i = m_i/\sigma_\beta$ and $\mu_i = (1 - m_i)/\sigma_\beta$ are the parameters of the distribution and σ_β is a measure of spread. Every abscissa m_i is assumed to have the same σ_β .

When $\sigma_\beta = 0$, the EQMOM is equivalent to the DQMOM. Otherwise, σ_β is used to find a set of "secondary" quadrature points distributed around the first (Figure 4-1). Thus the EQMOM employs two nested quadrature steps. Unlike the primary quadrature step, which relies on matrix inversion procedures that can estimate fewer than 10 quadrature points with accuracy, the secondary quadrature step is accurate and efficient up to any number of quadrature points. In Beta EQMOM, a simple coordinate transformation recasts the secondary quadrature problem in terms of Jacobi polynomials that are orthogonal with respect to a weight function described by λ_i and μ_i . In this special case, any number of quadrature points can be calculated exactly.

2.3.4.4 Numerical solution

The Supporting Methods describe the multi-step algorithm that the EQMOM uses to find σ_β and the primary and secondary quadrature points. Once these values are known, a "dual quadrature approximation" of the moment evolution equation is employed.⁵⁷ Note its similarity to the quadrature approximation used in the classical QMOM and the DQMOM (Equation 4-8).

$$\left[\frac{d\mu_k}{dt} \right]_{agg} = \frac{1}{2} \sum_{i_1=1}^{n_1} \sum_{i_2=1}^{n_2} \sum_{j_1=1}^{n_1} \sum_{j_2=1}^{n_2} \rho_{i_1, i_2} \rho_{j_1, j_2} [(m_{i_1, i_2} + m_{j_1, j_2})^k - m_{i_1, i_2}^k - m_{j_1, j_2}^k] \alpha_{ij} \beta_{ij}$$

$$\left[\frac{d\mu_k}{dt} \right]_{diss} = k \sum_{i_1=1}^{n_1} \sum_{i_2=1}^{n_2} m_{i_1, i_2}^{k-1} \rho_{i_1, i_2} A_{i_1, i_2} \quad \text{where } \rho_{i_1, i_2} = w_{i_1} w_{i_1, i_2}$$

Equation 4-17

2.3.4.5 Estimation of the Dissolution Flux

The EQMOM provides two approximations of the PSD: Equation 4-15 and Equation 4-17. In order to estimate the dissolution flux over a given time step, we integrated Equation 4-15 over the range of particle sizes predicted by A_{i_1, i_2} ($= dm_{i_1, i_2} / dt$) (Equation 4-19, below) to dissolve completely within that time step. Once the flux was estimated, the secondary abscissas were advected towards the lower boundary according to A_{i_1, i_2} . The weight associated with any abscissa that crossed the lower boundary was set to zero.

2.3.4.3 Choice of Moments

The matrix inversion algorithm from the classical QMOM requires the first $2n$ moments of the distribution.¹⁴² The EQMOM requires one additional moment ($2n+1$) in order to find σ_β .⁵⁷ The DQMOM and the SM do not rely on the matrix inversion algorithm, so any choice of moments will suffice.

In the DQMOM and the SM, we used the fractional moments of the distribution ($k = 0, 1/3, 2/3, 1$). For simplicity, we used integer moments in the EQMOM. The fractional moments were estimated *ex post facto* from the integral under the reconstructed particle size distribution (Equation 4-15) using the definition of the moments (Equation 4-5).

2.4 Test Cases

We applied the Sectional Method, the Direct Quadrature Method of Moments with and without ratio constraints, and the Extended Quadrature Method of Moments to problems of NP dissolution, homoaggregation, and simultaneous dissolution and aggregation in simple media in a zero-dimensional, no-flow (batch reactor) model such as would be used to describe a test tube experiment. This simplified system was chosen for the purpose of contrasting the three PB frameworks: Since all three are expected to perform similarly for transport processes such as aggregation, aggregate break-up, and settling, we simplified our analysis by using a single empirical parameter to describe their net effect. In contrast, as a particle growth/loss process that is subject to numerical diffusion in the SM⁵⁵ and the flux approximation in moment methods,⁵⁷ dissolution required a more detailed treatment.

2.4.1 Initial Conditions

Each simulation began with 100 g/m^3 of undissolved and unaggregated NPs that were lognormally distributed with respect to size. For the methods presented here, the size distribution can in fact take any arbitrary form at time 0 or throughout the simulation. However, lognormal distributions are widely used to describe NP distributions^{5, 8, 11} and other particles,^{55, 56} and their fractional and integer moments can be calculated directly from the distribution parameters. In addition, analytical solutions are available for “dissolution only” and “aggregation only” cases in which the initial particle size distribution is lognormal (see Supporting Methods, Section C.1.6).^{155, 156}

Since most experimental NP studies implicitly assume normality by reporting only the average particle radius and its standard deviation,^{20, 120} we used lognormal distributions with low skews. In particular, we fit our initial lognormal distributions to the following normal distributions: $5 \pm 1 \text{ nm}$, $15 \pm 3 \text{ nm}$, $50 \pm 10 \text{ nm}$, $100 \pm 20 \text{ nm}$, and $500 \pm 100 \text{ nm}$. We chose these sizes because the

standard deviations of newly synthesized NP populations generally increase along with their means.²⁰ We performed a coordinate transformation during the fitting procedure so that distributions were expressed in terms of our internal coordinate, particle mass, rather than radius. Note that symmetry with respect to radius implies skew with respect to mass (e.g., see Figure C-8). We also tested distributions with high skews and high monodispersity.

2.4.2 Dissolution Rate

We used the Noyes Whitney dissolution rate law as modified by Brunner and Tolloczko (1900)¹⁵⁷ to describe the change in the metal ion concentration in solution during NP dissolution as a function of $k_{S,mb}$, a surface-area normalized reaction rate, and S_{tot} , the total surface area of all particles in solution. $[Me^+]_t$ is the mass concentration of the metal ion in solution at time t and $[Me^+]_{eq}$ is the ion concentration in solution at equilibrium.

$$\frac{d[Me^+]_t}{dt} = k_{S,mb} S_{tot} ([Me^+]_{eq} - [Me^+]_t)$$

Equation 4-18

The Supporting Methods compare this model to the oft-cited but rarely used Nernst-Brunner modification^{37, 120, 121, 158} and describe how it is used to derive the rate law (A) found in Equation 4-1. Note that the empirical coefficient has changed and the right-hand side is re-expressed in terms of the particle mass by assuming spherical particles.

$$A = \frac{dm}{dt} = k_{S,pb} m^{2/3} ([Me^+]_t - [Me^+]_{eq})$$

Equation 4-19

We modeled dissolution in two ways. In the first case, the ion concentration in solution was increased until the equilibrium solubility was reached. The size dependence of the equilibrium solubility was estimated from the Ostwald-Freundlich relation (see Supporting Methods) using the initial characteristic diameter of the particles, which is described below.²⁰ In the second case, ions were assumed to be instantaneously removed from the solution ("sink conditions"). We present the results for the second approach, which maximizes the dissolution rate, the dissolution flux, and the numerical error associated with each model, in the main text. Results for the first approach are in Appendix C.

We chose a realistic value for $k_{S,pb}$ by calibrating our sectional model to experimental data on the ion release rate for 20 mg/L 52 ± 9 zinc oxide (ZnO) NPs in 25°C Moderately Hard Water reaching an equilibrium ion solubility of 2.04 mg/L (Figure C-1).¹⁵⁹ We chose ZnO NPs because they are produced in greater volumes than any other reactive NP and their dissolution behavior has been widely studied. Additionally, because ZnO NP dissolution is relatively rapid, models are more likely to exhibit numerical stiffness. ZnO NPs therefore provide a good test case for investigations of the limitations of each framework with respect to numerical instability.

For all test cases that included dissolution, the characteristic primary (unaggregated) particle size was taken to be the surface-weighted geometric mean diameter, $D_{geom,0}$.¹⁶⁰

$$D_{geom,0} = \exp \left[\frac{\sum_{i=1}^n W_i D_i^2 \ln D_i}{\sum_{i=1}^n W_i D_i^2} \right]$$

Equation 4-20

where D_i is the particle diameter associated with a given size class (SM) or quadrature point (QMOM) and W_i is the particle number concentration associated with that size class ($W_i=N_i$) or quadrature point ($W_i=w_i$). Note that D_i in Equation 4-20 was re-expressed in terms of mass before implementation by assuming a spherical particle.

This measure has several advantages over more traditional estimates of particle diameter including the (number-weighted) mean and the geometric mean. The geometric mean of a skewed distribution is a better estimate of its central tendency than its average. For reactive NPs, the surface-weighted diameter is more relevant than the number-weighted diameter because of the controlling influence of surface area on dissolution kinetics. In addition, the surface-weighted diameter does not rely on the zeroth moment (the total number concentration) and is thus robust to numerical errors introduced by approximation of the dissolution flux.

2.4.3 Aggregation Rate

For simplicity, we treated the attachment efficiency, α , as a known and size-independent constant. Our estimate of β assumed that collisions occur due to Brownian motion. In this case, Equation 4-21 describes the collision rate between aggregates of size m_i and m_j

$$\beta_{i,j} = \frac{2k_B T}{3\mu} (m_i^{1/D_f} + m_j^{1/D_f})(m_i^{-1/D_f} + m_j^{-1/D_f})$$

Equation 4-21

where D_f is the fractal dimension of the aggregates.^{154, 161} We assumed $D_f = 1.8$ (for all particle sizes), which is approximately correct for aggregates formed by Brownian diffusion.^{43, 161} More

detailed and rigorous alternatives to Equation 4-21 exist,¹⁶²⁻¹⁶⁵ but a simple approach is better suited to an illustrative analysis such as ours, performed largely in the absence of experimental data.

In order to estimate the constant α , we calibrated our sectional aggregation + dissolution model to the time-resolved Dynamic Light Scattering data corresponding with the ZnO NP samples used to estimate $k_{S,pb}$.¹⁵⁹ Because we used the single empirical parameter α to describe the net effect of aggregation, aggregate break-up, and settling, we do not expect it to apply broadly across NP types or media properties. However, it provides a reasonable first estimate for our comparison of model frameworks.

2.4.4 Simultaneous Aggregation & Dissolution

For the case of simultaneous NP dissolution and aggregation, we assumed an approximately monodisperse population of 50 ± 2 nm NPs. This allowed us to accurately estimate the number and size of the particles within aggregates of a given size. If each aggregate had contained particles of many different sizes, a joint size distribution would have been needed to describe both aggregation (which depends on the aggregate size) and dissolution (which depends on the primary particle sizes in each aggregate). The characteristic aggregate size was calculated as shown, where X_i is the geometric mean number of particles in an aggregate with a given mass.¹⁶²

$$D_{i,agg} = D_{geom,0} (X_{geom,i})^{1/D_f}$$

Equation 4-22

The effect of aggregation on the surface area available for dissolution is poorly understood at present for NPs, and is also an active area of research in the particle modeling community at large. In order to bound this effect, we considered two extreme cases. We first maximized the dissolution

rate by assuming that aggregation has no effect. This approach agrees loosely with experimental results, since small particles have been shown to dissolve faster than large particles even when they form larger or similarly sized aggregates.¹⁶⁶ In the second case, which placed a very conservative lower bound on the dissolution rate, we assumed that every aggregation event was followed by complete particle fusion to form a new hard sphere. This assumption is a common convenience in most models of NP homoaggregation based on the Smoluchowski equation.⁴³

2.4.5 Model Resolution

In order to ensure that runtimes reported in the Results reflected the most efficient model performance possible in each case, the procedure used to select the model resolution accounted for tradeoffs between accuracy and runtime. For the “dissolution only” and “aggregation only” test cases, we chose the lowest size resolution (i.e., the number of size bins and the bounds on the particle size domain in the SM; the number of primary quadrature points in the DQMOM and the EQMOM; and the number of secondary quadrature points in the EQMOM) for which the simulation outputs presented in Figure 4-2 fell within 2% of the analytical solution. Error was calculated as

$$Error (\%) = \frac{Value_{numerical}(t) - Value_{analytical}(t)}{Value_{analytical}(t=0)}$$

Equation 4-23

Because values often approached zero during the simulation, relative error approached infinity and could not be used. Error in characteristic diameter estimates was not used in the “aggregation only” case, since normalization by initial conditions in Equation 4-23 led to high percent errors (e.g., see

Figure C-7) even when absolute error was low. If the model was unable to achieve 2% error or less, the size resolution was simply increased until further increases failed to visibly reduce error.

For cases that included dissolution, the SM required $q=7$ (as defined in Equation 4-2). Aggregation required only $q=3$. Across all major test cases (Figure 4-2 and Figure C-2 to Figure C-4), the number of size bins implied by q varied from 144 to 353. For the DQMOM, three quadrature points were required for the “aggregation only” case. Only two were needed in cases that included dissolution. For the EQMOM, we used 2, 2, and 1 primary quadrature points and 20, 80, and 50 secondary quadrature points to describe “aggregation only,” “dissolution only,” and “aggregation and dissolution,” respectively.

For each trial, we chose the longest possible time step (within the nearest half order of magnitude) that exhibited numerical stability and maintained error within 2%.

2.4.6 System Properties

All simulations were run in MATLAB on a Dell XPS 8300 computer with an Intel(R) Core™ i7-2600 quad-core processor (3.40 GHz processor speed, 12.0 GB RAM).

4.3 Results

Figure 4-2(a) shows the time evolution of a population of 50 ± 10 nm ZnO NPs undergoing aggregation and dissolution (separately) and 50 ± 2 nm ZnO NPs undergoing simultaneous aggregation and dissolution in the SM, DQMOM, and EQMOM as calculated from the fractional moments $k=0, 1/3, 2/3, 1$. Trends agree with expectations: Aggregation caused a rapid decrease in the total particle number concentration (note the log scale) and an increase in the characteristic particle diameter. The total NP mass remained constant. We assumed that the surface area

obscured by contact points between particles in each aggregate was negligible such that the surface area concentration also remained constant. Dissolution decreased the average NP size, NP mass concentration (recall however that ions are formed such that the total metal mass remains the same), and surface area concentrations. The particle number concentration only began to decrease once the smallest particles in the system dissolved completely. The behavior in the aggregation + dissolution case was a hybrid of the behaviors observed for each process separately. Figure C-2 to Figure C-4 present these same results for NP populations of size 5 ± 1 nm, 15 ± 3 nm, 50 ± 10 nm, 100 ± 20 nm, and 500 ± 100 nm. As expected, small particles dissolved faster than large particles and aggregated more quickly. Although aggregation did not reach steady state within 48 hours, small particles also appeared to form larger aggregates. However, without explicit inclusion of processes such as settling and break-up, the influence of shear flow, or extensive model calibration to experimental results, these results should be viewed as supportive but not especially informative.

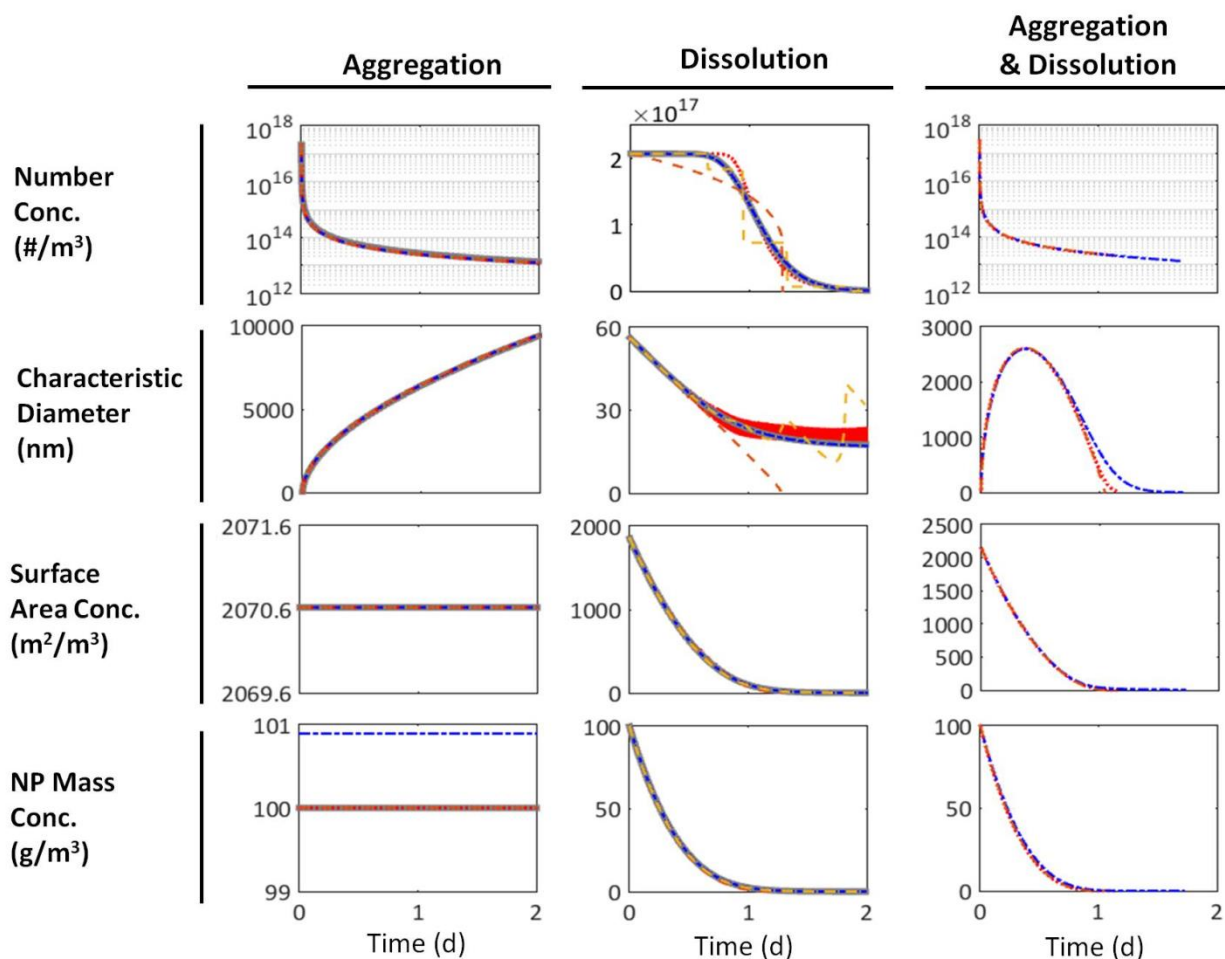


Figure 4-2. Model results for aggregation, dissolution, and aggregation + dissolution of 100 g/m^3 of a lognormal population of $\sim 50 \pm 10 \text{ nm}$ NPs (aggregation, dissolution) or $50 \pm 2 \text{ nm}$ NPs (aggregation + dissolution). Dissolution and aggregation rates were determined by calibration to data for ZnO NPs (Figure C-1). Solid grey = Analytical Solution, Dot-dashed blue = Sectional Method (SM), Dashed orange = Direct Quadrature Method of Moments (DQMOM) with ratio constraints, Dashed yellow = DQMOM without ratio constraints, Dotted red = Extended Quadrature Method of Moments (EQMOM). All methods are accurate for aggregation. Error arises in the DQMOM and the EQMOM for dissolution test cases due to the dissolution flux term.

For NP aggregation without dissolution, all three mathematical frameworks were equally accurate.

The one exception was a small ($< 1\%$) error in the SM estimate of the initial mass concentration that arose from the discretization of the initial size distribution. Although the models were comparably accurate, the DQMOM was up to 500 times faster than the SM for the test cases presented in Figure 4-2 and Figure C-4 (Table 4-1), and the EQMOM was up to 11 times faster. Time savings were

especially beneficial for 5 ± 1 nm NPs, since the rapid initial aggregation events undergone by unaggregated particles at early time steps demanded a small simulation time step ($0.05\ \mu\text{s}$). Even though we reduced runtimes significantly by increasing the time step later in the simulation, the absolute runtime for our SM simulation of 5 ± 1 nm NP aggregation took just under three hours. The DQMOM solved the same problem in less than 30 seconds.

Table 4-1. Runtime efficiencies of the three PB methods. Numbers represent the ratios of the SM method runtime relative to those of the QMOM models. The ranges represent the effects of different initial ZnO NPs sizes for aggregation and for dissolution to sink conditions and to equilibrium (Figure 4-2 and Figure C-2 to Figure C-4).

	Dissolution	Aggregation	Aggregation & Dissolution
SM	1	1	1
DQMOM	0.04 - 40	260 - 500	5300
EQMOM	0.02 - 0.3	3 - 11	750

For dissolution, the SM agrees well with the analytical solution. In contrast, neither the DQMOM flux approximation with ratio constraints (orange dashed line) or without ratio constraints (yellow dashed line) accurately described the changes in the number concentration or average particle size over time. Because of its stepwise nature, the DQMOM without ratio constraints was also highly unstable. The EQMOM captured the overall shape of the dissolution curve but ultimately under-predicted the dissolution rate at early time steps and over-predicted it later in the simulation. Error in the EQMOM for this case never exceeded 13%. Similar errors are observed for 5 to 500 nm NPs (Figure C-5). Although the EQMOM ran up to 60 times more slowly for dissolution than the SM, runtimes were not restrictive in the absence of aggregation; the SM ran in less than three minutes in all cases. In spite of their inaccuracies with respect to number concentrations and characteristic particle size, the moment methods accurately predicted changes in

the surface area concentration and mass concentration over time. Recall that the dissolution flux, which is the major source of error in moment methods, only affected the zeroeth moment (Equation 4-13), which was only used to calculate the number concentration.

All models performed similarly in the case of simultaneous aggregation and dissolution, which suggests that error in estimates of the size of the NPs comprising each aggregate had little impact on the number of aggregates or the characteristic aggregate size. The error in the SM could be greatly reduced by setting initial EQMOM and DQMOM values equal to initial SM values rather than their true values calculated from the parameters of the lognormal distribution. This reveals that much of the error in the SM again results from the initial discretization of the size distribution. Because a small initial time step was needed in this case, the SM took over 5.5 hours to run. In contrast, the EQMOM took less than 30 seconds and the DQMOM took less than four. All models were terminated once the mass concentration dropped below $1 \mu\text{g}/\text{m}^3$ to eliminate large errors that occurred when only a small number of particles remained in the system.

Figure 4-3 compares the time evolution of the particle size distribution as calculated directly by the SM to the estimate provided by the EQMOM using Equation 4-15. Size is expressed in terms of particle or aggregate mass in femtograms (10^{-15}). We truncated the peaks for plotting so that changes in the diffuse regions of the distribution could be inspected. Trends again match expectations: Dissolution caused a narrowing of the size distribution and a shift towards the lower boundary. Aggregation resulted in the formation of a large and increasingly diffuse peak. Since the analytical solution for the “aggregation only” case, which agreed well with our numerical predictions, assumed that the distribution remained lognormal over time, we can safely state that this was the case. In contrast, previous studies using the dissolution rate law presented here indicate that the distribution becomes increasingly skewed to the right as dissolution occurs, eventually losing its lognormal character.¹⁶⁷ Thus the distribution would not necessarily remain lognormal during

dissolution even if the lower portion of the distribution were not “falling off the end” of the size domain as particles fully dissolved. The “aggregation and dissolution” case blended the behaviors observed in the dissolution case and the aggregation case.

Although the EQMOM captured the peak behavior observed in the SM, it was not as faithful to the tails of the distribution. For dissolution, the bimodal nature of the approximation caused small but visible bimodality in the reconstructed distribution. The horizontal stripes in the reconstructed distribution reflect numerical error in the evaluation of the particle size distribution using Equation 4-16. This error also caused the variation in the EQMOM prediction of the characteristic diameter that can be observed in Figure 4-2.

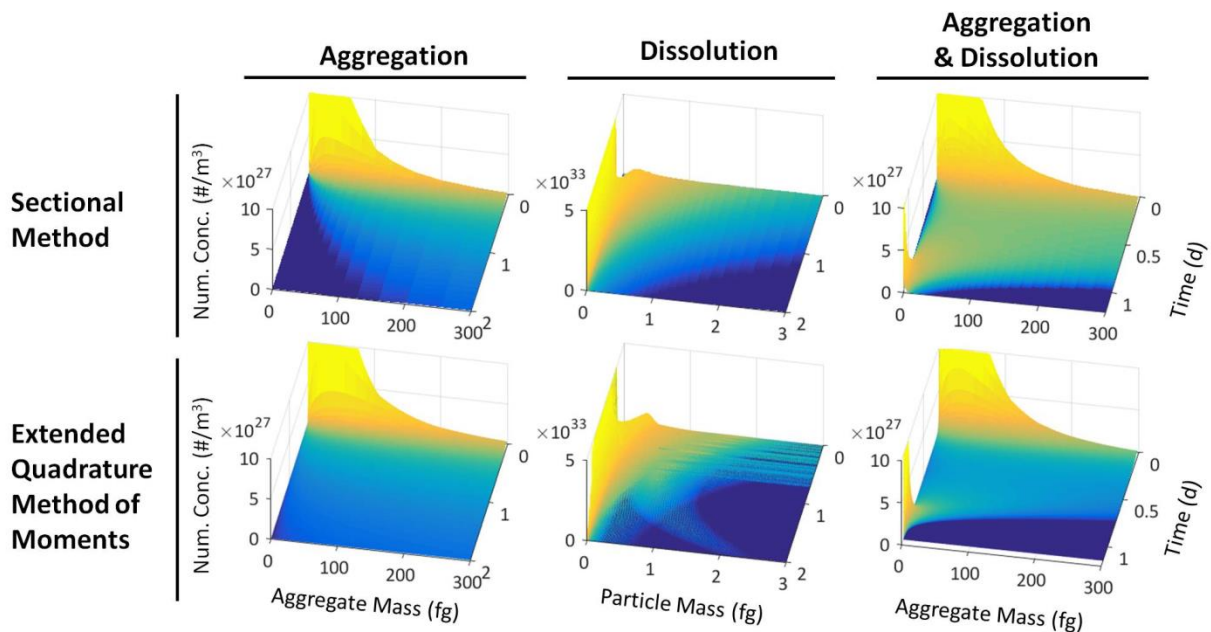


Figure 4-3. Evolution of the particle size distribution (PSD) for the cases shown in Figure 4-2. In the SM, the PSD is tracked directly. In the EQMOM, the size distribution is reconstructed from the moments at every time step. DQMOM cannot reproduce the size distribution.

All three frameworks tended to fail completely if the time step was too large. In contrast, decreasing the number of bins in the SM degraded model performance gradually. Figure 4-4 explores this

effect. For this analysis, we first narrowed the size domain to ensure that as many bins as possible fell within the 1-100 nm range. Size distributions corresponding with each case are shown in Figure C-6.¹⁶⁸

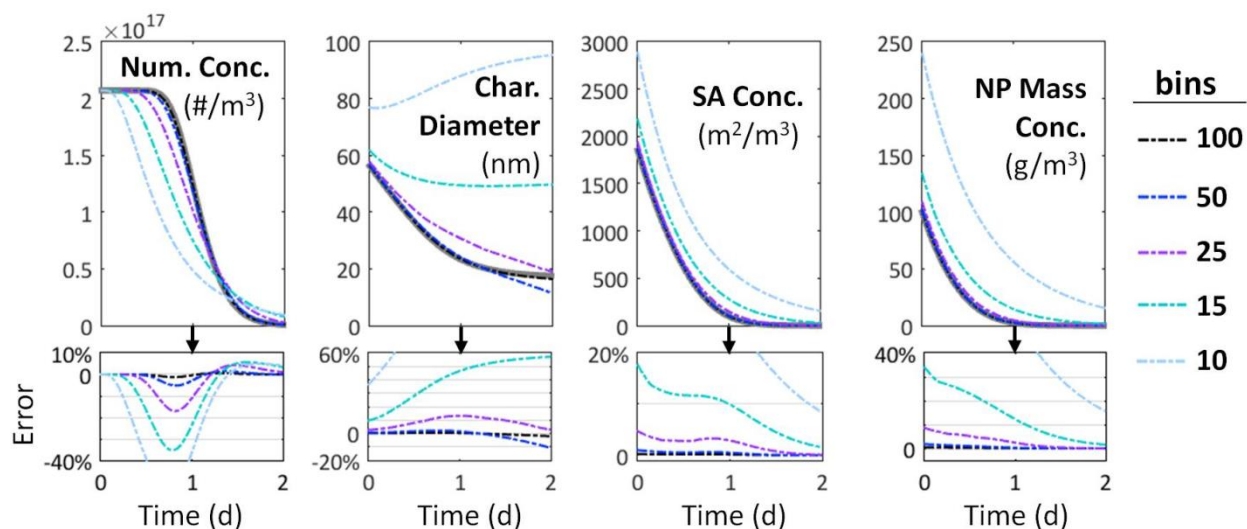


Figure 4-4. Effect of the number of size bins on error in the SM for dissolution of $\sim 50 \pm 10$ nm NPs. Error is reported relative to the analytical solution (solid grey) according to Equation 4-23.

With only 25 bins, error in the number concentration, characteristic diameter, and NP mass concentration approached or exceeded 10%. Model performance degraded quickly for bin numbers below 25. At 10 bins, error in the characteristic diameter and mass concentration estimates reached 140%. This error had several sources. First, simulations with small bin numbers poorly represented the initial particle size distribution. This resulted in poor initial estimates of the moments as well as errors introduced during the simulation because model predictions were based on a flawed initial distribution. Error likely also resulted from numerical diffusion. Recall that dissolution in discretized models that perform a particle number balance is described as a loss in the particle number in a given size bin (Equation 4-3). In effect, this approach forces complete dissolution of a fraction of the particles to occur in lieu of partial dissolution of all of the particles. The end result is

numerical dispersion during particle growth or shrinkage (e.g., processes that change the particle mass but do not change the particle number), which widens and flattens the size distribution unrealistically over time.¹⁶⁹ Figure C-7 shows results for aggregation.

Several authors suggest that ion release curves due to NP dissolution may be predicted by a simple two-parameter first-order linear inhomogeneous differential equation^{39, 159}

$$[Me^+]_t = [Me^+]_{eq}[1 - e^{-kt}]$$

Equation 4-24

in which k is an empirical rate constant determined by data fitting. In a batch reactor model, $[Me_xO_x]_t$ can be calculated directly from $[Me^+]_t$ because $[Me]_{total}$ (g Me/m^3) remains constant. Under sink conditions, $[Me^+]_t$ is set to zero and NP mass concentration can be assumed to undergo simple exponential decay. Figure 4-2 appears to agree. Figure 4-5(a) tests this simple model against benchmark results for particle size distributions that ranged from roughly exponential to roughly monodisperse, the two extremes of a unimodal distribution, when defined in terms of our internal coordinate, particle mass (see Figure C-8 for size distributions in terms of mass as well as radius). Polydispersity was varied by multiplying the “base case” scale parameter of the initial lognormal distribution by $1/4$ (most monodisperse), 2, and 4 (most polydisperse). Figure 4-5(b) shows model fits for the “aggregation and dissolution” case. The effect of aggregation on dissolution was bounded (blue shaded region) by assuming no fusion (lower bound) or complete fusion (upper bound) during aggregation as described in Section 2.4.4. Equation 4-24 was fit to the benchmark curves by minimizing root mean squared error over all time steps. The benchmarks for Figure 4-5(a) are SM results validated against the analytical solution; the benchmarks for Figure 4-5(b) are DQMOM results validated against EQMOM results.

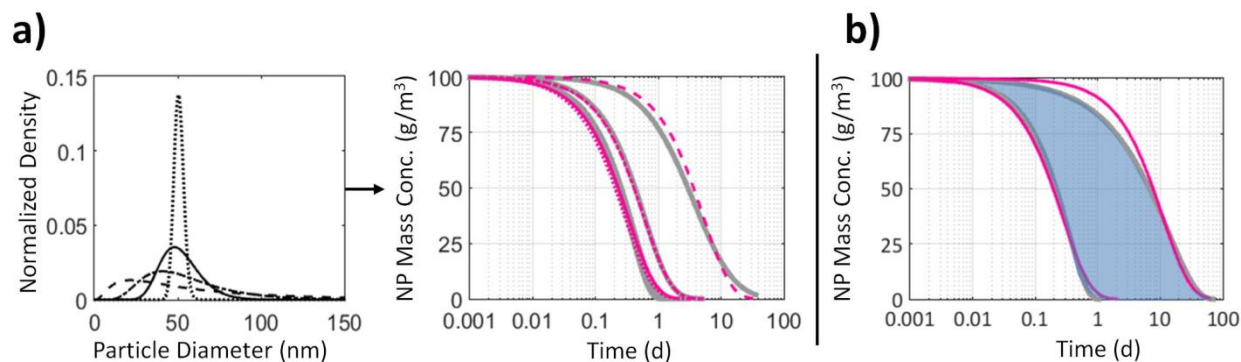


Figure 4-5. Comparison of a simple one-parameter, size-independent conventional mass balance model (pink) to benchmarked population balance models (solid grey) for initial distributions with varying polydispersity/skewness (indicated by line style). **a)** For both highly monodisperse and highly skewed distributions, the simple model captures changes in the NP mass concentration over time in the pure dissolution case. **b)** Conventional mass balance even performs reasonably when accounting for the possible influence of aggregation on dissolution. The blue shaded region bounds the effect of aggregation on dissolution (lower bound = no particle fusion following aggregation; upper bound = complete particle fusion following aggregation).

In all cases, this size-independent analytical approximation predicted the dissolution curve within 9% error. For the two-parameter case, which describes NP dissolution to equilibrium (Figure C-9), fits were exceptional except in the case of complete fusion during aggregation; error remained below 0.9% in all cases.

4.4 Discussion

We developed and compared three population balance frameworks with potential applications in NP fate and effects modeling: the Sectional Method,¹³⁰ the Direct Quadrature Method of Moments,¹³¹ and the Extended Quadrature Method of Moments.⁵⁷

The EQMOM was slower and less numerically stable than the DQMOM (with ratio constraints) and was less accurate than the SM in the case of pure dissolution. For dissolution, EQMOM simulations generally failed if more than three primary quadrature points were used. The EQMOM algorithm was also relatively complex and prone to failure during the search procedure to

find σ_p . In contrast, we found the DQMOM to be a powerful alternative to the SM for inert NPs (e.g., TiO₂, SiO₂, Al₂O₃) undergoing aggregation. Because it requires fewer scalars (e.g., 3 quadrature points instead of > 25 size bins), it is especially promising for model systems with high memory or runtime demands. Of the three frameworks, the DQMOM was also the simplest to implement. Numerical errors (ill-conditioning and singularities, described in Supporting Methods) were easily identified and managed. Although neither moment-based approach performed well for rapidly dissolving ZnO NPs in the absence of aggregation, both performed well for the more realistic case of simultaneous dissolution and aggregation.

The Sectional Method was the clear winner for NPs that exhibited fast dissolution. However, in cases where a fine resolution is required at the lower particle size boundary to accurately resolve rapid surface area-dependent processes such as dissolution or aggregation, over 100 bins may be needed to achieve accuracy within 2% even when using an expanding grid to improve model performance. In our dissolution case, SM models with fewer than 25 bins exhibited significant (>10%) model error. Most size-discretized NP fate models developed to date have used 5 or fewer bins^{8,11,46} or do not report the number of bins used.^{5,9} Whether or not the number of bins is adequate will vary from model to model depending on the reactivity of the NPs, the chosen numerical framework, and the required accuracy of model predictions. Modelers can demonstrate the adequacy of the chosen number of bins simply by showing that increasing the resolution of the size distribution does not improve the accuracy of model results.

We suggest several improvements upon current SM modeling frameworks. First, we find that expanding grids (as also employed by^{9,46}) are efficient and accurate alternatives to the uniform grids used to date in NP models at the river scale. Second, we find that the assumption that NPs fuse completely upon aggregation (Figure 4-5(b)), which is common in aggregation models,⁴³ can artificially increase particle lifetimes by nearly two orders of magnitude in those models that also

describe the surface-dependence of NP dissolution. For the case of pure aggregation, we present the numerical solution by Lister et al. as a robust alternative to the weight ratio approximation used previously.⁹ Finally, we recommend the use of particle mass, rather than radius, as the internal coordinate, and the use of surface-weighted geometric mean diameter as the characteristic particle diameter.

If data for model calibration or validation are sparse, error tolerance is within 10%, and only information on the ion release rate or NP loss rate is required, Equation 4-24 is an attractive alternative to population balance methods.¹⁵⁹ Quik et al. (2014) have similarly observed that first-order rates of NP removal due to aggregation and sedimentation show good agreement with a population balance alternative.¹³³ However, it is important to note that the dissolution rate of the particle population, and its attendant effects on (e.g.) the bioavailability of metal ions in nanotoxicity experiments, is a clear function of the distribution's skewness and polydispersity as well as its mean size; the first-order dissolution rates associated with the curves in Figure 4-5(a) varied by almost an order of magnitude.

Thus engineering models designed to predict environmental concentrations of NPs and compare them to mass-based toxicity thresholds may benefit little from population balance at present.¹⁴ However, incorporation of population balance models of aerosol particle chemistry and physics into global atmospheric models suggests that scale-up of the methods presented here is computationally feasible.^{55,56} Indeed, most of the cases presented in this work took only minutes to run. The exception--slow runtimes due to numerical instability in models that included the rapid initial aggregation of small unaggregated NPs--is easily addressed by seeding simulations with NPs that have already partially or fully aggregated. Nonetheless, large-scale systems that employ population balance have substantial memory and runtime demands relative to size-unresolved alternatives. To this end, they may benefit from the application of moment-based alternatives. For

highly soluble NPs, we hypothesize that the flux approximation error observed here for purely moment-based methods can be managed using a hybrid sectional/moment method, a promising area of future research.^{153, 169}

Bivariate or multivariate models are needed to resolve the influence of variation in particle morphology and composition on the behavior of particle populations with complex morphologies (e.g., rods and cubes) or complex compositions (e.g., heteroaggregates, core-shell structures, natural and engineered surface coatings, nanohybrids).^{170, 171} In fact, we show in this work that is impossible to retain information about the polydispersity of an NP population upon homoaggregation without using a bivariate framework to track the NP size within aggregates of a given size. In addition to primary and aggregate particle sizes, secondary internal coordinates of interest include surface area and surface charge. The literature from related fields suggests that the SM and Monte Carlo simulation will be too computationally demanding for use in bivariate models.^{172, 173} In contrast, moment methods are uniquely well-suited to such problems. In fact, DQMOM has already been used to describe the bivariate problem of NP aggregation and sintering during high-temperature syntheses.^{129, 171}

In summary, particle-particle interactions and NP surface-dependent chemical transformations in aqueous suspensions pose daunting modeling challenges. Size-resolved frameworks are not only more computationally burdensome than size-unresolved alternatives but are also subject to additional sources of model error. The ad hoc approaches developed to date fail to systematically address these potential shortcomings and means of overcoming them. This work presents several numerical frameworks that can be applied directly to problems of NP dissolution and aggregation, coupled with field-scale models, or adapted to describe other particle properties or processes of interest.

5 Summary, Outlook, and Policy Implications

5.1 Summary of Key Findings

Chapters 2-4 presented three analyses that improved understanding of NP fate and effects in environmental systems and provided guidance for the development of better models.

Chapter 2 presented a simple one-dimensional diagenetic model for predicting Ag NP distribution and silver ion speciation in freshwater sediments.⁶¹ The model was calibrated to data collected from Ag NP-dosed freshwater wetland mesocosms. Ag NP sulfidation retarded NP oxidation and ion release. Silver speciation and persistence in the sediment as predicted by the model depended on the seasonally variable availability of organic carbon and dissolved oxygen. The half-life of typical sulfidized (85% Ag₂S) Ag NPs varied from less than ten years to over a century depending on redox conditions. No significant difference in silver speciation and distribution was observed between $\geq 50\%$ Ag₂S and 100% Ag₂S Ag NPs. Formation and efflux of toxic silver ion was reduced in eutrophic systems and maximized in oligotrophic systems.

Chapter 3 presented a spatially resolved environmental fate model for the James River Basin, Virginia (USA) that explored the influence of daily variation in stream flow, sediment transport, and stream loads from point and non-point sources on water column and sediment concentrations of ZnO and Ag NPs and their reaction by-products.⁶³ Spatial and temporal variability in sediment transport rates led to high NP transport such that less than 6% of NP-derived metals were retained in the river and sediments. Chemical transformations entirely eliminated ZnO NPs and doubled Zn mobility in the stream relative to Ag. Agricultural runoff accounted for 23% of total metal stream loads from NPs. Average NP-derived metal concentrations in the sediment varied spatially up to nine orders of magnitude, highlighting the need for high resolution models. Overall, results suggested that "first generation" NP risk models have probably misrepresented NP fate in

freshwater rivers due to low model resolutions and the simplification of NP chemistry and sediment transport.

Chapter 4 developed and compared three population balance approaches in order to determine their strengths and weaknesses when applied to inert and highly soluble NPs: the Sectional Method (SM), the Direct Quadrature Method of Moments (DQMOM), and the Extended Quadrature Method of Moments (EQMOM). When describing aggregation, the DQMOM was up to three orders of magnitude faster than the SM. The SM was best for models tracking dissolution because the methods based on statistical moments (the DQMOM and EQMOM) had trouble handling complete NP dissolution. However, the SM required up to 25 size bins to accurately describe NP dissolution. Thus the five or fewer size bins currently favored in SM models of NP fate in surface waters are unlikely to suffice for soluble NPs. Because large-scale models are computationally demanding and SM runtimes increase exponentially as internal coordinates (particle properties) are added, moment-based frameworks have greatest potential for field-scale models and bivariate or multivariate models that describe NPs with complex morphologies or compositions, such as non-spherical NPs, core-shell structures, NPs coated in natural or engineered surfactants, and nanohybrids.

5.2 Recommendations for Future Work

5.2.1 Environmental Fate Modeling

NP fate models are evolving to reflect the dynamic and increasingly quantitative state of the science surrounding NP behaviors. The next generation of models will better address key NP-specific behaviors, including heteroaggregation and surface area-dependent chemical transformations. They will have improved spatial and temporal resolution. They will be able to handle a greater range of

NP types and environmental systems, including estuarine and coastal environments. It may take another generation or more before these models can credibly interface with NP bioaccumulation and trophic transfer models, which are being developed in parallel, but this too is expected. Such efforts, and discussions within the scientific community, should contribute to the development of an acceptable minimum set of principles for modeling NP fate in the aquatic environment in the not-distant future.

A critical review of the literature and the analyses presented in Chapters 2 through 4 suggests several high-priority areas for modelers focused on the next generation of NP fate models. Many will require input from experimentalists, as described shortly.

We suggest the following improvements to spatial and temporal resolution:

- (1) Shift from the national/regional scale to the watershed scale and smaller in order to predict local accumulation and effects and facilitate environmental management activities,
- (2) Parameterize models with site-specific data (e.g., environmental emissions, stream flow and sediment transport parameters, dissolved oxygen, sulfide, pH, and organic carbon),
- (3) Include high temporal and spatial resolution system hydrology/stream flow dynamics in river models, and
- (4) Investigate seasonal trends.

We suggest that modelers couple sensitivity analyses with experimental research in order to

- (1) Identify NP properties and environmental conditions that are dominant/irrelevant in complex systems for inclusion/exclusion from models,
- (2) Compare the influence of NP properties to that of environmental drivers to determine whether one or the other can be ignored in complex systems,

- (3) Determine the level of detail needed to model NP heteroaggregation with suspended particulate matter (SPM). (How many size classes are required? Should variation in geochemical identity be accounted for?),
- (4) Devise first-order alternatives to more complex rate equations, where justified,
- (5) Determine whether sources and sinks that are generally ignored in NP fate models are potentially significant (e.g., incinerators, landfill leachate, crop soil runoff, biouptake and trophic transfer), and
- (6) Be aware of sources of model error and uncertainty beyond parameter uncertainty, including model structure (e.g., choice of rate law, choice of framework) and discretization (numerical error, inadequate spatial and temporal resolution). Simple models generally have higher predictive power than complex models. This is especially true when data are limited and scientific uncertainty is high.

Models that include heteroaggregation and transport will benefit from approaches that

- (1) Apply kinetic, but not necessarily size-dependent, descriptors of heteroaggregation rather than equilibrium descriptors,
- (2) Model heteroaggregate break-up/disaggregation,
- (3) Express heteroaggregation rates as a function of environmental drivers (e.g. natural organic matter, pH, ionic strength) and NP properties (e.g., particle size, engineered coating, pH_{PZC}), and
- (4) Include bedload shift and other relevant sediment transport processes in stream models.

Models that include reactive NP chemistry will benefit from approaches that

- (1) Express reaction rates as a function of environmental drivers (e.g., oxygen, temperature, pH) and particle properties (e.g., surface area, size),

- (2) Express reaction rates as a function of particle transformations (e.g., NP dissolution rate as a function of particle sulfidation) and aggregation state (e.g., fractal dimension, coordinate number), and
- (3) Track the formation and speciation of reaction by-products (e.g., metal ions).

Promising next steps for population balance modeling of NPs include

- (1) Empirical or mechanistic models based on experimental research or (e.g.) principles of fractal geometry that describe the influence of aggregate morphology (e.g., coordination number, fractal dimension) on the surface area of aggregates available for surface-dependent transformation processes,
- (2) Direct comparisons of Monte Carlo methods to moment methods and sectional methods in order to determine their relative accuracy and runtimes,
- (3) Development of hybrid moment/sectional methods and “moving grid” sectional methods as efficient alternatives to purely moment-based or sectional approaches
- (4) (i) Incorporation of zero-dimensional population balance models into 2-D advection-dispersion river models or (ii) Modification of existing large-scale size-resolved NP fate models to explicitly incorporate rigorous numerical methods from the population balance literature (e.g., highly resolved particle size distributions, sectional models with non-linear binning schemes, computationally efficient frameworks such as moment methods)
- (5) Models of environmentally relevant bivariate or trivariate systems (Figure 5-1).

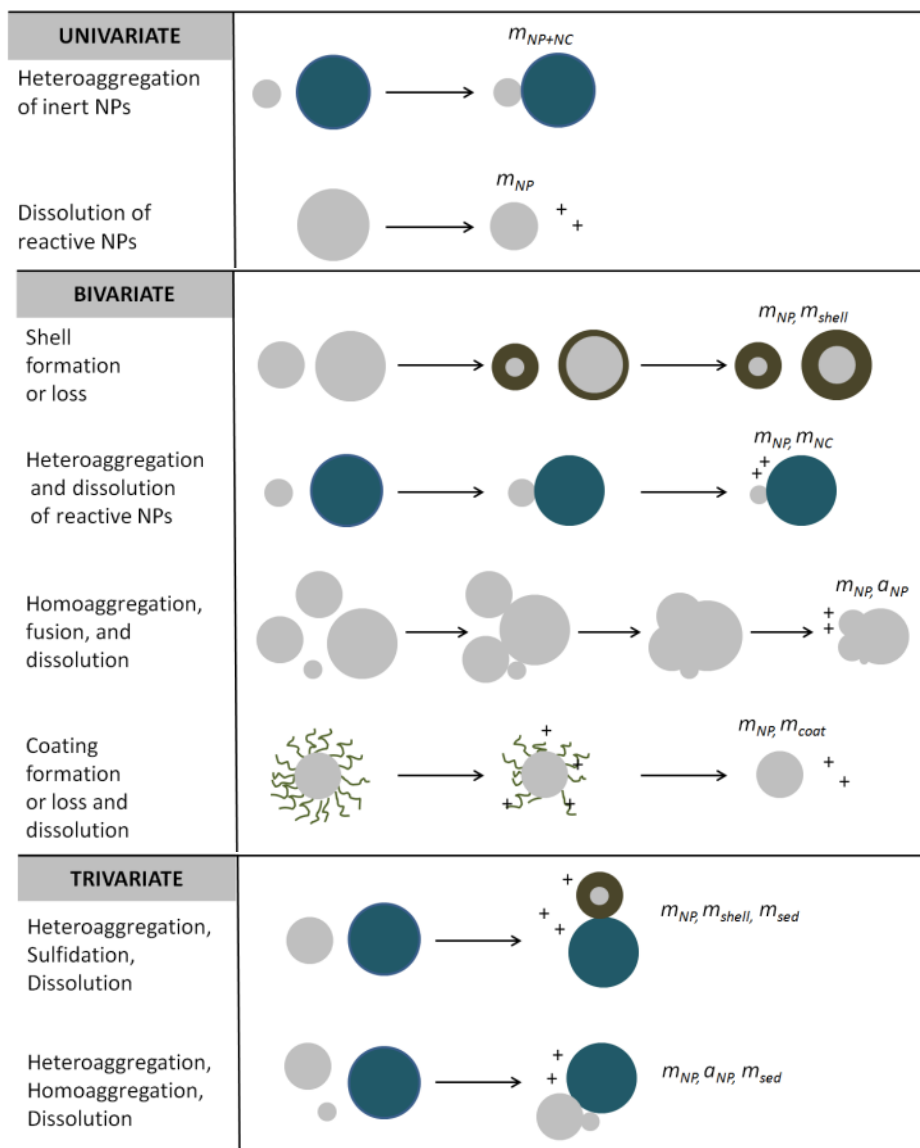


Figure 5-1. NP fate processes that require univariate, bivariate, and trivariate methods. The internal coordinates needed to describe the fate processes listed on the left are shown on the right. m_x =mass of x , a_x =surface area of x ; NP = nanoparticle, sed = sediment.

5.2.1 Experimental Research to Support Modeling Efforts

As a result of over a decade of research into NP fate and effects, it is now straightforward to identify key processes and anticipate the impact of various particle properties and environmental conditions on NP behaviors. However, experimental research is still needed to prioritize and quantify observed relationships. To facilitate model design and parameterization, fundamental research is still badly needed in the following areas:

(1) Identification of the key physicochemical properties of NPs and environmental conditions that impact NP fate and transport in the environment: Modeling efforts at large scales require an objective consensus on which NP properties, environmental properties, and fate and transport processes are needed to assess the environmental fate of NPs and which can be safely disregarded. Coupled with experimental research, side-by-side comparisons of alternate modeling frameworks and sensitivity and uncertainty analysis will enable modelers to determine which simplifying assumptions can be made safely at various scales and which cannot. Such analyses are of course the focus of this dissertation. However, much work remains.

(2) Quantification of reaction rates and heteroaggregation rates in a manner that reflects their dependence on NP properties and environmental conditions. Determining rates of heteroaggregation or chemical transformations is challenging for many reasons: (i) It is practically impossible to test every combination of NP property and environmental condition that could affect the aggregation and dissolution rates of an NP with a given elemental composition. (ii) Several NP transformation processes, such as aggregation and dissolution, are interdependent. (iii) Many NPs only partially transform, with the transformation rates of the partially transformed NPs being intermediate between pristine and fully transformed NPs. (iv) More laboratory studies are needed to capture behaviors observed in complex media but not simple media, such as disaggregation of heteroaggregates under changing environmental conditions,¹⁷⁴ reaction rate modification by microbes,⁶¹ or the impact of heterogeneity in naturally-occurring SPM on NP heteroaggregation.¹⁷

For inclusion in models, the relationships between particle properties and environmental conditions must be quantified using rate laws and rate constants rather than simply observed.

This will require assays that are well-controlled but that contain sufficient complexity to capture environmental behaviors.

(3) Finally, there is a need for further research into the form and (if possible) concentration of NPs within wastewater effluent and biosolids (e.g.,^{81,111}) for use in realistic emissions scenarios for NP fate models.

Current NP loadings are poorly quantified, and detection of NPs in complex environmental media is difficult to impossible. Absence of field and mesocosm-scale data for NP fate model calibration and validation is thus the biggest obstacle at present to obtaining accurate predictions of environmental NP concentrations and to confidence that NP fate models are predictive as well as descriptive. New analytical tools and NP-specific sample extraction protocols are badly needed to quantify NP amounts and speciation at environmentally relevant concentrations in environmentally complex samples.^{175,176}

We note finally that NP fate models only predict exposures. To determine risk, a function of both hazard and exposure, toxicology studies are needed that consider all relevant NP transformation states (as opposed to the current focus on the toxicity of pristine NPs).¹

5.2.3 Environmental Regulation of Nanomaterials in the U.S.

Relative to the European Union, whose rapid development of strict regulatory oversight of the nanotechnology industry has been "empirically and theoretically remarkable" given the recent economic crisis, scientific uncertainty, and a general lack of public outcry,¹⁷⁷ the U.S. has responded slowly to the possible environmental and consumer health risks of nanotechnology. U.S. regulatory agencies are still in the exploratory stage, and the future of nanomaterials regulation is uncertain.¹⁷⁸

The economic and social drivers behind differential E.U. and U.S. responses to new technologies

that pose possible ecotoxicological concerns and impact multiple industries as well as consumers--as demonstrated most dramatically by genetically modified foods--elude simple arguments (e.g., "The E.U. applies the precautionary principle, the U.S. does not.").^{179, 180} However, we can say with confidence that that the slower U.S. response reflects not only the evolving state of the science but a lack of pressure from the American public¹⁸¹ as well as experts: A recent survey reveals that even nano risk assessors and nano regulators generally perceive the benefits of nanotechnology to outweigh the risks.¹⁸² Further, in spite of over a decade of research, the scientific community has not yet reached a consensus on the question of whether or not nano risks are "novel" and demand new regulations.^{178, 182, 183} Although novelty is still hotly contested in the field of nanotoxicology for even the most widely studied NPs,¹⁸⁴ consensus has primarily been stymied by the staggering diversity of nanoparticle and nanohybrid compositions and morphologies that have yet to be tested at all.¹⁸⁵ To bridge remaining gaps, federal research funding agencies have increasingly invested in the development of rapid screening tools such as high-throughput and *in silico* toxicity tests.^{178, 186, 187} These efforts are still ongoing.

The exposure scenarios presented in Chapters 2-4 are far from comprehensive. Nonetheless, it is encouraging to see that--in agreement with both current public opinion and the average views of nano risk assessors and regulators, as described above--they suggest no cause for immediate concern. The sediment model and watershed model^{61, 63} supported experimental findings that ZnO NP and Ag NP toxicity decrease rapidly in environmental media due to dissolution and the subsequent transformation of metal ions.³¹ In addition, predicted environmental concentrations of Zn and Ag from ZnO and Ag NPs in the watershed model remained below existing regulatory thresholds for total metal concentrations.

Hot spots immediately downstream from production facilities do present a potential concern.⁶³ However, even in this case, industry-wide effluent limits already in place for metals are

likely to suffice because NPs will be indistinguishable from other sources of metals in the environment unless their direct ingestion by organisms or their dissolution within a confined medium (e.g., sediments) results in atypical ion release or other highly localized toxic effects (e.g., as observed recently for ZnO NPs in soils).¹⁸⁸ In the author's view, it is unlikely that these effects will enhance NP risks enough to undermine the effectiveness of the conservative regulatory limits already in place for metals.

Regulations can be classified as "upstream" or "downstream" according to where they fall in a material's life cycle. Two upstream regulations administered by the US EPA that explicitly differentiate nano formulations from their bulk or ionic counterparts include (1) the registration of nanopesticides under the Federal Insecticide, Fungicide, and Rodenticide Act (FIFRA), which uses data on nanosilver toxicity rather than data on ionic silver to evaluate the safety of nanosilver-containing pesticides,¹⁸⁹ and (2) the control of nanomaterial manufacturing, importation, or processing under the Toxic Substances Control Act (TSCA). Significant New Use Rules (SNURs) proposed or already promulgated under TSCA require companies to report their intent to manufacture specific NP types (e.g., functionalized carbon nanotubes, graphene nanoplatelets) 90 days prior to beginning these activities. EPA also intends to promulgate a new rule under Section 8(a) of TSCA in October 2016 that will introduce new reporting and recordkeeping requirements for all companies that manufacture nanomaterials.¹⁹⁰ The Federal Food, Drug, and Cosmetic Act (FFDCA) gives the U.S. Food and Drug Administration the authority to regulate food, drugs, cosmetics, dietary supplements, and medical devices on a product-by-product basis, but it does not explicitly distinguish nano-enabled products from others. "End-of-pipe" regulations such as the Resource Conservation and Recovery Act, the Clean Water Act, and the Safe Drinking Water Act would limit allowable NP concentrations or loads in industrial or commercial effluents or waste, surface waters, and drinking water.¹⁷⁸ At present, however, such downstream regulations are

impossible to implement for NPs because the analytical tools needed to differentiate NPs from their ionic or bulk counterparts in complex media are still under development.¹⁷⁵ In addition to these "hard" laws, agencies may issue "soft" laws, or recommendations for best practices. In August 2015, for example, the FDA provided guidance for the use of nanoparticles as an animal food additive.¹⁹¹

TSCA, FIFRA, and the FFDCa place the burden of proof of risk on the government rather than on the producer. They are subject to under-reporting, and they can be costly and inefficient relative to "end-of-pipe" regulations because the need for oversight is determined on a case-by-case basis.¹⁷⁸ In addition, most products regulated under the FFDCa do not require pre-market approval. Fortunately, recent surveys indicate that the nanotechnology industry views itself as responsible for the safety of its products and manufacturing processes.¹⁹² Industry can ameliorate public concerns about the current lack of regulatory oversight and industry concerns about strict regulatory oversight in the future by promoting voluntary reporting, establishing industry standards, and otherwise endorsing self-regulation.

Environmental fate models predict environmental concentrations and are therefore most relevant for decision-making when used to enforce or inform "end of pipe" environmental management efforts. My work has shown that if the complexity of the transformations that Me/MeO nanoparticles undergo in the environment is not adequately captured, the resulting estimates of contaminant concentrations of NPs will be worthless, as would be environmental policy developed based upon them. Given the evolving state of the science and the lack of data for model calibration and validation, predicted environmental concentrations from NP fate models of any type must currently be viewed as merely suggestive. However, as frameworks improve and data limitations decrease, the predictive performance of NP fate models could become a valid basis for regulatory decision-making. To make research relevant to decision-makers, experimentalists and

modelers must prioritize site-specific models validated against site-specific field data as well as extensive evaluation of model uncertainty and parameter uncertainty/variability.

5.3 Related Publications

In addition to the work presented in Chapter 2-4, I co-authored the following works during my graduate studies. Chapters 1 and 5 were based on excerpts from the first two works in this list, which expand upon the ideas presented here.

- **A. Dale**, E. Casman, G. Lowry, J. Lead, E. Viparelli, M. Baalousha. "Modeling nanomaterial environmental fate in aquatic systems." *Environmental Science & Technology*, 49 (5), 2587-2593
- **A. Dale**, G. Lowry, E. Casman. "Much ado about α : reframing the debate over appropriate fate descriptors in nanoparticle environmental risk modeling." *Environmental Science: Nano*, 2, 27-32
- S. Louie, **A. Dale**, E. Casman, G. Lowry. "Challenges Facing the Environmental Nanotechnology Research Enterprise." Chapter 1 of Wiley - IUPAC series on biophysico-chemical processes in environmental systems, Volume 4, "Engineered Nanoparticles and the Environment: Biophysicochemical Processes and Biototoxicity" by B. Xing, C. Vecitis, and N. Senesi (in press)
- C. Levard, E. Hotze, B. Colman, **A. Dale**, L. Truong, X. Yang, A. Bone, G. Brown Jr., R. Tanguay, R. Di Giulio, E. Bernhardt, J. Meyer, M. Wiesner, and G. Lowry. "Sulfidation of silver nanoparticles: Natural antidote to their toxicity." *Environmental Science & Technology*, 47 (23), 13440–13448

Bibliography

1. Wiesner, M. R.; Lowry, G. V.; Jones, K. L.; Hochella, J., Michael F; Di Giulio, R. T.; Casman, E.; Bernhardt, E. S., Decreasing Uncertainties in Assessing Environmental Exposure, Risk, and Ecological Implications of Nanomaterials. *Environ Sci Technol* **2009**, *43*, (17), 6458-6462.
2. Keller, A. A.; McFerran, S.; Lazareva, A.; Suh, S., Global life cycle releases of engineered nanomaterials. *Journal of Nanoparticle Research* **2013**, *15*, (6), 1-17.
3. Ramaswami, A.; Milford, J. B.; Small, M. J., *Integrated environmental modeling: pollutant transport, fate, and risk in the environment*. 1 ed.; John Wiley & Sons: New York, NY: **2005**.
4. Gottschalk, F.; Sun, T.; Nowack, B., Environmental concentrations of engineered nanomaterials: review of modeling and analytical studies. *Environmental Pollution* **2013**, *181*, 287-300.
5. Liu, H. H.; Cohen, Y., Multimedia environmental distribution of engineered nanomaterials. *Environ Sci Technol* **2014**, *48*, (6), 3281-3292.
6. Sun, T. Y.; Gottschalk, F.; Hungerbühler, K.; Nowack, B., Comprehensive probabilistic modelling of environmental emissions of engineered nanomaterials. *Environmental Pollution* **2014**, *185*, 69-76.
7. Gottschalk, F.; Lassen, C.; Kjoelholm, J.; Christensen, F.; Nowack, B., Modeling flows and concentrations of nine engineered nanomaterials in the Danish environment. *International journal of environmental research and public health* **2015**, *12*, (5), 5581-5602.
8. Praetorius, A.; Scheringer, M.; Hungerbühler, K., Development of Environmental Fate Models for Engineered Nanoparticles: A Case Study of TiO₂ Nanoparticles in the Rhine River. *Environ Sci Technol* **2012**, *46*, (12), 6705-6713.
9. Therezien, M.; Thill, A.; Wiesner, M. R., Importance of heterogeneous aggregation for NP fate in natural and engineered systems. *Science of The Total Environment* **2014**, *485*, 309-318.
10. Koelmans, A.; Quik, J.; Velzeboer, I., Lake retention of manufactured nanoparticles. *Environmental Pollution* **2015**, *196*, 171-175.
11. Sani-Kast, N.; Scheringer, M.; Slomberg, D.; Labille, J.; Praetorius, A.; Ollivier, P.; Hungerbühler, K., Addressing the complexity of water chemistry in environmental fate modeling for engineered nanoparticles. *Science of The Total Environment* **2015**, *535*, 150-159.
12. Praetorius, A.; Tufenkji, N.; Goss, K.-U.; Scheringer, M.; von der Kammer, F.; Elimelech, M., The road to nowhere: equilibrium partition coefficients for nanoparticles. *Environmental Science: Nano* **2014**, *1*, (4), 317-323.
13. Petosa, A. R.; Jaisi, D. P.; Quevedo, I. R.; Elimelech, M.; Tufenkji, N., Aggregation and deposition of engineered nanomaterials in aquatic environments: Role of physicochemical interactions. *Environ Sci Technol* **2010**, *44*, (17), 6532-6549.

14. Dale, A. L.; Lowry, G. V.; Casman, E., Much ado about α : Reframing the debate over appropriate fate descriptors in nanoparticle environmental risk modeling. *Environmental Science: Nano* **2015**, *2*, 27-32.
15. Cornelis, G., Fate descriptors for engineered nanoparticles: the good, the bad, and the ugly. *Environmental Science: Nano* **2015**, *2*, 19-26.
16. Velzeboer, I.; Quik, J.; van de Meent, D.; Koelmans, A., Rapid settling of nanoparticles due to heteroaggregation with suspended sediment. *Environmental Toxicology and Chemistry* **2014**, *33*, (8), 1766–1773.
17. Louie, S. M.; Spielman-Sun, E. R.; Small, M. J.; Tilton, R. D.; Lowry, G. V., Correlation of the Physicochemical Properties of Natural Organic Matter Samples from Different Sources to Their Effects on Gold Nanoparticle Aggregation in Monovalent Electrolyte. *Environ Sci Technol* **2015**, *49*, (4), 2188–2198.
18. Hotze, E. M.; Phenrat, T.; Lowry, G. V., Nanoparticle aggregation: Challenges to understanding transport and reactivity in the environment. *Journal of environmental quality* **2010**, *39*, (6), 1909-1924.
19. Nowack, B.; Ranville, J. F.; Diamond, S.; Gallego-Urrea, J. A.; Metcalfe, C.; Rose, J.; Horne, N.; Koelmans, A. A.; Klaine, S. J., Potential scenarios for nanomaterial release and subsequent alteration in the environment. *Environmental Toxicology and Chemistry* **2012**, *31*, (1), 50-59.
20. Mudunkotuwa, I. A.; Rupasinghe, T.; Wu, C.-M.; Grassian, V. H., Dissolution of ZnO nanoparticles at circumneutral pH: a study of size effects in the presence and absence of citric acid. *Langmuir* **2011**, *28*, (1), 396-403.
21. Levard, C.; Reinsch, B. C.; Michel, F. M.; Oumahi, C.; Lowry, G. V.; Brown Jr, G. E., Sulfidation processes of PVP-coated silver nanoparticles in aqueous solution: impact on dissolution rate. *Environ Sci Technol* **2011**, *45*, (12), 5260-5266.
22. Ma, R.; Levard, C. m.; Michel, F. M.; Brown Jr, G. E.; Lowry, G. V., Sulfidation mechanism for zinc oxide nanoparticles and the effect of sulfidation on their solubility. *Environ Sci Technol* **2013**, *47*, (6), 2527-2534.
23. Ma, R.; Stegemeier, J.; Levard, C.; Dale, J.; Noack, C. W.; Yang, T.; Brown, G.; Lowry, G., Sulfidation of copper oxide nanoparticles and properties of resulting copper sulfide. *Environmental Science: Nano* **2014**, *1*, 347-357.
24. Di Toro, D. M., *Sediment flux modeling*. Wiley-Interscience New York: **2001**.
25. Levard, C.; Hotze, E. M.; Colman, B. P.; Dale, A. L.; Truong, L.; Yang, X.; Bone, A. J.; Brown Jr, G. E.; Tanguay, R. L.; Di Giulio, R. T., Sulfidation of Silver Nanoparticles: Natural antidote to their toxicity. *Environ Sci Technol* **2013**, *47*, (23), 13440-13448.
26. Reinsch, B.; Levard, C.; Li, Z.; Ma, R.; Wise, A.; Gregory, K.; Brown Jr, G.; Lowry, G., Sulfidation of silver nanoparticles decreases Escherichia coli growth inhibition. *Environ Sci Technol* **2012**, *46*, (13), 6992-7000.

27. Levard, C.; Hotze, E. M.; Lowry, G. V.; Brown Jr, G. E., Environmental Transformations of Silver Nanoparticles: Impact on Stability and Toxicity. *Environ Sci Technol* **2012**, *46*, (13), 6900-6914.
28. Casas, A. M.; Crecelius, E. A., Relationship between acid volatile sulfide and the toxicity of zinc, lead and copper in marine sediments. *Environmental Toxicology and Chemistry* **1994**, *13*, (3), 529-536.
29. Di Toro, D. M.; McGrath, J. A.; Hansen, D. J.; Berry, W. J.; Paquin, P. R.; Mathew, R.; Wu, K. B.; Santore, R. C., Predicting sediment metal toxicity using a sediment biotic ligand model: Methodology and initial application. *Environmental Toxicology and Chemistry* **2009**, *24*, (10), 2410-2427.
30. US EPA. "Framework for Metals Risk Assessment." Report No. EPA 120/R-07/001. United States Environmental Protection Agency, Office of the Science Advisor, Risk Assessment Forum **2007**.
31. Lowry, G. V.; Gregory, K. B.; Apte, S. C.; Lead, J. R., Transformations of nanomaterials in the environment. *Environ Sci Technol* **2012**, *46*, (13), 6893-6899.
32. Mueller, N. C.; Nowack, B., Exposure modeling of engineered nanoparticles in the environment. *Environ Sci Technol* **2008**, *42*, (12), 4447-4453.
33. Gottschalk, F.; Sonderer, T.; Scholz, R. W.; Nowack, B., Modeled environmental concentrations of engineered nanomaterials (TiO₂, ZnO, Ag, CNT, fullerenes) for different regions. *Environ Sci Technol* **2009**, *43*, (24), 9216-9222.
34. Keller, A. A.; Lazareva, A., Predicted releases of engineered nanomaterials: From global to regional to local. *Environmental Science & Technology Letters* **2013**, *1*, (1), 65-70.
35. Sun, T. Y.; Conroy, G.; Donner, E.; Hungerbühler, K.; Lombi, E.; Nowack, B., Probabilistic modelling of engineered nanomaterial emissions to the environment: a spatio-temporal approach. *Environmental Science: Nano* **2015**, *2*, (4), 340-351.
36. Bornhöft, N. A.; Sun, T. Y.; Hilty, L. M.; Nowack, B., A dynamic probabilistic material flow modeling method. *Environmental Modelling & Software* **2016**, *76*, 69-80.
37. Meesters, J.; Koelmans, A. A.; Quik, J. T.; Hendriks, A. J.; Van de Meent, D., Multimedia Modeling of Engineered Nanoparticles with SimpleBox4nano: Model Definition and Evaluation. *Environ Sci Technol* **2014**, *48*, (10), 5726-5736.
38. Lowry, G. V.; Espinasse, B. P.; Badireddy, A. R.; Richardson, C. J.; Reinsch, B. C.; Bryant, L. D.; Bone, A. J.; Deonarine, A.; Chae, S.; Therezien, M., Long-term transformation and fate of manufactured Ag nanoparticles in a simulated large scale freshwater emergent wetland. *Environmental Science and Technology* **2012**, *46*, (13), 7027-7036.
39. Schwarzenbach, R. P.; Gschwend, P. M.; Imboden, D. M., *Environmental organic chemistry*. 2nd ed. Wiley-Interscience: **2005**.

40. Boxall, A.; Chaudhry, Q.; Sinclair, C.; Jones, A.; Aitken, R.; Jefferson, B.; Watts, C., Current and future predicted environmental exposure to engineered nanoparticles. *Central Science Laboratory, Department of the Environment and Rural Affairs, London, UK* **2007**.
41. Blaser, S. A.; Scheringer, M.; MacLeod, M.; Hungerbühler, K., Estimation of cumulative aquatic exposure and risk due to silver: Contribution of nano-functionalized plastics and textiles. *Science of the Total Environment* **2008**, *390*, (2), 396-409.
42. Gottschalk, F.; Ort, C.; Scholz, R.; Nowack, B., Engineered nanomaterials in rivers—Exposure scenarios for Switzerland at high spatial and temporal resolution. *Environmental Pollution* **2011**, *159*, (12), 3439-3445.
43. Elimelech, M.; Jia, X.; Gregory, J.; Williams, R., *Particle deposition and aggregation: measurement, modelling and simulation*. Butterworth-Heinemann: **1998**.
44. Markus, A.; Parsons, J.; Roex, E.; de Voogt, P.; Laane, R., Modelling the transport of engineered metallic nanoparticles in the river Rhine. *Water Research* **2016**, *91*, 214-224.
45. Arvidsson, R.; Molander, S.; Sandén, B. A.; Hassellöv, M., Challenges in exposure modeling of nanoparticles in aquatic environments. *Human and Ecological Risk Assessment* **2011**, *17*, (1), 245-262.
46. de Klein, J.; Quik, J. T.; Bauerlein, P.; Koelmans, A. A., Towards validation of the NanoDUFLOW nanoparticle fate model for the river Dommel, The Netherlands. *Environmental Science: Nano* **2016**. DOI: 10.1039/c5en00270b.
47. Quik, J. T.; de Klein, J. J.; Koelmans, A. A., Spatially explicit fate modelling of nanomaterials in natural waters. *Water research* **2015**, *80*, 200-208.
48. Dumont, E.; Johnson, A. C.; Keller, V. D.; Williams, R. J., Nano silver and nano zinc-oxide in surface waters—Exposure estimation for Europe at high spatial and temporal resolution. *Environmental Pollution* **2015**, *196*, 341-349.
49. Tyrrel, S.; Quinton, J. N., Overland flow transport of pathogens from agricultural land receiving faecal wastes. *Journal of Applied Microbiology* **2003**, *94*, (s1), 87-93.
50. Sharpley, A. N.; Chapra, S.; Wedepohl, R.; Sims, J.; Daniel, T. C.; Reddy, K., Managing agricultural phosphorus for protection of surface waters: Issues and options. *Journal of Environmental Quality* **1994**, *23*, (3), 437-451.
51. Tang, W.; Ao, L.; Zhang, H.; Shan, B., Accumulation and risk of heavy metals in relation to agricultural intensification in the river sediments of agricultural regions. *Environmental Earth Sciences* **2014**, *71*, (9), 3945-3951.
52. Westerhoff, P. K.; Kiser, M. A.; Hristovski, K., Nanomaterial removal and transformation during biological wastewater treatment. *Environmental Engineering Science* **2013**, *30*, (3), 109-117.
53. Wilcock, P. R.; Pitlick, J.; Cui, Y., Sediment transport primer: estimating bed-material transport in gravel-bed rivers. Gen. Tech. Rep. RMRS-GTR-226. Fort Collins, CO: U.S. Department of Agriculture, Forest Service, Rocky Mountain Research Station. **2009**.

54. Maurer-Jones, M. A.; Gunsolus, I. L.; Murphy, C. J.; Haynes, C. L., Toxicity of engineered nanoparticles in the environment. *Analytical chemistry* **2013**, *85*, (6), 3036-3049.
55. Jacobson, M. Z., *Fundamentals of atmospheric modeling*. Cambridge University Press: 2005.
56. Seinfeld, J. H.; Pandis, S. N., *Atmospheric chemistry and physics: from air pollution to climate change*. 2nd edition. John Wiley & Sons: **2012**.
57. Yuan, C.; Laurent, F.; Fox, R., An extended quadrature method of moments for population balance equations. *Journal of Aerosol Science* **2012**, *51*, 1-23.
58. Marchisio, D. L.; Pikturna, J. T.; Fox, R. O.; Vigil, R. D.; Barresi, A. A., Quadrature method of moments for population-balance equations. *AIChE Journal* **2003**, *49*, (5), 1266-1276.
59. Dale, A.; Casman, E. A.; Lowry, G. V.; Lead, J. R.; Viparelli, E.; Baalousha, M. A., Modeling nanomaterial environmental fate in aquatic systems. *Environ Sci Technol* **2015**, *49*, (5), 2587-2593.
60. Di Toro, D. M.; Mahony, J. D.; Hansen, D. J.; Berry, W. J., A model of the oxidation of iron and cadmium sulfide in sediments. *Environmental Toxicology and Chemistry* **1996**, *15*, (12), 2168-2186.
61. Dale, A. L.; Lowry, G. V.; Casman, E. A., Modeling Nanosilver Transformations in Freshwater Sediments. *Environ Sci Technol* **2013**, *47*, (22), 12920-12928.
62. USEPA (U.S. Environmental Protection Agency) *Chesapeake Bay Phase 5.3 Community Watershed Model*. Rep No. EPA 903S10002 - CBP/TRS-303-10. U.S. Environmental Protection Agency, Chesapeake Bay Program Office, Annapolis MD. **2010**.
63. Dale, A. L.; Lowry, G. V.; Casman, E. A., Stream dynamics and chemical transformations control the environmental fate of silver and zinc oxide nanoparticles in a watershed-scale model. *Environ Sci Technol* **2015**, *49*, (12), 7285-7293.
64. *2010 Nanotechnology Research Review*; Report Code: NAN047B; Business Communications Company, **2011**.
65. *Analysis of Consumer Products, Nanotechnology Project*; Project on Emerging Nanotechnologies, Woodrow Wilson International Center for Scholars. Accessed **2012**.
www.nanotechproject.org/inventories/consumer/analysis_draft
66. Liu, J.; Hurt, R. H., Ion release kinetics and particle persistence in aqueous nano-silver colloids. *Environ Sci Technol* **2010**, *44*, (6), 2169-2175.
67. Liu, J.; Sonshine, D. A.; Shervani, S.; Hurt, R. H., Controlled release of biologically active silver from nanosilver surfaces. *ACS nano* **2010**, *4*, (11), 6903-6913.
68. Dobias, J.; Bernier-Latmani, R., Silver release from silver nanoparticles in natural waters. *Environ Sci Technol* **2013**, *47*, (9), 4140-4146.

69. Ma, R.; Levard, C. m.; Marinakos, S. M.; Cheng, Y.; Liu, J.; Michel, F. M.; Brown Jr, G. E.; Lowry, G. V., Size-controlled dissolution of organic-coated silver nanoparticles. *Environ Sci Technol* **2011**, *46*, (2), 752-759.
70. Fabrega, J.; Luoma, S. N.; Tyler, C. R.; Galloway, T. S.; Lead, J. R., Silver nanoparticles: Behaviour and effects in the aquatic environment. *Environment international* **2011**, *37*, (2), 517-531.
71. Luoma, S.N., *Silver Nanotechnologies and the Environment: Old Problems or New Challenges?* Project on Emerging Nanotechnologies, Woodrow Wilson International Center for Scholars, **2008**.
72. Liu, J.; Pennell, K. G.; Hurt, R. H., Kinetics and mechanisms of nanosilver oxysulfidation. *Environ Sci Technol* **2011**, *45*, (17), 7345-7353.
73. Kim, B.; Park, C. S.; Murayama, M.; Hochella, M. F., Discovery and characterization of silver sulfide nanoparticles in final sewage sludge products. *Environmental Science and Technology* **2010**, *44*, (19), 7509.
74. Choi, O.; Hu, Z., Nitrification inhibition by silver nanoparticles. *Water science and technology: a journal of the International Association on Water Pollution Research* **2009**, *59*, (9), 1699.
75. Quik, J. T. K.; Stuart, M. C.; Wouterse, M.; Peijnenburg, W.; Hendriks, A. J.; van de Meent, D., Natural colloids are the dominant factor in the sedimentation of nanoparticles. *Environmental Toxicology and Chemistry* **2012**, *31*, (5), 1019–1022.
76. Keller, A. A.; Wang, H.; Zhou, D.; Lenihan, H. S.; Cherr, G.; Cardinale, B. J.; Miller, R.; Ji, Z., Stability and aggregation of metal oxide nanoparticles in natural aqueous matrices. *Environ Sci Technol* **2010**, *44*, (6), 1962-1967.
77. Zhou, D.; Abdel-Fattah, A.; Keller, A. A., Clay particles destabilize engineered nanoparticles in aqueous environments. *Environ Sci Technol* **2012**, *46*, (14), 7520-7526.
78. Burton, J., G.A., Sediment quality criteria in use around the world. *Limnology* **2002**, *3*, (2), 65-76.
79. Unrine, J. M.; Shoultz-Wilson, W. A.; Zhurbich, O.; Bertsch, P. M.; Tsyusko, O. V., Trophic Transfer of Au Nanoparticles from Soil along a Simulated Terrestrial Food Chain. *Environ Sci Technol* **2012**, *46*, (17), 9753-9760.
80. Boudreau, B. P., Metals and models: diagenic modelling in freshwater lacustrine sediments. *Journal of Paleolimnology* **1999**, *22*, (3), 227-251.
81. Kaegi, R.; Voegelin, A.; Ort, C.; Sinnet, B.; Thalmann, B.; Krismer, J.; Hagendorfer, H.; Elumelu, M.; Mueller, E., Fate and transformation of silver nanoparticles in urban wastewater systems. *Water research* **2013**, *47*, (12), 3866–3877.
82. Levard, C.; Mitra, S.; Yang, T.; Jew, A.; Badireddy, A. R.; Lowry, G. V.; Brown, G. E., The Effect of Chloride on the Dissolution Rate of Silver Nanoparticles and Toxicity to *E. coli*. *Environ Sci Technol* **2013**, *47*, (11), 5738-5745.

83. Feldberg, S. W., Optimization of explicit finite-difference simulation of electrochemical phenomena utilizing an exponentially expanded space grid: Refinement of the Joslin-Pletcher algorithm. *Journal of Electroanalytical Chemistry and Interfacial Electrochemistry* **1981**, 127, (1), 1-10.
84. Joslin, T.; Pletcher, D., The digital simulation of electrode processes. procedures for conserving computer time. *Journal of Electroanalytical Chemistry and Interfacial Electrochemistry* **1974**, 49, (2), 171-186.
85. Boudreau, B. P., *Diagenetic models and their implementation: modelling transport and reactions in aquatic sediments*. Springer Berlin: **1997**.
86. Boudreau, B. P., Is burial velocity a master parameter for bioturbation? *Geochimica et Cosmochimica Acta* **1994**, 58, (4), 1243-1249.
87. Kaegi, R.; Voegelin, A.; Sinnet, B.; Zuleeg, S.; Hagendorfer, H.; Burkhardt, M.; Siegrist, H., Behavior of metallic silver nanoparticles in a pilot wastewater treatment plant. *Environ Sci Technol* **2011**, 45, (9), 3902-3908.
88. Di Toro, D. M.; Mahony, J. D.; Carbonaro, R. F.; DeMarco, T.; Morrissey, J. C.; Pablo, R. J.; Page, J. J.; Shadi, T. S., *The Oxidation of Silver Sulfide and Other Heavy Metal Sulfides in Sediments*. Argentum V conference proceedings. Andren, A., Bober, T. W., Eds. University of Wisconsin System, Sea Grant Institute: **1998**.
89. Gąsiorowski, M., Deposition rate of lake sediments under different alternative stable states. *Geochronometria* **2008**, 32, (-1), 29-35.
90. Rose, N. L.; Morley, D.; Appleby, P. G.; Battarbee, R. W.; Alliksaar, T.; Guilizzoni, P.; Jeppesen, E.; Korhola, A.; Punning, J. M., Sediment accumulation rates in European lakes since AD 1850: trends, reference conditions and exceedence. *Journal of Paleolimnology* **2011**, 45, (4), 447-468.
91. Allison, J. D.; Allison, T. L., *Partition coefficients for metals in surface water, soil, and waste*. Rep No. EPA/600/R-05 **2005**.
92. Neubauer, S. C.; Miller, W. D.; Anderson, I. C., Carbon cycling in a tidal freshwater marsh ecosystem: a carbon gas flux study. *Marine Ecology Progress Series* **2000**, 199, 13-30.
93. Sotiriou, G. A.; Meyer, A.; Knijnenburg, J. T.; Panke, S.; Pratsinis, S. E., Quantifying the origin of released Ag⁺ ions from nanosilver. *Langmuir* **2012**, 28, (45), 15929-15936.
94. Cowan, J. L.; Boynton, W. R., Sediment-water oxygen and nutrient exchanges along the longitudinal axis of Chesapeake Bay: seasonal patterns, controlling factors and ecological significance. *Estuaries* **1996**, 19, (3), 562-580.
95. Kristensen, E., Organic matter diagenesis at the oxic/anoxic interface in coastal marine sediments, with emphasis on the role of burrowing animals. *Hydrobiologia* **2000**, 426, (1), 1-24.
96. Shoults-Wilson, W. A.; Reinsch, B. C.; Tsyusko, O. V.; Bertsch, P. M.; Lowry, G. V.; Unrine, J. M., Role of particle size and soil type in toxicity of silver nanoparticles to earthworms. *Soil Science Society of America Journal* **2011**, 75, (2), 365-377.

97. Lombi, E.; Donner, E.; Taheri, S.; Tavakkoli, E.; Jämting, Å. K.; McClure, S.; Naidu, R.; Miller, B. W.; Scheckel, K. G.; Vasilev, K., Transformation of four silver/silver chloride nanoparticles during anaerobic treatment of wastewater and post-processing of sewage sludge. *Environmental Pollution* **2013**, *176*, 193-197.
98. Maurer, F.; Christl, I.; Kretzschmar, R., Reduction and reoxidation of humic acid: Influence on spectroscopic properties and proton binding. *Environ Sci Technol* **2012**, *44*, (15), 5787-5792.
99. Akaighe, N.; MacCuspie, R. I.; Navarro, D. A.; Aga, D. S.; Banerjee, S.; Sohn, M.; Sharma, V. K., Humic acid-induced silver nanoparticle formation under environmentally relevant conditions. *Environ Sci Technol* **2011**, *45*, (9), 3895-3901.
100. Hammes, J.; Gallego-Urrea, J. A.; Hassellöv, M., Geographically distributed classification of surface water chemical parameters influencing fate and behavior of nanoparticles and colloid facilitated contaminant transport. *Water research* **2013**, *47*, (14), 5350-5361.
101. Palmer, M. D., *Water quality modeling: a guide to effective practice*. World bank publications: **2001**.
102. Förstner, U., Sediment dynamics and pollutant mobility in rivers: an interdisciplinary approach. *Lakes & Reservoirs: Research & Management* **2004**, *9*, (1), 25-40.
103. Merritt, W. S.; Letcher, R. A.; Jakeman, A. J., A review of erosion and sediment transport models. *Environmental Modelling & Software* **2003**, *18*, (8), 761-799.
104. Garner, K. L.; Keller, A. A., Emerging patterns for engineered nanomaterials in the environment: a review of fate and toxicity studies. *Journal of Nanoparticle Research* **2014**, *16*, (8), 1-28.
105. Ambrose, B.; Wool, T.; Martin, J., *The Water Quality Analysis Simulation Program, WASP6, User Manual*. US EPA: Athens, GA: **2001**.
106. Martucci, S. K.; Krstolic, J. L.; Raffensperger, J. P.; Hopkins, K. J. *Development of Land Segmentation, Stream-Reach Network, and Watersheds in Support of Hydrological Simulation Program-Fortran(HSPF) Modeling, Chesapeake Bay Watershed, and Adjacent Parts of Maryland, Delaware, and Virginia* **2006**.
107. Brosch, C., *Estimates of county-level nitrogen and phosphorous data for use in modeling pollutant reduction*. Documentation for Scenario Builder version 2.2. **2010**.
108. Hendren, C. O.; Badireddy, A. R.; Casman, E.; Wiesner, M. R., Modeling nanomaterial fate in wastewater treatment: Monte Carlo simulation of silver nanoparticles (nano-Ag). *Science of the Total Environment* **2013**, *449*, 418-425.
109. USEPA, *Biosolids generation, use, and disposal in the United States*. Rep No. EPA 530-R-99-009. Solid Waste and Emergency Response, U.S. Environmental Protection Agency, Washington, DC. **1999**.
110. Lombi, E.; Donner, E.; Tavakkoli, E.; Turney, T. W.; Naidu, R.; Miller, B. W.; Scheckel, K. G., Fate of zinc oxide nanoparticles during anaerobic digestion of wastewater and post-treatment processing of sewage sludge. *Environ Sci Technol* **2012**, *46*, (16), 9089-9096.

111. Ma, R.; Levard, C.; Judy, J. D.; Unrine, J. M.; Durenkamp, M.; Martin, B.; Jefferson, B.; Lowry, G. V., Fate of Zinc Oxide and Silver Nanoparticles in a Pilot Wastewater Treatment Plant and in Processed Biosolids. *Environ Sci Technol* **2013**, *48*, (1), 104-112.
112. Quik, J.; Velzeboer, I.; Wouterse, M.; Koelmans, A.; van de Meent, D., Heteroaggregation and sedimentation rates for nanomaterials in natural waters. *Water research* **2014**, *48*, 269-279.
113. Schnoor, J. L.; Sato, C.; McKechnie, D.; Sahoo, D. *Processes, coefficients, and models for simulating toxic organics and heavy metals in surface waters*. Rep No. EPA/600/3-87/015. Environmental Research Agency, U.S. Environmental Protection Agency: **1987**.
114. Ambrose, R. B., Sediment Transport: Theory and Implementation in WASP7. Modules 1, 2, and 3. Lecture slides courtesy of Timothy Wool. **2010**.
115. Moriasi, D.; Arnold, J.; Van Liew, M.; Bingner, R.; Harmel, R.; Veith, T., Model evaluation guidelines for systematic quantification of accuracy in watershed simulations. *Trans. ASABE* **2007**, *50*, (3), 885-900.
116. Peltier, E.; Dahl, A. L.; Gaillard, J.-F., Metal speciation in anoxic sediments: When sulfides can be construed as oxides. *Environ Sci Technol* **2005**, *39*, (1), 311-316.
117. Donner, E.; Howard, D. L.; Jonge, M. D. d.; Paterson, D.; Cheah, M. H.; Naidu, R.; Lombi, E., X-ray absorption and micro X-ray fluorescence spectroscopy investigation of copper and zinc speciation in biosolids. *Environ Sci Technol* **2011**, *45*, (17), 7249-7257.
118. Emerson, H. P.; Hart, A. E.; Baldwin, J. A.; Waterhouse, T. C.; Kitchens, C. L.; Mefford, O. T.; Powell, B. A., Physical transformations of iron oxide and silver nanoparticles from an intermediate scale field transport study. *Journal of nanoparticle research* **2014**, *16*, (2), 1-14.
119. Yu, S.; Wu, Q.; Li, Q.; Gao, J.; Lin, Q.; Ma, J.; Xu, Q.; Wu, S., Anthropogenic land uses elevate metal levels in stream water in an urbanizing watershed. *Science of The Total Environment* **2014**, *488*, 61-69.
120. Bian, S.-W.; Mudunkotuwa, I. A.; Rupasinghe, T.; Grassian, V. H., Aggregation and dissolution of 4 nm ZnO nanoparticles in aqueous environments: influence of pH, ionic strength, size, and adsorption of humic acid. *Langmuir* **2011**, *27*, (10), 6059-6068.
121. David, C. A.; Galceran, J.; Rey-Castro, C.; Puy, J.; Companys, E.; Salvador, J.; Monné, J.; Wallace, R.; Vakourov, A., Dissolution kinetics and solubility of ZnO nanoparticles followed by AGNES. *The Journal of Physical Chemistry C* **2012**, *116*, (21), 11758-11767.
122. Franklin, N. M.; Rogers, N. J.; Apte, S. C.; Batley, G. E.; Gadd, G. E.; Casey, P. S., Comparative toxicity of nanoparticulate ZnO, bulk ZnO, and ZnCl₂ to a freshwater microalga (*Pseudokirchneriella subcapitata*): the importance of particle solubility. *Environ Sci Technol* **2007**, *41*, (24), 8484-8490.
123. Miao, A. J.; Zhang, X. Y.; Luo, Z.; Chen, C. S.; Chin, W. C.; Santschi, P. H.; Quigg, A., Zinc oxide-engineered nanoparticles: Dissolution and toxicity to marine phytoplankton. *Environmental Toxicology and Chemistry* **2010**, *29*, (12), 2814-2822.

124. Borah, D.; Bera, M., Watershed-scale hydrologic and nonpoint-source pollution models: review of mathematical bases. *Transactions of the ASAE* **2003**, *46*, (6), 1553-1566.
125. Shanahan, P.; Harleman, D. R., Transport in lake water quality modeling. *Journal of Environmental Engineering* **1984**, *110*, (1), 42-57.
126. Pizzuto, J., Long-term storage and transport length scale of fine sediment: Analysis of a mercury release into a river. *Geophysical Research Letters* **2014**, *41*, (16), 5875-5882.
127. Tobiasson, J. E.; O'melia, C. R., Physicochemical aspects of particle removal in depth filtration. *Journal (American Water Works Association)* **1988**, 54-64.
128. Ginn, T. R.; Wood, B. D.; Nelson, K. E.; Scheibe, T. D.; Murphy, E. M.; Clement, T. P., Processes in microbial transport in the natural subsurface. *Advances in Water Resources* **2002**, *25*, (8), 1017-1042.
129. Zucca, A.; Marchisio, D. L.; Vanni, M.; Barresi, A. A., Validation of bivariate DQMOM for nanoparticle processes simulation. *AIChE Journal* **2007**, *53*, (4), 918-931.
130. Lister, J.; Smit, D.; Hounslow, M., Adjustable discretized population balance for growth and aggregation. *AIChE Journal* **1995**, *41*, (3), 591-603.
131. Marchisio, D. L.; Fox, R. O., Solution of population balance equations using the direct quadrature method of moments. *Journal of Aerosol Science* **2005**, *36*, (1), 43-73.
132. Riemer, N.; West, M.; Zaveri, R. A.; Easter, R. C., Simulating the evolution of soot mixing state with a particle-resolved aerosol model. *Journal of Geophysical Research: Atmospheres (1984–2012)* **2009**, *114*, (D9).
133. Quik, J. T.; van De Meent, D.; Koelmans, A. A., Simplifying modeling of nanoparticle aggregation–sedimentation behavior in environmental systems: A theoretical analysis. *Water research* **2014**, *62*, 193-201.
134. Vikas, V.; Hauck, C.; Wang, Z.; Fox, R. O., Radiation transport modeling using extended quadrature method of moments. *Journal of Computational Physics* **2013**, *246*, 221-241.
135. Rosner, D. E.; McGraw, R.; Tandon, P., Multivariate population balances via moment and Monte Carlo simulation methods: an important sol reaction engineering bivariate example and “mixed” moments for the estimation of deposition, scavenging, and optical properties for populations of nonspherical suspended particles. *Industrial & engineering chemistry research* **2003**, *42*, (12), 2699-2711.
136. Zhao, H.; Maisels, A.; Matsoukas, T.; Zheng, C., Analysis of four Monte Carlo methods for the solution of population balances in dispersed systems. *Powder Technology* **2007**, *173*, (1), 38-50.
137. Liu, H. H.; Surawanvijit, S.; Rallo, R.; Orkoulas, G.; Cohen, Y., Analysis of nanoparticle agglomeration in aqueous suspensions via constant-number Monte Carlo simulation. *Environ Sci Technol* **2011**, *45*, (21), 9284-9292.

138. Fan, R.; Marchisio, D. L.; Fox, R. O., Application of the direct quadrature method of moments to polydisperse gas–solid fluidized beds. *Powder technology* **2004**, *139*, (1), 7-20.
139. Tojo, C.; Blanco, M.; Lopez-Quintela, M., Preparation of nanoparticles in microemulsions: a Monte Carlo study of the influence of the synthesis variables. *Langmuir* **1997**, *13*, (17), 4527-4534.
140. Ethayaraja, M.; Dutta, K.; Muthukumaran, D.; Bandyopadhyaya, R., Nanoparticle formation in water-in-oil microemulsions: experiments, mechanism, and Monte Carlo simulation. *Langmuir* **2007**, *23*, (6), 3418-3423.
141. Mukherjee, D.; Leo, B. F.; Royce, S. G.; Porter, A. E.; Ryan, M. P.; Schwander, S.; Chung, K. F.; Tetley, T. D.; Zhang, J.; Georgopoulos, P. G., Modeling physicochemical interactions affecting in vitro cellular dosimetry of engineered nanomaterials: application to nanosilver. *Journal of Nanoparticle Research* **2014**, *16*, (10), 1-16.
142. McGraw, R., Description of aerosol dynamics by the quadrature method of moments. *Aerosol Science and Technology* **1997**, *27*, (2), 255-265.
143. Yu, M.; Lin, J.; Chan, T., Numerical simulation of nanoparticle synthesis in diffusion flame reactor. *Powder Technology* **2008**, *181*, (1), 9-20.
144. Talukdar, S. S.; Swihart, M. T., Aerosol dynamics modeling of silicon nanoparticle formation during silane pyrolysis: a comparison of three solution methods. *Journal of Aerosol Science* **2004**, *35*, (7), 889-908.
145. Fox, R. O.; Laurent, F.; Massot, M., Numerical simulation of spray coalescence in an Eulerian framework: direct quadrature method of moments and multi-fluid method. *Journal of Computational Physics* **2008**, *227*, (6), 3058-3088.
146. Hounslow, M.; Ryall, R.; Marshall, V., A discretized population balance for nucleation, growth, and aggregation. *AIChE Journal* **1988**, *34*, (11), 1821-1832.
147. Barton, L. E.; Therezien, M.; Auffan, M.; Bottero, J.-Y.; Wiesner, M. R., Theory and Methodology for Determining Nanoparticle Affinity for Heteroaggregation in Environmental Matrices Using Batch Measurements. *Environmental Engineering Science* **2014**, *31*, (7), 421-427.
148. Labille, J.; Harns, C.; Bottero, J.-Y.; Brant, J. A., Heteroaggregation of titanium dioxide nanoparticles with natural clay colloids. *Environ Sci Technol* **2015**, *49*, (11), 6608-6616.
149. Kostoglou, M.; Karabelas, A., Evaluation of numerical methods for simulating an evolving particle size distribution in growth processes. *Chemical Engineering Communications* **1995**, *136*, (1), 177-199.
150. Upadhyay, R.; Ezekoye, O., Treatment of size-dependent aerosol transport processes using quadrature based moment methods. *Journal of aerosol science* **2006**, *37*, (7), 799-819.
151. McGraw, R.; Wright, D. L., Chemically resolved aerosol dynamics for internal mixtures by the quadrature method of moments. *Journal of Aerosol Science* **2003**, *34*, (2), 189-209.

152. Yuan, C.; Fox, R. O., Conditional quadrature method of moments for kinetic equations. *Journal of Computational Physics* **2011**, *230*, (22), 8216-8246.
153. Massot, M.; Laurent, F.; Kah, D.; De Chaisemartin, S., A robust moment method for evaluation of the disappearance rate of evaporating sprays. *SIAM Journal on Applied Mathematics* **2010**, *70*, (8), 3203-3234.
154. Fox, R., Bivariate direct quadrature method of moments for coagulation and sintering of particle populations. *Journal of Aerosol Science* **2006**, *37*, (11), 1562-1580.
155. Williams, M., The time-dependent behavior of aerosols with growth and deposition. I. Without coagulation. *Journal of Colloid and Interface Science* **1983**, *93*, (1), 252-263.
156. Park, S.; Xiang, R.; Lee, K., Brownian coagulation of fractal agglomerates: Analytical solution using the log-normal size distribution assumption. *Journal of colloid and interface science* **2000**, *231*, (1), 129-135.
157. Dokoumetzidis, A.; Macheras, P., A century of dissolution research: from Noyes and Whitney to the biopharmaceutics classification system. *International journal of pharmaceutics* **2006**, *321*, (1), 1-11.
158. Borm, P.; Klaessig, F. C.; Landry, T. D.; Moudgil, B.; Pauluhn, J.; Thomas, K.; Trottier, R.; Wood, S., Research strategies for safety evaluation of nanomaterials, part V: role of dissolution in biological fate and effects of nanoscale particles. *Toxicological Sciences* **2006**, *90*, (1), 23-32.
159. Majedi, S. M.; Kelly, B. C.; Lee, H. K., Combined effects of water temperature and chemistry on the environmental fate and behavior of nanosized zinc oxide. *Science of The Total Environment* **2014**, *496*, 585-593.
160. Merkus, H. G., *Particle size measurements: fundamentals, practice, quality*. Springer Science & Business Media: **2009**.
161. Kostoglou, M.; Konstandopoulos, A. G., Evolution of aggregate size and fractal dimension during Brownian coagulation. *Journal of Aerosol Science* **2001**, *32*, (12), 1399-1420.
162. Jeldres, R. I.; Concha, F.; Toledo, P. G., Population balance modelling of particle flocculation with attention to aggregate restructuring and permeability. *Advances in Colloid and Interface Science* **2015**, *224*, 62-71.
163. Bähler, M. u. U.; Moussa, A. S.; Soos, M.; Morbidelli, M., Structure and kinetics of shear aggregation in turbulent flows. I. Early stage of aggregation. *Langmuir* **2010**, *26*, (16), 13142-13152.
164. Flesch, J. C.; Spicer, P. T.; Pratsinis, S. E., Laminar and turbulent shear-induced flocculation of fractal aggregates. *AIChE journal* **1999**, *45*, (5), 1114-1124.
165. Veerapaneni, S.; Wiesner, M. R., Hydrodynamics of fractal aggregates with radially varying permeability. *Journal of Colloid and Interface Science* **1996**, *177*, (1), 45-57.

166. Wong, S. W.; Leung, P. T.; Djurišić, A.; Leung, K. M., Toxicities of nano zinc oxide to five marine organisms: influences of aggregate size and ion solubility. *Analytical and bioanalytical chemistry* **2010**, *396*, (2), 609-618.
167. Seo, Y.; Brock, J., Distributions for moment simulation of aerosol evaporation. *Journal of aerosol science* **1990**, *21*, (4), 511-514.
168. Roache, P. J., Perspective: a method for uniform reporting of grid refinement studies. *Journal of Fluids Engineering* **1994**, *116*, (3), 405-413.
169. Adams, P. J.; Seinfeld, J. H., Predicting global aerosol size distributions in general circulation models. *Journal of Geophysical Research: Atmospheres (1984–2012)* **2002**, *107*, (D19), AAC 4-1-AAC 4-23.
170. Yoon, C.; McGraw, R., Representation of generally mixed multivariate aerosols by the quadrature method of moments: II. Aerosol dynamics. *Journal of aerosol science* **2004**, *35*, (5), 577-598.
171. Wright, D. L.; McGraw, R.; Rosner, D. E., Bivariate extension of the quadrature method of moments for modeling simultaneous coagulation and sintering of particle populations. *Journal of Colloid and Interface Science* **2001**, *236*, (2), 242-251.
172. Buffo, A.; Vanni, M.; Marchisio, D.; Fox, R. O., Multivariate quadrature-based moments methods for turbulent polydisperse gas-liquid systems. *International Journal of Multiphase Flow* **2013**, *50*, 41-57.
173. Salenbauch, S.; Cuoci, A.; Frassoldati, A.; Saggese, C.; Faravelli, T.; Hasse, C., Modeling soot formation in premixed flames using an Extended Conditional Quadrature Method of Moments. *Combustion and Flame* **2015**, *162*, (6), 2529-2543.
174. Baalousha, M., Aggregation and disaggregation of iron oxide nanoparticles: influence of particle concentration, pH and natural organic matter. *Science of the total Environment* **2009**, *407*, (6), 2093-2101.
175. Von der Kammer, F.; Ferguson, P. L.; Holden, P. A.; Masion, A.; Rogers, K. R.; Klaine, S. J.; Koelmans, A. A.; Horne, N.; Unrine, J. M., Analysis of engineered nanomaterials in complex matrices (environment and biota): general considerations and conceptual case studies. *Environmental Toxicology and Chemistry* **2012**, *31*, (1), 32-49.
176. Nowack, B.; Baalousha, M.; Bornhöft, N.; Chaudhry, Q.; Cornelis, G.; Cotterill, J.; Gondikas, A.; Hassellöv, M.; Lead, J.; Mitrano, D. M., Progress towards the validation of modeled environmental concentrations of engineered nanomaterials by analytical measurements. *Environmental Science: Nano* **2015**, *2*, (5), 421-428.
177. Justo-Hanani, R.; Dayan, T., European risk governance of nanotechnology: Explaining the emerging regulatory policy. *Research Policy* **2015**, *44*, (8), 1527-1536.
178. Beaudrie, C. E.; Kandlikar, M.; Satterfield, T., From cradle-to-grave at the nanoscale: gaps in US regulatory oversight along the nanomaterial life cycle. *Environ Sci Technol* **2013**, *47*, (11), 5524-5534.

179. Anderson, K.; Jackson, L. A., Why are US and EU policies toward GMOs so different? . *The Journal of Agrobiotechnology Management and Economics* **2004**, *6*, (3).
180. Justo-Hanani, R.; Dayan, T., Explaining Transatlantic Policy Divergence: The Role of Domestic Politics and Policy Styles in Nanotechnology Risk Regulation. *Global Environmental Politics* **2015**, *16*, (1), 79-98.
181. Giles, E. L.; Kuznesof, S.; Clark, B.; Hubbard, C.; Frewer, L. J., Consumer acceptance of and willingness to pay for food nanotechnology: a systematic review. *Journal of Nanoparticle Research* **2015**, *17*, (12), 1-26.
182. Beaudrie, C. E.; Satterfield, T.; Kandlikar, M.; Harthorn, B. H., Scientists versus regulators: precaution, novelty & regulatory oversight as predictors of perceived risks of engineered nanomaterials. *PLoS one* **2014**, *9*, (9), e106365.
183. Powell, M. C., New risk or old risk, high risk or no risk? How scientists' standpoints shape their nanotechnology risk frames. *Health, Risk & Society* **2007**, *9*, (2), 173-190.
184. Donaldson, K.; Poland, C. A., Nanotoxicity: challenging the myth of nano-specific toxicity. *Current opinion in biotechnology* **2013**, *24*, (4), 724-734.
185. Saleh, N. B.; Aich, N.; Plazas-Tuttle, J.; Lead, J. R.; Lowry, G. V., Research strategy to determine when novel nanohybrids pose unique environmental risks. *Environmental Science: Nano* **2015**, *2*, (1), 11-18.
186. Nel, A.; Xia, T.; Meng, H.; Wang, X.; Lin, S.; Ji, Z.; Zhang, H., Nanomaterial toxicity testing in the 21st century: use of a predictive toxicological approach and high-throughput screening. *Accounts of chemical research* **2012**, *46*, (3), 607-621.
187. Nel, A. E.; Nasser, E.; Godwin, H.; Avery, D.; Bahadori, T.; Bergeson, L.; Beryt, E.; Bonner, J. C.; Boverhof, D.; Carter, J., A multi-stakeholder perspective on the use of alternative test strategies for nanomaterial safety assessment. *ACS nano* **2013**, *7*, (8), 6422-6433.
188. Judy, J. D.; McNear Jr, D. H.; Chen, C.; Lewis, R. W.; Tsyusko, O. V.; Bertsch, P. M.; Rao, W.; Stegemeier, J.; Lowry, G. V.; McGrath, S. P., Nanomaterials in biosolids inhibit nodulation, shift microbial community composition, and result in increased metal uptake relative to bulk/dissolved metals. *Environ Sci Technol* **2015**, *49*, (14), 8751-8758.
189. US EPA. EPA Response to "Petition for Rulemaking Requesting EPA Regulate Nano-Silver Products as Pesticides." Office fo Chemical Safety and Pollution Prevention. **2015**.
190. US EPA. Control of Nanoscale Materials Under the Toxic Substances Control Act. <http://www.epa.gov/reviewing-new-chemicals-under-toxic-substances-control-act-tsca/control-nanoscale-materials-under>.
191. US FDA. "Guidance for Industry: Use of Nanomaterials in Food for Animals." August 14 **2015**.

192. Becker, S., Nanotechnology in the marketplace: how the nanotechnology industry views risk. *Journal of nanoparticle research* **2013**, *15*, (5), 1-13.
193. Westrich, J. T.; Berner, R. A., The role of sedimentary organic matter in bacterial sulfate reduction: The G model tested. *Limnology and Oceanography* **1984**, 236-249.
194. Berg, P.; Rysgaard, S.; Funch, P.; Sejr, M. K., Effects of bioturbation on solutes and solids in marine sediments. *Aquatic Microbial Ecology* **2001**, *26*, (1), 81-94.
195. Benjamin, M. M.; Leckie, J. O., Multiple-site adsorption of Cd, Cu, Zn, and Pb on amorphous iron oxyhydroxide. *Journal of Colloid and Interface Science* **1981**, *79*, (1), 209-221.
196. Roberts, M. H.; Vogelbein, M.; Richards, M. A.; Seivard, L.; De Lisle, P. F., Chemical and Toxicological Characterization of Tidal Freshwater Areas in the James River, Virginia Between Jordan Point and Richmond. Report to Virginia Department of Environmental Protection. **2002**.
197. OR DEQ *Aquatic Life Water Quality Criteria for Toxic Pollutants* (Table 30, Document D). Draft for Advisory Committee Review. State of Oregon Department of Environmental Quality: **2013**.
198. USEPA *Ambient water quality criteria for zinc--1987*. Rep No. EPA-440/5-87-003. Office of Water Regulations and Standards: Washington, DC., **1987**.
199. Hong, Y. S.; Kinney, K. A.; Reible, D. D., Acid volatile sulfides oxidation and metals (Mn, Zn) release upon sediment resuspension: Laboratory experiment and model development. *Environmental toxicology and chemistry* **2011**, *30*, (3), 564-575.
200. Hong, Y.; Reible, D. D., Modeling the Effect of pH and Salinity on Biogeochemical Reactions and Metal Behavior in Sediment. *Water, Air, & Soil Pollution* **2014**, *225*, (1), 1-20.
201. US EPA, Mid-Atlantic Integrated Assessment (MAIA) Estuaries 1997-1998. Summary Report. December 2002. Rep No. EPA/620/R-02/003. **2002**.
202. Metcalf & Eddy.; Tchobanoglous, G.; Burton, F. L.; Stensel, H. D., *Wastewater engineering: Treatment and reuse* 4ed.; McGraw-Hill: Boston, **2003**.
203. Cornelis, G.; DooletteMadeleine Thomas, C.; McLaughlin, M. J.; Kirby, J. K.; Beak, D. G.; Chittleborough, D., Retention and dissolution of engineered silver nanoparticles in natural soils. *Soil Science Society of America Journal* **2012**, *76*, (3), 891-902.
204. Amidon, G. L.; Lee, P. I.; Topp, E. M., *Transport processes in pharmaceutical systems*. CRC Press: **1999**.
205. Dette, H.; Studden, W., *The Theory of Canonical Moments with Applications in Statistics, Probability, and Analysis*. 1997. *Jon Wiley and Sons, New York* **1997**.
206. Shen, J.; Tang, T.; Wang, L.-L., *Spectral methods: algorithms, analysis and applications*. Springer Science & Business Media: **2011**.

Appendix A. Supplement to Chapter 2, the Sediment Model

A.1 Supporting Methods

A.1.1 Silver Ion Partitioning

The partitioning of the total silver ion concentration ($[Ag_T^+]$) between the dissolved form (Ag^+) and the two sorbed forms ($Ag\equiv POC$ and $Ag\equiv FeOOH$) is governed by the partitioning coefficients K_{OC} and K_{FeOOH} .

$$K_{OC} = \frac{[Ag\equiv POC]}{[Ag^+][\equiv POC]}$$

Equation A-1

$$K_{FeOOH} = \frac{[Ag\equiv FeOOH]}{[Ag^+][\equiv FeOOH]}$$

Equation A-2

where $[\equiv POC]$ and $[\equiv FeOOH]$ are the concentration of available binding sites on the organic carbon and iron oxyhydroxide, respectively.

From these and other principles of solid phase partitioning (see Di Toro *et al.*, 1996), the following equations can be derived.

$$[Ag\equiv POC] = \frac{K_{OC}[Ag^+]\sigma_{POC}[POC]}{1 + K_{OC}[Ag^+]}$$

Equation A-3

$$[Ag\equiv FeOOH] = \frac{K_{FeOOH}[Ag^+]\sigma_{FeOOH}[FeOOH]}{1 + K_{FeOOH}[Ag^+]}$$

Equation A-4

where σ_{FeOOH} and σ_{POC} represent the specific binding capacity of the sorbent, such that

$$\sigma_{POC} = \frac{[\equiv POC]_T}{[POC]}$$

Equation A-5

$$\sigma_{FeOOH} = \frac{[\equiv FeOOH]_T}{[FeOOH]}$$

Equation A-6

Here, $[\equiv FeOOH]_T$ and $[\equiv POC]_T$ represent the total concentration of binding sites (free and silver-bound).

It can be shown that the dissolved ion concentration is the solution for x in the cubic equation $q_3x^3 + q_2x^2 + q_1x + q_0 = 0$, where $x = [Ag^+]$.

$$\begin{aligned} q_3 &= K_{FeOOH}K_{OC}\phi \\ q_2 &= K_{FeOOH}K_{OC}(\phi-1)\rho([\equiv FeOOH]_T + [\equiv POC]_T) \\ &\quad - \phi(K_{FeOOH} + K_{OC}) + K_{FeOOH}K_{OC}[Ag_T^+] \\ q_1 &= K_{OC}(\phi-1)\rho([\equiv POC]_T) + K_{FeOOH}(\phi-1)\rho([\equiv FeOOH]_T) \\ &\quad + (K_{FeOOH} + K_{OC})[Ag_T^+] - \phi \\ q_0 &= [Ag_T^+] \end{aligned}$$

Equation A-7

A.1.2 Exponential Expanding Finite Difference Grid

The distance between volume elements i and $i+1$ in an exponentially expanding finite difference grid expands with overall distance from the top boundary according to the formula:

$$\Delta z_i = \Delta z e^{\beta(i-1)}$$

Equation A-8

where Δz is the thickness of the first volume element and $0 < \beta < 0.5$ is a constant. In our model, $\beta = 0.005$.

The following equations describe the distance between the top boundary (the sediment-water interface) and the inner and outer boundary of each grid volume, respectively.

$$z_i' = \Delta z \frac{e^{\beta(i-1)} - 1}{e^{\beta} - 1}$$

Equation A-9

$$z_i'' = \Delta z \frac{e^{\beta i} - 1}{e^{\beta} - 1}$$

Equation A-10

The location of the average concentration in each grid volume is described by the following equation:

$$\bar{z}_i = \Delta z \frac{e^{\beta(i-0.5)} - 1}{e^{\beta} - 1}$$

Equation A-11

Note that this point is not located exactly in the center of each volume element (Figure A-6). To correct for this, the non-uniform grid is mapped to a uniform grid by adjusting the mixing coefficients D_p and D_d (denoted here as the general term D). In this case, dimensionless diffusion coefficients at the upper and lower boundaries of each grid space are calculated as:

$$D'_i = \frac{D^*}{e^{2\beta(i-0.25)}} \quad i \geq 2$$

Equation A-12

$$D''_i = \frac{D^*}{e^{2\beta(i-0.75)}}$$

Equation A-13

$$D'_1 = D^* \frac{e^\beta - 1}{e^{0.5\beta} - 1}$$

Equation A-14

where $D^* = D\Delta t / \Delta x^2$ is simplifying notation used in the solution to the mass balance equation.

As a proof of concept, consider a species C_1 present entirely in either its dissolved or particulate form ($f_p=1$ or $f_d=1$) undergoing a single reaction that is first order with respect to two reactants. For a uniform grid, the fully implicit form of the solution to the mass balance equation can be expressed in its simplest form as:

$$C_1(i, n+1) = C_1(i, n) + \left\{ \begin{array}{l} D^* \{C_1(i+1, n+1) - C_1(i, n+1)\} \\ -D^* \{C_1(i, n+1) - C_1(i-1, n+1)\} \\ -\Delta t k C_1(i, n+1) C_2(i, n+1) \end{array} \right\}$$

Equation A-15

Note that, in our model, D 's are depth-dependent before implementation of the exponentially expanding grid.

For a non-uniform grid, taking into account changes in \bar{z} as well as changes in diffusion coefficients, the solution becomes

$$C_1(i, n+1) = C_1(i, n) + \Delta t \left\{ \begin{array}{l} \frac{D}{\Delta z_i} \left\{ \frac{C_1(i+1, n+1) - C_1(i, n+1)}{\bar{z}_{i+1} - \bar{z}_i} \right\} \\ - \frac{D}{\Delta z_i} \left\{ \frac{C_1(i, n+1) - C_1(i-1, n+1)}{\bar{z}_i - \bar{z}_{i-1}} \right\} \\ - k C_1(i, n+1) C_2(i, n+1) \end{array} \right\}$$

Equation A-16

Applying the equations above and simplifying, the solution takes the form:

$$C_1(i, n+1) = C_1(i, n) + \left\{ \begin{array}{l} D_i'' \{C_1(i+1, n+1) - C_1(i, n+1)\} \\ - D_i' \{C_1(i, n+1) - C_1(i-1, n+1)\} \\ - \Delta t k C_1(i, n+1) C_2(i, n+1) \end{array} \right\}$$

Equation A-17

which must be then solved for the unknown concentration at time step $n+1$, $C_1(i, n+1)$, using the quadratic equation.

A complete treatment of this approach is provided by Feldberg (1981).

A.2 Supporting Tables

Table A-1. Sediment model state variables^a

POC ₁	G ₁ carbon (most reactive)	g C/g-sed
POC ₂	G ₂ carbon (less reactive)	g C/g-sed
POC ₃	G ₃ carbon (unreactive on the timescale considered)	g C/g-sed
O ₂	Dissolved oxygen	g O ₂ /m ³
FeS	Iron sulfide	mol/m ³
FeOOH	Iron oxyhydroxide	mol/m ³
Ag ⁰	Elemental silver (associated with Ag NP)	mol/m ³
Ag ₂ S (NP)	Silver sulfide (coating particle surface)	mol/m ³
Ag ₂ S (free)	Silver sulfide (not coating particle surface)	mol/m ³
Ag _T ⁺	Dissolved (Ag ⁺) and sorbed (Ag≡POC, Ag≡FeOOH) silver	mol/m ³

^a The organic carbon concentration is divided into three fractions (f_{POC1} , f_{POC2} , f_{POC3} ; see Table 2-1), each having different reactivity, i.e. ability to be oxidized. This simplification is based on the G model first proposed by Westrich and Berner in 1984¹⁹³ and presents a reasonable first approximation of organic carbon diagenesis in sediments.⁸⁵ Note that Ag⁺ can bind to labile POC, which is included in the model despite not being able to oxidize.

Table A-2. Sediment model reaction equations and terms^a

Variable	Reaction	Equation
POC ₁	Loss by aerobic oxidation	$R_{POC_1,O_2} = -k_{POC_1,O_2} \theta_{POC_1,O_2}^{(T-20)} \frac{[O_2]}{[O_2] + K_{M,O_2}} [POC_1]$
	Loss by anaerobic oxidation	$R_{POC_1,SO_4} = -k_{POC_1,SO_4} \theta_{POC_1,SO_4}^{(T-20)} \frac{K_{M,O_2}}{[O_2] + K_{M,O_2}} [POC_1]$
POC ₂	Loss by aerobic oxidation	$R_{POC_2,O_2} = -k_{POC_2,O_2} \theta_{POC_2,O_2}^{(T-20)} \frac{[O_2]}{[O_2] + K_{M,O_2}} [POC_2]$
	Loss by anaerobic oxidation	$R_{POC_2,SO_4} = -k_{POC_2,SO_4} \theta_{POC_2,SO_4}^{(T-20)} \frac{K_{M,O_2}}{[O_2] + K_{M,O_2}} [POC_2]$
FeS	Gain by anaerobic oxidation of POC	$-a_{FeS,POC} (R_{POC_1,SO_4} + R_{POC_2,SO_4})$
	Loss by oxidation	$R_{FeS,O_2} = -k_{FeS,O_2} \theta_{FeS,O_2}^{(T-20)} [FeS][O_2]$
	Loss by displacement	$a_{FeS,Ag^+} R_{Disp}$
FeOOH	Gain by oxidation of FeS	$-R_{FeS,O_2}$
Ag ⁰	Loss by oxidation	$R_{Ag^0,O_2} = -k_{Ag^0,O_2} \theta_{Ag^0,O_2} [Ag^0][O_2]$
	Loss by sulfidation	$R_{sulf} = -k_{sulf} [Ag^0][FeS][O_2]$
Ag ₂ S (NP)	Gain by sulfidation	$-a_{Ag_2S,Ag^0} R_{sulf}$
	Loss by oxidation	$R_{Ag_2S_{NP},O_2} = -k_{Ag_2S,O_2} \theta_{Ag_2S,O_2}^{(T-20)} [Ag_2S(NP)][O_2]$
Ag ₂ S (free)	Gain by displacement	$-a_{Ag_2S,Ag^+} R_{Disp}$
	Loss by oxidation	$R_{Ag_2S_{free},O_2} = -k_{Ag_2S,O_2} \theta_{Ag_2S,O_2}^{(T-20)} [Ag_2S(free)][O_2]$
Ag ⁺	Gain by oxidation of Ag ⁰	$-R_{Ag^0,O_2}$
	Gain by oxidation of Ag ₂ S (NP)	$-a_{Ag^+,Ag_2S} R_{Ag_2S_{NP},O_2}$
	Gain by oxidation of Ag ₂ S (free)	$-a_{Ag^+,Ag_2S} R_{Ag_2S_{free},O_2}$
	Loss by displacement	$R_{Disp} = -k_{Disp} \{f_{d,Ag^+}(z,t)[Ag_T^+]\} [FeS]$
O ₂	Loss by oxidation of POC ₁	$a_{O_2,POC} R_{POC_1,O_2}$
	Loss by oxidation of POC ₂	$a_{O_2,POC} R_{POC_2,O_2}$
	Loss by oxidation of Ag ₂ S (NP)	$a_{O_2,Ag_2S} R_{Ag_2S_{NP},O_2}$
	Loss by oxidation of Ag ₂ S (free)	$a_{O_2,Ag_2S} R_{Ag_2S_{free},O_2}$
	Loss by oxidation of Ag ⁰	$a_{O_2,Ag^0} R_{Ag^0,O_2}$
	Loss by sulfidation	$a_{O_2,Ag_2S} R_{sulf}$
	Loss by oxidation of FeS	$a_{O_2,FeS} R_{FeS,O_2}$

^a Reaction equations are of the general form $R_j = k_j \theta_j^{(T-20)} [C_1][C_2]$, where k_j is the reaction rate constant, θ_j is the Arrhenius temperature coefficient, T is the temperature in degrees Celsius, and $[C_1]$ and $[C_2]$ are the concentrations of the reactants. Each reaction is represented by a single R_j ; stoichiometric coefficients, denoted $a_{1,2}$, relate R_j to all reactants and products for that equation.

Table A-3. Justification of model parameter values in Table 2-1 ^a

Parameter	
<p>General note on Arrhenius temperature coefficients, θ: A range of 1.08-1.15 reflects the variation in temperature dependence reported by Di Toro (2001)²⁴ throughout the text. We assumed the nominal values assumed by Di Toro et al. (1996)⁶⁰ [as reported in Di Toro (2001)] in the cadmium sediment model on which this work is based (referred to below as “the Cd model”). The temperature dependence of Ag⁰ and Ag₂S oxidation (θ_{Ag^0, O_2} and θ_{Ag_2S, O_2}) was assumed to equal θ_{FeS} and θ_{CdS} from the Cd model.</p>	
<p>General note on organic carbon fractions 1, 2, and 3 and associated oxidation rates: Ranges were based on Table 12.1 and 12.2 of Di Toro (2001), pp. 253-254 (data pooled from 9 sources).</p>	
ϕ	Range: See Figure 4.9, p.130 (observed ϕ values pooled from 10 sources)
k_ϕ	Nominal value: Determined by calibration
ρ	Range: See text, p. 4 Nominal value: As in the Cd model
D_d	Range: Table 2.1, p.42 provides an average diffusion coefficient of 1.22(±0.52) cm ² /d. Note that this does not reflect the full natural variability in D_d ; Berg et al. (2001) report that bioturbation by sediment-dwelling fauna may double solute transport. ¹⁹⁴ In contrast, tortuosity will decrease apparent mixing rates. ⁸⁰ Nominal value: As in the Cd model
D_p	Range: Min to max values in Table 1, p.1245 (observed values from >30 tracer studies). Note unit conversion. Nominal value: Determined by calibration
z_{D_p}	Range: Min to max values in Table 1, p. 1245 (for mixing depth L ; observed values from >30 tracer studies) Nominal value: Represents the reported worldwide mean mixing depth of 9.8 ± 4.5 cm
f_{POC_1}	Range: See general note above on organic carbon fraction and associated oxidation rates Nominal value: As in the Cd model
f_{POC_2}	Nominal value: As in the Cd model
k_{POC_1, O_2}	Nominal value: Rates assumed in the Cd model were an order of magnitude higher than suggested by Table 12.2 of Di Toro (2001) Here, rate constants were chosen to be twice the rate of anaerobic decay.
k_{POC_2, O_2}	Nominal value: Rates chosen to be twice the rate of anaerobic decay
k_{POC_1, SO_4}	Nominal value: Average value reported in Table 12.2 of Di Toro (2001)
k_{POC_2, SO_4}	Nominal value: Average value reported in Table 12.2 of Di Toro (2001)
K_{M, O_2}	Nominal value: As in the Cd model
k_{FeS, O_2}	Range: See Table 21.3, p. 523 and text, p. 521 of Di Toro (2001) (note unit conversions) Nominal case: Calibrated values determined for the Cd model (Experiments 1 and 2) were used. The calibrated value based on the field experiment data (Experiment 3) was not used because it resulted in an unexpectedly low value due to oligotrophic lake conditions.
$k_{Ag^0, O_2} (S/Ag = 0)$	Range: Upper bound is the oxidation rate constant reported for 4.8 nm unsulfidized Ag NPs by Liu et al. (2010) adjusted for oxygen-dependence assuming 8 mg/L DO (“air-saturated”). Lower bound is the lowest oxidation rate estimated from the equilibrium solubility of Ag NPs reported by Ma et al. (2012) assuming 8.6 mg/L DO (reported). Other estimates from the literature cited fall within this range. Nominal value: Determined by calibration
c_{pass}	Experimental data (Figure 6 from Levard et al. (2011) for Ag NP oxidation; Table S3 from Kaegi et al. (2011) for Ag NP sulfidation) was fit to the passivation equation (Equation 2-13, this work). Values from the fits ranged from 14-21 for Ag NP sulfidation and 24 for Ag NP oxidation. A representative value of 20 was selected for the nominal case. Although Ag NP oxidation and Ag NP sulfidation both exhibit surface passivation due to the formation of an Ag ₂ S shell, the sulfidation rate decreased so rapidly within the first time step after dosing (for a dose of 100% Ag ⁰ Ag NPs) that truncation error due to the finite difference approximation significantly overestimated the rate of both processes (i.e., led to numerical instability). Decreasing the timestep to 3 min greatly increased the model runtime but had no significant effect on model output. The rate of sulfidation was therefore modeled instead as a constant, as described below.
k_{sulf}	Nominal: Liu et al. (2011) report a long-term “second stage” rate of sulfidation of 0.00016 (mM Ag) ⁻¹ min ⁻¹ for 30 nm Ag NPs at pH 11. We assume the DO and sulfide concentrations reported in the text (DO≈0.25 mM, S ²⁻ ≈1 mM) and a speed-up factor of 3.5 from pH 11 to pH 7 (the factor found by the authors for the “first stage” rate). Range: We assume a lower bound of zero for the sulfidation of a predominantly Ag ₂ S Ag NP sulfidizing by a dissolution-precipitation mechanism (in agreement with the lower bound on Ag ₂ S oxidation of 0). The upper bound is based on an observation (not reported) that Ag NPs sulfidized fully within 4 months during the mesocosm study (t _{95%,sulf} =120 days).
<p>Caution should be used if extrapolating these values to other studies. Sulfidation is more accurately represented as a passivation process (e.g., see Equation 2-13 in this work). Experimental fits of Table S3 data by Kaegi et al. (2013) assuming the reported DO and sulfide concentrations (Adjusted R² values of 0.66-0.96)</p>	

	suggest the <i>initial</i> rate of sulfidation (e.g., for a fully unsulfidized particle) may be much faster, on the order of 0.041–0.0086 (mmol S ²⁻ /m ³)(mg O ₂ /m ³)d ⁻¹ for 10 nm Ag NPs and 0.0016–0.00058 (mmol S ²⁻ /m ³)(mg O ₂ /m ³)d ⁻¹ for a mix of 10-100 nm Ag NPs. 100 nm Ag NPs showed effectively no sulfidation over 24 hours, revealing the strong size-dependence of the sulfidation rate.
$f_{Ag^0,init}$	Nominal value: Percent sulfidation reported by Kaegi et al. (2011) for Ag NPs in the effluent of a pilot WWTP Derivation: With a forward difference approximation, we see that a first-order rate constant k can be described in terms of the concentration of the reacting chemical species:
	$\frac{-\partial C}{\partial t} = kC \Rightarrow k \approx -\frac{1}{C} \frac{C_{t+\Delta t} - C_t}{\Delta t}$
k_{Ag_2S,O_2}	Multiplying numerator and denominator by a constant volume (and noting that Ag mass is conserved), we see that the rate constant provided by Di Toro et al. (1998)—expressed as (rate of Ag released/mass of Ag present) in units of mg Ag/(g Ag-day)—approximates the more familiar first-order rate constant in units day ⁻¹ with a simple unit conversion (mg Ag to g Ag). Oxidation rates in Figure 5 (Di Toro et al., 2001) were estimated using the software tool GraphClick (http://www.arizona-software.ch/graphclick/) for the spiked sediment (nominal case) and the sediment core (upper bound). A second-order rate constant was approximated assuming [O ₂]=8000 mg/L for the values reported. A lower bound of zero was chosen based on the insolubility of Ag ₂ S.
k_{Disp}	Nominal value: Chosen to match the calibrated value for the three experiments reported in Table 21.3 p. 523. Good agreement was found during calibration to mesocosm data.
$J_{POC,max}$	Range: POC deposition fluxes were assumed based on observed sedimentation accumulation fluxes and an assumed organic carbon content of settling solids of 20%. Gasiowski et al. (2008) provide mean sedimentation rates for five shallow lakes in Poland. Rose et al. (2011) provide sediment accumulation rates for 207 European lakes (incl. mountain lakes and lowland lakes). For a eutrophic lake in China, Wan et al. (2005) estimate J _{POC} =160 to 440 mg/m ² -d (note unit conversion) between 1970-1997 with an average value of 270 mg/m ² -d, suggesting that 300 is an acceptable upper limit for a nutrient-enriched system. It was necessary to limit the range of values considered in the model to ensure numerical stability.
$\log K_{OC}$	Range: See Table 4, p. 3-11 for log(K _d) values for Ag ⁺ partitioning between pore water and sediments (2.1-5.8). We assume all Ag ⁺ is bound to organic carbon and L.O.I. is 1.83% (value observed in mesocosms, transformed assuming $f_{oc} \approx L.O.I./2$). From Schwarzenbach et al. (2002), p. 292: ³⁹
	$K_{OC} = \frac{K_d}{f_{oc}}$
σ_{OC}	Nominal value: Assumed in the Cd model (for cadmium). Benjamin and Leckie (1981) suggest Cd ²⁺ and Ag ⁺ exhibit comparably low critical adsorption densities Γ^* for sorption to amorphous iron oxyhydroxides, ¹⁹⁵ revealing the two species have similar preferences for a small number of preferred binding sites (Γ^* values ordered by metal species: Pb < Ag < Cd < Cu < Hg < Zn < Co). Ag ⁺ adsorption to mineral species is relatively poorly studied.
K_{FeOOH}	Nominal value: As in the Cd model (for cadmium). Overlapping K _d values were reported for cadmium (mean of 3.3, range of 0.5-7.3) and silver (mean of 3.6, range of 2.1-5.8) by Allison and Allison (2005). ⁹¹ Ag ⁺ and Cd ²⁺ preferentially sorb to POC, suggesting this assumption has little impact on the system response.
σ_{FeOOH}	Nominal value: As in the Cd model (for cadmium). See notes for S_{OC} and K_{FeOOH}
π_{FeS}	Range: Calibrated values calculated in the Cd model (Table 21.3, p. 523). Natural variability in this parameter is likely larger than reported. Nominal value: Calibrated values determined for the Cd model (Experiments 1 and 2)

Initial and Boundary Conditions

$O_2(z=0)$	Range: Values represent a range of conditions at the sediment-water interface, from anoxic to oxic Range: See text, p. 15 of Di Toro et al. (2001) for observed values for coastal marine and harbor sediments.
$f_{oc}(t=0)$	Range agrees with Schwarzenbach et al. (2002) (Figure 9.7, p.292). ³⁹ Field studies report L.O.I. values from 1 to 70%. Assuming $f_{om}=2*f_{oc}$ suggests a wider range for f_{oc} of 0.5-0.35, but we do not think it is equally representative. Nominal: Selected from Figure 1.9, p. 16 of Di Toro et al. (2001) to represent a “typical” (non-eutrophic, non-oligotrophic) system.
$FeS(t=0)$	Range: See Figure 1.9, p.16 of Di Toro (2001) for AVS (acid volatile sulfide) concentrations for coastal marine and harbor sediments. FeS is a proxy for AVS in this model. Nominal value: Selected from Figure 1.9 to represent a “typical” (non-eutrophic, non-oligotrophic) system.

^aListed tables, figures, and page numbers correspond with sources cited in Table 1-1

Table A-4. Sediment model elasticities, ranked from highest to lowest

Symbol	Parameter	Elasticity ^d
θ_{Ag_2S,O_2}	Correction for Arrhenius temperature dependence	16
θ_{D_p}	Correction for Arrhenius temperature dependence	-16
θ_{D_d}	Correction for Arrhenius temperature dependence	9.5
θ_{FeS,O_2}	Correction for Arrhenius temperature dependence	-2.3
θ_{Ag^0,O_2}	Correction for Arrhenius temperature dependence	2.2
ϕ_0	Sediment porosity at the sediment-water interface	2.2
$O_2(z=0)$	Oxygen concentration at the interface	1.9
$f_{oc}(t=0)$	Fraction of organic carbon in sediment (at t=0)	-1.3
ρ	Sediment density	-1.1
θ_{POC_2,SO_4}	Correction for Arrhenius temperature dependence	-1.0
k_{Ag_2S,O_2}	Rate of oxidation of sulfur in Ag ₂ S	0.99
D_p	Particle mixing velocity	-0.87
σ_{OC}	Sorption capacity for POC	-0.86
K_{OC}	Partition coefficient to POC	-0.86
D_d	Molecular diffusion coefficient	0.61
θ_{POC_1,SO_4}	Correction for Arrhenius temperature dependence	-0.58
$J_{POC,max}$	Flux of organic carbon from the overlying water	-0.46
f_{POC_1}	Fraction of POC in G ₁ reactivity class	-0.37
$k\phi$	Rate of decrease in sediment porosity with depth	-0.36
π_{FeS}	Partition coefficient for FeS: [FeS _p]/[FeS _d]	0.20
f_{POC_2}	Fraction of POC in G ₂ reactivity class	-0.16
k_{FeS,O_2}	Rate of oxidation of FeS to form FeOOH	-0.13
θ_{POC_2,O_2}	Correction for Arrhenius temperature dependence	0.083
k_{POC_2,SO_4}	Rate of anaerobic oxidation of G ₂ carbon	-0.060
z_{D_p}	e-folding depth of particle mixing	-0.053
k_{POC_1,O_2}	Rate of aerobic oxidation of G ₁ carbon	0.032
k_{POC_1,SO_4}	Rate of anaerobic oxidation of G ₁ carbon	-0.028
k_{POC_2,O_2}	Rate of aerobic oxidation of G ₂ carbon	0.027
k_{Disp}	Rate of displacement reaction	-0.021
θ_{POC_1,O_2}	Correction for Arrhenius temperature dependence	-0.0040
$f_{Ag^0,init}$	Percent elemental silver by mass in input dose of NPs	0.0038
$k_{Ag^0,O_2} (S/Ag = 0)$	Initial rate of nanoparticle dissolution	0.0034
σ_{FeOOH}	Sorption capacity for FeOOH	-0.00093
K_{M,O_2}	Half saturation constant for oxidation using O ₂	0.00089
K_{FeOOH}	Partition coefficient to FeOOH	-0.00081
FeS(t=0)	Sediment iron sulfide (AVS) concentration (at t=0)	-0.00057
k_{sulf}	Rate of Ag NP sulfidation	0.00039
ϕ_{pass}	Rate of decrease in Ag ⁰ oxidation rate as a function of S/Ag	0.00

^a The measured output is the peak concentration of dissolved silver ion in the sediment within six months of dosing. Green shading indicates parameters for which uncertainty stems predominantly from natural variability. Blue shading indicates parameters for which uncertainty stems predominantly from experimental uncertainty in constants or coefficients. The most influential parameters appear to be the temperature coefficients of the reaction and mixing rates. However, the effect of temperature sensitivity on model results is limited by relatively small uncertainty surrounding the

true values of these parameters (Table 1-1). System parameters such as porosity at the interface, ϕ_0 , the initial organic carbon composition of the sediment, $f_{oc}(t=0)$, sediment density, ρ , and the oxygen concentration at the sediment-water interface, $O_2(z=0)$, reveal the importance of sediment redox conditions in determining the extent of nanoparticle oxidation. The most influential reaction rate constants and coefficients are the rate of oxidation of sulfur in silver sulfide, k_{Ag_2S,O_2} , and parameters describing the partitioning behavior of silver ion (the silver ion-organic carbon partition coefficient, K_{OC} , and the sorption capacity for organic carbon, σ_{OC}).

A.3 Supporting Figures

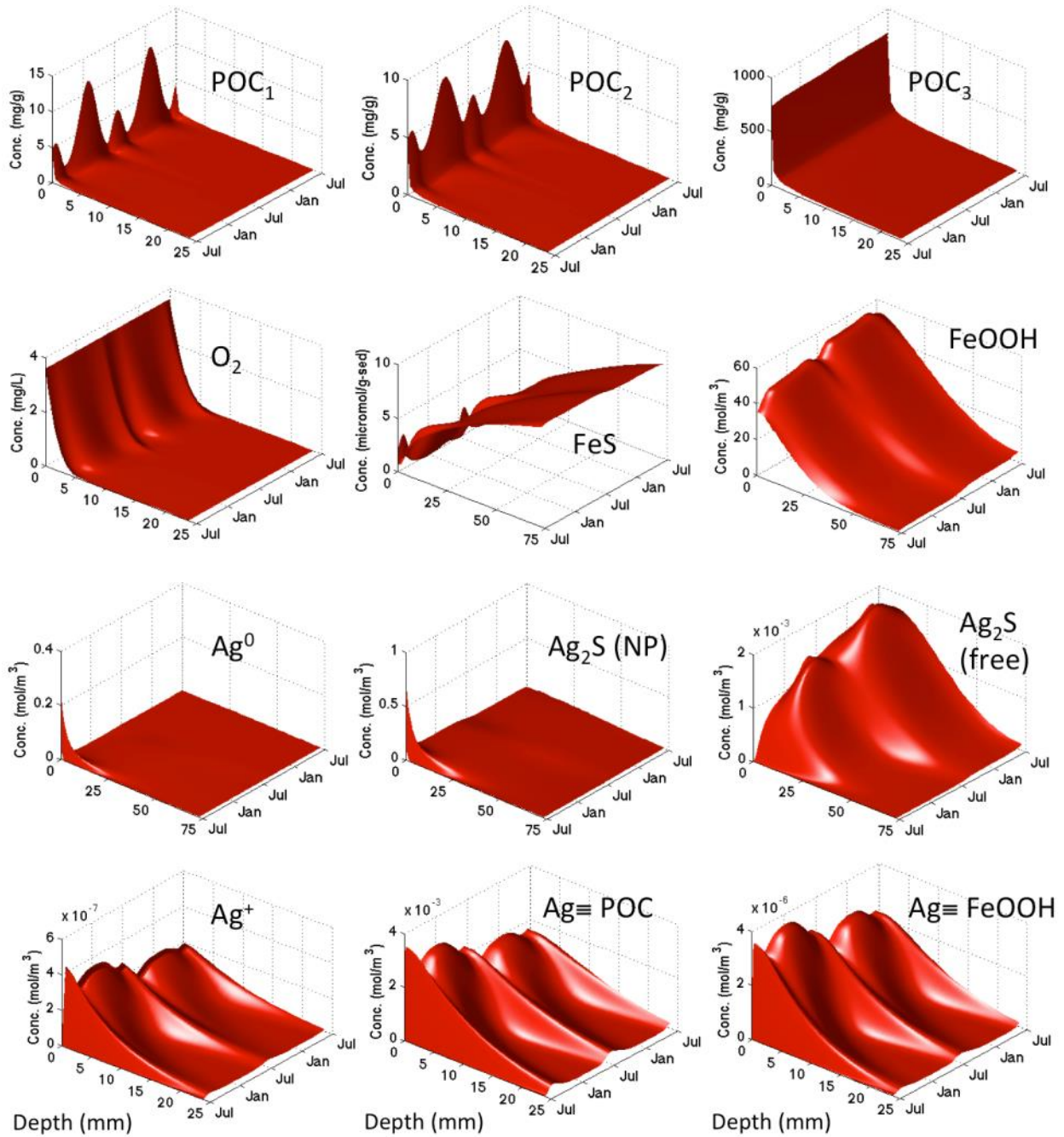


Figure A-1. Change in depth profiles of all state variables over time after a pulse input of 2.9 g of 85% sulfidized nanoparticles. Temperature and oxygen availability are anticyclical (oxygen concentration peaks in winter). Since high oxygen concentrations (winter) and high temperatures (summer) both facilitate oxidation, complex periodic behavior results. Natural systems are expected to exhibit more complexity and variability.

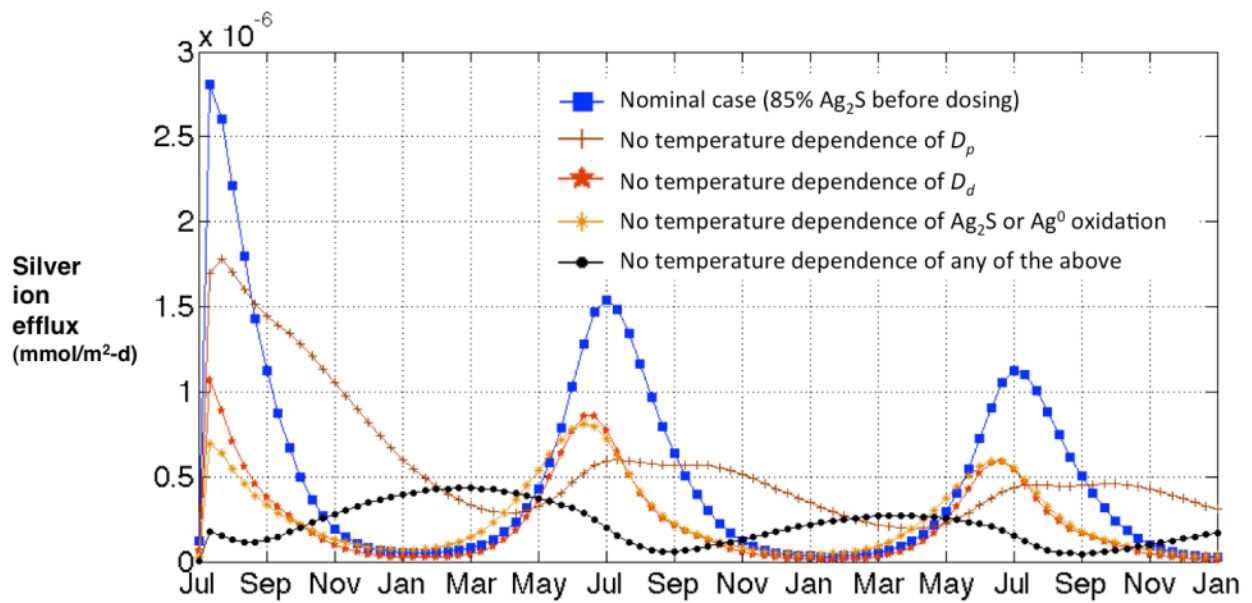


Figure A-2. Sensitivity of seasonal trends in Ag⁺ efflux to temperature coefficients and oxygen availability. In spite of increased oxygen penetration in winter, the model predicts Ag⁺ will peak in summer due to increased oxidation and increased mixing (particulate and dissolved).

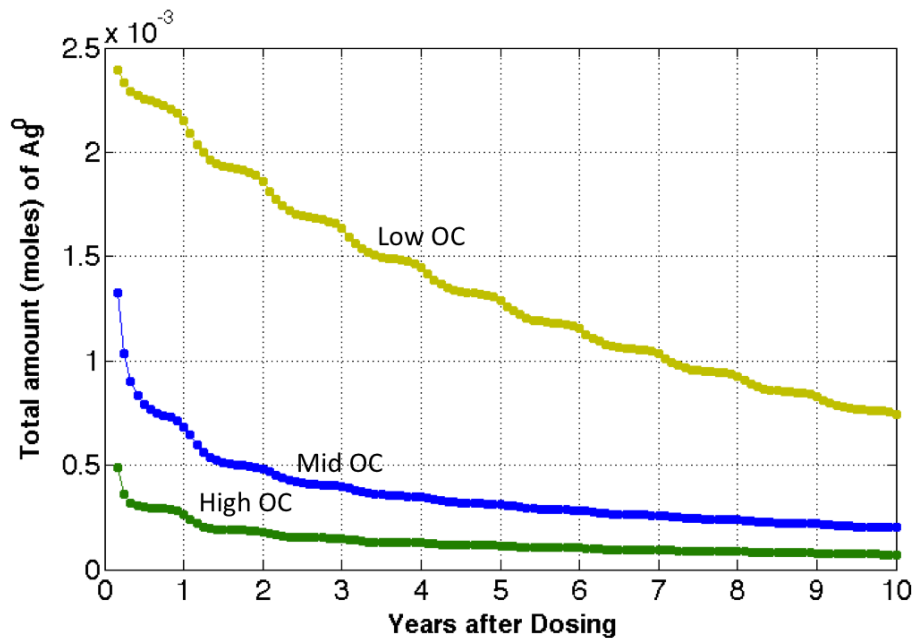


Figure A-3. Loss of Ag^0 over time for a pulse input of 85% sulfidized Ag NPs. Sulfidation of Ag NPs during nanoparticle influx leads to lower peak amounts of Ag^0 in environments with more organic carbon (higher sulfide availability). The cores are affected by two loss processes simultaneously (Ag NP oxidation leading to Ag^+ release and sulfidation). The overall loss rate decreases over time, and the first order decay exhibited by the entire transformed Ag NP (Figure 2-4) is not observed.

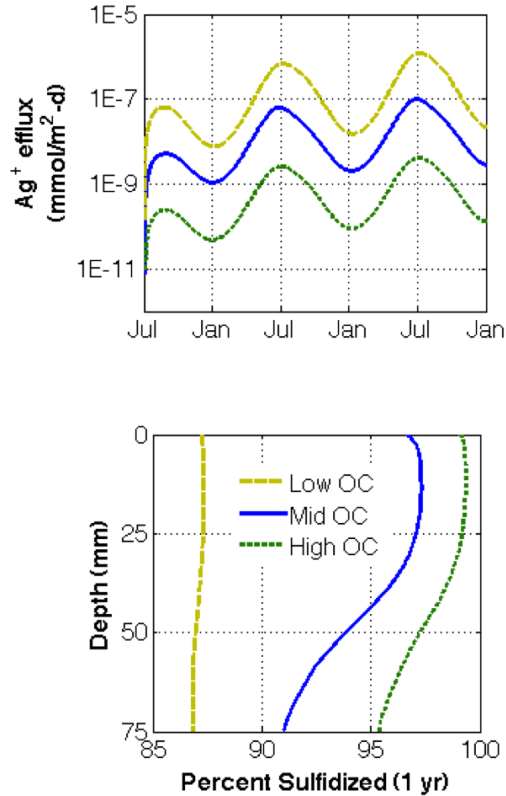


Figure A-4. System response to constant inputs of 85% sulfidized nanoparticles ($0.03 \text{ mg Ag/m}^2\text{-d}$). Above: Silver ion efflux vs. time after dosing for low ($J_{\text{POC,max}}=50 \text{ mg/m}^2\text{-d}$, $f_{\text{oc}}=0.001$), middle ($J_{\text{POC,max}}=150$, $f_{\text{oc}}=0.02$), and high ($J_{\text{POC,max}}=300$, $f_{\text{oc}}=0.15$) levels of organic carbon (OC). Silver ion release will be maximized in low carbon environments, which have lower oxygen demand and thus correspond to oxic conditions. The accumulation of Ag NPs over time leads to an increase in the formation and efflux of silver ion from the sediment. Below: Percent sulfidation within a year of dosing increases as the organic carbon content of the sediments increases, since sulfide is formed by the degradation of organic carbon in the anoxic sediments.

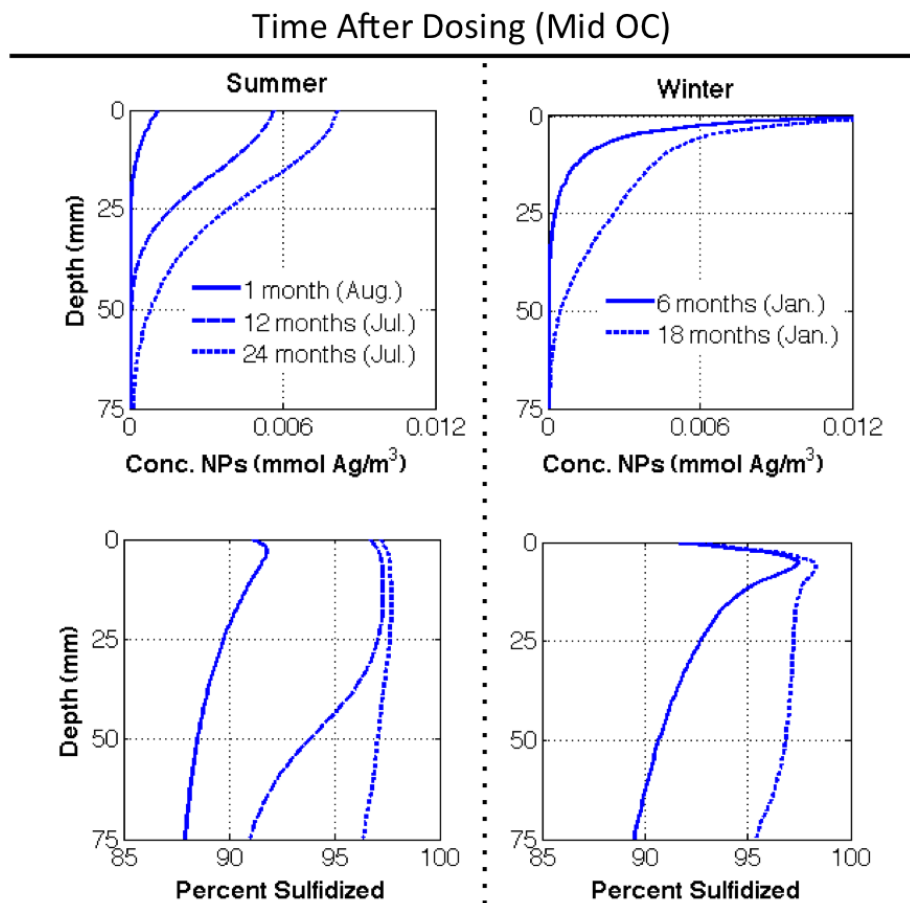


Figure A-5. Change in concentration profile (above) and sulfidation (below) of Ag NPs in the sediment over time. Results are shown only for the mid OC case ($J_{\text{POC,max}}=150$, $f_{\text{oc}}=0.02$). For the concentration profiles, only minor differences are observed between this case and the low/high OC cases because the Ag NPs are highly persistent. Ag NP concentrations at the interface decrease in summer as a result of increased particle mixing and increased oxidation, which results from higher temperatures. Liu et al. (2011) have shown that Ag NP sulfidation requires a strong oxidant, which we assume is dissolved oxygen. Thus there is a greater extent of sulfidation near the oxic sediment-water interface than occurs at depth. The extent of sulfidation drops at the interface, reflecting the less sulfidized nature of the incoming particles.

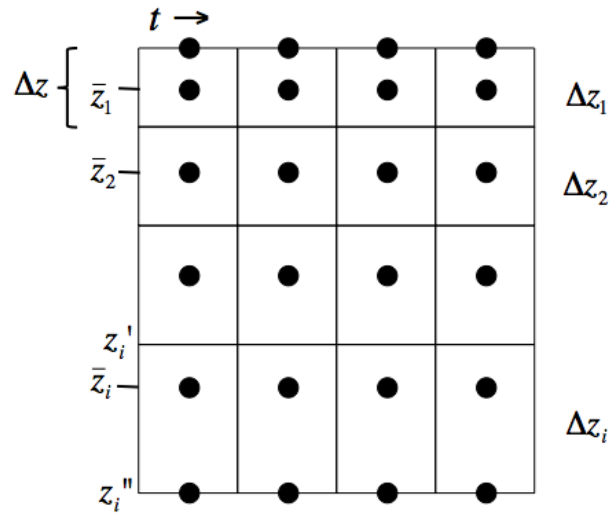


Figure A-6. A diagram of the exponentially expanding grid space showing key variables.

Appendix B. Supplement to Chapter 3, the Watershed Model

B.1 Supporting Methods

As referenced in the main text, the following sections provide more details on (1) the model used to estimate ZnO NP speciation in wastewater effluent, (2) the calibration of the suspended sediment concentrations in the river model, (3) the equations WASP7 uses to transport NPs as a function of stream flow, and (4) the selection of regulatory thresholds displayed in Figure 3-4.

B.1.1 Aeration tank model

ZnO NPs dissolve so rapidly that it is unlikely they will enter the environment in their pristine form. To predict the speciation of ZnO NPs in sewage treatment plant effluent, a simple box model receiving a constant (arbitrary) load of pristine NPs was built in WASP7 to mimic the speciation of ZnO NPs that remain in aqueous suspension in a sewage treatment plant aeration tank. Modeled processes included inflow/outflow, ZnO NP dissolution, metal ion reaction with sulfides, and metal ion sorption/complexation with suspended solids. System parameters are provided in Table B-4. Reaction rates and sorption constants were the same as those used in the river model (Table B-2, described in the main text).

Table B-5 shows the model output (percent speciation of the ZnO NPs) for a range of possible system conditions and rate constants. This model is very sensitive to assumptions. However, the river model is not sensitive to the output from this aeration tank model. Figure B-8 shows ZnO speciation in the water column and sediment bed for a scenario where the dissolution rate was set to its lowest possible value (Table B-2) in both the aeration tank model and the river simulation. In this scenario, 85% of the original ZnO NPs remain untransformed in wastewater effluent. The Zn speciation in the river and sediment bed for this scenario is similar to that in Figure 3-2.

B.1.2 TSS calibration

Predicted total suspended sediment (TSS) concentrations were compared to observations from a USGS station downstream in the basin (Figure B-9, top panel). Because monthly averages are more representative than daily estimates, the 761 observations available for that station were averaged for every month and compared to simulated monthly average TSS. Data were used if there were at least 10 observations in a given month.

The Nash-Sutcliffe Efficiency (NSE), which measures the divergence of simulated values from a 1:1 fit with observations, was used to calibrate the model. Other tests determined bias (PBIAS) and the ratio of the error to the standard deviation (RSR).¹¹⁵ The bottom panel of Figure B-9 compares observed monthly averages to simulated values. The table inset in this panel provides the values of the calibration metrics. The calibration exhibits low bias and is satisfactory (although not exceptional) with respect to RSR and NSE. An NSE between zero and one (optimal) indicates the model would outperform a simpler model that used the mean observed value.¹¹⁵

B.1.3 WASP7 sediment transport equations

Here, we briefly introduce the equations that WASP7 uses to describe sediment resuspension and deposition as a function of geographic and temporal variation in stream flow. These equations are currently being updated for WASP8 and were documented with the help of Dr. Robert Ambrose (WASP development team, pers. corr.). Any mistakes are our own.

Sediment transport in streams is driven by the shear stress of the stream flow at the sediment-water interface. For a given stream reach at a given time step, the boundary shear stress, τ_b (N/m²) is calculated as

$$\tau_b = \frac{0.24\rho u^2}{8\log^2(12H/k_s)}$$

where ρ is the water density (kg/m^3), u is the segment water velocity (m/s), H is the segment water depth (m), and k_s is the equivalent roughness height (m), which is the larger of either $0.01*H$ or $3*D_{50}$, the median sediment diameter for the bed. Transport processes will occur when τ_b exceeds (resuspension) or drops below (deposition) the critical shear stress for that process, which is either calculated from the diameter of the sediment particles, parameterized using site-specific data, or determined by calibration.

Rates of sediment mass transfer between the water column and the surface sediments (in units of g/s) are calculated at each time step as $W*C*A_{bed}$, where W is the sediment transport velocity in m/s, C is the sediment concentration in the water column (for deposition) or surface sediments (for resuspension), and A_{bed} is the cross-sectional area of the bed. A_{bed} is specified for each stream reach based on its initial geometry (length and width). Equations for sediment transport velocities (W) are described below for each process. Sediment burial rates are simply the net effect of resuspension and deposition processes at each time step.

For our model, values for all sediment parameters (bolded below) are provided in Table B-2.

B.1.3.1 Deposition

The maximum settling rate for sediment particles in a given size class i is their gravitational settling velocity, $W_{s,i}$ (m/s), which is defined by Stokes' equation. This equation can be expressed in the (less common) form

$$W_{s,i} = \frac{R_{d,i}}{18} \sqrt{g_i' D_i}$$

where $R_{d,i} = \frac{D_i \sqrt{g_i' D_i}}{\nu}$ is the sediment particle densimetric Reynolds number (we will use this later),

$$g_i' = g \left(\frac{\rho_{s,i}}{\rho} - 1 \right),$$

D_i is the particle diameter, g is acceleration due to gravity (9.81 m/s²), $\rho_{s,i}$ is

the sediment particle density (kg/m³), and ν is the dynamic viscosity of water (m²/s).

The boundary shear stress, τ_b , provides a barrier to deposition as described in the following equation. $\alpha_{D,i}$ the probability that the particles deposit once they reach the sediment bed, is assumed to decrease at a rate $n_{dep,i}$ (the shear stress exponent for deposition, which defaults to 1) from the lower critical shear stress, $\tau_{c,lo,i}$ (under which deposition always occurs) to the upper critical shear stress, $\tau_{c,hi,i}$ (above which no deposition occurs).

$$W_{D,i} = W_{s,i} \alpha_{D,i} \text{ where } \begin{cases} \alpha_{D,i} = 1, \tau_b \leq \tau_{c,lo,i} \\ \alpha_{D,i} = \left(\frac{\tau_{c,hi,i} - \tau_b}{\tau_{c,hi,i} - \tau_{c,lo,i}} \right)^{n_{dep,i}}, \tau_{c,lo,i} < \tau_b < \tau_{c,hi,i} \\ \alpha_{D,i} = 0, \tau_b \geq \tau_{c,hi,i} \end{cases}$$

B.1.3.2 Non-cohesive resuspension

The sand fraction (greater than 0.1 mm in diameter) always acts "non-cohesively." If the silt/fines fraction (less than 0.1 mm) in the sediments remains below the critical cohesive sediment fraction, the silts/fines fraction also acts non-cohesively.

In WASP7, non-cohesive resuspension is treated as a two-step process in which sediment first erodes into a boundary layer, then entrains from the boundary layer. The size-dependent resuspension velocity, $W_{RS,i}$ is thus only a fraction, $f_{RS,i}$ of the erosion velocity, $W_{E,i}$ (m/s), where $W_{E,i} = E_{noncoh,i} * W_{s,i}$ and $E_{noncoh,i}$ is the dimensionless net erosion rate for non-cohesive sediments. Note that this implies that E_{noncoh} is the ratio of the speed at which sediments erode

into the boundary layer and the speed at which they settle back onto to the sediment bed from the boundary layer.

$$W_{RS,i} = f_{RS,i} W_{E,i} \text{ where } \begin{cases} f_{RS,i} = 0, \tau_b < \tau_{CRS,i} \\ f_{RS,i} = \frac{\ln\left(\frac{u_*}{W_{S,i}}\right) - \ln\left(\frac{u_{*CRS,i}}{W_{S,i}}\right)}{\ln(4) - \ln\left(\frac{u_{*CRS,i}}{W_{S,i}}\right)}, \tau_b \geq \tau_{CRS,i} \\ f_{RS,i} = 1, u_* \geq 4W_{S,i} \end{cases}$$

Here, u_* is the shear velocity in m/s ($\sqrt{\tau_b/\rho}$) and $u_{*CRS,i}$ is the critical shear velocity for resuspension ($\sqrt{\tau_{CRS,i}/\rho}$). The critical shear stress for resuspension is expressed separately for each resuspending size fraction of sediment as

$$\tau_{CRS,i} = \frac{0.1(400W_{S,i})^2}{\rho/1000} D_i \left[\frac{\left(\frac{\rho_{s,i}}{\rho} - 1 \right) g}{v^2} \right]^{-2/3}$$

The critical shear stress for non-cohesive erosion, $\tau_{CE,i}$ (N/m²), is calculated internally for each sediment size fraction (rather than determined by calibration).

$$\tau_{CE,i} = (0.22R_{d,i}^{-0.6} + 0.06 * 10^{(-7.7R_{d,i}^{-0.6})}) \rho g D_i$$

The non-dimensional rate of non-cohesive sediment erosion is defined as

$$E_{noncoh,i} = 0.015 \frac{D_i}{k_s} \tau_{*,i}^{1.5} R_{d,i}^{-0.2} \text{ where } \begin{cases} \tau_{*,i} = 0, \tau_b < \tau_{CE,i} \\ \tau_{*,i} = \left(\frac{\tau_b}{\tau_{CE,i}} - 1 \right), \tau_b \geq \tau_{CE,i} \end{cases}$$

The exponent, 1.5, is the recommended and default value for the shear stress exponent for non-cohesive resuspension listed as a parameter in Table B-2.

B.1.3.3 Cohesive resuspension

When the silts/fines fraction exceeds the critical cohesive sediment fraction, which is generally the case in the model presented here, the resuspension velocity (m/s) is defined as

$$W_{coh} = \frac{f_{coh} M \tau_*^{n_{coh}}}{C_{coh}} \text{ where } \begin{cases} \tau_* = 0, \tau_b < \tau_{cE,noncoh} \\ \tau_* = \left(\frac{\tau_b}{\tau_{cE,noncoh}} - 1 \right), \tau_b \geq \tau_{cE,noncoh} \end{cases}$$

where M is the shear stress multiplier ($\text{g}/\text{m}^2\text{-s}$), f_{coh} is the fraction of cohesive sediment in the surface sediment layer, C_{coh} is the concentration of cohesive sediments (g/m^3) in the surface sediment layer, n_{coh} is the shear stress exponent, and $\tau_{cE,noncoh}$ is the critical shear stress for cohesive resuspension.

B.1.4 Regulatory thresholds

The USEPA and individual U.S. states provide a range of chronic and acute regulatory criteria for metals in freshwater and saltwater. In freshwater, USEPA acute Criteria Maximum Concentrations (CMCs) for zinc and silver and chronic Criteria Continuous Concentrations (CCCs) for zinc are expressed as a function of water hardness. Sediment quality guidelines are reported either as "effects range-median" (adverse effects in 50% of reviewed data) or "effects range-low" (adverse effects in 10% of reviewed data).¹⁹⁶ Figure 3-4 shows only the lowest (most conservative) of the relevant thresholds: the Ag surface water threshold is the proposed freshwater CCC for Oregon¹⁹⁷ (the USEPA does not have a chronic toxicity threshold for Ag), the Zn surface water threshold is the USEPA freshwater CCC for a hardness of 50 mg/L,¹⁹⁸ and the Ag and Zn thresholds are the lowest ERLs for each reported by Roberts et al.¹⁹⁶ Note that these thresholds are generally applied only to the acid soluble metal fraction, and therefore their comparison in this work to the total metal concentration is also conservative.

B.2 Supporting Tables

Table B-1. Land uses modeled in the Phase 5.3.2 Chesapeake Bay Watershed Model. Land uses that receive biosolids are highlighted. See the WSM documentation for details.⁶² NM = nutrient managed, CSS = combined sewer system.

	Land Use Code	Description	Category
1	hom	Conventional tillage, no manure	Row crops
2	nho	Conventional tillage, no manure (NM)	
3	hwm	Conventional tillage with manure	
4	nhi	Conventional tillage with manure (NM)	
5	lwm	Conservation tillage with manure	
6	nlo	Conservation tillage with manure (NM)	
7	hyw	Hay, fertilized	Hay
8	nhy	Hay, fertilized (NM)	
9	alf	Alfalfa	
10	nal	Alfalfa (NM)	Pasture
11	hyo	Hay, not fertilized	
12	pas	Pasture	
13	npa	Pasture (NM)	
14	trp	Degraded riparian pasture	
15	afo	Animal feeding operations	
16	cfo	Confined animal feeding operations	Forest
17	for	Forest, woodlots, wooded areas	
18	hvf	Harvested forest	
19	cid	Impervious developed (CSS)	
20	rid	Impervious developed, regulated	Impervious urban
21	nid	Impervious developed, non-regulated	
22	cpd	Pervious developed (CSS)	
23	rpd	Pervious developed, regulated	Pervious urban
24	npd	Pervious developed, non-regulated	
25	ccn	Construction (CSS)	
26	rcn	Regulated construction	
27	cex	Extractive (CSS)	Extractive (active and abandoned mines)
28	rex	Extractive, regulated	
29	nex	Extractive, non-regulated	
30	urs	Nursery	

Table B-2. James River Basin model inputs (constants only)

Parameter	Value	Units	Expected Range	Source (notes)	
Ag Loadings					
Biosolids concentration	1.6	mg Ag/kg d.w.	1.4 x 10 ⁻⁶ -5.9	<i>Nominal:</i> Mode for U.S. ³³ The more recent estimates for the U.S. by Hendren ¹⁰⁸ et al are somewhat lower for effluent and are far lower for biosolids. We note that estimates for Europe are in approximate agreement with these values, although the most recent European estimates ⁶ could not be used because they ignored any mass lost due to transformations during sewage treatment. <i>Range:</i> Lower bound ¹⁰⁸ to upper bound ³³	
Effluent concentration	21	ng Ag/L	0.133-236	<i>Nominal:</i> Mode for U.S. ³³ <i>Range:</i> ¹⁰⁸	
Ag Transformation Rates					
Dissolution rate, silver sulfide/ sulfidized Ag NP ^{*†}	2.1 x 10 ⁻⁶	L/mg-d	0 - 4.5x10 ⁻⁴	<i>Nominal:</i> Rate of oxidative dissolution for an 85% sulfidized Ag NP for a calibrated sediment model ⁶¹ <i>Range:</i> Lower and upper bounds for Ag ₂ S oxidation ^{61, 88}	
Sulfidation rate, Ag ⁺ ^{*‡}	10	g/μmol-d		Set high (very rapid) ^{24, 199}	
Log K _d , Ag ⁺	4.9	L/kg	1.5-6.3	⁹¹	
Zn Loadings					
Biosolids concentration	23	mg ZnO/kg d.w.	10-120	<i>Nominal:</i> Mode for U.S. ³³ <i>Range:</i> Lower bound from ⁴ ; Upper bound is for the San Francisco Bay area. ³⁴	
Effluent concentration	300	ng ZnO/L	220-12,000	<i>Nominal:</i> Mode for U.S. ³³ <i>Range:</i> Lower bound from ³³ ; Upper bound is for the San Francisco Bay area. ³⁴	
Zn Transformation Rates					
Dissolution rate, ZnO NP [*]	72	/d	1-220	<i>Nominal:</i> 1 hour to equilibrium concentration (t _{95%}) assuming exponential decay <i>Range:</i> estimated from time to equilibrium concentration observed in ZnO NP solubility studies (20 minutes to 72 hours). ^{20, 22, 120-123} Upper bound agrees with highest rate observed by David et al. (2012) ¹²¹ ; 0.17 min ⁻¹	
Dissolution rate, ZnS ^{*†}	0.025	L/mg-d	0.0038-0.05	^{199, 200}	
Sulfidation rate, Zn ²⁺ ^{*‡}	10	g/μmol-d		Set high (very rapid) ^{24, 199}	
Log K _d , Zn ²⁺	4.8	L/kg	1.5-6.9	⁹¹	
System Parameters (WASP7)					
Pore water exchange rate [*]	7.5 x 10 ⁻⁵	m ² /d	7 x 10 ⁻⁵ to 1.7 x 10 ⁻⁴	²⁴	
Particle diameter for silts/fines	6.35	μm	4-63	<i>Nominal:</i> Chesapeake Bay Program (CBP) Phase 5 Model <i>Range:</i> WASP	
Particle diameter for sand	127	μm	63-2,000	<i>Nominal:</i> CBP Phase 5 Model <i>Range:</i> WASP	
Sulfide concentration, water column and surface sediments	6x10 ⁻⁵	mg/L	1 x 10 ⁻⁶ to 5 x 10 ⁻³	⁷²	
Sulfide concentration in deep sediments	100	μmole/g	0.01-100	<i>Nominal:</i> Set to upper end of range (anoxic conditions) <i>Range:</i> ²⁴	
Sediment Transport Parameters (All nominal values determined by calibration, all ranges provided in WASP)					
Critical cohesive sediment fraction		0.5	--	0-1	Critical cohesive sediment fraction
Critical shear stress for erosion of cohesive bed		0.5	N/m ²	0.5-8	Critical shear stress for erosion of cohesive bed
Shear stress multiplier for cohesive resuspension		0.12	g/m ² -s	0.01-100	Shear stress multiplier for cohesive resuspension
Shear stress exponent for cohesive resuspension		2.5	--	1.6-4	Shear stress exponent for cohesive resuspension
Shear stress exponent for noncohesive resuspension		1.5	--	1.5-2	Shear stress exponent for noncohesive resusp.
Lower critical shear stress for silt		0.05	N/m ²	0-0.05	Lower critical shear stress for silt
Upper critical shear stress for silt		0.2	N/m ²	0.01-0.2	Upper critical shear stress for silt
Shear stress exponent for silt deposition		2.0	--	0-2.0	Shear stress exponent for silt deposition
Lower critical shear stress for sand		0.2	N/m ²	0-0.2	Lower critical shear stress for sand;
Upper critical shear stress for sand		0.2	N/m ²	0.01-0.2	Upper critical shear stress for sand
Shear stress exponent for sand deposition		2.0	--	0-2.0	Shear stress exponent for sand deposition
Bed compaction time step (dynamic bed volume)		1	d	--	Bed compaction time step (dynamic bed volume)

*temperature dependent

†oxygen dependent

‡sulfide dependent

Table B-3. Maximum of simulated 95th percentile total metal concentrations originating from NP sources over all segments (averaged over 2 cm sediment depth) compared to observed metal concentrations (from all sources) in the James River basin downstream of the modeled region.^{196, 201}

	Water Column (ng Me/L)		Surface Sediments (ng Me/g-dry)	
	PEC	Observation	PEC	Observation
Total Ag	1.55	(≤ 100)	9.78	(100 to 750)
Total Zn	43.6	(3,600 to 16,000)	41.9	(500 to 230,000)

Table B-4. Aeration tank model system parameters and outputs

Parameter	Value	Source (notes)
Basin volume	1500 m ³	4 h hydraulic retention time (3-5 h expected for CMAS reactor) ²⁰²
Flow rate	0.1 m ³ /s	Range from 0 to > 4.38 m ³ /s ²⁰²
Wastewater temperature	15°C	Typical wastewater temperature ²⁰²
Sulfide concentration	0.1 mg/L	0.001 to 10 mg/L expected for WWTPs ⁷²
Oxygen concentration	2 mg/L	Value maintained in aeration basins ²⁰²
TSS concentration	3000 mg/L	1500-4000 mg/L expected for a CMAS reactor ²⁰²

Table B-5. ZnO speciation in the aeration tank model for different scenarios. Percent ZnS is low in all cases because of low sulfide concentrations and high TSS, since Zn²⁺ is assumed to preferentially sorb to mixed liquor suspended solids. Percentages do not sum to 100% because of rounding.

Scenario	% ZnO NP	% Zn ²⁺	% ZnS
Nominal ("best guess")	7.4	92.6	0.001
Highest ZnO dissolution rate	2.6	97.5	0.001
Lowest ZnO dissolution rate	85.2	14.8	0.0002
Highest sulfide concentration	7.4	92.5	0.1
Lowest sulfide concentration	7.4	92.6	1E-05

B.3 Supporting Figures

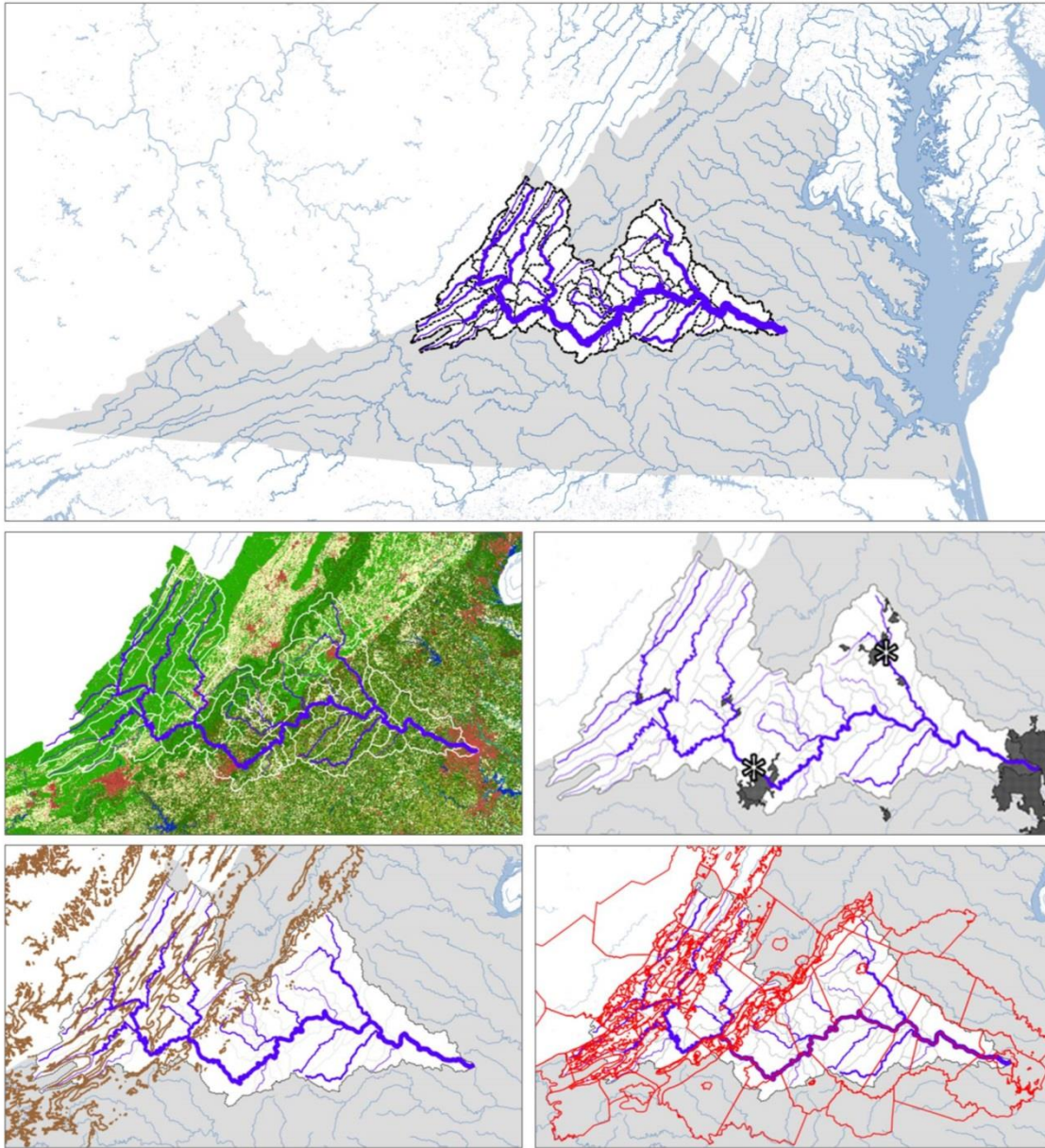


Figure B-1. GIS plots of the James River Basin. Above: Segmentation of the river network (68 segments) and location with respect to Virginia and the Chesapeake Bay (stream segment width proportional to flow rate). Middle left: NLDAS land cover data showing the division of the modeled region into forest (green, 80%), agriculture (yellow, 13%), and urban regions (red, 5%). Middle right: Dark grey regions indicate urban centers, including three cities (Lynchburg, Charlottesville, and Richmond). Asterisks indicate the inflow points of the segments containing the two largest point source dischargers, which contribute 68% of the effluent load (among 82 dischargers). Lower left: Elevation plot showing the Ridge and Valley physiographic province. Lower right: Land segments (county lines) overlaid on river segments.

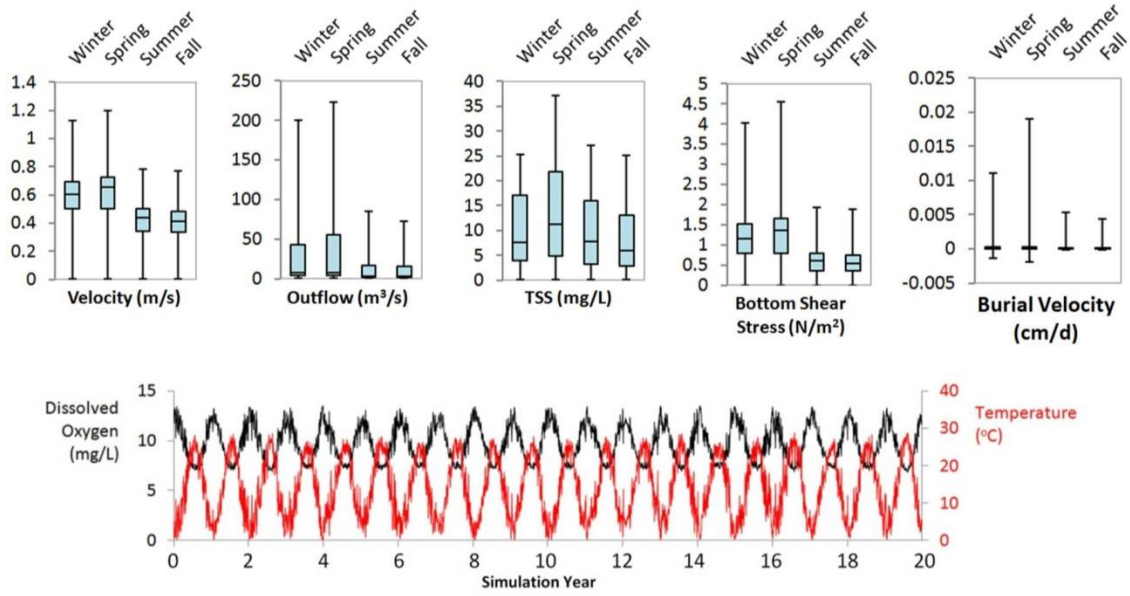


Figure B-2. Seasonal trends in key environmental drivers (system conditions). Parameters which varied spatially are shown as boxplots, which represent the statistical distribution across the river segments (min, Q1, median, Q3, max). High bottom shear stress corresponds with high sediment resuspension from the river bed and low sediment deposition. Negative burial velocities indicate scour. Temperature and oxygen (below) were varied across time but held at average values across segments.

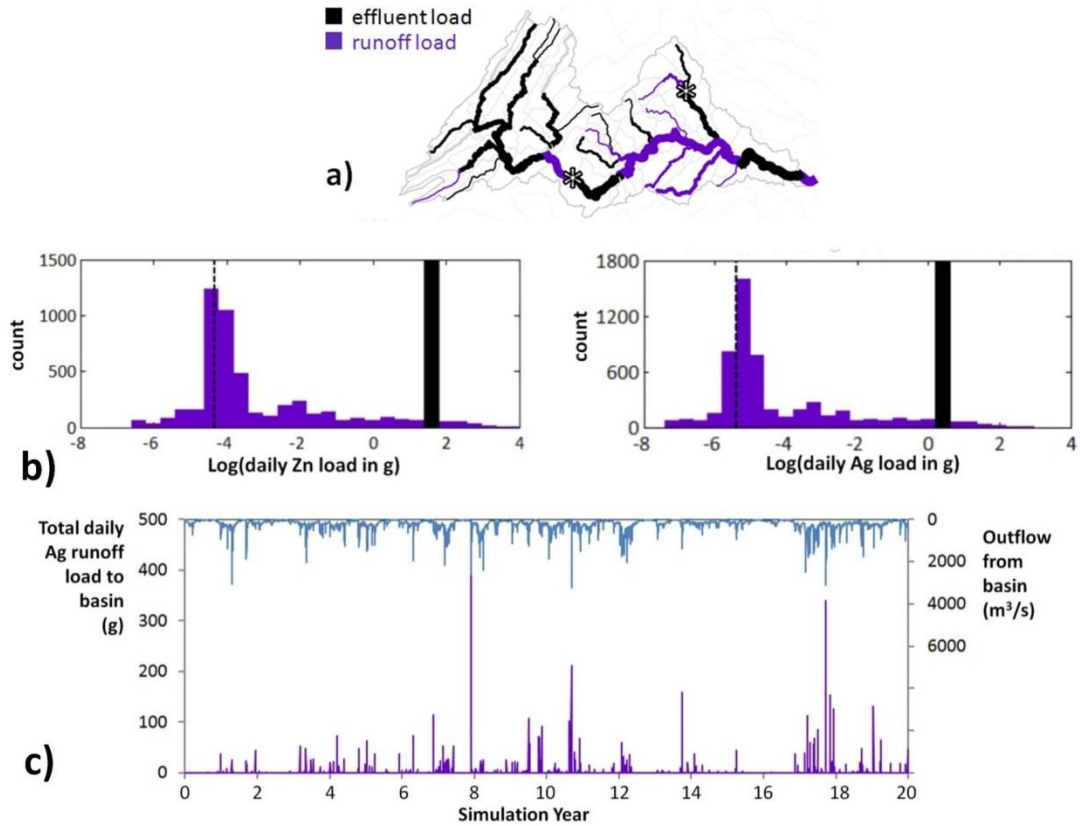


Figure B-3. Non-point versus point sources of NP stream loads in the James River Basin model. a) GIS plot of the modeled region showing river segments in which the predicted total runoff load over the course of the simulation (kg Ag or Zn) exceeds the effluent load (purple) or vice versa (black). Two stream segments receive 68% of effluent loads and are marked with asterisks at the inflow points. b) Comparison of the distribution of the log daily zinc (left) and silver (right) runoff load over all segments (purple) to the time-invariant log of the basin-wide daily effluent load (black) reveals that daily runoff loads are highly skewed and can exceed effluent loads. c) Daily runoff load of Ag basin-wide over time (purple) compared to the basin outflow (secondary axis, blue). Note the reversed secondary axis (right). Peaks in runoff loads occur during high flow events in the watershed. Zn results are proportional (not shown).

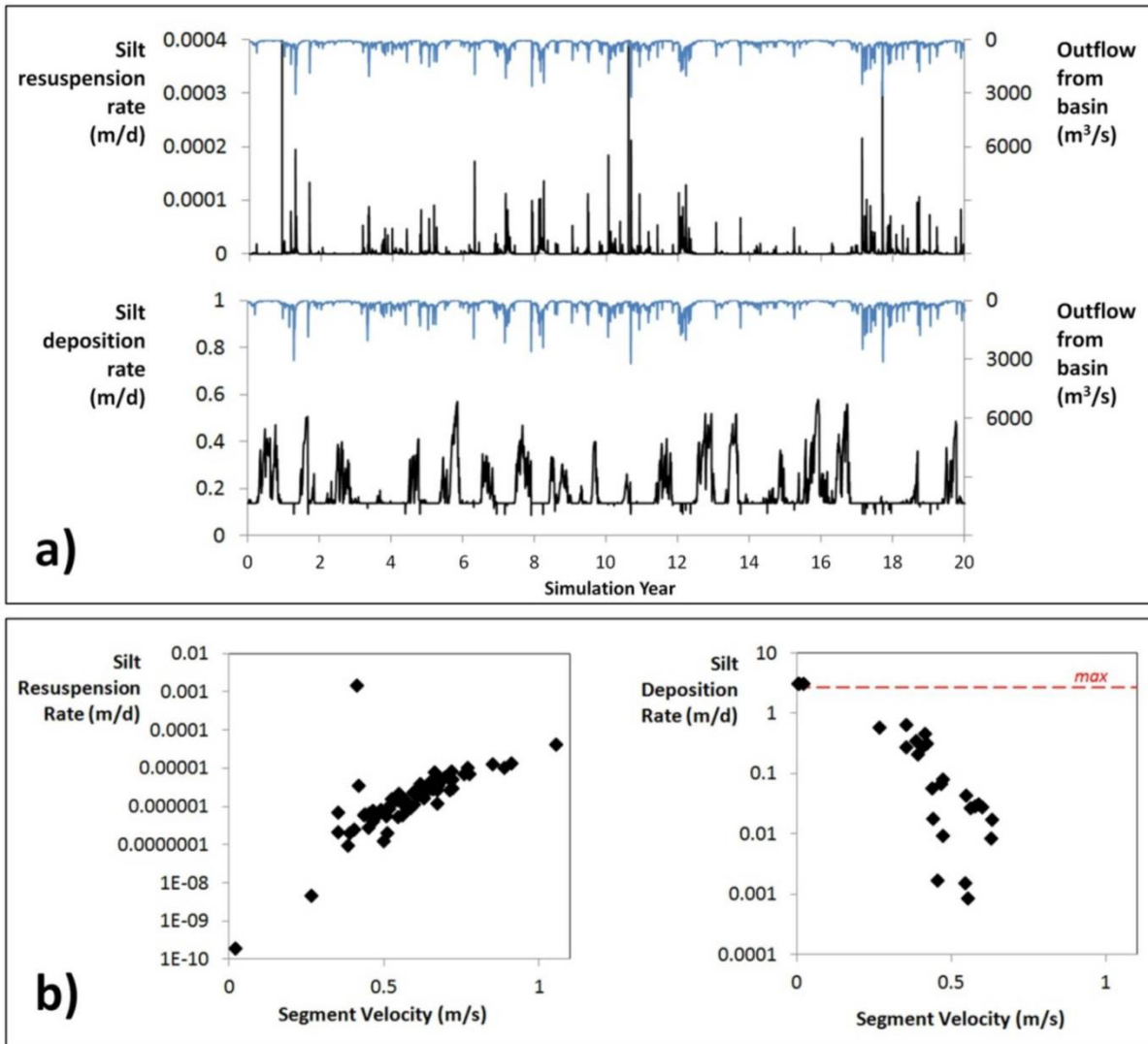


Figure B-4. Resuspension and deposition rate predictions in the James River Basin model. a) Spatially averaged resuspension and deposition rates for silt (the NP-carrying sediment fraction) at each time step. Rates are plotted against the basin outflow (secondary axis, reversed, in blue) to show that, as expected, resuspension rates are highest, and deposition is lowest, when stream flows are high. Deposition is near-constant in some segments, resulting in the flat non-negative baseline observed in the lower plot. b) Temporally averaged resuspension and deposition rates plotted as a function of the average stream reach velocity show the same trends observed in (a). Sand transport also exhibits these trends. The segment represented by the potential outlier in the resuspension plot in (b) is atypically shallow, and the high average resuspension rate appears to result from a handful of specific resuspension events on days when the segment depth is exceptionally low. Deposition rates never exceed the maximum deposition rate specified by the Stokes Law, 2.7 m/d (red dashed line). Omitting the outlier segment to reduce upward bias, the spatially and temporally averaged silt resuspension rate (used in the alternative sediment transport scenario in Figure 3-3) is 3.3×10^{-6} m/d (1.2 mm/year).

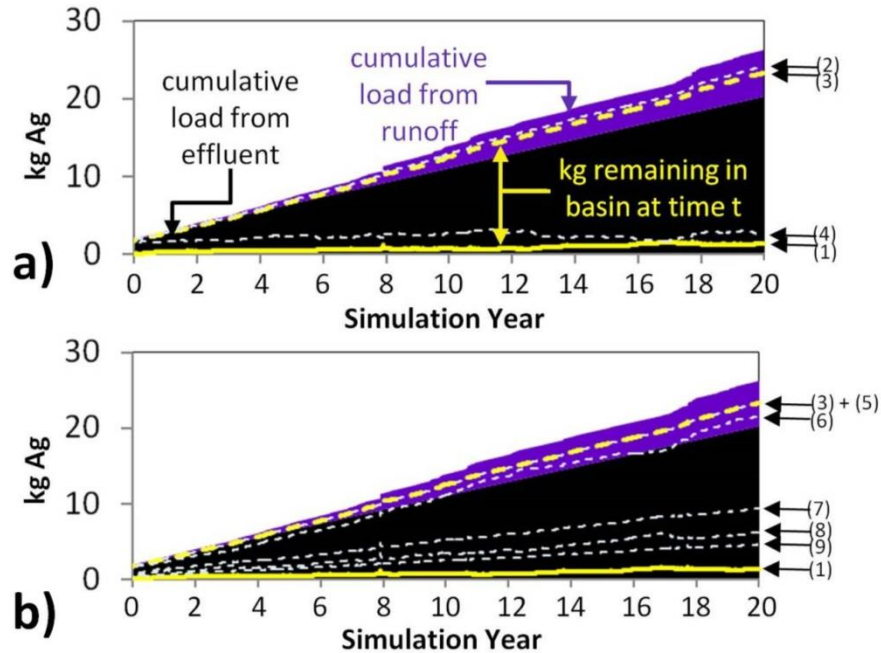


Figure B-5. Sensitivity of the accumulation of Ag NPs in the river and sediments over time to spatiotemporal variability in sediment resuspension and deposition rates. a) Comparison of (1) the "base case" (Figure 3-3) to alternative sediment transport scenarios in which there is no barrier to deposition (gravitational settling according to Stokes' Law) and the spatiotemporally invariant resuspension rate is set at (2) a value used in previous NP fate models, 0.1 mm/yr,^{8, 11, 41} (3) the average value predicted in the base case, used in Figure 3-3 (1.2 mm/year), and (4) the maximum value suggested previously for cohesive sediments in rivers based on model calibrations (30 mm/year).¹¹³ b) Comparison of the influence of spatial and temporal variability in sediment transport rates on model predictions. In scenarios (3), (5), and (6), deposition is maximized as shown in (a). In scenarios (7), (8), and (9), the average deposition rate predicted in the base case was used in place of the gravitational settling velocity, thus accounting for the ability of stream flow to create a barrier to deposition. In scenarios (5) and (8), spatial variation in stream flow effects was removed by setting constants to their average value. In scenarios (6) and (9), temporal variation in stream flow effects was removed. Results reveal that over-prediction of NP accumulation occurs systematically when spatial or temporal variation is ignored, since average rates fail to capture the high flow events and high flow regions that drive sediment mobility; that the large jump in NP accumulation in sediments observed when disregarding spatiotemporal variation in sediment transport is due largely to ignoring the ability of stream flow to provide a barrier to deposition; and that spatial variation has a larger effect on Ag accumulation than temporal variation, although both play a role.

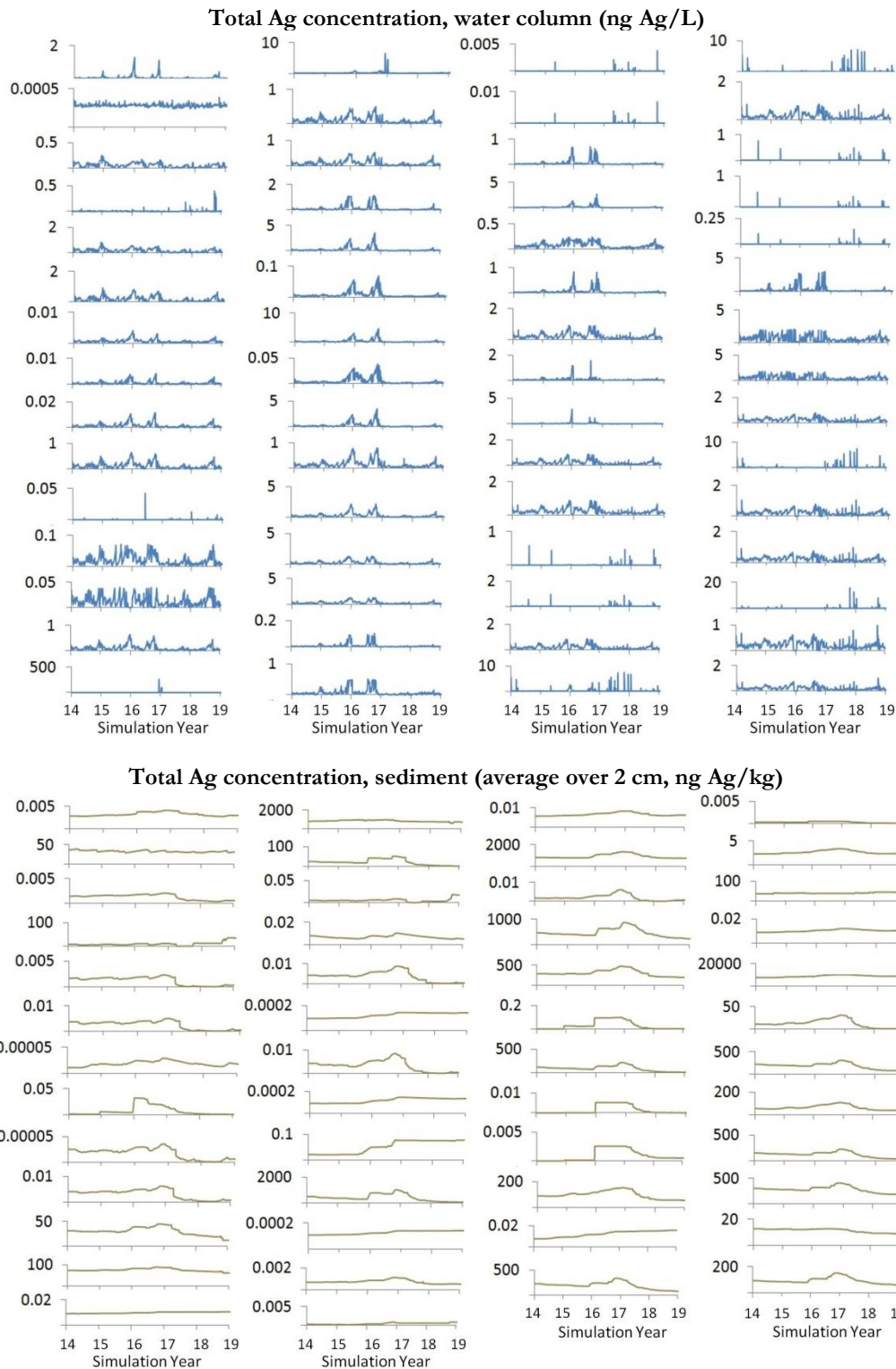


Figure B-6. Total Ag concentrations for each segment in which concentrations are non-zero for the five year stretch which contains the driest (15-16) and wettest (17-18) years in the simulation. Compare water column concentrations to Figure 3-6. Figure 3-4 and Figure 3-5 (note change in units) show that sediment segments with the highest concentrations have high stream loads but also have relatively high sediment deposition.

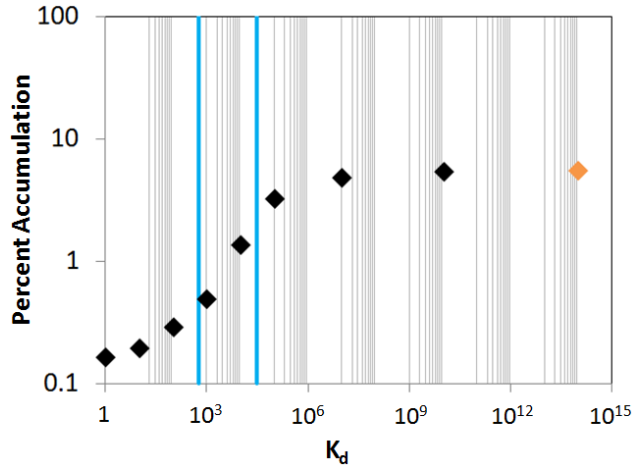


Figure B-7. Sensitivity of the predicted mass accumulation of Ag in the river and sediments at $t = 20$ years (see Figure 3-3) to assumptions about the strength of the association of Ag NPs with sediments in the water column and river bed. In the base case (results reported in the main text), we assume an effective solid-water "partition coefficient" (K_d , in units of L/kg) of infinity, or complete NP association with the silts/fines (orange diamond). The percent of the cumulative Ag NP load to the basin remaining at the end of the simulation appears to have a lower bound of approximately 0.15%. Because NP suspensions never reach equilibrium, kinetic descriptors of heteroaggregation are preferable to the partition coefficients used here. However, K_d values do permit simple sensitivity analysis as shown. Experimentally reported K_d values for Ag NPs are shown as blue bars.^{108, 203}

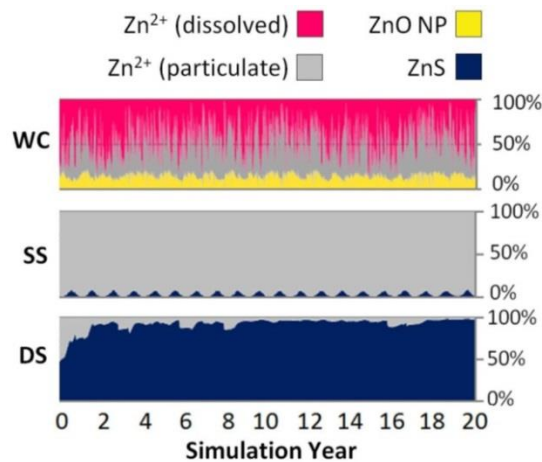


Figure B-8. Speciation of Zn in the WASP7 river simulation model for an alternative input scenario in which 85% of Zn in effluent is present as ZnO NPs (based on the aeration tank model sensitivity analysis, Table B-5) and the lowest ZnO dissolution rate is used. Even in this extreme case, ZnO NPs do not dominate speciation in the water column and sediment speciation is indistinguishable from the base case of 7.5% Zn present as ZnO NPs (Figure 3-2).

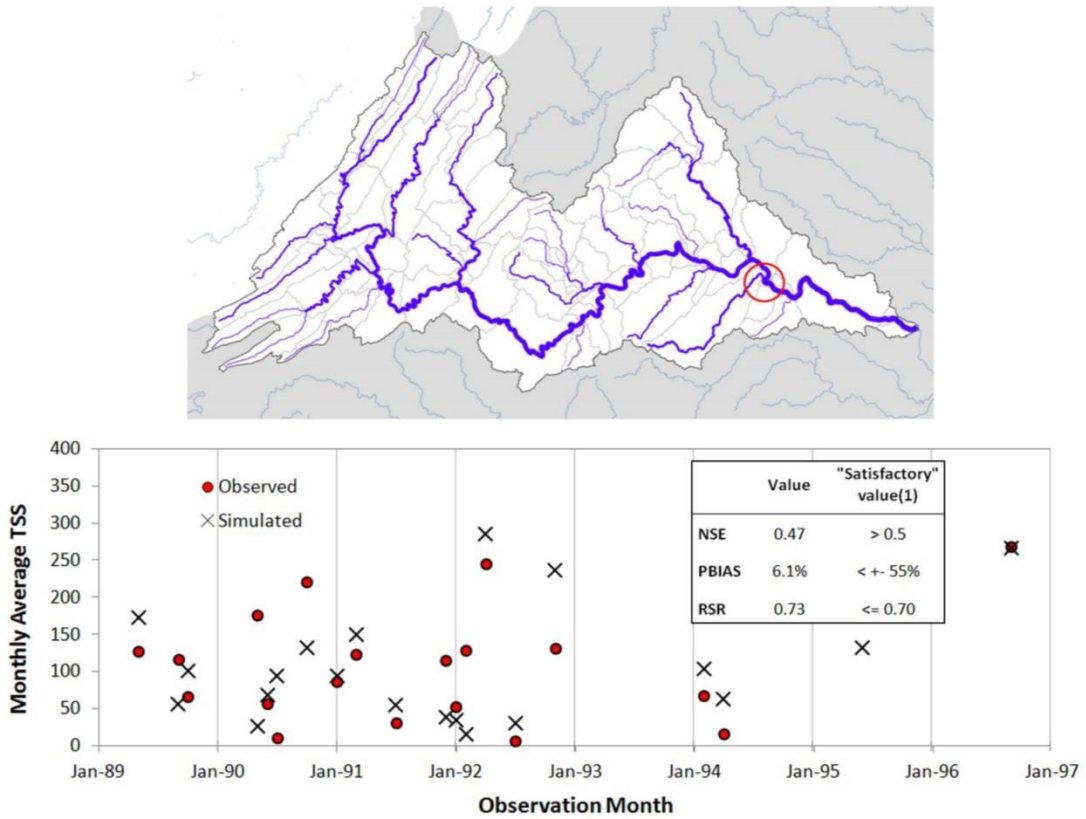


Figure B-9. Total suspended solids (TSS) calibration details. Above: Location of USGS monitoring station used (circled in red). Below: Comparison of observed monthly average TSS concentrations to simulated concentrations. Table inset (below): Calibration metrics.

Appendix C. Supplement to Chapter 4, the Population Balance Models

C.1 Supporting Methods

Nomenclature

k_B	Boltzmann constant
R	Gas constant
μ	Viscosity of water
T	Temperature
V_{sol}	Solution volume
S_{tot}	Total initial NP surface area in solution
\bar{V}	Molar volume of Me_xO_x
γ	Particle surface free energy
ρ_p	Density of Me_xO_x
D_{Me^+}	Me^+ diffusion coefficient in water
$\alpha_{Me_xO_x/Me^+}$	Stoichiometric coefficient for Me_xO_x dissolution to form Me^+
h	Particle boundary layer thickness (Nernst-Brunner modified Noyes Whitney)
$[Me^+]_t$	Metal ion concentration at time t
$[Me^+]_{eq}$	Metal ion concentration at equilibrium
$[Me_xO_x]_t$	Me_xO_x concentration at time t
t	Time
r	Particle radius
m	Particle mass
$D_{geom,0}$	"Characteristic diameter" of primary NPs: Surface-weighted geometric mean diameter
$D_{l,agg}$	"Characteristic diameter" of aggregates
<hr/>	
Total Mass Balance	
$M_{NP,tot}$	Total (size-unresolved) NP mass in solution
k_{mb}	Dissolution rate constant, total mass balance model
$k_{s,mb}$	Surface-area normalized reaction rate, total mass balance model
<hr/>	
Population Balance (all)	
$f(m)$	Particle size distribution (function of mass)
m_i	SM: representative bin size for bin i
w_i	Moment methods: abscissa associated with quadrature point i
w_i	Weight associated with quadrature point i (moment methods)
m_{avg}	Average primary particle mass
r_{avg}	Average primary particle radius
n	Number of quadrature points (moment methods)
X_i	Number of primary particles in aggregates of size i
μ_k	k th moment of the particle size distribution
N	Total particle number concentration at time t ($N_0 =$ initial concentration)
A	Dissolution rate, dm/dt
$k_{s,pb}$	Surface-area normalized reaction rate, population balance
K	Proportionality constant for permeable aggregates colliding due to Brownian motion
D_f	Fractal dimension of the aggregate
β	Collision rate due to Brownian motion
α	Attachment efficiency
φ	Dissolution flux
<hr/>	
Sectional Method	
N_i	Number concentration of particles in bin i
m_{rat}	Ratio used to select bin sizes
q	Exponent used to select bin sizes
$m_{i,lo}$	Mass at the lower boundary of size bin i
m_{min}	Minimum particle mass

m_{max}	Maximum particle mass
n_{bins}	Number of size bins
Direct QMOM	
a_i	Derivative of weight associated with quadrature point i with respect to t
b_i	Derivative of weighted abscissa associated with quadrature point i with respect to t
S_k	Source term for NP processes
Extended QMOM	
n_2	Number of secondary quadrature points
σ_β	Measure of spread around primary quadrature points
$\sigma_{\beta,max}$	Upper bound on σ_β
w_{i_1,i_2}	Weight associated with secondary quadrature point i_1, i_2
m_{i_1,i_2}	Abscissa associated with secondary quadrature point i_1, i_2
ρ_{i_1,i_2}	$w_{i_1} w_{i_2}$
λ_i	First parameter of the beta distribution associated with primary quadrature point i
μ_i	Second parameter of the beta distribution associated with primary quadrature point i
$\tilde{\mu}_k$	Transformed moment set
$\tilde{\mu}_k^*$	Transformed star moment set
\tilde{p}_k^*	Canonical star moment set
\tilde{p}_k	Transformed canonical star moment set
$\underline{H}_{2k}, \overline{H}_{2k+1}, \underline{H}_{2k+1}, \overline{H}_{2k}$	Hankel determinants of the transformed star moment set
J_i	Difference between predicted and known value of the 2nth moment for a given estimate of σ_β
ε	First parameter of the weight function w used to find the secondary quadrature points
ζ	First parameter of the weight function w used to find the secondary quadrature points
a_j	Diagonals of the Jacobi matrix
b_j	Co-diagonals of the Jacobi matrix
J	Jacobi matrix used to find the secondary quadrature points
Analytical Solutions	
μ_{ln}	Location parameter of the lognormal distribution at time t ($\mu_{ln,0}$ = initial condition)
σ_{ln}	Scale parameter of the lognormal distribution at time t ($\sigma_{ln,0}$ = initial condition)

C.1.i. An introduction to our notation, *et cetera*:

In recognition of the complexity and diversity of these methods, and the reader's need to assess their most fundamental features without getting bogged down by mathematical obscura, we use a set of notations that (we hope) is as simple as possible. In so doing, we have played "fast and loose" with more rigorous formulations found in many of the original works. We hope the reader will forgive this approach.

The methods provided here emphasize model development for a simple batch reactor and the practical identification and treatment of common errors that arise during their execution, rather

than (e.g.) theory, the mathematical derivations of these methods, or the execution of their many permutations and extensions. For details, we refer the reader to the original works.

C.1.1. Total Mass Balance

Conventional mass balance differs from population balance as described in Section C.1.2 in that the particle size distribution (and/or its statistical properties) are not resolved or tracked over time.

Instead, only the total mass concentration of each species of interest (here, the metal oxide and its ions) is tracked.

In a simple batch reactor (complete dispersion, no advection), and in the absence of dissolution, aggregation has no effect on the total NP mass. When dissolution does occur, the following simple first-order linear inhomogeneous differential equation³⁹ has been used to describe dissolution.¹⁵⁹

$$\frac{d[Me^+]_t}{dt} = k_{mb}([Me^+]_{eq} - [Me^+]_t)$$

$$\text{Analytical solution: } [Me^+]_t = [Me^+]_{eq}[1 - e^{-k_{mb}t}]$$

Equation C-1

In Equation C-1, $[Me^+]_t$ is the mass concentration of the ion in solution at time t , $[Me^+]_{eq}$ is the ion concentration in solution at equilibrium, and k_{mb} is an empirical rate constant determined by data fitting. In a batch reactor model, $[Me_xO_x]_t$ can be calculated directly once $[Me^+]_t$ is known because the total metal concentration remains constant. Since an analytical solution is available, simulation runtimes are trivial. As a matter of historical interest, we note that Equation C-1 is the

original 1897 form of the Noyes Whitney equation before its modification by Nernst and Brunner to the form used most often today (see Section C.1.2.b).¹⁵⁷

As written, Equation C-1 is not a function of particle size. The size dependence of k_{mb} may be determined by data fitting. The size dependence of the equilibrium solubility, $[Me^+]_{eq}$, is either determined by data fitting or estimated using the Ostwald-Freundlich relation, a theoretical model that attributes the observed increase in solubilities as particle radii (r) decrease to an increase in surface curvature.

$$\frac{[Me^+]_{eq}(r)}{[Me^+]_{eq}(bulk)} = e^{2\gamma\bar{V}/RT r}$$

Equation C-2

where γ is the surface free energy, \bar{V} is the molar volume, R is the gas constant, and T is the temperature. Early efforts suggest that Equation C-2 may over-estimate the equilibrium solubility of NPs.^{20, 120-122} Since our analysis is purely theoretical and questions about the appropriateness of these models for NPs can only be answered with experiments, we use Equation C-2 in this work (applying it in both mass balance and population balance models). Determination of the best rate law formulations for NPs is left for future work.

In Equation C-2, we used the initial surface-weighted geometric mean radius as the characteristic particle size for the distribution. In general, the surface-weighted geometric mean diameter, $D_{geom,0}$ (where “0” here indicates "primary" or unaggregated particles, and not $t=0$) was calculated at every time step as shown.

$$D_{geom,0} = \exp \left[\frac{\sum_{i=1}^n W_i D_i^2 \ln D_i}{\sum_{i=1}^n W_i D_i^2} \right]$$

Equation C-3

where D_i is the particle diameter associated with a given size class (SM) or quadrature point (QMOM) and W_i is the particle number concentration associated with that size class ($W_i=N_i$) or quadrature point ($W_i=w_i$).

Eq. 3 was used wherever a measure of the primary particle size was needed.¹⁶⁰ This measure has several advantages over more traditional estimates of particle diameter including the (number-weighted) mean and the geometric mean. The geometric mean of a skewed distribution is a better estimate of its central tendency than its average. For reactive NPs, the surface-weighted diameter is more relevant than the number-weighted diameter because of the controlling influence of surface area on dissolution kinetics. In addition, the surface-weighted diameter does not rely on the zeroth moment (the total number concentration) and is thus robust to numerical errors introduced by approximation of the dissolution flux.

C.1.2. Population Balance: General Principles

Although definitions vary (e.g., population balance is often defined simply as an implementation of the "population balance equation," Equation C-4, and its derivatives),^{58, 130} population balance may be defined most generally as a means of modeling particle populations in which the continuity equation describes the distribution of particle properties (so-called "internal coordinates") across the population in addition to tracking changes in the average or total properties of the population (e.g., mass concentration) across space and time ("external coordinates").¹³¹ The internal coordinate of greatest interest in population balance is nearly always particle size, and we will focus exclusively on this property here.

By tracking changes in an entire particle size distribution over time and space, rather than merely tracking the total particle mass (Section C.1.1), population balance models are able to track

changes in the number concentration, surface area concentration, and primary and/or aggregate particle sizes in addition to the total NP and ion mass concentrations. Additionally, population balance allows the modeler to explicitly account for size-dependent differences in dissolution and aggregation rates across the population at each time step. However, the mathematical complexity, data requirements, and runtime demands of population balance methods are, unsurprisingly, substantially greater than that of total mass balance. Modelers should thus not use this method unless it is truly better suited to answering major questions of interest.¹⁴

The particle size distribution is described differently by different population balance methods. The three most popular alternatives are sectional methods, moment methods, and Monte Carlo methods.^{58, 134-136} In the sectional method (SM), the size domain is divided into sections or "bins" such that the particle size distribution is treated like a histogram. Moment methods conserve computational resources relative to the SM by only tracking the evolution of the lower-order statistical moments of a particle size distribution instead of tracking the entire distribution.^{58, 142} As described in Section C.1.2.d, the moments of a distribution capture most of the essential features of the distribution and can also, in some cases, be used to reconstruct it. Monte Carlo methods, which we do not attempt in this work, explicitly model the behavior of a finite population of (e.g., $> 10^3$ - 10^4)^{58, 136} particles and thus may require high runtimes relative to moment methods to achieve a given accuracy.¹³⁴ Importantly, there are an impressive number of variants upon, and alternatives to, these three major approaches.

We compare two moment methods in this work: The Direct Quadrature Method of Moments (DQMOM)^{131, 145} and the Extended Quadrature Method of Moments (EQMOM).⁵⁷ Differences between these methods, their application to NPs, and their advantages over "classical" QMOM¹⁴² are described in detail below (Sections C.1.4 and C.1.5). We chose DQMOM because it is extremely fast and relatively simple to implement. We chose EQMOM because it is specifically

designed to deal with the "dissolution flux problem" described in the main text and Section C.1.2.e.iii, which is crippling for most moment-based approaches.

C.1.2.a. The population balance equation for dissolution and aggregation

The following population balance equation (PBE) may be used to describe a change in the particle size distribution, f , over time, t , due to dissolution and aggregation^{43, 55, 56, 58, 130, 142}

$$\begin{aligned}\frac{\partial f}{\partial t} &= \left(\frac{\partial f}{\partial t}\right)_{diss} + \left(\frac{\partial f}{\partial t}\right)_{agg} \\ \left(\frac{\partial f}{\partial t}\right)_{diss} &= -\frac{\partial(Af)}{\partial m} \\ \left(\frac{\partial f}{\partial t}\right)_{agg} &= \frac{1}{2} \int_0^m \alpha(m-m', m') \beta(m-m', m') f(m-m') f(m') dm' \\ &\quad - f(m) \int_0^\infty \alpha(m, m') \beta(m, m') f(m') dm'\end{aligned}$$

Equation C-4

where m (particle mass) is our chosen size coordinate (for reasons described subsequently), $A=dm/dt$ is the dissolution rate law described in Section C.1.2.b,^{130, 142, 146} β is the frequency of particle-particle collisions ($\#/m^3$) that may lead to an aggregation event, and α is the probability that two particles will remain attached upon collision. α is alternatively called the "sticking coefficient" or "attachment efficiency," and is a major focus of current investigation in the experimental NP fate literature.^{112, 147,}

¹⁴⁸ Several other terms may be included in the PBE if other processes (e.g., aggregate breakage, settling) are of interest. Note, however, that $\left(\frac{\partial f}{\partial t}\right)_{agg}$ applies equally to both NP homoaggregation, modeled in this work, and heteroaggregation (e.g., as demonstrated by Therezien et al.).⁹

The first term on the right-hand side of the equation for $\left(\frac{\partial f}{\partial t}\right)_{agg}$ describes the formation of new aggregates of size m via the aggregation of primary (unaggregated) particles or aggregates of size $(m-m')$ with those of size m' (the coefficient, $1/2$, simply eliminates double-counting). The third term describes the loss of particles of size m due to the aggregation of particles of size m with those of any other size. Note that both terms are simply second-order rate laws in which the aggregation rate, described by the product $\alpha\beta$, is assumed to be linearly proportional to the number concentrations of particles of each size.

C.1.2.b. Dissolution rate

We use the 1900 variant on Eq. 1 (the original Noyes Whitney equation) by Brunner and Tolloczko¹⁵⁷ to describe the size-dependent dissolution of NPs. In this form, k_{mb} is replaced with the product of a surface area-normalized rate, $k_{S,mb}$, and S_{tot} , the total surface area of all particles in solution.

$$\frac{d[Me^+]_t}{dt} = k_{S,mb}S_{tot}([Me^+]_{eq} - [Me^+]_t)$$

Equation C-5

Thus this expression simply states that particle dissolution is surface-area dependent and proceeds by exponential decay until equilibrium is achieved.

To use Equation C-5 in population balance, we must rewrite the right hand side in terms of our internal coordinate, particle mass. We must also rewrite the entire expression in terms of the mass loss of a single particle of a given size, rather than the gain in the ion concentration due to dissolution of all particles. A derivation follows in which we assume spherical particles, ignore the dependence of the total number concentration on time, and assume that the particle population is monodisperse. These assumptions are not applied elsewhere in our work; they are simply a

convenience that allows us to find an appropriate form of Equation C-5 for use in our model.

$a_{Me_xO_x/Me^+}$ is the stoichiometric coefficient for Me_xO_x dissolution (g Me_xO_x lost / g Me^+ formed), $M_{NP,tot}$ is the total NP mass in solution, V_{sol} is the solution volume, and N_0 is the initial total particle number concentration.

$$\begin{aligned}\frac{d[Me^+]_t}{dt} &= k_{S,mb}S_{tot}([Me^+]_{eq} - [Me^+]_t) \\ \frac{dM_{NP,tot}}{dt} &\approx a_{Me_xO_x/Me^+}V_{sol}k_{S,mb}S_{tot}([Me^+]_t - [Me^+]_{eq}) \\ \frac{dm_i}{dt} &\approx \frac{a_{Me_xO_x/Me^+}V_{sol}k_{S,mb}S_{tot}}{N_0V_{sol}}([Me^+]_t - [Me^+]_{eq}) \\ \frac{dm_i}{dt} &\approx \frac{a_{Me_xO_x/Me^+}V_{sol}k_{S,mb}(N_0V_{sol}4\pi r_i^2)}{N_0V_{sol}}([Me^+]_t - [Me^+]_{eq}) \\ \frac{dm_i}{dt} &\approx a_{Me_xO_x/Me^+}V_{sol}k_{S,mb}4\pi\left(\frac{3}{4\rho_p\pi}\right)^{2/3}m_i^{2/3}([Me^+]_t - [Me^+]_{eq}) \\ A_i &= \frac{dm_i}{dt} = k_{S,pb}m_i^{2/3}([Me^+]_t - [Me^+]_{eq})\end{aligned}$$

Equation C-6

As an alternative to Equation C-5, many authors have proposed the Nernst-Brunner modified Noyes Whitney equation, a second modification of Equation C-1.^{20, 120-122}

$$\frac{d[Me^+]_t}{dt} = \frac{D_{Me^+}S_{tot}}{hV_{sol}}([Me^+]_{eq} - [Me^+]_t)$$

Equation C-7

D_{Me^+} is the rate of ion diffusion in water and b is the thickness of a boundary layer around the surface of the particles through which ions must diffuse for dissolution to occur.

If we apply the same logic we applied to Equation C-5 and assume that b approximately equals the particle radius, which is generally the case below 30 microns in size,^{5,204} we get Equation C-8, which is equivalent to the Maxwellian flux expression used in many atmospheric chemistry models (compare to Eq. 12.9, p. 591, in⁵⁶). When mass is the internal coordinate,

$$A_i = \frac{dm_i}{dt} = K2\pi D_{Me^+} \left(\frac{6m_i}{\rho_p \pi} \right)^{1/3} ([Me^+]_t - [Me^+]_{eq})$$

Equation C-8

Here, K is a coefficient that arises during the conversion and should approximately (if not exactly) equal the stoichiometric coefficient.

Equation C-6 has many advantages over Equation C-8 for our purposes, and will thus be used in this work. First, Equation C-8 assumes that the rate-limiting step of dissolution is the diffusion of metal ions away from the particle surface. However, for metals and metal sulfides, the rate-limiting step is more likely to be the rate of surface oxidation. Second, the empirical form (Equation C-6) is preferable to the theoretical form (Equation C-8) until the theoretical form has been extensively tested against experimental data. Third, Equation C-8 may be unusable in cases where the radius, rather than the particle mass, is chosen as the internal coordinate, since dr/dt will approach infinity as r approaches zero.

The effect of aggregation on dissolution is poorly understood at present. In order to bound its effect, we consider two extreme cases. In the first, our "base case," we maximize the dissolution rate by assuming that aggregation has no effect. This approach is in general agreement with

experimental results, for which the influence of aggregation is uncertain at best, and for which small particles have been shown to dissolve faster than large particles even when they form larger aggregates.¹⁶⁶ We proceed as follows: The model is run once for a "dissolution only" case in order to determine the average primary (unaggregated) particle mass at each time step, $m_{avg}(t)$. It is then run a second time for the case of simultaneous dissolution and aggregation. For the second run, Equation C-8 is evaluated for $D_{geom,0}(t)$, then is multiplied for each aggregate size by the geometric mean number of primary particles in the aggregate, X_p , to determine the overall dissolution rate of the aggregate. To minimize error in $D_{geom,0}(t)$, we assume a monodisperse primary particle population.

In the second case, which provides a conservative lower bound on the dissolution rate, we assume that aggregation leads to complete fusion of the particles, forming a new spherical particle whose dissolution behavior is determined by the aggregate mass, m_i .

C.1.2.c. Collision rate

In this work, we treat α (the probability of attachment upon collision) as a known constant with a fixed value between 0 and 1. Collisions, which determine the collision rate (β), are assumed to result from Brownian motion.

One advantage of choosing mass as our size coordinate is that the mass of every newly formed aggregated can be calculated exactly from the masses of the colliding species. In contrast, the radius of the aggregate must be estimated from the assumed geometry of the colliding species and the aggregate itself. However, even if mass is our size coordinate, we must make an assumption about the porosity of the aggregates and its effect on their collision rates. We use the following expression for the collision rate between aggregates of size m_i and m_j

$$\beta_{i,j} = \frac{2k_B T}{3\mu} (m_i^{1/D_f} + m_j^{1/D_f})(m_i^{-1/D_f} + m_j^{-1/D_f})$$

Equation C-9

where D_f is the fractal dimension of the aggregates.^{154, 161} We assume $D_f = 1.8$ (for all particle sizes), which is approximately correct for aggregates formed by Brownian diffusion.^{43, 161} More detailed and theoretically rigorous rate laws exist,¹⁶²⁻¹⁶⁵ but a simple approach suffices for an illustrative analysis performed largely in the absence of experimental data.

The characteristic aggregate diameters reported in our results (e.g., Figure 4-2), are estimated from the characteristic primary particle diameters at time t , $D_{geom,0}(t)$, as shown in Equation C-10. In the absence of dissolution, $D_{geom,0}(t) = D_{geom,0}(0)$.¹⁶²

$$D_{i,agg} = D_{geom,0}(X_i)^{1/D_f}$$

Equation C-10

C.1.2.d. Statistical moments of a distribution

The statistical moments, μ_k , of a particle size distribution, $f(m)$, are given as¹⁴²

$$\mu_k = \int m^k f(m) dm$$

Equation C-11

It is easily seen that μ_0 (the "zeroth moment") is the total particle number concentration. By the same logic, the moment sequence $k = 0, 1/3, 2/3, 1$ creates a sequence of values that are directly proportional to the total particle number concentration, the sum of all particle radii (which can, for

example, be divided by μ_0 to find the average particle size), the surface area concentration, and the total mass concentration of the particle population. By tracking this moment sequence over time, we are then able to track any dose metric of practical interest with ease. If radius were our internal coordinate, the moment sequence needed to calculate these metrics would be $k = 0, 1, 2, 3$.

If the particle size distribution is described exactly by a particular distribution (e.g., exponential, lognormal), its moments can often be calculated directly from the parameters of the distribution using known formulas (e.g., see Section C.1.6). The EQMOM relies on such formulas, which can also be used in the EQMOM and the DQMOM to determine the initial ($t = 0$) moments of a known distribution.

C.1.2.e. Introduction to Moment Methods

C.1.2.e.i. The Quadrature Approximation

In classical quadrature-based moment methods, Equation C-11 (the moment equation) is replaced with a discrete approximation using an " n -point Gaussian quadrature rule."¹⁴²

$$\mu_k = \int m^k f(m) dm = \sum_{i=1}^n m_i^k w_i$$

Equation C-12

In effect, the continuous function $f(m)$ is replaced with a particular discrete approximation defined by its "quadrature points," or the set of n "abscissas" and "weights" (m_i, w_i). The great strength of n -point Gaussian quadrature is that it allows the quadrature points to be calculated from the lower-order moments of the distribution, thus solving the so-called "closure problem" that characterizes moment methods.¹⁴²

C.1.2.e.ii. Numerical Solution: The Moment Evolution Equations and Matrix Inversion

In classical QMOM, the population balance equation used in the SM (Equation C-4) is replaced with a continuity equation (the "moment evolution equation") that combines Equation C-4 with the derivative of Equation C-11 to instead balance the moments of the distribution, $\frac{d\mu_k}{dt}$. The moment evolution equations for the processes of dissolution and aggregation are as follows:¹⁴²

$$\begin{aligned}\frac{d\mu_k}{dt} &= \left[\frac{d\mu_k}{dt}\right]_{diss} + \left[\frac{d\mu_k}{dt}\right]_{agg} \\ \left[\frac{d\mu_k}{dt}\right]_{diss} &= k \int_0^\infty m^{k-1} A(m) f(m) dm \\ \left[\frac{d\mu_k}{dt}\right]_{agg} &= \frac{1}{2} \int_0^\infty \int_0^\infty \alpha(m, m') \beta(m, m') [(m + m')^k - m^k - (m')^k] f(m) f(m') dmdm'\end{aligned}$$

Equation C-13

The quadrature approximation of Equation C-13 is

$$\frac{d\mu_k}{dt} \approx k \sum_{i=1}^n m_i^{k-1} A_i w_i + \frac{1}{2} \sum_{i=1}^n \sum_{j=1}^n \alpha_{ij} \beta_{ij} [(m_i + m_j)^k - m_i^k - m_j^k] w_i w_j$$

Equation C-14

Classical QMOM proceeds as follows: (1) Quadrature points are estimated from the moments calculated during the previous time step (or the initial conditions) using a matrix inversion algorithm such as Product-Difference (described shortly). The moments of the distribution are then evolved from one time step to the next using the Euler approximation of Equation C-14.

Although the DQMOM and EQMOM differ from the classical QMOM in their description of the particle size distribution and their treatment of its dynamic evolution, the algorithms for all three methods require the implementation of a matrix inversion procedure in which the lower-order moments of the distribution are used to determine its quadrature points. In this work, we employ the Product-Difference algorithm.^{58, 142} The modified Wheeler algorithm (MATLAB code provided in Appendix A of¹⁵², "Adaptive 1-D quadrature algorithm") is a popular alternative that readily identifies and handles numerical problems resulting from the use of too many quadrature points (where n should not exceed 5-10).⁵⁷ However, we found that its use of an iterative approach to determine an ideal number of quadrature points was unnecessary for successful implementation of the DQMOM and unnecessarily complicated our implementation of the EQMOM.

C.1.2.e.iii. The Dissolution Flux Problem

As particles dissolve completely, they cross the lower boundary of the size domain. This creates an efflux of particles from the system, φ , which may be estimated as shown:⁵⁷

$$\varphi = A(0)f(0)$$

Equation C-15

Classical moment methods only track six or fewer quadrature points, and these points will not generally lie close enough to the lower boundary to allow an accurate prediction of $f(0)$. We will refer to this as the "dissolution flux" problem of classical moment methods. Although it could be a crippling problem when modeling reactive NPs, which readily dissolve completely, it does not seem to be of great concern to the population balance modeling community at large; in fact, it is the focus

of only a few recent works (in which it is generally described in terms of evaporating sprays and thus referred to as the "evaporation flux" problem). In this work, we test three proposed solutions to the problem: The Direct Quadrature Method of Moments with and without ratio constraints and the Extended Quadrature Method of Moments.

C.1.3. Population Balance #1: The Sectional Method

C.1.3.a. Binning approach

In the sectional method (SM), particles are distributed to sections ("bins") based on their size. In this work, we apply the binning method and numerical solution proposed by Hounslow et al.¹⁴⁶ and extended by Lister et al.¹³⁰ This method differs from sectional methods used to date in the nanoparticle fate literature^{5, 8, 9, 11, 37} in that it uses a geometric series to create a grid with expanding bin sizes rather than breaking the grid into equal intervals. Two benefits of such a method are that (1) it allows the modeler to capture a particle size distribution spread over many orders of magnitude in size (e.g., aggregates typically occur in the micron size range)^{20, 120, 122} with a relatively small number of bins, and that (2) the highest model resolution (and computational burden) is placed on the smallest particles, for which aggregation and dissolution occur more rapidly, numerical error is more likely to arise, and the dissolution flux (introduced in Section C.1.2.e.iii) must be estimated.

The grid of bin sizes is defined as follows: A ratio, m_{rat} is chosen such that the representative particle size at the lower boundary of each bin $i+1$, $m_{i+1,lo}$ is related to the size of the lower boundary of next smallest bin, bin i , by the non-negative integer q , as shown.

$$m_{rat} = m_{i+1,lo} / m_{i,lo} = 2^{1/q} \quad q \geq 1$$

Equation C-16

Note that, when $q = 1$ ($m_{rat} = 2$), the representative size in each bin is twice the size of the previous bin.¹⁴⁶ In practice, higher q 's result in a higher resolution to the size distribution. However, little to no benefit is generally observed for $q \geq 7$.

The representative lower boundary size of each bin can then be expressed in terms of the lower boundary of the entire size distribution, m_{min} .¹⁴⁹

$$m_{i,lo} = (m_{rat})^i m_{min}$$

Equation C-17

The total number of bins needed to describe the size distribution is⁵⁵

$$n_{bins} = 1 + \frac{\ln(m_{max}/m_{min})}{\ln(m_{rat})}$$

Equation C-18

For the purpose of calculating the moments of the distribution, the central estimate of the representative size of each bin, m_i is estimated for a given moment of the distribution, k , as follows^{146, 149}

$$m_i = \frac{m_{rat}^{k+1} - 1}{(k + 1)(m_{rat} - 1)} m_{i,lo}^k$$

Equation C-19

C.1.3.b. Numerical solution for dissolution

We rewrote the Second Order Finite Difference approximation by Hounslow et al. and Kostoglou and Karabelas in order to describe particle dissolution under an arbitrary rate law \mathcal{A}_i (Section C.1.2.b) as opposed to growth.^{146, 149}

$$\left(\frac{dN_i}{dt}\right)_{diss} = \frac{1}{m_{i,lo}} (aA_{i-1}N_{i-1} + bA_iN_i + cA_{i+1}N_{i+1})$$

$$\text{where } a = -\frac{2m_{rat}}{(1+m_{rat})(m_{rat}^2-1)}$$

$$b = -\frac{2}{1+m_{rat}}$$

$$c = \frac{2m_{rat}}{(1+m_{rat})(m_{rat}^2-1)}$$

Equation C-20

N_i is the number of particles in bin i at time t .

For dissolution, we used partially implicit time integration via Gauss-Seidel iteration with Type I (zero concentration) boundary conditions.³ We also tested an explicit alternative and a partial step procedure, fourth-order Runge-Kutta. Explicit methods were too unstable; Runge-Kutta was slow and provided no noticeable improvement in accuracy.

C.1.3.c. Numerical solution for aggregation

For aggregation, we use the formulation by Lister et al. (Eq 35 in ¹³⁰), which captures all possible particle re-binning events that may occur on the geometric grid described by Equation C-17 during an aggregation event between two particles of any size.

$$\left(\frac{dN_i}{dt}\right)_{agg} = \sum_{j=1}^{i-Q(q)-1} \alpha_{i-1,j} \beta_{i-1,j} N_{i-1} N_j \frac{2^{\frac{j-i+1}{q}}}{2^{\frac{1}{q}-1}}$$

$$+ \sum_{k=2}^q \sum_{j=i-Q(q-k+2)-k+1}^{i-Q(q-k+1)-k} \alpha_{i-k,j} \beta_{i-k,j} N_{i-k} N_j \frac{2^{\frac{j-i+1}{q}-1+2\frac{k-1}{q}}}{2^{\frac{1}{q}-1}}$$

$$\begin{aligned}
& + \frac{1}{2} \alpha_{i-q, i-q} \beta_{i-q, i-q} N_{i-q}^2 \\
& + \sum_{k=2}^q \sum_{j=i-Q(q-k+1)-k+1}^{i-Q(q-k+2)-k+2} \alpha_{i-k+1, j} \beta_{i-k+1, j} N_{i-k+1} N_j \frac{-2 \frac{j-i}{q} + 2 \frac{1}{q} - 2 \frac{k-1}{q}}{\frac{1}{2^q-1}} \\
& - \sum_{j=1}^{i-Q(q)} \alpha_{i, j} \beta_{i, j} N_i N_j \frac{2 \frac{j-1}{q}}{\frac{1}{2^q-1}} \\
& - \sum_{j=i-Q(q)+1}^{\infty} \alpha_{i, j} \beta_{i, j} N_i N_j
\end{aligned}$$

Equation C-21

where $Q(q) = \sum_{l=1}^q l$. For aggregation, we use explicit time integration and the Euler method. As with dissolution, an alternative solution that used fourth-order Runge-Kutta provided no clear benefit and was discarded.

C.1.4. Population Balance #2: The Direct Quadrature Method of Moments (DQMOM)

DQMOM approximates the particle size distribution as a sum of i Dirac delta functions with n weights w_i at locations (abscissas) $m_i, i = 1 \dots n$.

$$f(m) = \sum_{i=1}^n w_i \delta(m - m_i)$$

Equation C-22

In the univariate case (i.e., when only one internal coordinate is considered), this representation is mathematically identical to the quadrature point approximation used in classical QMOM (Section C.1.2.e).¹³¹ In the DQMOM, however, the continuity equation (Equation C-4) is re-written in terms of the derivatives of the weights and abscissas of the distribution so that the quadrature points may

be evolved *directly* at each time step. This approach contrasts with that of classical QMOM, for which the continuity equation is expressed in terms of the derivatives of the moments such that quadrature points must be recalculated from the moment set at each time step (e.g., using a matrix inversion procedure, see Section C.1.2.f). Direct QMOM is, unsurprisingly, much faster than the classical approach.¹³¹

C.1.4.a. Numerical solution of the DQMOM

Marchisio and Fox (2005) derive the DQMOM formulation for the Williams spray equation, a specific implementation of the PBE (Equation C-4) that accounts for non-homogeneous flow.^{131, 145}

We focus here on implementation of their method in a simple batch reactor model (no-flow, homogeneous). Based on¹⁴⁵, we propose two means of addressing the dissolution flux problem.

Let a_i and b_i describe the evolution of weights and weighted abscissas over time

$$a_i = \frac{\partial w_i}{\partial t}, b_i = \frac{\partial (w_i m_i)}{\partial t}$$

Equation C-23

a_i and b_i may then be found by solving the following system of equations, where S_k is a placeholder for functions that describe the evolution of the particle size distribution over time due to specific processes (compare to Equation C-14).¹⁵⁴

$$(1 - k) \sum_{i=1}^n m_i^k a_i + k \sum_{i=1}^n m_i^{k-1} b_i = \overline{S_k}$$

$$\overline{S_k} = S_{k,diss} + S_{k,agg}$$

$$S_{k,diss} = k \sum_{i=1}^n m_i^{k-1} A_i w_i$$

$$S_{k,agg} = -\frac{1}{2} \sum_{i=1}^n \sum_{j=1}^n \alpha_{ij} \beta_{ij} [(m_i + m_j)^k - m_i^k - m_j^k] w_i w_j$$

Equation C-24

Equation C-24 is solved with linear algebra as described in the Appendix of ¹³¹.

We use the Euler method in conjunction with a_i and b_i to update the weights and abscissas from one time step to the next. The moments may be determined from the set (m_i, w_i) at any time step by simple application of the quadrature approximation (Equation C-12).

C.1.4.b. Error in the DQMOM

Two sources of error in DQMOM are of especial importance: The matrix defined by the coefficients on the left-hand side of Equation C-24 may be ill-conditioned, or it may be singular. An "ill-conditioned" matrix is one for which error is introduced during matrix inversion because the solution to the linear equation is highly sensitive to round-off error in the coefficient matrix. Poorly conditioned matrices have higher condition numbers than well-conditioned matrices, where the condition number is defined as the ratio of the largest singular values of the matrix to the smallest. In numerical methods, ill-conditioning causes numerical instability.

We found ill-conditioning occurred readily during NP aggregation because it causes a rapid increase in the values of the abscissas used to calculate the coefficient matrix. We solved this problem, or at least greatly reduced it, by re-scaling the abscissas at each time step using the scale factor introduced in Section 2.4 of ¹⁴⁵, $\max(m_i), i = 1 \dots n$. In our case, re-scaling was not needed in the absence of aggregation. Furthermore, we found that this simple re-scaling procedure made the stability of the DQMOM comparable to that of the EQMOM and the SM. Thus we did not

attempt more rigorous approaches such as singular value decomposition and/or iterative solution methods.^{145, 154}

When the condition number of a matrix is infinite, the matrix is *singular*. In the univariate DQMOM, singularity reflects a lack of independence in the moment sequence, which results when two or more abscissas are identical (i.e., the distribution has zero variance). In this case, the system of equations does not have a unique solution.¹³¹ In our experience, this rare but fatal error often results from initial conditions⁵⁸ and can generally be eliminated by reducing the number of quadrature points; n should not, in any case, exceed 5 or 6.¹⁵⁴ Alternatively, the problem can usually be solved by perturbing non-distinct abscissas (keeping weights the same) or by averaging the values of a_i and b_i found at neighboring points.¹³¹

C.1.4.c. Estimating dissolution flux with ratio constraints

As described in Section C.1.2.e.iii, a flux term must be added to Equation C-24 when NPs are able to undergo complete dissolution.

$$(1 - k) \sum_{i=1}^n m_i^k a_i + k \sum_{i=1}^n m_i^{k-1} b_i - \delta_{k0} \varphi = \overline{S_k}$$

Equation C-25

Here, φ is the dissolution flux and δ_{k0} equals one for $k=0$ and zero for any other value of k .

It is important to note that Equation C-25 assumes that the lower boundary of the particle size distribution occurs at zero. In fact, the DQMOM is implemented on a semi-infinite domain, $[0, \infty)$, rather than the finite domain $[m_{min}, m_{max}]$ used in the SM and (Beta) EQMOM. However, we found that the SM and the EQMOM were insensitive to our choice of m_{min} . Thus any error arising from

the use of a different lower boundary in the DQMOM had no appreciable effect on model predictions.

The EQMOM tackles the dissolution flux problem head-on, reconstructing the particle size distribution at each time step in order to evaluate it. Since no reconstruction is available in the DQMOM, we are left with a system of equations that has one too many unknowns. As suggested by ¹⁴⁵, however, we can approximate a solution with relative ease by adding two more constraints to Equation C-25. These "ratio constraints," which are applied only when calculating the influence of dissolution on the weights and abscissas, simply state that the change in the particle size distribution due to dissolution will be smooth.

$$\frac{d}{dt} \left(\frac{w_i}{w_{i+1}} \right) = 0, \quad \frac{d}{dt} \left(\frac{m_i}{m_{i+1}} \right) = 0$$

Equation C-26

The ratio constraints for the weights (see Section 2.3 of ¹⁴⁵ for the derivation) provide a new system of equations which can be solved for $i=1, \dots, n-1$ (e.g., via matrix inversion) to find b_i .

$$w_{i+1}m_{i+1}b_i^* - w_i m_i b_{i+1}^* = E_i$$

$$E_i = w_i w_{i+1} (m_i A_{i+1} - m_i A_i)$$

$$\text{where } b_i^* = b_i - w_i A_i$$

Equation C-27

Once b_i is known, a_i is found using Equation C-28

$$a_i = \frac{w_i k \sum_{i=1}^n m_i^{k-1} (b_i^*)}{(k-1) \sum_{i=1}^n m_i^k w_i}$$

Equation C-28

Any value of k other than 1 may be used in Equation C-28.

Finally, solving Equation C-25 for $k=0$ gives an approximation of the dissolution flux

$$\varphi = -\sum_{i=1}^n a_i$$

Equation C-29

φ cannot be negative. If the procedure described above results in $\varphi < 0$, it is set to zero along with a_i and b_i^* .

In traditional DQMOM (Equation C-24), scaling factors are only applied to the abscissas when re-scaling to ensure numerical stability (Section C.1.4.b). When the dissolution flux term is added to Equation C-24, weights must then be rescaled as well. We use the scaling factor $\sum_{i=1}^n w_i$ as suggested by ¹⁴⁵.

Because the ratio constraints assume that the particle size distribution transforms smoothly over time, it is expected to perform poorly for highly monodisperse particle populations. In such cases, traditional DQMOM may work better. The following simple procedure is employed: Whenever an abscissa crosses the lower size boundary, its corresponding weight is set to zero. The abscissa itself remains unchanged.

C.1.4.d. Initial conditions

The DQMOM uses an efficient and relatively simple approach to transform the weights and abscissas of the particle size distribution over time in response to aggregation and dissolution. However, it does not specify the initial value of the set (w_p, m_p) . At $t = 0$, we express the locations and weights of the initial quadrature points in terms of the lower order moments of the distribution and solve using a matrix inversion procedure such as the Product Difference algorithm (see Section C.1.2.e.ii).

C.1.5. Population Balance #3: (Beta) Extended Quadrature Method of Moments (EQMOM)

As its name suggests, extended quadrature method of moments is an extension of classical QMOM (Section C.1.2.e). In both methods, the particle size distribution is approximated by a set of quadrature points, which are calculated from the lower-order moments of the distribution at each time step using a matrix inversion algorithm, and the moments are evolved directly at each time step.

In classical QMOM and DQMOM, the PSD is represented by a sum of Dirac delta functions. In EQMOM, each abscissa m_i is instead assumed to describe the central tendency of a new statistical distribution, $\delta_{\sigma_\beta}(m, m_i)$. The entire distribution is thus described by a weighted sum of probability density functions (pdfs) as shown:

$$f(m) = \sum_{i=1}^n w_i \delta_{\sigma_\beta}(m, m_i)$$

Equation C-30

$\delta_{\sigma_\beta}(m, m_i)$ takes a pre-specified form. We employ the Beta distribution (Beta EQMOM) in this work; ref⁵⁷ provides details for both Beta and Gamma EQMOM.

When $\delta_{\sigma_\beta}(m, m_i)$ represents a Beta distribution, $f(m)$ may be rewritten as follows:

$$f(m) = \sum_{i=1}^n w_i \frac{m^{\lambda_i-1} (1-m)^{\mu_i-1}}{B(\lambda_i, \mu_i)}$$

Equation C-31

where $\lambda_i = m_i/\sigma_\beta$ and $\mu_i = (1 - m_i)/\sigma_\beta$ are the parameters of the distribution and σ_β captures the spread of the each Beta distribution around each "primary" abscissa. Note that every primary abscissas is assumed to have the same σ_β . When $\sigma_\beta = 0$, EQMOM is equivalent to DQMOM and (in the univariate case) classical QMOM. Otherwise, σ_β is used to find a set of "secondary" quadrature points, each of which is distributed around the first. Thus EQMOM employs two nested quadrature steps at each time step.

Unlike the primary quadrature step, which only estimates 4-6 quadrature points with accuracy, the secondary quadrature step is highly efficient and accurate up to any number of quadrature points. As such, the EQMOM provides two relatively accurate approximations of the PSD: Equation C-31 and the discrete "dual quadrature approximation," Equation C-41(below). As described in Section C.1.5.f, Equation C-31 can be used to (1) reconstruct the particle size distribution from its quadrature points and (2) estimate the particle efflux from the system due to complete dissolution.

C.1.5.a. First coordinate transformation

The Beta EQMOM defines the particle size distribution on the domain $[0, 1]$, rather than upon the finite interval $[m_{min}, m_{max}]$.^{134, 205} At each time step, the first step in the BEQMOM is thus to perform

the following coordinate transformation on the moment set calculated during the previous time step²⁰⁵

$$\widetilde{\mu}_k = \frac{1}{(m_{max}-m_{min})^k} \sum_{j=0}^k \frac{k!}{j!(k-j)!} (-m_{min})^{k-j} \mu_k$$

Equation C-32

A few notes are in order regarding our choice of moments. In the DQMOM and the SM, we solve for the fractional moments of the distribution. In contrast, for simplicity, we tracked only the integer moments in EQMOM. Fractional moments (e.g., as shown in Figure 4-2) were estimated *ex post facto* from the reconstructed distribution at each time step using Equation C-11 and Equation C-31.

The matrix inversion algorithm used in classical QMOM (e.g., Product-Difference) requires the first $2n$ moments of the distribution (where n is the number of quadrature points). The EQMOM requires one additional moment ($2n+1$) in order to find σ_β . The DQMOM and the SM do not rely on a matrix inversion procedure, so any choice of moments will suffice.

C.1.5.b. Set-up for primary quadrature

EQMOM uses an iterative procedure to simultaneously select σ_β and determine the set of primary quadrature points. This step begins with an initial guess for σ_β , such as its theoretical lower bound of zero (see Section C.1.5.c for details on the bounds of σ_β).

The parameters of a beta distribution have a known relationship to its moments:

$$\mu_k = \frac{m_i + (k-1)\sigma_\beta}{1 + (k-1)\sigma_\beta} \mu_{k-1}, k > 0$$

Equation C-33

Let us call the set of (transformed) moments that could be estimated from the primary quadrature points of the distribution the "star moments":

$$\widetilde{\mu}_k^* = \sum_{i=1}^n m_i^k w_i$$

Equation C-34

Equation C-33 suggests that the (transformed) moment set of the distribution, which is known from the previous time step, can be expressed as a function of the $2n$ (transformed) star moments of the distribution and a set of k coefficients, γ_k , which are solely a function of σ_β (see ⁵⁷ for the derivation).

$$\widetilde{\mu}_k = \gamma_k \widetilde{\mu}_k^* + \gamma_{k-1} \widetilde{\mu}_{k-1}^* + \cdots + \gamma_1 \widetilde{\mu}_1^* \text{ for } k \geq 1$$

Equation C-35

For example,

$$\widetilde{\mu}_0 = \widetilde{\mu}_0^*$$

$$\widetilde{\mu}_1 = \widetilde{\mu}_1^*$$

$$\widetilde{\mu}_2 = \frac{1}{1 + \sigma_\beta} (\widetilde{\mu}_2^* + \sigma_\beta \widetilde{\mu}_1^*)$$

$$\widetilde{\mu}_3 = \frac{1}{(1 + 2\sigma_\beta)(1 + \sigma_\beta)} (\widetilde{\mu}_3^* + 3\sigma_\beta \widetilde{\mu}_2^* + 2\sigma_\beta^2 \widetilde{\mu}_1^*)$$

$$\widetilde{\mu}_4 = \frac{1}{(1 + 3\sigma_\beta)(1 + 2\sigma_\beta)(1 + \sigma_\beta)} (\widetilde{\mu}_4^* + 6\sigma_\beta \widetilde{\mu}_3^* + 11\sigma_\beta^2 \widetilde{\mu}_2^* + 6\sigma_\beta^3 \widetilde{\mu}_1^*)$$

In order to find the star moments, $\widetilde{\mu}_k^*$ ($k=0, 1, \dots, 2n-1$), this system of equations is written in matrix form and solved via matrix inversion. The star moment set itself is then inverted using a classical QMOM algorithm such as Product-Difference in order to find the set of n primary quadrature points suggested by the initial choice of σ_β . Finally, these quadrature points are used in Equation C-34 to estimate the $2n$ th star moment, $\widetilde{\mu}_{2n}^*$.

The "goodness of fit" between the true distribution and the distribution suggested by our choice of σ_β is described by $\widetilde{\mu}_{2n} - \widetilde{\mu}_{2n}^*$, or Equation C-36. Let us call this difference $J_i(\sigma_\beta)$.

$$J_i(\sigma_\beta) = \widetilde{\mu}_{2n} - \gamma_{2n} \widetilde{\mu}_{2n}^* - \gamma_{2n-1} \widetilde{\mu}_{2n-1}^* - \dots - \gamma_1 \widetilde{\mu}_1^*$$

Equation C-36

The best choice for σ_β is the value for which $J_i(\sigma_\beta)=0$. We use a root-finding algorithm to find the smallest σ_β which meets this condition.

C.1.5.c. Procedure to find σ_β

σ_β is bounded on the interval $[0, \sigma_{\beta,max}]$, where $\sigma_{\beta,max}$ is either chosen arbitrarily¹³⁴ or is calculated from the Hankel determinants of the distribution, which are defined as follows for all integer moments k :

$$\underline{H}_{2k} = \begin{vmatrix} \widetilde{\mu}_0^* & \cdots & \widetilde{\mu}_k^* \\ \vdots & \ddots & \vdots \\ \widetilde{\mu}_k^* & \cdots & \widetilde{\mu}_{2k}^* \end{vmatrix}, \overline{H}_{2k+1} = \begin{vmatrix} \widetilde{\mu}_0^* - \widetilde{\mu}_1^* & \cdots & \widetilde{\mu}_k^* - \widetilde{\mu}_{k+1}^* \\ \vdots & \ddots & \vdots \\ \widetilde{\mu}_k^* - \widetilde{\mu}_{k+1}^* & \cdots & \widetilde{\mu}_{2k}^* - \widetilde{\mu}_{2k+1}^* \end{vmatrix},$$

$$\underline{H}_{2k+1} = \begin{vmatrix} \widetilde{\mu}_1^* & \cdots & \widetilde{\mu}_{k+1}^* \\ \vdots & \ddots & \vdots \\ \widetilde{\mu}_{k+1}^* & \cdots & \widetilde{\mu}_{2k+1}^* \end{vmatrix}, \overline{H}_{2k} = \begin{vmatrix} \widetilde{\mu}_1^* - \widetilde{\mu}_2^* & \cdots & \widetilde{\mu}_k^* - \widetilde{\mu}_{k+1}^* \\ \vdots & \ddots & \vdots \\ \widetilde{\mu}_k^* - \widetilde{\mu}_{k+1}^* & \cdots & \widetilde{\mu}_{2k-1}^* - \widetilde{\mu}_{2k}^* \end{vmatrix}$$

Equation C-37

The Hankel determinants (Eq. 1.4.3, p. 20 in ²⁰⁵) are first used in Equation C-38 (Eq. 1.4.5, p. 20 in ²⁰⁵) to find the "canonical" moments, \widetilde{p}_k^* , corresponding with the (transformed) star moment set $\widetilde{\mu}_k^*$. $\sigma_{\beta,max}$ is then expressed in terms of the canonical moments (Equation C-39):

$$\widetilde{p}_k^* = \frac{\underline{H}_{2k+1}\overline{H}_{2k}}{\underline{H}_{2k+1}\overline{H}_{2k} + \overline{H}_{2k+1}\underline{H}_{2k}} \text{ where } \underline{H}_{-1} = \overline{H}_{-1} = \underline{H}_0 = \overline{H}_0 = 1$$

Equation C-38

$$\sigma_{\beta,max} = \begin{cases} \frac{\widetilde{p}_2^*(1-\widetilde{p}_3^*)}{1-\widetilde{p}_1^*-2*\widetilde{p}_2^*-\widetilde{p}_1^*\widetilde{p}_2^*+2\widetilde{p}_2^*\widetilde{p}_3^*} \text{ if } \widetilde{p}_k^* > \frac{\widetilde{p}_1^*+\widetilde{p}_2^*-\widetilde{p}_1^*\widetilde{p}_2^*}{1+\widetilde{p}_2^*} \\ 0.99999 * \frac{\widetilde{p}_2^*}{1-\widetilde{p}_2^*} \text{ if } \widetilde{p}_k^* = \frac{\widetilde{p}_1^*+\widetilde{p}_2^*-\widetilde{p}_1^*\widetilde{p}_2^*}{1+\widetilde{p}_2^*} \\ \frac{\widetilde{p}_2^*\widetilde{p}_3^*}{\widetilde{p}_1^*+\widetilde{p}_2^*-\widetilde{p}_1^*\widetilde{p}_2^*-2\widetilde{p}_2^*\widetilde{p}_3^*} \text{ if } \widetilde{p}_k^* < \frac{\widetilde{p}_1^*+\widetilde{p}_2^*-\widetilde{p}_1^*\widetilde{p}_2^*}{1+\widetilde{p}_2^*} \end{cases}$$

Equation C-39

The coefficient 0.99999 is added in the second case to ensure that the $\sigma_{\beta,max}$ remains finite when $\widetilde{p}_2^* = 1$ (Dr. Frédérique Laurent-Nègre, École Centrale Paris, personal correspondance).

Recall that the purpose of the search procedure is to find the smallest value of σ_{β} such that $J_i(\sigma_{\beta}) = 0$. Once the bounds on σ_{β} are known, they can be narrowed using an unbounded search procedure such as the secant method until a new interval is found for which $J_i(\sigma_{\beta,min})$ and $J_i(\sigma_{\beta,max})$ straddle the y -axis. Since $J_i(0)$ is, by definition, positive, this search procedure generally

reduces $\sigma_{\beta,max}$ until $J_i(\sigma_{\beta,max}) < 0$. At this point, we may switch to a bounded search procedure such as Ridder's method in order to rapidly converge on a solution.

We found that it sometimes helped to start our search procedure with a non-zero but very low lower bound such as 10^{-50} . However, the reader should be aware that this approach may require other small changes to the search procedure; $J_i(0)$ is guaranteed to be non-negative, but no such guarantee applies to an arbitrarily selected non-zero lower bound.

In practice, the value of σ_{β} chosen by the search procedure may lead to a "unrealizable" or invalid star moment set, or one for which one or more abscissas fall outside of the size domain. The star moment set is realizable if its lowest Hankel determinant (Equation C-37) is positive (see Appendix B in ⁵⁷ for details). If our moment set was found to be unrealizable, we simply discarded that estimate in favor of the smallest value of σ_{β} tried during the search procedure for which a realizable star moment set was generated (as suggested by ¹³⁴).

C.1.5.d. Secondary quadrature and the second coordinate transformation

We have now successfully discovered σ_{β} and a set of primary quadrature points and can proceed to find the secondary quadrature points of the distribution.

By performing a second (simpler) coordinate transformation on the transformed moment set to define it on the domain [-1,1] instead of [0,1], we can express the beta distribution as a Jacobi polynomial that is orthogonal with respect to the following weight function $w(t) = (1 - t)^{\varepsilon}(1 + t)^{\zeta}$ where $\varepsilon = \mu_i - 1$ and $\zeta = \lambda_i - 1$ (note that, in this case, t is not time).⁵⁷ The quadrature points associated with Jacobi polynomials can be calculated with high accuracy and low computational demands. Details are provided by ref ²⁰⁶ (Chapter 3). This algorithm closely mirrors the Product-Difference and modified Wheeler algorithms as described by refs ^{58, 142, 152}.

Briefly, ε and ζ are used in the following recurrence relation to determine a_j and b_j , the diagonals and co-diagonals of the Jacobi matrix, J (Eq. 3.143a p.84 of ²⁰⁶):

$$a_j = \frac{\zeta^2 - \varepsilon^2}{(2j + \varepsilon + \zeta)(2j + \varepsilon + \zeta + 2)}$$

$$b_j = \frac{4j(j + \varepsilon)(j + \zeta)(j + \varepsilon + \zeta)}{(2j + \varepsilon + \zeta - 1)(2j + \varepsilon + \zeta)^2(2j + \varepsilon + \zeta + 1)}$$

$$J = \begin{bmatrix} a_0 & \sqrt{b_1} & & & \\ \sqrt{b_1} & a_1 & \sqrt{b_2} & \ddots & \\ & \ddots & \ddots & \ddots & \\ & & \sqrt{b_{N-1}} & a_{N-1} & \sqrt{b_N} \\ & & & \sqrt{b_N} & a_N \end{bmatrix}$$

The i th abscissa associated with each secondary quadrature point is the i th eigenvalue of the Jacobi matrix. The i th weight, w_i , is the squared value of the first component of the i th eigenvector.

Once secondary weights and abscissas are determined for each primary quadrature point to create the two-dimensional set of secondary quadrature points, $(w_{i_1, i_2}, m_{i_1, i_2})$, we perform another coordinate transformation to once again define them on the domain $[0,1]$.

We now have the so-called "dual quadrature" representation of the particle size distribution:

$$f(m) = \sum_{i_1=1}^{n_1} \sum_{i_2=1}^{n_2} \rho_{i_1, i_2} \delta(m - m_{i_1, i_2}) \quad \text{where } \rho_{i_1, i_2} = w_{i_1} w_{i_2}$$

Equation C-40

Note that $\delta(m - m_{i_1, i_2})$ is the Dirac delta function as seen in Equation C-22, and not the continuous alternative seen in Equation C-30, $\delta_{\sigma_\beta}(m, m_i)$.

C.1.5.e. Evolution of the moments

Yuan et al.⁵⁷ use the dual quadrature approximation to derive expressions for the moment evolution equations, $\frac{d\mu_k}{dt}$. The equations for dissolution and aggregation closely parallel the moment evolution equations used in classical QMOM (Equation C-14) and the source terms used in DQMOM (Equation C-24). Note that the first coordinate transformation must be reversed before evolving the moments from one time step to the next in order to place the moment set back on its true domain, $[m_{min}, m_{max}]$.

$$\left[\frac{d\mu_k}{dt}\right]_{agg} = \frac{1}{2} \sum_{i_1=1}^{n_1} \sum_{i_2=1}^{n_2} \sum_{j_1=1}^{n_1} \sum_{j_2=1}^{n_2} \rho_{i_1, i_2} \rho_{j_1, j_2} [(m_{i_1, i_2} + m_{j_1, j_2})^k - m_{i_1, i_2}^k - m_{j_1, j_2}^k] \alpha_{ij} \beta_{ij}$$

Equation C-41

$$\left[\frac{d\mu_k}{dt}\right]_{diss} = k \sum_{i_1=1}^{n_1} \sum_{i_2=1}^{n_2} m_{i_1, i_2}^{k-1} \rho_{i_1, i_2} A(m_{i_1, i_2})$$

Equation C-42

C.1.5.f. Calculation of the dissolution flux

Equation C-31 allows us to reconstruct the particle size distribution from its primary quadrature points at each time step. Evaluating Equation C-31 at m_{min} also allows us to approximate the dissolution flux using Equation C-15. Of course, for our numerical solution, we must estimate the dissolution flux during a time step rather than at a particular time. To do so, we take the integral of

Equation C-31 over the range of particle sizes expected to dissolve completely within that time step (calculated using Equation C-6). All secondary abscissas are then advected towards the lower boundary (again according to Equation C-6), and the weights of any quadrature point that crosses the lower boundary is set to zero.

The dissolution flux may also be approximated as the sum of the weights (particle number) associated with each quadrature point that crosses the lower boundary during a time step. However, this approach is slower than the integral approach because it requires far more secondary abscissas per primary abscissa. For example, upwards of 1000 abscissas could be required, as opposed to the (e.g.) $5 \leq n_2 \leq 80$ suggested when using the integral approximation.⁵⁷

C.1.6. Analytical Solutions

Consider a lognormal distribution such as we have at the start of our simulation. The following are some useful properties of this distribution.

Probability density function (used in the analytical solution):

$$f(m, t) = \frac{N}{\sigma_{\ln} m \sqrt{2\pi}} e^{-\frac{(\ln m - \mu_{\ln})^2}{2(\sigma_{\ln}^2)}}$$

Equation C-43

Cumulative distribution function, where $\text{erfc}()$ is the complementary error function (used in the

Sectional Method to bin the initial NP population):

$$F(m, t) = \frac{N}{2} \text{erfc}\left(-\frac{\ln m - \mu_{\ln}}{\sigma_{\ln} \sqrt{2}}\right)$$

Equation C-44

Fractional moments (used to initialize the moments in the EQMOM and DQMOM):

$$\mu_k(t) = N e^{k\mu_{ln} + \frac{1}{2}k^2\sigma_{ln}^2}$$

Equation C-45

Williams et al. (1982) provide the following analytical solution for a particle size distribution with any known initial functional form n_0 dissolving according to the rate law $\frac{dm}{dt} = F_d m^d$, where F_d and d are arbitrary constants.¹⁵⁵

$$f(m, t) = \left[1 - \frac{(1-d)F_d t}{m^{1-d}}\right]^{\frac{d}{1-d}} f_0([m^{1-d} - (1-d)F_d t]^{1/(1-d)})$$

Equation C-46

In our case, under sink conditions (i.e., $[Me^+]_{t=0}$), $d = 2/3$ and $F_d = -k_{s, pb}[Me^+]_{eq}$ (see Equation C-6).

Park et al. (2000) provide an analytical solution for aggregation of an initially lognormal particle size distribution according to the rate law given in Equation C-9. In this case, the distribution is assumed to remain lognormal (of the form given by Equation C-43).¹⁵⁶ Parameters change over time according to Equation C-47, where $K = \alpha \frac{2k_B T}{3\mu}$ (see Equation C-9), $\sigma_d(t) = e^{\sigma_{ln}/3}$ and $v_d(t) = e^{\mu_{ln}}$.

$$\ln^2 \sigma_d = \frac{1}{9} \ln \left[2 + \frac{X}{Y}\right]$$

$$v_d = v_{d,0} \frac{\exp(9 \ln^2 \sigma_{d,0}/2) Y}{[2 + \frac{X}{Y}]}$$

$$N = N_0 \frac{1}{Y}$$

where $X = \exp(9 \ln^2 \sigma_{d,0}) - 2$

$$Y=1 + \{1 + \exp(9 \ln^2 \sigma_{d,0}/D_f^2)\}KN_0t$$

Equation C-47

Equation C-46 and Equation C-47 are used in the appropriate expressions (e.g., the moment definition equation, Equation C-11) in order to calculate values of interest (values plotted in Figure 4-2 of the main text). Integral expressions were evaluated over the particle size domain. Thus, particle flux during dissolution was accounted for simply by omitting from the solution the portion of the size distribution that fell below the lower size boundary.

C.2 Supporting Figures

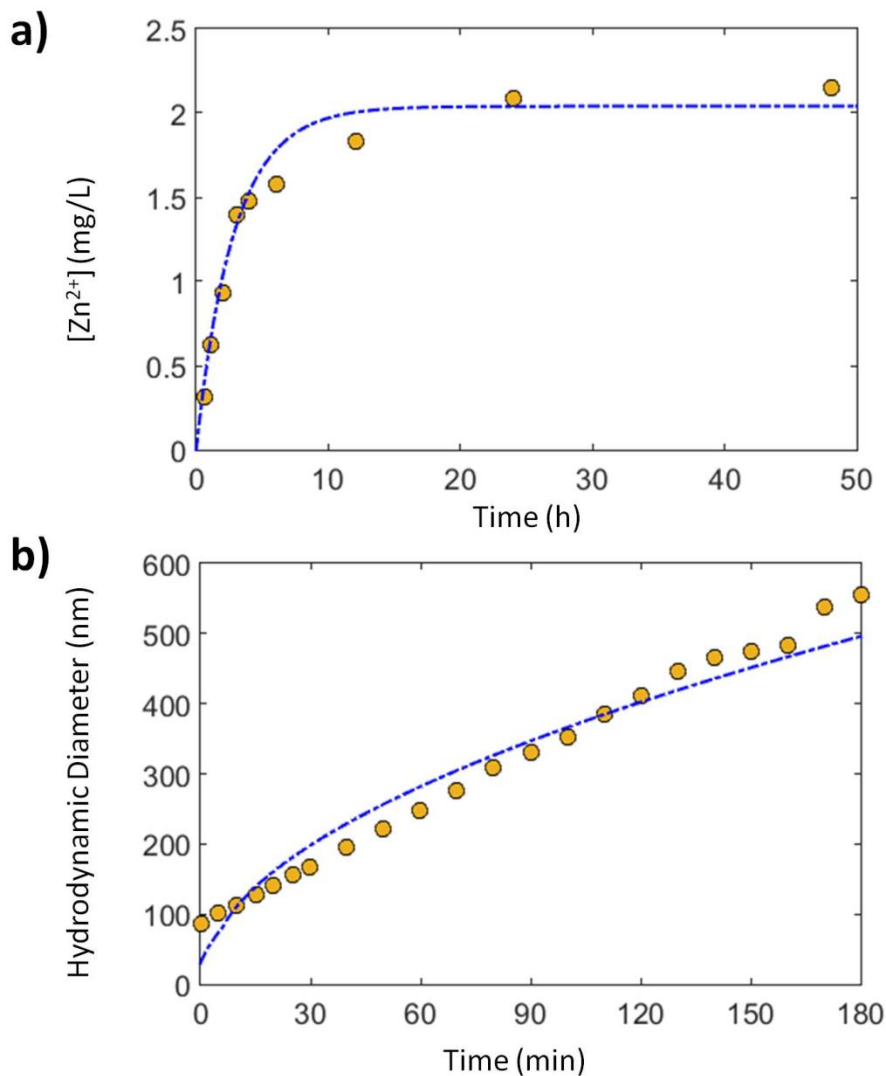


Figure C-1. Model results (dot-dashed blue line, from the Sectional Method) compared to experimental data (yellow dots) for the calibration procedure used to provide an order-of-magnitude estimate of the ZnO NP dissolution rate and aggregation rate for all test cases. Experimental data is from Majedi et al. for moderately hard water (MHW) at 25°C (compare to Fig. 3b and Fig. 1c).¹⁵⁹ Model inputs: Mean (52 nm), standard deviation (9 nm), equilibrium ion concentration (2.04 mg/L), and initial concentration (20 mg/L). We assume that the hydrodynamic diameter of the particles is 60% of their collision diameter (Equation 4-22).⁴³

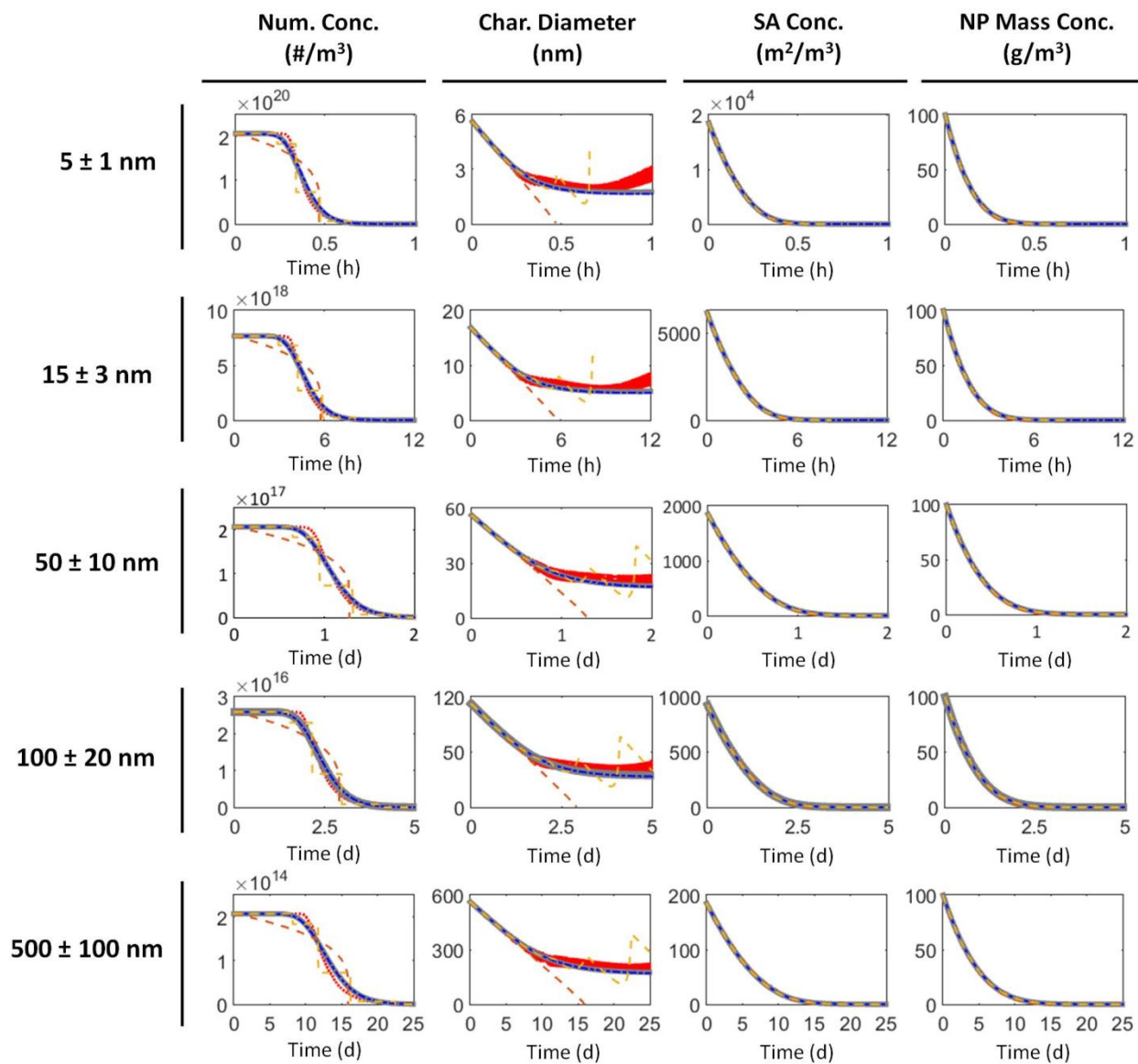


Figure C-2. Model results for dissolution of 100 g/m³ of a lognormal population of NPs (low skew) with different initial particle sizes for sink conditions (ion concentration in bulk solution is set to zero). Solid grey = Analytical Solution, Dot-dashed blue = Sectional Method (SM), Dashed orange = Direct Quadrature Method of Moments (DQMOM) with ratio constraints, Dashed yellow = DQMOM without ratio constraints, Dotted red = Extended Quadrature Method of Moments (EQMOM).

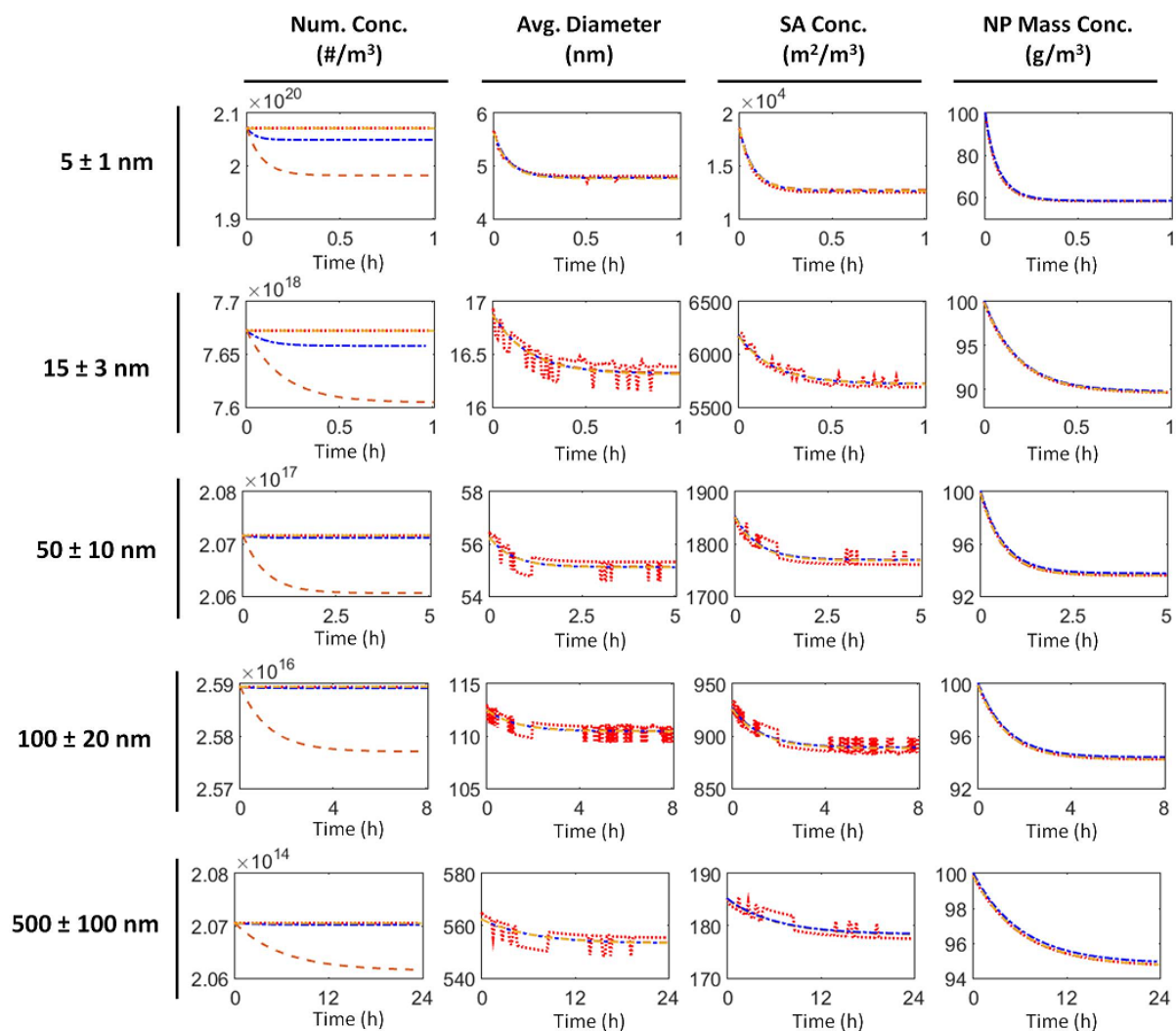


Figure C-3. Model results for dissolution of 100 g/m^3 of a lognormal population of NPs (low skew) with different initial particle sizes for dissolution to equilibrium (ion concentration in bulk solution increases until equilibrium is reached, at which point dissolution stops). Dot-dashed blue = Sectional Method (SM), Dashed orange = Direct Quadrature Method of Moments (DQMOM) with ratio constraints, Dashed yellow = DQMOM without ratio constraints, Dotted red = Extended Quadrature Method of Moments (EQMOM). No analytical solution is available for this case.

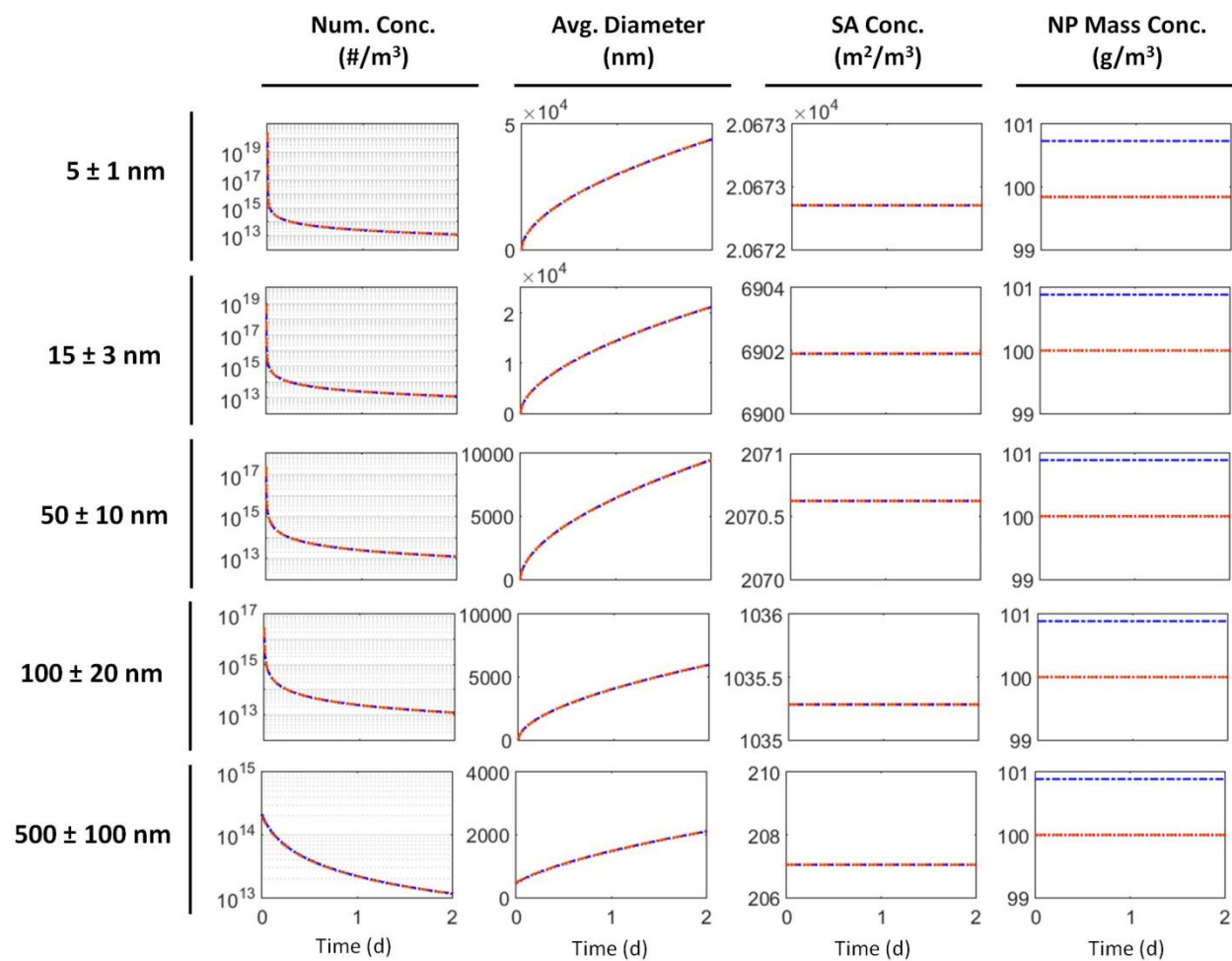


Figure C-4. Model results for aggregation of 100 g/m^3 of a lognormal population of NPs (low skew) with different initial particle sizes. Dot-dashed blue = Sectional Method (SM), Dashed orange = Direct Quadrature Method of Moments (DQMOM) with ratio constraints, Dotted red = Extended Quadrature Method of Moments (EQMOM). Analytical solution not shown.

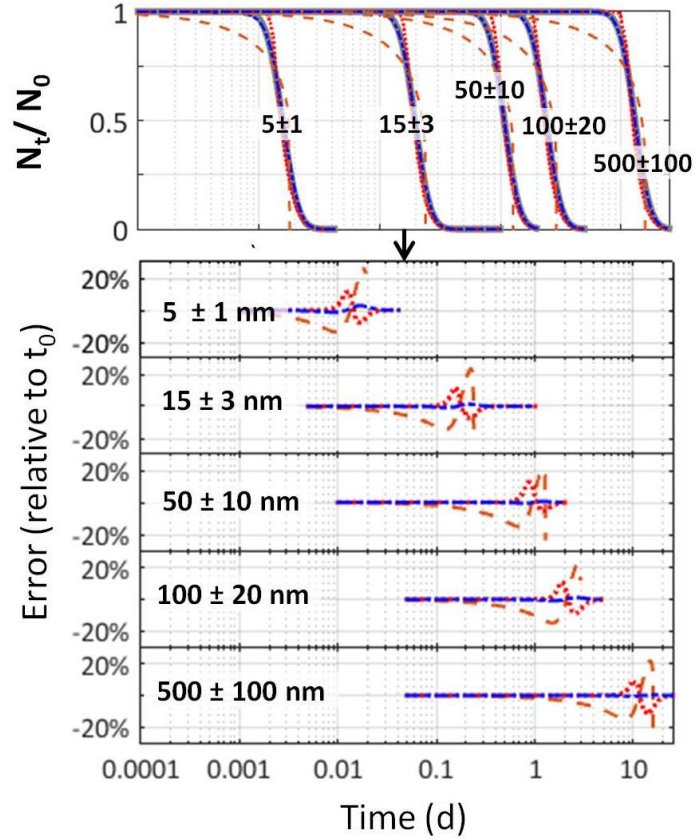


Figure C-5. Error in the EQMOM (dotted red), the DQMOM without ratio constraints (dashed orange), and the SM (dot-dashed blue) compared to the analytical solution (solid grey) for estimates of the evolution of the (normalized) number concentration during dissolution. Worst-case scenario (“sink conditions”) are assumed in order to maximize possible error (see Figure C-3(b) for results to equilibrium). The error calculation is not normalized. Error remains below 20% for the EQMOM, which also largely captures the nature of the dissolution curve.

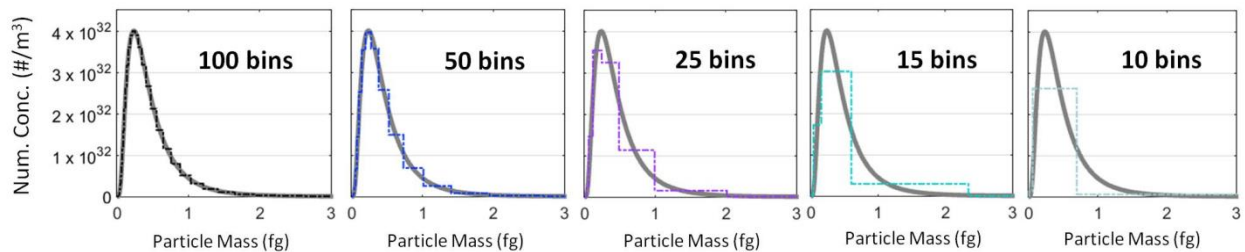


Figure C-6. Initial particle size distributions in the Sectional Method for the error analysis shown in Figure 4-4. Distributions were normalized by the bin width so that they could be overlain on the continuous distribution as shown.

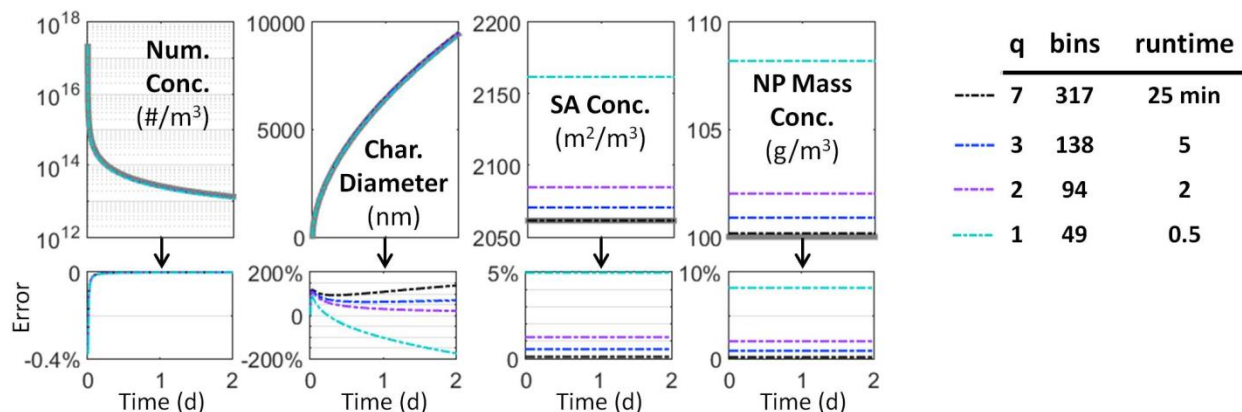


Figure C-7. Effect of the resolution of the size coordinate on error and runtimes in the SM for aggregation of $\sim 50 \pm 10$ nm NPs. Error is given relative to the analytical solution (solid grey). Unlike the numerical solution for dissolution, which can use an arbitrary binning scheme, the numerical solution for aggregation requires the geometric binning scheme defined in Equation 4-2. Thus q could not be reduced below 1 and the number of bins could not be reduced below 49.

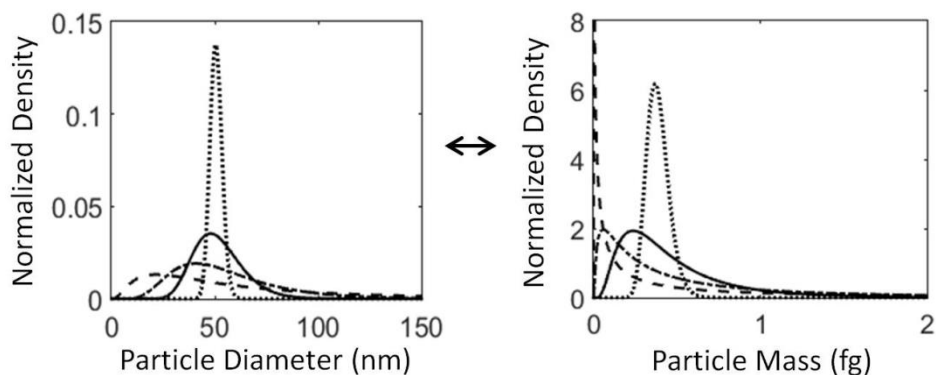


Figure C-8. Initial particle size distributions used in the analysis presented in Figure 4-5 (main text) transformed to be in terms of the internal coordinate, particle mass. Size distributions expressed in terms of mass are more skewed than distributions expressed in terms of diameter. The solid black curve represents the initial size distribution for 50 ± 10 nm NPs in our "base case" (e.g., Figure 4-2).

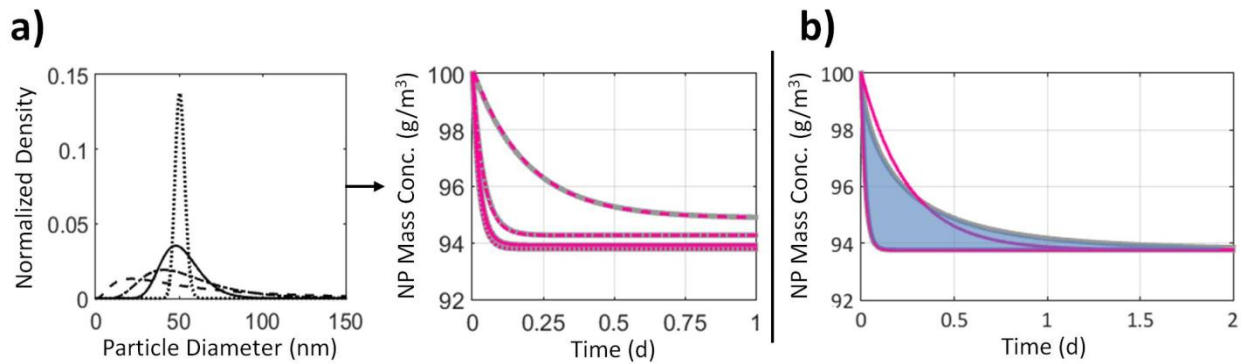


Figure C-9. First-order linear inhomogenous equation (Equation 4-24) fit for the case of dissolution to equilibrium (compare to Figure 4-5). The equilibrium ion concentration was calculated from the Ostwald-Freundlich relation using the initial surface-weighted geometric mean diameter. Benchmark curves (solid grey) in (a) represent the SM validated against the EQMOM and the DQMOM. In (b), curves represent the DQMOM validated against the EQMOM.